Control over Crystallography in Biological Mineralization - New Template Directed Biomimetic Approach

THESIS SUBMITTED TO

UNIVERSITY OF PUNE

FOR THE DEGREE OF

DOCTOR OF PHILOSOPHY

IN

PHYSICS

BY

DEBABRATA RAUTARAY

PHYSICAL & MATERIALS CHEMISTRY DIVISION
NATIONAL CHEMICAL LABORATORY
PUNE 411 008
INDIA

DECEMBER 2004

Dedicated to my Family

& to my mentor, Dr.Murali Sastry

C E R T I F I C A T E

This is to certify that the work discussed in the thesis entitled **"CONTROL OVER CRYSTALLOGRAPHY IN BIOLOGICAL MINERALIZATION - NEW TEMPLATE DIRECTED BIOMIMETIC APPROACH"** by **DEBABRATA RAUTARAY**, for the degree of philosophy in physics was carried out under my supervision at the Physical & Materials Chemistry Division of National Chemical Laboratory, Pune. Such material as has been obtained by other sources has been duly acknowledged in this thesis. To the best of my knowledge, the present work or any part thereof, has not been submitted to any other University for the award of any other degree or diploma.

Date: **Dr. Murali Sastry**

Place: Pune (Research Guide)

CANDIDATE`S DECLARATION

I, Mr. Debabrata Rautaray hereby declare that the work incorporated in this thesis entitled "**Control over crystallography in biological mineralization - new template directed biomimetic approach**" for the degree of philosophy in physics was carried out by me under the guidance of Dr. Murali Sastry (Physical & Materials Chemistry Division of National Chemical Laboratory, Pune). Such material as has been obtained by other sources has been duly acknowledged in this thesis. I declare that present work or any part thereof, has not been submitted to any other university for the award of any other degree or diploma.

Date: **Mr. Debabrata Rautaray**

Place: Pune

Acknowledgements

Debabrata Rautaray

I extend my sincere gratitude and appreciation to many people who made this PhD thesis possible. First and foremost, I would like to extend my sincere thanks to my supervisor ***Dr. Murali Sastry*** *for his dedicated help, advice, inspiration, encouragement and continuous support, throughout my PhD. His overly enthusiasm and integral view on research and his mission for providing only high-quality work and not less, has made a deep impression on me. I owe him lots of gratitude for having me shown this way of research. He might not even have realized, how much have I learned from him. Besides being an excellent supervisor, Dr. Sastry has always been very keen for his student's future. I am really glad to have known such a person like Dr. Murali Sastry in my life.*

Out with the work setting, I would also like to offer my fondest regards to my parents, brothers, sisters, brothers in law and sister in law who continue to give off themselves so that I will prosper in building my career. A special mention of thanks goes to my sister, brother in law and niece who have always extended their help and love whenever I needed the most.

*I am grateful to Dr. Absar Ahmad from Biochemical Sciences Division, National Chemical Laboratory***,** *Dr. A. V. Limaye, Dr. Arun Banpurkar from Department of Physics, University of Pune, and Dr. P. Wadgaonkar, Polymer Chemisry Division, NCL for fruitful collaborations. I could not have wished for better collaborators. Their contributions, detailed comments and insight have always been of great value to me and it was a great pleasure to work with them.*

I take this opportunity to express my gratitude to Dr. Sudhakar Sainkar who has contributed more than he can imagine to this thesis. I owe much to him for helping me throughout the period of my research by providing advice, support and a good training on Scanning Electron Microscope.

In my lab at NCL, I was surrounded by knowledgeable and friendly colleagues, who helped me daily. I would like to acknowledge, with much appreciation, the crucial role of Sumant, Saikat, Anita, Dr. Senthil Kumar, Kannan, Shankar, Hrushikesh, Ambarish, Akhilesh, Amit, Vipul, Atul, Sourabh, Ritwik, Pratap, Tanushree, Minakshi, Deepti, Dr.Banger and Dr.Ankamwar for embarking with me on this thesis journey. I thank you all for your care and attention.

The road to my graduate degree has been long and winding, so I would also like to thank some people from the early days. I would like to thank my seniors Dr.Anand, Ashavani, Murli, and Dr. Jaspreet who have gone out of their way in getting me familiarized with all the lab facilities and making me feel comfortable during my initial days of PhD. I would also like to take this opportunity to thank Mrs. S. Adyanthaya and Dr. B. L. V. Prasad who has always helped me in one-way or the other.

I would like to thank Dr. K. N. Ganesh and Mr. Pravin S. Shirude, Organic Chemistry (Synthesis) Division, for the fruitful work done with the Isothermal tritration calorimeter.

I am grateful to many people in the Center for Materials Characterization, NCL who have assisted me in the course of this work. My sincere thanks to Mrs. Renu Pasricha, Dr. N. R. Pavaskar and Mr. A. B. Gaikwad for making the facilities available during the research work.

I am grateful to Vipul, Amit, Kannan, Akhilesh and Ritwik for proof-reading thesis chapters and giving me valuable suggestions to improve it. Thanks, guys.

I had the pleasure to work with Kaustav, Aditya, Ragini and Gayatri who did their graduation projects in this lab and have been somehow beneficial for the presented work in this thesis.

Many thank to the staff member of our division, who have helped me in innumerable ways. Especially thanks to Deepak and Punekar.

I am grateful to Dr. P. Ratnasamy and Dr. S. Sivaram, former and present Directors of NCL, and Dr. P.Ganguly, Dr. S. K. Date and Dr. S. Pal, former and present Heads of, Physical Chemistry Division, NCL for giving me an opportunity to work in this institute and making most of the facilities available for carrying out research.

Department of Science and Technology (DST), India is greatly acknowledged for providing me valuable financial support.

Last but not the least, I would like to thank those closest to me, whose presence helped make the completion of my PhD thesis possible.

Table of Contents

Chapter 4: Mineral Growth at a Liquid-Liquid Interface

Chapter 5: Aqueous Foams as Templates for the Synthesis of Minerals

Chapter 6: Nano-Gold Membranes as Scaffolds for the Growth of Minerals

Chapter 7: Biological Synthesis of Minerals using Microorganisms

Chapter 8: Conclusions

List of Publications

CHAPTER I

Introduction

This chapter is an introduction to the thesis and starts with the motivation behind the work, carried out in this thesis followed by an overview of biomineralization process explaining the complex inorganic crystalline materials synthesized by natural organisms. The formation of various biomineral types and their specific biological functions has also been discussed. It further emphasizes the importance of biomimetic approach to construct and design new synthetic materials. The different biomimetic synthesis protocols currently in vogue for biomineral synthesis have been discussed. This chapter also briefly describes the motive behind the new biomimetic templates we have used for the crystallization of (bio)minerals. Finally, a chapter wise outline of the protocols described in this thesis, has been presented.

1. Introduction

1.1 Motivation

Crystals have always fascinated mankind [1] and yet crystallization remains to a large extent, a mystery [2]. No recipe exists to predict the shape, size, or system of crystals. The most interesting possibility is the engineering of crystals at the molecular level [3,4]. One of the ultimate goals of this field is engineering and construction of functional crystalline materials at the nano-scale. There is no doubt that crystal design can be performed by choosing building blocks and/or crystallization conditions, but in order for a crystal to have any practical utilization, it must have a controllable size and a shape, and often an orientation, that is adequate to the desired function. Crystalline materials are finding important applications in fields of optics, biomedical implants, drug delivery systems, pigments, cosmetics, ceramics polymers, and catalysis [5].

With evolution, Nature has ingeniously succeeded in giving rise to an impressive variety of inorganic crystals [6]. When biological systems are actively involved in the creation of inorganic solids, scientists speak of biomineralization. Scientists and engineers have long been inspired by the beautiful structures and functional properties of the materials formed within living organisms [7]. Nature knows how to build extremely specialized materials, which are constructed, indeed engineered, to exert specific biological functions [8]. Can we learn from nature how to build tailor-made crystals? This thesis is an attempt, taken ahead in this direction.

1.2 An Overview on Biomineralization Process

Biomineralization as a field of study involves many scientific disciplines including inorganic chemistry, molecular biology, geology, crystallography, materials science and condensed matter physics [4]. The term biomineralization represents the formation of inorganic solids by living organisms. Biominerals have a variety of biological functions, which rely on a hierarchical structuring of bioorganic-inorganic composites on several length scales from the Angstrom to the centimeter scale [6]. This phenomenon is widespread in the biological world and is mediated mostly by plants and animals. More than 60 biominerals are currently known, most of which are calcium carbonates, calcium phosphates, silicates, and iron oxides or sulfides [7-9].

A majority of animals and plants are known to synthesize biominerals [7-9]. For many species, survival depends on their ability to deposit the inorganic matrix quickly and efficiently. In plants, the biomineral is generally composed of silica or bioglass. A large class of organisms, forming a vast array of patterned biominerals, are the diatoms, which are one of the most plentiful organisms on the planet, low down on the marine food chain [10]. Mammals, birds and marine animals offer biominerals formed *via* the precipitation of calcium-based materials [11]. Hence the mechanism for their formation, at least in terms of their chemistry will be very different for these two classes of materials.

Growth and form of biominerals. The complex nature of inorganic materials formed in association with living organisms is not only expressed at the macro scale but resides in the nanoscopic, mesoscopic and microscopic organization of biomineralized structures [12]. Indeed, different length scales bring into operation different controlling forces and hence hierarchical orders of construction [12]. Despite these complicated hierarchical structures, one finds it most interesting to observe that the smallest building blocks in such materials are generally on the nanometer length scale. For example, the brick and mortar structure of nacre where the thickness of the aragonite bricks is around a few hundred nanometers [13]. The nanostructure of bone consists of mineral crystal platelets with thickness around a few nanometers embedded in a collagen matrix [14].

Minerals, macromolecules and water are the major components of these biomaterials. Among the biological materials that are formed under relatively controlled conditions, they can be differentiated based on the organization of their mineral constituents as follows [8b]. The first type is composed of multicrystalline arrays, in which the individual crystals are generally all aligned at least in one direction, and often in all three directions. The best known examples of such materials are bones, teeth and shells of various types. In the second type, a single crystal or a limited array of relatively larger crystals constitutes the entire structure. The echinoderms are best known for forming such large single crystal skeletal structures of calcite [8b,15]. The third group produce biological materials containing an amorphous mineral, the most common being amorphous silica. These structures can vary enormously in size and particularly in shape. The components that perhaps mostly distinguish biological materials from synthetic materials are biological macromolecules. They form an intimate mix or composite with

the mineral phase at all the different hierarchical levels, starting at the scale of nanometers. It was recognized that many of these macromolecules have common chemical attributes - they are rich in carboxylate groups [8a,16]. These may be constituents of the protein moieties and/or the polysaccharide moieties. Many of this class of macromolecules also have, in addition to the carboxylate groups, phosphate and/or sulfate groups. The presence of all these charged groups makes these macromolecules excellent candidates for interacting with the mineral ions in solution or with the surfaces of the solid phase [8a,16].

There are a variety of types of biominerals, as indicated in Table 1, and these biominerals can be found in various phyla of plant and animal.

Table 1. Variety of biomineral types and biological systems [17]

Biogenic Minerals	Formula	Organism	Biological location	Biological Function
Calcium Carbonates (calcite, vaterite, aragonite, Mg-calcite,amorphous)	$CaCO_3$ $(Mg,Ca)CO_3$ $CaCO \cdot nH_2O$	Many marine organisms, Aves, Plants, Mammals	Shell, Eye Lens, Crab Cuticle, Eggshells, Leaves, Inner ear	Exoskeleton, Optical, Mechanical strength, protection, Gravity receptor, buoyancy device, calcium storage
Calcium Phosphates (hydroxyapatite, dahllite,octacalcium phosphate)	$Ca_{10}(PO_4)_6(OH)_2$ $Ca_5(PO_4,CO_3)_3(OH)$ $Ca_8H_2(PO_4)_6$	Vertebrates, Mammals, Fish, Bivalves	Bone, Teeth, Scales, Gizzard plates, Gills Mitochondria	Endoskeleton, Ion store, Cutting/grinding, Protection, Precursor
Calcium Oxalates (whewellite, wheddellite)	$CaC_2O_4 . H_2O$ $CaC_2O_4 . 2H_2O$	Plants, Fungi, Mammals	Leaves, Hyphae, Renal stones	Protection/deterrent, Ca storage/removal, Pathological
Iron Oxides (magnetite,goethite, lepidocrocite, ferrihydrite)	Fe_3O_4 a-FeOOH, g –FeOOH $5Fe_2O_3 \cdot 9H_2O$	Bacteria, Chitons, Tuna/salmon, Mammals	Intracellular, Teeth, Head, Filaments, Ferritin protein	Magnetotaxis, Magnetic orientation, Mechanical strength, Iron storage
Sulfates (gypsum, celestite, barite)	$CaSO_4 \cdot 2H_2O$ $SrSO_4$, $BaSO_4$	Jellyfish, Acantharia, Loxodes, Chara	Statoconia, Cellular,Intrac-ellular, tatoliths	Gravity receptor, Skeleton, Gravity Device/Receptor
Silicon oxides (silica)	$SiO_2 \cdot nH_2O$	Diatoms, Radiolaria, Plants, etc.	Cell wall, Cellular, Leaves	Exoskeleton, Skeleton, Protection

Calcium carbonate ($CaCO_3$) is one of the most abundant biominerals formed by organisms. $CaCO_3$-based biominerals such as nacre of mollusk shells [13] and coccoliths [18] have complex structures of nano to sub-micrometer length scales. $CaCO_3$ has three anhydrous stable crystalline polymorphs, which have typical morphologies: calcite (the most stable, though not necessarily the most common; rhombohedral), aragonite (the strongest and metastable; needles), and vaterite (the highest energy configuration; polycrystalline spheres) in the order of increasing solubility and decreasing stability [10a,19]. Calcite has trigonal/rhombohedral symmetry, aragonite has orthorhombic symmetry and vaterite has hexagonal symmetry. In addition, amorphous $CaCO_3$ as well as crystalline mono- and hexahydrates are also known. While, calcite and aragonite are widespread in marine organisms, vaterite, monohydrocalcite, and amorphous calcium carbonate are formed and stabilized by a few organisms only [10a,19]. Most shells are constructed of calcite and aragonite in various arrangements with small amount of proteins. Many sea organisms such as corals, algae and diatoms make their shells out of calcite, they use carbon dioxide from environment dissolved in the seawater to accomplish this in a near reverse of the reaction above [7,8]. Most bivalve animals and corals secrete aragonite for their shells and pearls are composed of mostly aragonite. The pearlization and iridescent colors in seashells such as abalone are made possible by several minute layers of aragonite. One of the most studied shell structures is nacre, or mother-of-pearl, which is a layered structure of aragonite plates, 0.5 μm thick and several microns wide [13]. While the details of shell formation are not understood, it is clear that the organic content contains proteins capable of selectively nucleating calcite or aragonite in a specific orientation. The vaterite form of calcium carbonate often occurs in laboratory crystallization and is occasionally found in shells. There is also evidence for precipitation of amorphous, hydrated calcium carbonate as a metastable precursor for the crystal [20].

In addition to calcium carbonate, many biominerals rely on **calcium phosphate** as their inorganic material. Such biominerals differ considerably from the seemingly closely related calcium carbonate materials. Those based on calcium phosphate, are mostly variants of hydroxyapatite [$Ca_{10}(PO_4)_6(OH)_2$; HAP]. Of the several commonly encountered calcium phosphate phases, HAP is thermodynamically the most stable and is usually assumed to be a model structural component for biological mineral phases [21].

However, other phases such as dicalcium phosphate, dicalcium phosphate dihydrate, octacalcium phosphate, and tricalcium phosphate, may also participate in the crystallization reaction. Crystallization of many sparingly soluble salts probably involves the formation of metastable precursor phases such as amorphous calcium phosphate, which subsequently dissolve and transform as the precipitation reaction proceeds to the thermodynamically more stable HAP [22]. Examples in this class include the human skeleton and teeth. Biomineralization of bone involved the deposition of apatitic crystals on a matrix rich in collagen fibrils, the structural macromolecules that create the scaffold within which the biological mineral is formed [23].

While these groupings dominate, they are not exclusive. Other inorganic phases found in nature are mostly of Iron oxides, barite, calcium sulfates, barium or strontium carbonates, calcium oxalate, and gypsum [7-9]. Nature employs the varying chemical nature of the substituents to tailor a material for a particular purpose [16, 23].

1.3 Biomimetic Engineering : The Art of Imitation

Material scientists are trying to learn from nature to develop new synthetic materials with sophisticated properties. The attempts to adopt/utilize the constructional principles of natural materials have acquired the term biomimetics: the art of mimicking biology [24]. Scientists are supporting biomimetic research with a view to learn the way biological systems process information. Material scientists view biomimetics as a tool for learning to synthesize new materials. Engineers attempt to explore the relationship between structure and function in natural systems with a view to achieve analogous synthetic design and manufacture. On the whole, the field of biomimetics addresses more than one issue.

Designs found in nature are the result of millions of years of competition for survival [24,25]. Nature makes economic use of materials by optimizing the design of the entire structure or system to meet multiple needs [7-9]. Seemingly, it would be difficult for the materials engineer to mimic complex cellular processes, however, the materials chemistry aspects of it can be studied by model systems, and can be utilized for biomimetic engineering. One particular aspect of interest to the materials scientist is the means by which organisms use organic constituents to mediate the growth of the mineral phases. For example, macromolecular templates are used to direct the nucleation event,

vesicular compartments to delineate particle size and shape, and solubilized proteins to regulate the kinetics of crystal nucleation and growth [26]. An exciting report was presented by Mann and Walsh [27], who have created hollow shells from their reticulated aragonite films by casting them on the surface of microscopic, gold-coated polystyrene beads, which they subsequently dissolved away using acetone and ethanol. Placed side by side with a coccolithophore shell, Mann's hollow spheres are a convincing imitation of nature [27].

Studies over the last few years show that there are several distinct characteristics of biomineralization.

(a) Biomineralization occurs in well-constructed compartments or microenvironments.

(b) These compartments have the ability to promote the nucleation and growth of crystals of the required inorganic material at chosen sites while effectively preventing the formation of crystals at other sites.

(c) The crystal size and shape are well defined and show little variation, if any.

(d) Formation of the macroscopic structure is through the packaging of many such units. The structures arisen are highly organized from molecular (1–100 Å) to macro-scales through nanometric (10–100 nm) and mesoscopic (1–100 μm) domains. These are hierarchical in nature and meet the functional requirements.

Thus, biomineral systems offer ample opportunity for investigations directed at the development of biomimetic strategies for the synthesis and processing of inorganic-organic composites and templated crystals [26].

1.4 Different protocols for Biomineral synthesis

Most of the researchers' interest lies in understanding how the organized inorganic materials with complex morphological form can be produced by biomineralization processes and how such complexity can be reproducibly synthesized in biomimetic systems. Because of the complexity of the natural biomineralization systems, mineralization research has been studied on model organic interfaces. Various synthetic protocols with a view to mimic biomineralization are outlined below.

1.4.1 Langmuir-Blodgett (LB) Monolayers

Langmuir monolayers are organized molecular films of amphiphilic molecules formed at the air-liquid interface [28]. Crystal growth at the air-water interface is an important area of research that involves the use of Langmuir monolayers of surfactant molecules as molecular templates for the oriented nucleation of inorganic crystals [29]. Mann and co-workers used compressed Langmuir monolayers of appropriate molecular structures for the controlled nucleation of inorganic crystals such as $CaCO_3$ [30] and $BaSO_4$ [31]. The effect of head group identity, polarity and the packing arrangement of the amphiphiles on the crystallization of minerals have been systematically investigated [30,31]. For example, Heywood and Mann have studied the oriented nucleation of $BaSO_4$ under compressed Langmuir monolayers of long chain alkyl phosphonate resulted in plate-like outgrowth as well as bow-tie morphology [32] and under n-eicosyl sulfate/eicosanoic acid monolayer, resulted in unusual and complex morphology of $BaSO_4$ crystals [31b]. Similarly, compressed Langmuir monolayers of saturated long alkyl chains induce oriented calcite and vaterite crystals [30a,33]. Litvin *et al.* [30e] and Heywood *et al.* [30d] have also succeeded in growing the metastable polymorph aragonite crystals at the air-water interface using compressed monolayers of 5-hexadecyloxyisophthalic acid and under monolayers of eicosanoic acid and n-eicosyl sulfate. Such controlled nucleation at the inorganic-organic interface was explained by using model based on electrostatic, geometric and stereochemical interactions. Monolayers of amphiphiles such as tricarboxyphenylporphyrin iron (III) μ[SA1]-oxo dimers [34] and *N,N*' dioctadecyltriazine-2,4,6-triamine [35] were used to grow oriented calcite crystals. Oriented crystallization of calcite single crystals were grown underneath monolayers of tetracarboxyresorcarenes by Volkmer *et al* [36]. Very recently, Kim and co-workers have shown the controlled growth of vaterite and aragonite polymorphs of $CaCO_3$ crystals at the air-water interface by the mediation of poly(ethyleneimine) [37]. Langmuir films at the air-water interface have also been used as templates for the nucleation and growth of iron oxides [38] and hydroxyapatite [39] crystals.

1.4.2 Self-Assembled Monolayers (SAMs)

Self-assembled monolayers (SAMs), which have better ordered structures compared to Langmuir monolayers, are expected to serve as templates for more precise

control over crystallization [40]. SAMs are molecular assemblies formed spontaneously by immersion of an appropriate substrate into a solution of an active surfactant in an organic solvent [41]. The most studied system is that of an alkanethiol [$HS(CH_2)X$ with $X=CH_3$, CF_3, $CHCH_2$, CH_2OH, COOH, etc.] interacting with a gold surface [42]. Tremel and co-workers examined the effects of chain length and the ω-substituents of thiols on the morphology and polymorphs of $CaCO_3$ [43]. They have shown that aragonite was favored for SAMs of substituted disulfides derived from anthracene-2-carboxylic acid [43d]. They formed centered rectangular lattices when assembled on a gold (111) surface. They have also used gold colloids instead of flat gold surface as templates where crystallite assemblies of calcite were formed around the gold colloids coated with *p*-sulfonylphenol SAMs [44]. Aizenberg and co-workers used micropatterned SAMs for $CaCO_3$ crystal growth [45]. The patterned SAMs of alkanethiols on the metal substrates by microcontact printing into acid- and methyl-terminated regions [45a]. By a suitable choice of pattern spacing, calcite crystals nucleated exclusively on the acid terminated regions. Unusual needle like aragonite crystals have been obtained from a solution containing 4-mercaptobenzoic acid capped gold nanoparticles and Mg^{2+} [46]. SAMs prepared from *p*-mercaptophenol as the substrate was also used for the crystallization of $SrCO_3$ crystals resulted in a needle like morphology [47].

1.4.3 Polymers

In nature, biological organisms produce polymer inorganic hybrid materials such as bone, teeth, diatoms, and shells. These hybrids have superior mechanical properties when compared with synthetic hybrids. Bio- and synthetic polymers for the modification of mineral morphologies have been studied in great details.

1.4.3.1 Biopolymers

Biopolymers direct an *in vitro* study of biomineralization, which provides useful information for the design of organic templates [48]. Biopolymers are used as frameworks for inorganic crystals such as calcium carbonate, hydroxyapatite, iron oxide, and silica [49]. Falini and co-workers assembled in vitro a complex containing the major matrix components present in a mollusk shell, namely, chitin, silk fibroin-like protein, and water soluble acidic macromolecules [19a]. When this assemblage was placed in a

saturated solution of calcium carbonate, multi crystalline spherulites formed within the complex. They extracted aspartic acid-rich glycoproteins from an aragonitic mollusk shell layer or a calcitic layer. These were aragonite if the added macromolecules were from an aragonitic shell layer or calcite if they were derived from a calcitic shell layer [19a]. Addai and co-workers purified the soluble macromolecules by ion-exchange chromatography from an aragonitic shell layer of the mollusk *Atrina serrata* to better understand their individual functions of the fractionated proteins in an *in vitro* system [50]. A small fraction within the entire macromolecular ensemble, consisting of only 6 mol % of the total amino acids, has a remarkable ability to nucleate aragonite. Belcher *et al.* demonstrated *in vitro* studies of the crystallization of calcium carbonate in the presence of soluble polyanionic proteins extracted from abalone shell [51]. Morphology variation and polymorph selectivity of $CaCO_3$ crystals has been achieved by using suitably designed additives such as proteins extracted from $CaCO_3$-rich bioorganisms [19a,52]. The effects of macromolecules extracted from sea-urchins have been used as soluble additives for the crystallization of calcium carbonate [53,54]. For example, ordered macroporous structures have been produced by templating echinoid (sea-urchin) skeletal plates [54]. Polymorph and morphology of $CaCO_3$ crystals have been induced by mollusk shell proteins extracted from nacre [52a,55]. A peptide phosphorylated hexapeptide (DpSpSEEK) derived from the *N*-terminus of the salivary protein statherin was observed to inhibit hydroxyapatite growth as well [56].

1.4.3.2 Synthetic polymers

The influence of synthetic polymer additives on the nucleation and crystal growth of minerals has been studied by a number of authors. The influence of α, ω-dicarboxylates on the morphology of calcite crystals grown from supersaturated bicarbonate solution was systematically studied by Mann and coworkers [57]. A rigid, unsaturated molecule such as maleate, with a short linkage between terminal carboxylates was a more effective inhibitor than the homologous saturated molecule succinate. The surface complexation of calcite by small molecules appears to follow the general rules that apply to complexation in solution [58]. The polymorphs and morphologies of $CaCO_3$ crystals were influenced in the presence of phosphorus- or sulfate-containing anions [59]. Ogino *et al.,* stated that ethylenediamine-tetrakis-*N*,*N*,*N*,*N*-(methylenephosphonic acid)

(EDTMPA) completely inhibited the phase transitions of metastable calcium carbonate phases [60]. In the presence of EDTMPA, vaterite modification agglomerates were formed, with primary vaterite spheres strongly bound by an amorphous mass.

Water insoluble polymers such as chitin [61], collagen [62], elastin [63], carboxylate containing polyamides [64] and polyacrylate [65] have also been used for mineral growth by various groups. The process of crystallization and the interactions between polymers and crystals have been extensively examined. Biomimetic synthesis of $BaSO_4$ [66] and hydroxyapatite [67] in the presence of an insoluble organic polymer matrix has also been investigated for the preparation of mineral-polymer composites.

Dendrimers are spherical molecular assemblies and were recently discovered as active additives for controlled $CaCO_3$ precipitation. Because of unique and well-defined secondary structures of the dendrimers, they are good candidates for studying inorganic crystallization. Dendrimer allows the interaction with a large amount of surfactants, this system appears extremely versatile with respect to chemical functionality and shape of the dendrimer aggregates and thus $CaCO_3$ morphology and polymorph [68].

Double hydrophilic block copolymers (DHBCs) are a simplified model system for active proteins in biomineralization without hydrophobic domains and with acidic peptide domains [48]. They consist of a hydrophilic block, which does not, or only weakly interact with crystal surfaces providing stearic stabilization in water and a second polyelectrolyte block, which interacts with inorganic surfaces. For example, with a poly(ethylene glycol)-blockpoly(methacrylic acid) block copolymer (PEG-b-PMAA), at least two different mechanisms were found for the morphology control of $CaCO_3$ [69]. Apart from $CaCO_3$ [70], other mineral compositions such as $BaSO_4$ [71], $BaCO_3$ [72], $BaCrO_4$ [71a,73] and calcium phosphate [74] have also been successfully generated by using DHBCs as crystal modifiers. Yu *et al.,* have reported highly ordered funnel-like $BaCrO_4$ and long $BaSO_4$ fiber bundles by using sodium polyacrylate as crystal growth modifiers [71a]. They have also reported on the morphogenesis of $BaCrO_4$ by using DHBCs as crystal growth modifiers [73].

1.4.4 Crystal growth in a Constrained Environment

Various attempts have also been made to control the morphology of inorganic crystals nucleated in constrained environments such as those afforded by microemulsions

[75-83], vesicles [84], and gel matrices [85]. Microemulsions have attracted considerable attentions in view of their applications in the preparation of fine particles [75-83]. Microemulsion made up of anionic surfactant sodium bis-2-ethylhexyl-sulfosuccinate (AOT) have been used in the synthesis of nanoparticles of barium chromate [75], barium sulfate [76], calcium sulfate [77], calcium carbonate [78], barium carbonate [79], silica [80] and copper [81]. Li *et al.* have reported the formation of linear chains, rectangular super lattices and long filaments of $BaCrO_4$ using AOT reverse micelle and microemulsions [75]. Kim and co-worker has employed reverse micelle templating method for the synthesis of $BaCrO_4$ and $BaWO_4$ assemblies using LB technique [82]. The synthesis of nanowires of $BaCO_3$ [79] and $SrCO_3$ [83] was also achieved successfully using microemulsions. Similarly, vesicles [84] and gel matrices [85] have been used as confined reaction cavities for the controlled synthesis of dispersed inorganic nanocomposites. For example, Falini *et al.,* investigated $CaCO_3$ crystallization on cross-linked gelatin films containing polyelectrolytes [85b], which induced oriented growth of calcite crystals. Partially oriented aragonite crystals have also been obtained in the uniaxially elongated gelatin films containing poly-L-asparate [85c]. The involvement of vesicles appears to be a general feature of many biomineralization processes [7d,84]. Surfactant molecules possessing one head group and two alkyl tails generally form vesicles in aqueous solution. For example structures such as phospholipid vesicles. The vesicles are secreted and assembled prior to biomineralization and function as membrane-bounded reaction environments for inorganic deposition. In some organisms, groups of vesicles are used spatially to pattern and organize the mineral crystals into arrays and superstructures. For example, an elliptical ring of vesicles is assembled prior to the formation of elaborate calcium carbonate structures called coccoliths [18,86].

1.4.5 Designed and Small molecular additives

A growing area of research in crystal growth is growth inhibition, which leads to interesting morphology change/ polymorph control. Numerous studies have shown how morphology and crystallography may be affected or induced upon molecular adsorption of additives onto specific faces of growing crystals, which alters the relative growth rates of the different crystallographic faces. Leeuw *et al* have suggested that these foreign ions play an important role during crystal growth and interact *via* long-range electrostatic

forces and short-range forces, including both the repulsions and the Vander Waals attractions between neighboring electron charge clouds [87]. Davis *et al* have pointed that the incorporation of impurities molecules induces strain in the solid lattice, thereby increasing the internal free energy of the crystal [88]. Many impurity ions are found to affect inorganic crystal growth. The effect of incorporating foreign ions such as Cd, Sr [89], Cu, Mn [90], Fe [89,91], Co [92], Li [93], Mg [89,94] and organic matter [95] into $CaCO_3$ crystals has been studied in great detail. In particular, Mg^{2+} has been studied extensively as an additive [89,94], mainly because Mg^{2+} ions are found in biological environments in high concentrations and are believed to play a critical role in $CaCO_3$ formation in nature [96]. A different morphological form can be induced in oriented calcite crystals by adding Li^{+} ions to the subphase of a Langmuir trough [97]. When this ion introduced in to a subphase of supersaturated calcium bicarbonate under compressed monolayers of a long chain alkyl sulfate, triangular calcite crystals were nucleated. Oriented calcite crystals have been observed for calcite nucleation under eicosanoic monolayers in the presence of low level of Mg^{2+} ions [30f]. Dalas and co-worker have shown vaterite stabilization from aqueous solution in the presence of organic solvents such as ethanol, isopropanol and diethylene glycol [98]. Selective binding of amino acids to mineral surfaces such as $BaCO_3$ [99] and $CaCO_3$ [100] crystals have also been studied extensively. For example, the generation of calcite chiral morphologies in the presence of aspartic acid [100].

1.5 Templates used for Mineral growth in this thesis

One of the most common ways in which organisms exercise architectural control over the formation of their structural and functional components is by the use of templates to guide the growth process. For example, organic tissues template the formation of bone and shell. We have used new chemical templates such as thin lipid matrix, liquid-liquid interface, aqueous foam and polymeric matrix, and biological templates such as microorganisms for the crystallization of minerals/biominerals. A very brief overview on each template is outlined below.

1.5.1 Thin Lipid Matrix

Inorganic materials in nature are generally grown within an organic matrix that exerts a strong influence on the shape of the crystals [101]. In bone (where the matrix is primarily the protein collagen), the crystals of apatite formed are flat plates; in tooth (where the matrix consists largely of the proteins enamelin) the crystals are in the form of needles [14]. In shell, two different forms of calcium carbonate (calcite and aragonite) grow within protein matrix, which determines both the carbonate phase and the crystal shape [13]. The degree of control exerted on crystal growth during biomineral formation extends over a wide range of length scales, from the atomic (the organic matrix can determine the way in which ions are packed together in the crystal) to the macroscopic (organics are responsible for the overall patterning of many skeletal and shell shapes).

How does the organic material exercise this influence? It seems likely that it acts as a kind of template, imposing certain constraints in the way that the inorganic ions stick to its surface [24]. There are several ways in which these constraints can be applied. One is through complimentarity of charge: a positive (calcium) ion will prefer to stick to negatively charged region of matrix, such as an acidic site containing a carboxylate group [16,24]. Another is the deposition of these binding sites, the distance between them, and their geometric arrangements. The spacing between ion in a crystal generally differs depending on the direction in which we look at the crystal structure-that is, it varies for different crystal faces. So if ion-binding sites within the organic matrix are disposed so as to secure ions in an arrangement corresponding to that along a particular crystal face, the preferential growth of that crystal face can be encouraged. The crystal then grows with its axes in particular orientation. One might recognize this as a process akin to epitaxial growth: the substrate (the organic lipid matrix) acts as a template for epitaxial growth of the inorganic crystal [101].

It has been established in this laboratory that thermally evaporated fatty lipid films can spontaneously organize themselves *via* selective ionic interactions of various cations/anions by immersion of the lipid films in the appropriate electrolyte solutions [102]. The electrostatic entrapment of metal ions in the lipid matrix leads to an organized lamellar film structure similar to *c* - axis oriented Y-type Langmuir-Blodgett films. These well defined compartments or specific cells can be used to influence the final shape of the

minerals. In chapter 3, we have attempted to mimic the principle of nature by using the potential of ionizable lipids in the form of thin film as a crystallization template.

1.5.2 Liquid-liquid Interface

Interfaces play a key role in modern science and technology and the unique features and phenomena induced in them have attracted the interest of researchers in many different fields. In particular, liquid-liquid interfaces have drawn much attention; not only do these interfaces have structural and dynamical nonlinear properties which are not observed in bulk liquids, but also they are integral to many physical, chemical and biological systems. The liquid-liquid interface has been used with considerable success in the synthesis of numerous inorganic materials. However, in all these studies, the interface at which the synthesis is carried out was static. In chapter 4, we have used a Hele-Shaw set up (normally used for studying viscous fingering formation) as a dynamic charged liquid-liquid interface for assembling minerals.

Hele-Shaw cell. The viscous fingering is a process, in which high viscosity liquid when displaced by low viscosity liquid in a thin linear channel, results into a finger like structure [103]. This process has been efficiently simulated using a simple experimental setup famous by name Hele-Shaw cell. Hele-Shaw cell is commonly used for investigating viscous fingering [103-105]. A Hele-Shaw cell consists of two parallel plates with a narrow spacing; when a less viscous fluid is driven to displace a more viscous one in the cell, an initially flat interface between the two fluids evolves into a *viscous fingering* pattern. The evolution of viscous fingering patterns can be controlled by various parameters, like miscibility, surface tension, displacing force, channel width for displacement, viscosity etc.

While the Hele-Shaw cell has been used extensively in understanding the underlying physics of dynamic instabilities at liquid-liquid interfaces, its use in chemistry in probing surfactant-mediated interfacial recognition events has only recently been attempted, such as the influence of chemical reaction on hydrodynamic instabilities (the fingering instability) originating from a difference in viscosity/density between two fluids. Sastry *et al.,* in 2001 showed interesting changes in the viscous fingering patterns when experimented with non-Newtonian fluids in the presence of surfactant [106]. They have used a surfactant solution (water + SDS) where the surfactant concentration is

above the critical micellar concentration (CMC), and paraffin oil (a more viscous fluid). This study shows that in rectilinear Hele-Shaw flows, the finger width relative to the width of the channel is larger than the asymptotic limit of ½ observed for the Saffman-Taylor finger at high capillary numbers. They have also observed that the fingers were wider than the standard patterns, with a fractal dimension of about 1.8 [106]. Very recently Fernandez and Homsy (2003) have also studied the interaction between viscous fingering patterns and the chemical reaction [107].

1.5.3 Aqueous Foams

Aqueous foams are a mixture of a gas and a liquid stabilized by a surfactant, consisting of gas bubbles dispersed in a liquid. They belong to a wide class of non-equilibrium systems such as emulsions or off-critical decomposing mixtures that rearrange and coarsen with time [108]. Aqueous foams are typically 95% air and only 5% liquid, and the liquid itself is often 99% water. The remaining consists of surfactants and other foam stabilizing additives. The presence of surfactant or surface-active reagent help to reduce the surface tension enabling foaming [108]. Gravity also acts on the liquid in the foam films, gradually draining it out of the films. As a result, the films in foam are rendered metastable, that is stable with respect to small disturbances. As the foam drains, the bubbles remaining in the foam respond to the changing balance of forces by changing from spheres into polyhedrons. Fig.1.1 shows a generalized picture of the length-scales (from microscopic to macroscopic) associated with aqueous foam.

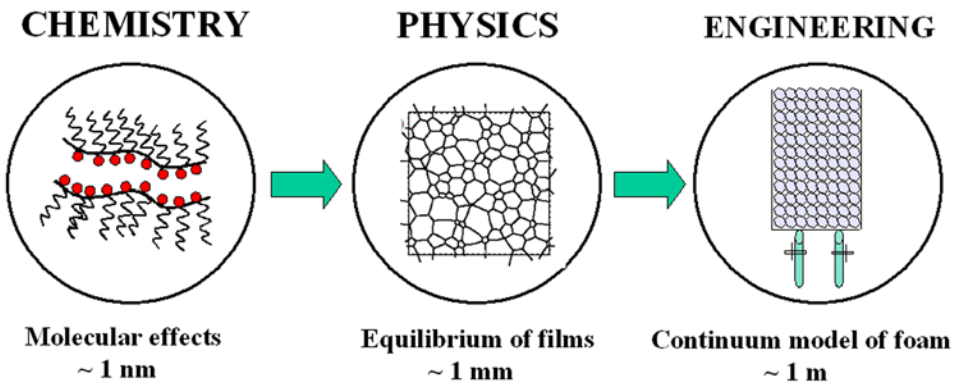

Fig.1.1: *A generalized picture focused on various length-scales from the microscopic to the macroscopic.*

Role of Surfactants. A surfactant's surface activity depends on the sizes of these groups and their relative solubilities. Because of the differing solubilities, surfactants are

surface active, that is, they accumulate at surfaces. In particular, the hydrophobic groups on the surfactant molecules accumulate at air-water interface. For surfactant molecules, the surface is not as energetically unfavorable as it is for water molecules. Consequently, the surface tension is reduced because the surfactant molecules occupy the surface positions and the water or liquid molecules can occupy places in the bulk liquid. Without this reduction in surface tension, the liquid can not be transformed from its bulk state, which has a minimal surface area into foam with its myriad films, which gives the liquid a far larger total surface [108].

Two factors govern the ability of a liquid (under the influence for example of mechanical agitation) to froth into foam [109]. The first is surface tension, which causes contracting forces along the surface of the liquid. As a result, liquids always try to minimize their surface area. The reason why a bubble remains stable and does not collapse is that there is an excess pressure inside the bubble, which produces forces acting on the bubble surface that exactly balance the forces due to surface tension. The second factor is that, there are attractive forces between the molecules of the liquid. These forces are electrical and originate from individual charges or dipoles (permanent distribution of charges) on the molecules of the liquid. Molecules deep in the liquid have identical surroundings in all directions, they are attracted isotropically or equally in all directions by their neighbours. In contrast, molecules near the surface have few if any neighbors closer to the surface, thus they are attracted preferentially towards the bulk fluid. Moving a molecule from the bulk fluid to the surface therefore requires work against the forces in the liquid. Hence the surface is in a higher energy state than the bulk of the fluid. The unbalanced molecular forces near the surface manifest themselves as surface tension or surface energy [108].

The radius of curvature R of a liquid film with surface tension γ and pressure difference Δp between the bubbles it separates, is given by the Laplace-Young law [109]:

$$R = 4\gamma / \Delta p$$

According to this law, liquid films will be curved towards the lesser pressure region. Smaller bubbles will have higher pressure.

Foam Structure. In a foam, the basic distinction is between wet and dry foams. In wet foam, the liquid content is high, so the walls of the cells are thick. As a result, the cells

are far enough apart so that one does not distort another. Hence the cells are spherical, for the same reason that water droplets are spherical: surface tension causes isolated bubbles or drops to take a spherical shape, which minimizes their surface area. As liquid leaves the foam so that the foam dries, its geometry becomes more complex. The cells now separated by thinner walls, begin to influence one another. Thus, the spherical bubbles become polyhedrons. Typical wet and dry foam pictures have been shown as Fig.5.2 in chapter 5.

The physics that determine the geometry of dry polyhedral foam emerge from observations made by the Belgian physicist Joseph Plateau nearly a century ago [109]. From his observations he developed a set of rules, which govern the equilibrium of soap films and foams:

1. Three soap films meet at angles of 120 degrees.
2. The films form a curved triangular channel known as a *Plateau border*.
3. Four Plateau borders meet at angles of 109.6 degrees to form a *vertex*.

Plateau borders are the channels that form where films meet. Most of the liquid in foam is in the Plateau borders. When three films produce a Plateau border, the angles between them are equal, at 120 degrees, owing to a balance of surface tension forces. The meeting of four Plateau borders must always take the form of a tetrahedral vertex so that the angle between any two of the borders is the tetrahedral angle of about 109 degrees [109].

Foam Stability. Once a liquid has foamed, the question is whether the foam can persist for any appreciable length of time. The development and stability of a liquid foam is governed by three main processes [110]:

Drainage: liquid will drain through the Plateau border channels until an equilibrium state is reached.

Coarsening: gas diffuses between bubbles - some grow while others shrink and disappear. The net result of this process is that the average bubble size grows in time.

Film rupture: if a foam film gets too thin and weak, it will rupture. Eventually the foam will collapse and vanish.

Drainage in Foam. Foam drainage plays an important part in the formation and evolution of liquid foams [111]. A freshly formed foam is not in equilibrium under gravitational and capillary forces, and liquid drains out of it until such an equilibrium is

attained (Fig.1.2). This is free drainage. Forced drainage, on the other hand, is the steady flow through otherwise static foam, which can be produced by continuous addition of liquid at the top.

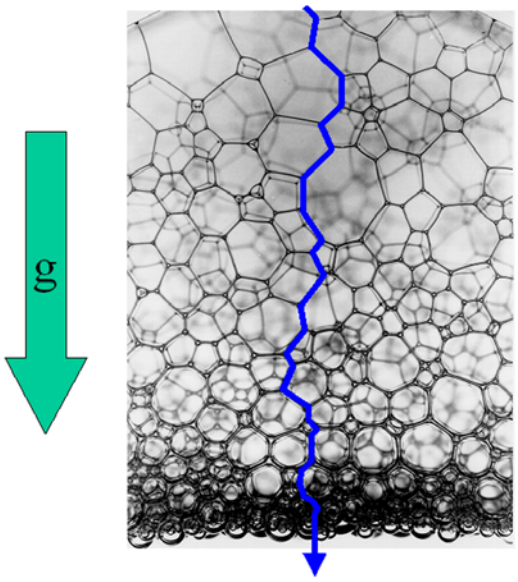

Fig.1.2: *A typical foam in a column shown under the influence of gravity, the liquid drains downwards in between the bubbles - primarily through the Plateau borders. As the drainage proceeds, the Plateau borders shrinks.*

The drainage in aqueous foams occurs in the Plateau border channels. Flow in such a channel is described as a Poiseuille flow in a cylindrical tube with the same cross-sectional area [111]. The channels have a random orientation toward the direction of gravity (Fig.1.2) and their cross sections are independent of their orientation.

Coarsening. The gradual growth of the average size of the bubbles in foam, known as coarsening [112], which is due to the exchange of gas between bubbles. As the foam drains, the bubbles remaining in the foam respond to the changing balance of forces by changing from spheres (wet foam) into polyhedrons (dry foam).

Film rupture. Thus films drain into the Plateau borders by capillary suction [109,111]. As the liquid drains down, the liquid films become thinner and, due to instability, break. Thus, foam stability can be controlled by altering its drainage characteristics.

We have exploited the dynamic nature and the large interfacial area provided by bubbles in aqueous foam as a crystallizing template for the synthesis of minerals and this aspect will be presented in chapter 5.

1.5.4 Polymeric Matrix as a means of Bone Implant/Grafting

The development of new biomaterials for medical applications is one of the challenging tasks for materials science today. In particular, there is an obvious need for better implants as well as the manufacturing of artificial tissues. A characteristic feature of this research area is the importance of biologically inspired approaches. Bio-inspired materials open new models for manufacturing implants for bone replacement. Bone is the major calcification present in a human body [113], which serves as structural (mechanical) support for the body. Bone is an inorganic–bioorganic composite material consisting mainly of collagen proteins and hydroxyapatite, and its properties depend intimately on its nano-scale structures [114]. From the chemical point of view, bone is a composite material of calcium phosphate and collagen [7a,114,115]. Different routes for new bone implant materials are presented using the principle of functional gradation. The scaffold has to be functionally graded in order to create an optimized mechanical behavior as well as the intended improvement of the bone ingrowth [116]. Consider the example of orthopedic implants for shoulder and knee joint replacements [116]. In order to improve the acceptance of artificial implants by living tissues, a functionally graded interlayer of biopolymers is a favorable approach [116].

The development and optimization of bone regeneration techniques represent a major clinical need [117]. A large number of bone fractures have been treated by bone grafting. High amounts of autogenous bone grafts are needed in revision surgery with severe loss of bone [118]. Bone fractures are usually treated with metallic wires, nails, screws and plates; joints are replaced by artificial endoprostheses (hip or knee), and lost teeth are replaced by metallic implants in the jaw, to name a few examples [113]. As soon as foreign materials come into internal contact with the body, the question of biocompatibility becomes paramount, as any adverse effect (namely toxicity, allergy, inflammation, corrosion, and mechanical failure) must be strictly avoided. The search for optimally designed biomaterials is still ongoing as a joint effort of physicians, engineers, chemists, and physicists [119]. Calcium phosphate ceramics have received much attention as potential bone graft substitutes during the past decades primarily because of their biocompatibility, bioactivity, and osteoconduction characteristics [120].

Biomedical applications of polymeric materials have faced many critical obstacles such as undesirable protein adsorption and cell adhesion, due to the poor biocompatibility of conventional polymer surfaces. To solve these problems, an enormous number of basic and applied researches have been devoted to the surface modifications of polymeric materials [121]. Synthetic polymers have the advantage of sustaining the release of the encapsulated therapeutic agent over a period of days to several weeks compared to natural polymers, which have a relatively short duration of drug release, they are in general limited by the use of relatively harsher formulation conditions [122]. The synthetic polymeric scaffold for medical applications like implants and tissue engineering matrices must have sufficient mechanical stability and elasticity as well as desired stability towards degradation, and should be non-toxic [123]. It has been shown that methods of implant surface preparation can significantly affect the resultant properties of the surface and subsequently the biologic responses [124].

In chapter 6 we have presented a biocompatible polymeric scaffold used for the synthesis of bioactive ceramics such as calcium carbonates and phosphates.

1.5.5 Biogenic Strategies

Investigation of biomaterial formation and structure-property correlation provides lessons for novel material fabrication through biology [125]. It is worthwhile to learn what a biological hard tissue is composed of including physical and chemical characteristics in its various structural components. Biosynthesis processes are environment-friendly, energy requirements are minimal, and by-products are non-existent.

Studies of biomineralization have highlighted the role of proteins in mediating the formation of biogenic materials [26]. Biominerals are composites of inorganic crystals and organic macromolecules (a combination of proteins, polysaccharides, and lipids) [7]. Biomaterials are synthesized by organisms under mild conditions, i.e., in aqueous solutions at neutral pH, room temperature and pressure. The synthesis of biological hard tissues is controlled by an organic matrix that is mostly proteinaceous [26]. Proteins not only act as chemical agents but also as physical ones. They collect inorganic ions into critical concentrations for synthesis, and catalyze them into specific mineral forms. They may provide substrates for nucleation of an inorganic component and, as a habit modifier,

control its morphology; they also provide compartments within which the inorganic crystals grow into specific sizes or shapes. For example, the crystals form in the vesicles, surrounded by a membrane [84].

Organisms use atmospheric CO_2 for the precipitation of biogenic carbonates either extra- and/or intra-cellularly. For example, coral reefs are the most conspicuous life-supporting calcareous structures, the majority of biogenic carbonate precipitation is carried out by planktonic microorganisms (algae), particularly coccolithophorids [126]. Dissolved CO_2 in the ocean surface is taken up by phytoplanktons through photosynthesis [127]. Adour *et al.,* in a report in 2002 have highlighted the role of microorganisms such as fungi and actinomycetes in the emission of carbon dioxide during aerobic respiration [128]. For each microorganism, the same maximum of CO_2 concentration was observed irrespective of the medium used [128]. The main part of the released CO_2 resulted from photosynthesis and few parts resulted from cellular maintenance. The maximum CO_2 concentration was expected to be concomitant to the maximum growth rate [128, 129].

Microorganisms. For the biological synthesis of minerals, we have extensively used eukaryotic organisms such as fungi and prokaryotic organisms such as actinomycetes (bacteria).

Fungi are nonmotile eukaryotic microorganisms that contain nucleus and produces filamentous and branched structures. Fungi exist as either a yeast form; as a filamentous form (mould/mold) or rarely as both forms dependent on the incubation temperature. Morphology is used to determine the fungus to Genus level and biochemical characteristics are used to determine to species level. The majority of fungi grow between 0 ^{o}C and 35 ^{o}C with an optimum temperature between 25 ^{o}C and 30 ^{o}C. Incubation temperature for isolation of environmental fungi is recommended at 25 ^{o}C. Fungi prefer an acid environment for growth, therefore, the optimum isolation medium for fungi should have a pH of 6 or less [130]. Many fungi can grow in media that have a pH as low as 4.5. For mineral synthesis, we have used various fungi such as plant pathogenic fungus, *Fusarium oxysporum* and *Fusarium* sp., an endophytic fungus, *Verticillium* sp. (isolated from the *Taxus* plant) and an alkalotolerant fungus, *Trichothecium* sp.

Actinomycetes are microorganisms that share important characteristics of fungi and prokaryotes such as bacteria [130,131]. Actinomycetes have phenomenal ability to

produce secondary metabolites such as antibiotics [132]. Actinomycetes are gram-positive bacteria that can be isolated using general, selective, and/or differential microbiological media incubated under the proper conditions of temperature, humidity and in the presence or absence of oxygen. They are isolated in pure culture and are subjected to a series of physiological and biochemical tests to identify them to Genus and species level. Bacterial identification is based upon morphological and biochemical characteristics. Morphology ranges from coryneform (bacilli) to well developed branching filaments. The majority of aerobic actinomycetes are capable of growth at 25-30 ^{o}C, however, some genera are capable of growth at 50 ^{o}C (thermophiles). For mineral synthesis, we have used a novel alkalotolerant actinomycete, *Rhodococcus* sp., having optimum growth at pH 7 at 27 ^{o}C [isolated from fig trees (*Ficus carica,* family Moraceae) from the Pune district of Maharastra, India] and an alkalothermophilic (extremophilic) actinomycete *Thermomonospora* sp. [44] (isolated from self-heating compost). Non-thermophilic actinomycetes are commonly isolated on media used for the isolation of fungi. Extremophiles are microorganisms, which thrive under extremes of temperature [from -14 °C (psychrophiles) to 45 °C (thermophiles) to 110 °C (hyperthermophiles)]; extremes of pH [from 1 (acidophiles) to 9 (alkalophiles)]; very high barostatic pressure (barophiles); non-aqueous environment containing 100% organic solvents; excess heavy metal concentration; etc.

The role of microorganisms such as fungi and actinomycetes, as both paradigm and tool for the fabrication of minerals will be discussed in detail in Chapter 7.

1.6 Description of work presented in the thesis

The work described in this thesis lays emphasis on new biomimetic methods for the size and shape controlled synthesis of minerals. We have addressed the use of anisotropic templates (ionizable lipids in the form of thin films) and charged liquid-liquid interfaces (static and dynamic) on the controlled synthesis of minerals, as well as the need of their large-scale production in nanometer dimensions using aqueous foams as templates. Attempt was also made to address the need for biocompatible surfaces to induce and support mineral growth for possible biomedical applications. Finally, a completely biological method used to produce truly biogenic metal carbonates by challenging microorganisms is described.

Chapter wise outline of the thesis.

The thesis consists of eight chapters. Chapter I is an introduction to the thesis and gives a brief review about the process of formation of biominerals in nature, their multifunctional properties, the importance of biomimetic approach, and different biomimetic protocols previously used and currently in vogue for biomineral synthesis. Finally, this chapter discusses brief background about the templates (chemical and biological) we have used for controlling the crystallization of minerals/biominerals.

Chapter II describes different experimental characterization techniques used for characterization of mineral crystals. The physical principles on which each of these techniques works and its application to understand various aspects of mineralization have been discussed.

Chapter III discusses the use of an anisotropic constrained environment for mineral growth by using thin films of thermally evaporated lipid bilayers as templates. In this laboratory, a versatile technique has been developed earlier, that uses thermally evaporated ionizable lipid thin films as hosts for the electrostatic entrapment of inorganic ions [102]. We have extended this protocol for the synthesis of minerals by entrapping appropriate metal ions sequentially into the confines of thin lipid bilayer stacks. The growth of minerals such as $BaSO_4$, $BaCrO_4$, $SrCO_3$ and $CaCO_3$ within thermally evaporated sodium bis-2-ethylhexyl-sulfosuccinate (aerosol OT, AOT) and stearic acid (StA) thin films were successfully achieved by a process of sequential entrapment of Ba^{2+}, Sr^{2+}, Ca^{2+} followed by SO_4^{2-}, CrO_4^{2-}, CO_3^{2-} ions. The formation of the minerals is believed to occur *via* hydrophobic association of the respective crystallites that are covered by a monolayer of the surfactant used. The issue of crystal morphology variation, polymorph selectivity and the kinetics of crystal growth in different thermally evaporated templating matrices were presented in detail. Control experiments were performed to clearly illustrate the effect of templates in modulating the morphology and polymorph selection of the mineral crystals.

Chapter IV describes mineral growth at a liquid-liquid interface with suitable surfactants adsorbed at the interface. The role of static and expanding charged liquid-liquid interface as templates for the controlled nucleation and growth of minerals was presented in detail. Realizing that the dynamic liquid-liquid interface in a Hele-Shaw cell would provide opportunities to control a variety of time-scales associated with material

formation, the growth of $BaSO_4$, $SrCO_3$ and $CaCO_3$ crystals was accomplished by taking fatty acids such as StA/AOT in the organic phase and carrying out the reaction of the appropriate metal ions ($Ba^{2+}/Sr^{2+}/Ca^{2+}$) with the corresponding counterions (SO_4^{2-}/CO_3^{2-}) present in the aqueous phase (injected phase). The reaction leading to mineral formation occurred at the interface due to strong complexation of the metal cations with the charged fatty acid/AOT leading to unusual crystal morphologies and particle assemblies. By simple variation of the experimental conditions such as the separation between the plates in the Hele-Shaw cell, the supersaturation of the salt solutions, the volumetric flow rate, the nature of the surfactant used and the role of viscosity has been shown to modulate morphology, determining the polymorph and assembly of crystallites in a radial Hele-Shaw cell. The above study of mineral growth at the expanding charged interface was compared with by growing minerals at a static liquid-liquid interface, which clearly revealed the effect of nature of interface on mineral growth.

Chapter V describes the use of foam lamellae as a dynamic biomimetic template for mineral growth. A combination of extremely large interfacial templating area provided by the liquid lamellae in foams (stabilized by ionizable surfactants) and the dynamic nature of the foam bubbles was used for the large-scale synthesis of $CaCO_3$ crystals. This is accomplished by first electrostatically complexing Ca^{2+} ions with AOT molecules at the air-bubble solution interface followed by reaction with Na_2CO_3 solution. The effect of drainage period, bubble size and impurity ions on the morphology and crystallography of $CaCO_3$ crystals was studied and presented in this chapter.

Chapter VI illustrates the preparation of biocompatible surfaces to induce and support mineral growth by aiming biomedical applications such as bone implants/grafting in bone surgery. In this laboratory a free-standing gold nanoparticle membrane was synthesized at the interface between chloroform containing bis(2-(4-aminophenoxy)ethyl)ether (DAEE) and aqueous chloroauric acid solution [133]. The gold nanoparticle membrane thus formed is extremely stable, robust and can be grown over large areas and thickness. We have investigated the possibility of using these membranes of gold nanoparticles for mineral growth. For the growth of minerals, the amino acids aspartic acid and cysteine together with an aromatic bifunctional molecule, anthranilic acid, were used to modify the surface of the gold nanoparticles in the membrane. The free carboxylic acid groups on the gold nanoparticles further to

functionalization with these molecules were then used to bind Ca^{2+} and reacted with CO_2/PO_4^{2-} to yield calcium carbonate and calcium phosphate crystals respectively. The nature of calcium carbonate and calcium phosphate crystals formed was found to be a strong function of the nanogold surface modifier. In comparisons, the growth of calcium carbonate and phosphate crystals were also accomplished on suitably functionalized plain gold nanoparticles.

Chapter VII describes the possibility of biological synthesis of minerals of variable morphology and in polymorph selectivity by challenging microorganisms. The fact that fungi and actinomycetes also act as source of CO_2 makes this a truly biogenic method for the synthesis of minerals and is thus not merely biomimetic as shown in above chapters. Biogenic metal carbonates such as $CaCO_3$, $SrCO_3$ and $BaCO_3$ crystals of controlled morphology and polymorph selectivity were obtained by simple exposure of aqueous Ca^{2+}, Sr^{2+} and Ba^{2+} ions to fungi and actinomycetes respectively. Both extra- and intracellular synthesis methods, crucial roles played by specific proteins secreted by organisms in stabilizing and directing the crystal growth, and the location of the proteins in the crystals were studied in great details and presented in this chapter.

Chapter VIII summarizes the work presented in the thesis and emphasizes on possible further research in this area.

1.7 References

[1] (a) Braga, D. *Angew. Chem. Int. Ed.* **2003**, *42*, 5544. (b) Desiraju, G. R. *Nature* **2003**, *423*, 485.

[2] Ball, P. *Nature* **1996**, *381*, 648.

[3] (a) Mann, S. *Nature* **1988**, *332*, 119. (b) Weissbuch, I.; Addadi, L.; Lahav, M.; Leiserowitz, L. *Science* **1991**, *253*, 637. (c) Braga, D.; Desiraju, G. R.; Miller, J.; Orpen, A. G.; Price, S. S. *CrystEngComm* **2002**, *4*, 500. (d) Mann, S. *Nature* **1993**, *365*, 499.

[4] Baeuerlein, E. *Biomineralization*, Wiley-VCH, Weinheim, Germany **2000**.

[5] (a) Mann, S.; Ozin, G. A. *Nature* **1996**, *382*, 313. (b) Matijevic, E. *Curr. Opin. Colloid Interface Sci.* **1996**, *1*, 176.

[6] (a) Baurerlein, E. *Angew. Chem. Int. Ed.* **2003**, *42*, 614. (b) Ozin, G. A. *Acc. Chem. Res.* **1997**, *30*, 17.

[7] (a) Lowenstam, H. A. *Science*, **1981**, *211*, 1126. (b) Bommel, K. J. C. V.; Friggeri, A.; Shinkai, S. *Angew. Chem. Int. Ed.* **2003**, *42*, 980. (c) Mann, S.; Webb, J.; William, R. J. P. *Biomineralization; Chemical and Biochemical Perspectives*, VCH Publishers, Weinheim **1989**. (d) Lowenstam, H. A.; Weiner, S. *On Biomineralization*, Oxford University Press, Oxford, **1989**.

[8] (a) Addadi, L.; Weiner, S. *Angew. Chem. Int. Ed.* **1992**, *31*, 153. (b) Weiner, S.; Addadi, L. *J. Mater. Chem.* **1997**, *7*, 689.

[9] Simkiss, K.; Wilbur, K. M. *Biomineralization*, Academic, San Diego **1989**.

[10] (a) McGrath, K. M. *Adv. Mater.* **2001**, *13*, 989. (b) Cook, G.; Timms, P. L.; Spickermann, C. G. *Angew. Chem. Int. Ed.* **2003**, *42*, 557. (c) Valtchev, V.; Smaihi, M.; Faust, A. C.; Vidal, L. *Angew. Chem. Int. Ed.* **2003**, *42*, 2782. (d) Anderson, M. W.; Holmes, S. M.; Hanif, n.; Cundy, C. S. *Angew. Chem. Int. Ed.* **2000**, *39*, 2707. (e) Wang, Y.; Tang, Y.; Dong, A.; Wang, X.; Ren, N.; Gao, Z. *J. Mater. Chem.* **2002**, *12*, 1812. (f) Levi, C.; Barton, J. L.; Guillemet, C.; Bras, E. L.; Lehuede, P. *J. Mater. Sci. Lett.* **1989**, *8*, 337. (g) Simpson, T. L.; Volcani, B. E. *in Silicon and Siliceous Structures in Biological Systemsi,* Springer, New York, **1981**.

[11] Baeuerlein, E. *Angew. Chem. Int. Ed.* **2003**, *42*, 614.

[12] Mann, S. *J. Chem. Soc*., *Dalton Trans*. **1997**, 3953.

[13] (a) Gao, H.; Ji, B.; Jager, I. L.; Arzt, E.; Fratzl, P. *Proc. Natl. Acad. Sci. USA* **2003**, *100*, 5597. (b) Currey, J. D. *Proc. R. Soc. London Ser. B* **1997**, *196***,** 443. (c) Menig, R.; Meyers, M. H.; Meyers, M. A.; Vecchio, K. S. *Acta Mater.* **2000**, *48***,** 2383. (d) Jackson, A. P.; Vincent, J. F. V.; Turner, R. M. *Proc. R. Soc. London Ser. B* **1988**, *234*, 415. (e) Addadi, L.; Weiner, S. *Angew. Chem.* 1992, *104*, 159. (f) Addadi, L.; Weiner, S. *Angew. Chem. Int. Ed. Engl.* 1992, *31*, 153. (g) Lowenstam, H. A.; Weiner, S. *On Biomineralization*, Oxford Univ. Press, New York, 1989, 324 pp. (h) Addadi, L.; Weiner, S. *Nature* 1997, *389*, 912. (i) Kuhn-Spearing, L. T.; Kessler, H.; Chateau, E.; Bllarini, R.; Heuer, A. *J. Mater. Sci.* 1996, *31*, 6583. (j) Mann, S. *Nature* 1993, *365*, 499.

[14] (a) Landis, W. J. *Bone* **1995**, *16*, 533. (b) Landis, W. J.; Hodgens, K. J. *J. Struct. Biol.* **1996**, *117***,** 24. (c) Roschger, P.; Grabner, B. M.; Rinnerthaler, S.; Tesch, W.; Kneissel, M.; Berzlanovich, A.; Klaushofer, K.; Fratzl, P. *J. Struct. Biol.* **2001**, *136***,** 126.

[15] Addadi, L.; Azenberg, J.; Beniash, E.; Weiner, S. *Crystal Engineering : From Molecules and Crystals to Materials* (Eds. Braga, D. *et al*) Kluwer Academic Publishers. Netherlands **1999**.

[16] Weiner, S.; Traub, W.; Lowenstam, H. A. *in Biomineralization and Biological Metal Accumulation* (Eds. Westbroek, P.; Jong, E. W.; Dordrecht, R.) **1983**, p. 205.

[17] (a) Gower, L. A. "*Variety of Biomineral Types and Biological Systems*" http://www.gower.mse.ufl.edu/research.html. (b) Mann, S. *Inorganic Materials 2nd Edition* (Edited by Bruce, D. W.; O'Hare, D.) John Wiley & Sons Ltd, **1996**.

[18] Young, J. R.; Didymus, J. M.; Bown, P. R.; Prins, B.; Mann, S. *Nature* **1992**, *356*, 516.

[19] (a) Falini, G.; Albeck, S.; Weiner, S.; Addadi, L. *Science* **1996**, *271*, 67. (b) DeOliveira, D. B.; Laursen, R. A. J. *Am. Chem. Soc.* **1997**, *119*, 10627

[20] (a) Raz, S.; Weiner, S,.; Addadi, L. *Adv. Mater.* **2000**, *12*, 38. (b) Addadi, L.; Raz, S.; Weiner, S. *Adv. Mater.* **2003**, *15*, 959. (c) Weiner, S.; Kalisman, Y. L.; Raz, S.; Addadi, L. *Connect. Tissue Res.* **2003**, *14*, 214.

[21] (a) Dalas, E.; Koutsoukos, P. G. *J. Chem. Soc. Faraday Trans.* **1989**, *85*, 2465. (b) Christoffersen, J.; Christoffersen, M. R. *J. Cryst. Growth* **1981**, *53*, 42. (c) Hirai, T.; Hodono, M.; Komasawa, I. *Langmuir* **2000,** *16*, 955.

[22] Liu, Y.; Nancollas, G. H. *J. Phys. Chem. B*, **1997**, *101*, 3464.

[23] Bigi, A.; Boanini, E.; Panzavolta, S.; Roveri, N. *Biomacromolecules* **2000**, *1*, 752.

[24] Bal, P. *Made to Measure* Prineton University Press, Princeton, New Jersy **1997**.

[25] (a) Ramachandra Rao, P. *Sadhana* **2003**, *28*, 657. (b) Sarikaya, M.; Fong, H.; Sopp, J. M.; Katti, K. S.; Mayer, G. *15th ASCE Engineering Mechanics Conference* (Columbia University, New York) June 2-5, **2002**.

[26] (a) Calvert, P.; Mann, S. *J. Mater. Chem.* **1988**, *23*, 3801. (b) Addadi, L.; Moradian, J.; Shai, E.; Maroudas, N.; Weiner, S. *Proc. Natl. Acad. Sci. USA*. **1987**, *84*, 2732. (c) Albeck, S.; Aizenberg, J.; Addadi, L.; Weiner, S. *J. Am. Chem. Soc.* **1993**, *115*, 11691. (d) Shenton, W.; Pum, D.; Sleytr, U. B.; Mann, S. *Nature* **1997**, *389*, 585. (e) Vaucher, S.; Dujardin, E.; Lebeau, B.; Hall, S. R.; Mann, S. *Chem.Mater*. **2001**, *13*, 4408. (f) Zaremba, C. M.; Belcher, A. M.; Fritz, M.; Li, Y.; Mann, S.; Hansma, P. K.; Morse, D. E.; Speck, J. S.; Stucky, G. D. *Chem. Mater.***1996**, *8*, 679.

[27] Walsh, D.; Mann, S. *Nature* **1995**, *377*, 320.

[28] *Langmuir-Blodgett Films* : *An Introduction* (Ed. M. C. Petty), Cambridge, University Press, Cambridge, **1996**.

[29] (a) Heywood, B. R.; Mann, S. *J. Am. Chem. Soc.* **1992**, *114*, 4681. (b) Jacquemain, D.; Wolf, S. G.; Leveiller, F.; Deutsch, M.; Kjaer, K.; Nielsen, J. A.; Lahav, M.; Leiserowitz, L. *Angew. Chem. Int. Ed. Engl.* **1992**, *31*, 130.

[30] (a) Mann, S.; Heywood, B. R.; Rajam, S.; Birchall, J. D. *Nature* **1988**, *334*, 692. (b) Rajam, S.; Heywood, B. R.; Walker, J. B. A.; Mann, S.; Davey, R. J.; Birchall, J. D. *J. Chem. Soc., Faraday Trans.* **1991**, *87*, 727. (c) Heywood, B. R.; Rajam, S.; Mann, S. *J. Chem. Soc., Faraday Trans.* **1991**, *87*, 735. (d) Heywood, B. R.; Mann, S. *Chem. Mater.* **1994**, *6*, 311. (e) Litvin, A. L.; valiyaveettil, S.; Kaplan, D. L.; Mann, S. *Adv. Mater.* **1997**, *9*, 124. (f) Heywood, B. R.; Mann, S. *Adv. Mater.* **1994**, *6*, 9.

[31] (a) Heywood, B. R.; Mann, S. *Langmuir.* **1992**, *8*, 1492. (b) Heywood, B. R.; Mann, S. *J. Am. Chem. Soc.* **1992**, *114*, 4681.

[32] (a) Heywood, B. R.; Mann, S. *Langmuir* **1992**, *8*, 1492. (b) Bromley, L. A.; Cottier, D.; Davey, R. J.; Dobbs, B.; Smith, S. *Langmuir* **1993**, *9*, 3594.

[33] Heywood, B. R.; Rajam, S.; Mann, S. *J. Chem. Soc. Faraday Trans.* **1991**, *87*, 735.

[34] Lahiri, J.; Xu, G.; Dabbs, D. M.; Yao, N.; Aksay, I. A.; Grooves, J. T. *J. Am. Chem. Soc.* **1997**, *119*, 5449.

[35] Champ, S.; Dickinson, J. A.; Fallon, P. S.; Heywood, B. R.; Mascal, M. *Angew. Chem. Int. Ed.* **2000**, *39*, 2716.

[36] Volkmer, D.; Fricke, M.; Agena, C.; Mattay, J. *CrystEngComm* **2002**, *4*, 288.

[37] Park, H. K.; Lee, I.; Kim, K. C*hem. Commun.* **2004**, 24-25.

[38] Rieke, P. C.; Tarasevich, B. J.; Wood, L. L.; Engelhard, M. H.; Baer, D. R.; Fryxell, G. E. *Langmuir* **1994**, *10*, 619.

[39] Lin, H.; Yanagi, T.; Seo, W. S.; Kuwabara, K. Koumoto, *Phosphorus. Res. Bull.* **1996**, *6*, 39.

[40] Kato, T.; Sugawara, A.; Hosoda, N. *Adv. Mater.* **2002**, *14*, 869.

[41] Bigelow, W. C.; Pickett, D. L.; Zisman, W. A. *J. Colloid Interface Sci.* **1946**, *1*, 513.

[42] Nuzzo, R. G.; Alara, D. L. *J. Am. Chem. Soc.* **1983**, *105*, 4481.

[43] (a) Kuther, J.; Tremel, W. *Chem. Commun.* **1997**, 2029. (b) Kuther, J.; Seshadri, R.; Neelles, G.; Butt, H. J.; Knoll, W.; Tremel, W. *Adv. Mater.* **1998**, *10*, 401. (c)

Kuther, J.; Seshadri, R.; Neelles, G.; Tremel, W. *J. Mater. Chem.* **1998**, *8*, 641. (d) Kuther, J.; Neelles, G.; Seshadri, R.; Schaub, M.; Butt, H. J.; Tremel, W. *Chem. Eur. J.* **1994**, *4*, 1834.

[44] Kuther, J.; Seshadri, R.; Tremel, W. *Angew. Chem. Int. Ed.* **1998**, *37*, 3044.

[45] (a) Aizenberg, J.; Black, A. J.; Whitesides, G. M. *Nature* **1999**, *398*, 495. (b) Aizenberg, J.; Black, A. J.; Whitesides, G. M. *J. Am. Chem. Soc.* **1999**, *121*, 4500. (c) Aizenberg, J. *J. Cryst. Growth* **2000**, *211*, 143.

[46] Lee, I.; Han, S. W.; Choi, H. J.; Kim, K. *Adv. Mater.* **2001**, *13*, 1617.

[47] (a) Kuther, J.; Nelles, G.; Seshadri, R.; Schaub, M.; Butt, H. J.; Tremel, W. *Chem. Eur. J.* **1998**, *4*, 1834. (b) Kuther, J.; Bartz, M.; Seshadri, R.;Vaughan, G. B. M.; Tremel, W. *J. Mater. Chem.* **2001**, *11*, 503.

[48] Colfen, H. *Current Opinion in Colloid and Interface Science* **2003**, *8*, 23.

[49] Naka, K.; Chujo, Y. *Chem. Mater.* **2001,** *13,* 3245 and references there in.

[50] Levi, Y.; Albeck, S.; Brack, A.; Weiner, S.; Addadi, L. *Chem. Eur.J.* **1998**, *4*, 389.

[51] Belcher, A. M.; Wu, X. H.; Christensen, R. J.; Hansma, P. K.; Stucky, G. D.; Morse, D. E. *Nature* **1996**, *381*, 56.

[52] (a) Kato, T.; Suzuki, T.; Amamiya, T.; Irie, T. Komiyama, M. *Supramolecular Science* **1998**, *5*, 411. (b) MacKenzie, C. R.; Wilbanks, S. M.; McGrath, K. M. *J. Mater. Chem.* **2004**, *14*, 1238. (c) Xu, G.; Wang, W.; Groves, J. T.; Hecht, M. H. *Proc. Natl. Acad. Sci. USA* **2001**, *98*, 3652.

[53] (a) A. Berman, J. Hanson, L. Leiserowitz, T. F. Koetzle, S. Weiner, L. Addadi, *Science* **1993**, *259*, 776. (b) Berman, A.; Addadi, L.; Weiner, S. *Nature* **1988**, *331*, 546 (c) McGrath, K. M. *Adv. Mater.* **2001**, *13*, 989. (d) Raz, S.; Hamilton, P. C.; Wilt, F. H.; Weiner, S.; Addadi, L. *Adv. Funct. Mater.* **2003**, *13*, 480.

[54] Seshadri, R.; Meldrum, F. C. *Adv. Mater.* **2000**, *12*, 1149.

[55] (a) Feng, Q. L.; Pu, G.; Pei, Y.; Cui, F. Z.; Li, H. D.; Kim, T. N. *J. Cryst. Growth* **2000**, *216*, 459. (b) Miyamoto, H.; Miyashita, T.; Okushima, M.; Nakano, S.; Morita, T.; Matsushiro, A. *Proc. Natl. Acad. Sci. USA* **1996**, *93*, 9657. (c) Gao, H.; Ji, B.; Jager, I. L.; Arzt, E.; Fratzl, P. *Proc. Natl. Acad. Sci. USA* **2003**, *100*, 5597. (d) Kato, T. *Adv. Mater.* **2000**, *12*, 1543. (e) Gower, L. A.; Tirrell, D. A. *J. Cryst. Growth* **1998**, *191*, 153. (f) Gower, L. B.; Odom, D. J. *J. Cryst. Growth* **2000**, *210*, 719. (g) Kato, T.; Amamiya, A. *Chem. Lett.* **1999**, 199. (h) Kato, T.; Suzuki, T.;

Irie, T. *Chem. Lett.* **2000**, 186. (h) Sugawara, A.; Kato, T. *Chem. Commun.* **2000**, 487. (i) Hosoda, N.; Kato, T. *Chem. Mater.* **2001**, *13*, 688. (j) Zhang, S.; Gonsalves, K. E. *Langmuir* **1998**, *14*, 6761. (k) Xu, G.; Yao, N.; Aksay, I. A.; Grooves, J. T. *J. Am. Chem. Soc.* **1998**, *120*, 11977. (l) Tanaka, Y.; Nemeto, T.; Naka, K.; Chujo, Y. *Polym. Bull.* **2000**, *45*, 447.

[56] Long, J. R.; Dindot, J. L.; Zebrosk, H.; Kiihne, S.; Clark, R. H.; Campbell, A. A.; Stayton, P. S.; Drobny, G. P. *Proc. Natl. Acad. Sci. USA* **1998**, *95*, 12083.

[57] Mann, S.; Didymus, J. M.; Sanderson, N. P.; Heywood, B. R.; Samper, E. J. A. *J. Chem. Soc., Faraday Trans*. **1990**, *86*, 1873.

[58] Geffroy, C.; Foissy, A.; Persello, J.; Cabane, B. *J. Colloid Interface Sci.* **1999**, *211*, 45.

[59] Didymus, J. M.; Oliver, P.; Mann, S.; Devries, A. L.; Hauschka, P. V.; Westbroek, P. *J. Chem. Soc., Faraday Trans*. **1993**, *89*, 2891.

[60] Ogino, T.; Tsunashima, N.; Suzuki, T.; Sakaguchi, M.; Sawada, K. *Nippon Kagaku Kaishi* **1988**, *6*, 899.

[61] Manoli, F.; Koutsopoulous, S.; Dalas, E. *J. Cryst. Growth* **1997**, *182*, 116.

[62] Dalas, E.; Koutsopoulous, S. *Langmuir* **1988**, *4*, 907.

[63] Manoli, F.; Dalas, E. *J. Cryst. Growth* **1999**, *204*, 369.

[64] Ueyama, N.; Hosoi, T.; Yamada, Y.; Doi, M.; Okamura, T.; Nakamura, A. *Macromolecules* **1998**, *31*, 7119.

[65] Ueyama, N.; Kozuki, H.; Doi, M.; Yamada, Y.; Takahashi, K.; Onoda, A.; Okamura, T.; Yamamoto, H. *Macromolecules* **2001**, *34*, 2607.

[66] (a) Uchida, M.; Sue, A.; Yoshioka, T.; Okuwaki, A. *CrystEngComm* **2001**, *5*, 1. (b)

[67] (a) Tanahashi, M.; Yao, T.; Kokubo, T.; Minoda, M.; Miyamoto, T.; Nakamura, T.; Yamamuro, T. *J. Am. Ceram. Soc*. **1994**, *77*, 2805. (b) Taguchi, T.; Kishida, A.; Akashi, M. *Chem. Lett*. **1998**, 711.

[68] (a) Naka, K.; Tanaka, Y.; Chujo, Y. **2002**, *18*, 3655. (b) Donners, J. J. J. M.; Heywood, B. R.; Meijer, E. W.; Nolte, R. J. M.; Roman, C.; Schenning, A. P. H. J. *Chem. Commun.* **2000**, *19*, 1937. (c) Donners, J. J. J. M.; Heywood, B. R.; Meijer, E. W.; Nolte, R. J. M.; Sommerdijk, N. A. J. M. *Chem. Eur. J.* **2002**, *8*, 2561.

[69] Colfen, H.; Qi, L. M. *Progr. Colloid Polym. Sci.* **2001**, *117*, 200.

[70] (a) Qi, L.; Li, J.; Ma, J. *Adv. Mater.* **2002**, *14*, 300. (b) Colfen, H.; Antonietti, M. *Langmuir* **1998**, *14*, 582. (c) Marentette, J. M.; Norwig, J.; Stockelmann, E.; Meyer, W. H.; Wegner, G. *Adv. Mater.* **1997**, *9*, 647.

[71] (a) Yu, S.; Antonietti, M.; Colfen, H.; Hartmann, J. *Nano. Lett.* **2003**, *3*, 379. (b) Qi, L.; Colfen, H.; Antonietti, M. *Angew. Chem. Int. Ed.* **2000**, *39*, 604.

[72] (a) Yu, S.; Colfen, H.; Antonietti, M. *J. Phys. Chem. B* **2003**, *107*, 7396. (b) Yu, S.; Colfen, H.; Xu, A. W.; Dong, W. *Crystal Growth & Design* **2004**, *1*, 33.

[73] Yu, S.; Colfen, H.; Antonietti, M. *Chem. Eur. J.* **2002**, *8*, 2937.

[74] Antonietti, M.; Breulmann, M.; Goltner, C. G.; Colfen, H.; Wong, K. K.; Walsh, D.; Mann, S. *Chem. Eur. J.* **1998**, *4*, 2493.

[75] Li, M.; Schnablegger, H.; Mann, S. *Nature* **1999**, *402*, 393.

[76] (a) Hopwood, J. D.; Mann, S. *Chem. Mater.* **1997**, *9*, 1819. (b) Li, M.; Mann, S. *Langmuir* **2000** *16*, 7088. (c) Summers, M.; Eastoe, J.; Davis, S. *Langmuir* **2002,** *18* 5023.

[77] Rees, G. D.; Gowing, R. E.; Hammond, S. J.; Robinson, B. H. *Langmuir* **1999**, *15* 1993.

[78] (a) Kandori, K.; Konno, K.; Kitahara, A. *J. Colloid Interface Sci.* **1988**, *122*, 78. (b) Li, M.; Mann, S. *Adv. Funct. Mater.* **2002**, *12*, 773. (c) Li, M.; Lebeau, B.; Mann, S. *Adv. Mater.* **2003**, *15*, 2032. (d) Roman, J. P.; Hoornaert, P.; Faul, D.; Biver, C.; Jacquet, F.; Martt, J. M. *J. Colloid Interface Sci.* **1991**, *144*, 324.

[79] Qi, L.; Ma, J.; Cheng, H.; Zhao, Z. *J. Phys. Chem. B* **1997**, *101*, 3460.

[80] Arriagada, F. J.; Osseo-Asare, K. J. *J. Colloid Interface Sci.* **1995,** *170*, 8.

[81] Lisiecki, I.; Bjorling, M.; Motte, L.; Ninham, B.; Pileni, M. P. *Langmuir* **1995**, *11*, 2385.

[82] (a) Kim, F.; Kwan, S.; Akana, J.; Yang, P. *J. Am. Chem. Soc*. **2001**, *123*, 4360. (b) Kwan, S.; Kim, F.; Akana, J.; Yang, P. *Chem. Commun.* **2001**, 447-448.

[83] Wang, L.; Zhu, Y. *Chem. Lett.* **2003**, *32*, 594.

[84] Mann, S.; Hannington, J. P.; Williams, R. J. P. *Nature* **1986**, *324*, 565.

[85] a) Yang, D.; Qi, Y.; Ma, J. *Chem. Commun.* **2003**, 1180-1181. (b) Falini, G.; Gazzano, M.; Ripamonti, A. *Adv. Mater.* **1994**, *6*, 46. (c) Falini, G.; Fermani, S.; Gazzano, M.; Ripamonti, A. *Chem. Eur. J. Nature* **1997**, *3*, 1807. (d) Zhan, J.; Lin, H. P.; Mou, C. Y. *Adv. Mater.* **2003**, *15*, 621. (e) Boggavarapu, S.; Chang, J.;

Calvert, P. *Mater. Sci. Eng*. **2000**, *11*, 47. (f) Calvert, P.; O'Kelly, J.; Souvignier, C. *Mater. Sci. Eng*. **1998**, *C6*, 167.

[86] Didymus, J. M.; Young, J. R.; Mann, S. *Proc. R. Soc. London*, *Ser.B* **1994**, *258*, 237.

[87] Leeuw, N. H.; Parker, S. C. *J. Phys. Chem. B* **1998**, *102*, 2914.

[88] Davis, K. J.; Dove, P. M.; Yoreo, J. D. *Science* **2000**, *290*, 1134.

[89] Leeuw, N. H. *J. Phys. Chem. B* **2002**, *106*, 5241.

[90] Aboukais, N. N.; Boughriet, A.; Fischer, J. C.; Wartel, M.; Langelin, H. R.; Aboukais, A. *J. Chem. Soc.*, *Faraday Trans.* **1996**, *92*, 3211.

[91] Katz, J. L.; Reick, M. R.; Herzog, R. E.; Parsiegla, K. J. *Langmuir* **1993**, *9*, 1423.

[92] Braybrook, A. L.; Heywood, B. R.; Jackson, R. A.; Pitt, K. *J. Crystal Growth* **2002**, *243*, 336.

[93] (a) Pastero, E. Costa, M. Bruno, M. Rubbo, G. Sgualdino and D. Aquilano *Crystal Growth and Design* **2004**, *4*, 485. (b) Rajam, S.; Mann, S. *J. Chem. Soc.*, *Chem. Commun.* **1990**, 1789.

[94] (a) Davis, K. J.; Dove, P. M.; Yoreo, J. D. *Science* **2000**, *290*, 1134. (b) Han, Y. J.; Aizenberg, J. *J. Am. Chem. Soc.* **2003**, *125*, 4032. (c) Zhang, Y.; Dawe, R. A. *Chemical Geology* **2000**, *163*, 129. (d) Sugawara, A.; Kato, T. *Chem. Commun.* **2000**, 487. (e) Meldrum, F. C.; Hyde, S. T. *J. Crystal Growth* **2001**, *231*, 544. (f) Loste, E.; Wilson, R. M.; Seshadri, R.; Meldrum, F. C. *J. Crytal Growth* **2003**, *254*, 206. (g) Falini, G.; Fermani, S.; Gazzano, M.; Ripamonti, A. *J. Mater. Chem.* **1998**, *8*, 1061.

[95] Gower, L. A.; Tirell, D. A. *J. Crystal Growth* **1998**, *191*, 153.

[96] Stanley, S. M.; Ries, J. B.; Hardie, L. A. *Proc. Natl. Acad. Sci. USA* **2002**, *99*, 1523.

[97] Rajam, S.; Mann, S. *J. Chem. Soc. Chem. Commun.* **1990**, 1789.

[98] Manoli, F.; Dalas, E. *J. Cryst. Growth* **2000**, *218*, 359. (b) Dickinson, S. R.; Mcgrath, K. M. *J. Mater. Chem.* **2003**, *13*, 928.

[99] Buijnsters, P. J. J. A.; Donners, J. J. J. M.; Hill, S. J.; Heywood, B. R.; Nolte, R. J. M.; Zwanenburg, B.; Sommerdijk, N. A. J. M. *Langmuir* **2001**, *17*, 3623.

[100] Orme, C. A.; Noy, A.; Wierzbick, A.; McBride, M. T.; Grantham, M.; Teng, H. H.; Dove, P. M.; DeYoreo, J. J. *Nature* **2001**, *411*, 775.

[101] (a) Lowenstam, H. A. *Science* **1981**, *211*, 1126. (b) Heuer, A. H.; Fink, D. J.; Laraia, V. J.; Arias, J. L.; Calvert, P. D.; Kendall, K.; Messing, G. L.; Blackwell, J.;

Rieke, P. C.; Thompson, D. H.; Wheeler, A. P.; Veis, A.; Caplan, A. I. *Science* **1992**, *255*, 1098.

[102] (a) Ganguly, P.; Sastry, M.; Pal, S.; Shashikala, M. N. *Langmuir* **1995**, *11*, 1078. (b) Patil, V.; Malvankar, R. B.; Sastry, M. *Langmuir* **1999**, *15*, 8197. (c) Sastry, M.; Rao, M.; Ganesh, K.N. *Acc. Chem. Res.* **2002**, *35*, 847. (d) Damle, C.; Kumar, A.; Sastry, M. *J. Mater. Chem.* **2002**, *12*, 1860.

[103] (a) Saffman, P. G., *J. Fluid Mech.* **1986**, *173*, 73. (b) Homsy, G. M. *Ann. Rev. Fluid Mech.* **1987**, *19***,** 271.

[104] (a) Saffman, P. G.; Taylaor, G. I. *Proc. R. Soc. Lond. A* **1958**, *245*, 312. (b) Ben-Jacob, E.; Garik, P. *Nature* **1990**, *343*, 523.

[105] (a) Bonn, D.; Kellay, H.; Amar, B. M.; Meunier, J. *Phys. Rev. Lett.* **1995**, *75*, 2132. (b) Ben-Jacob, E.; Deutscher, G.; Garik, P.; Godenfeld, N. D.; Lareah, Y. *Phys. Rev. Lett.* **1986**, *57*, 1903.

[106] Sastry, M.; Gole, A.; Banpurkar, A. G.; Limaye, A. V.; Ogale, S. B. *Current Science* **2001**, *81*, 191.

[107] Fernandez, J.; Homsy, G. M. *J. Fluid Mech.* **2003**, *480*, 267.

[108] (a) Berkman, S.; Egloff, G. "The Physical Chemistry of Foams" *Eighty Fifth Meeting of the American Chemical Society, Washington, D. C.* March **1933**. (b) Gardiner, B. S.; Dlugogorski, B. Z.; Jameson, G. J. *Ind. Eng. Chem. Res.* **1999**, *38*, 1099.

[109] Weaire, D.; Hutzler, S. *"The Physics of Foam"* Clarendon Press, Oxford, **1999**.

[110] (a) Hedreul, C.; Frens, G. *Colloids and Surfaces A: Physicochem. Eng. Aspects* **2001**, *186*, 73. (b) Neethling, S. J.; Lee, H. T. Cilliers, J. J. *J. Phys.: Condens. Matter* **2002**, *14*, 331.

[111] (a) Stein, H. N.; Laven, J. *J. Colloid Interface Sci* .**2001**, *244***,** 436. (b) Jalmes, A.; Lagevin, D. *J. Phys.: Condens. Matter* **2002**, *14*, 9397. (c) Koehler, S. A.; Hilgenfeldt, S. Stone, H. A. *Langmuir* **2000,** *16,* 6327.

[112] Hilgenfeldt, S.; Koehler, S. A.; Stone, H. A. *Phys. Rev. Lett.* **2001**, *86*, 4704.

[113] (a) Dorozhkin, S. V.; Epple, M. *Angew. Chem. Int. Ed.* **2002**, *41*, 3130. (b) Koutsopoulos, S.; Dalas, E. *Langmuir* **2000**, *16*, 6739. (c) Koutsopoulos, S.; Dalas, E. *J. Colloid Interface Sci.* **2000**, *231*, 207. (d) Koutsopoulos, S.; Dalas, E. *Langmuir* **2001**, *17*, 1074.

[114] (a) Zhang, Y.; Zhou, L.; Xue, N.; Xu, X.; Li, J. *Chem. Phys. Lett.* **2003**, *376*, 493. (b) Weiner, S.; Wagner, H. D. *Annu. Rev. Mater. Sci.* **1998**, *28*, 271. (c) Daniel, M. D.; Ilhan, A. A.; *Annu. Rev. Mater. Sci.* **2000**, *30*, 601.

[115] Tracy, B. M.; Doremus, R. H. *J. Biomed. Mater. Res.* **1984**, *18*, 719.

[116] Pompe, W.; Worch, H.; Epple, M.; Friess, W.; Gelinsky, M.; Greil, P.; Hempele, U.; Scharnweber, D.; Schulte, K. *Mat. Sci. & Eng.* **2003**, *362*, 40.

[117] Rodrigues, C. V. M.; Serricella, P.; Linhares, A. B. R.; Guerdes, R. M.; Borojevic, R.; Rossi, M. A.; Duarte, M. E. L.; Farina, M. *Biomaterials* **2003**, *24*, 4987.

[118] Schnettler, R.; Alt, V.; Dingeldein, E.; Pfefferle, H. J.; Kilian, O.; Meyer, C.; Heiss, C.; Wenisch, S. *Biomaterials* **2003**, *24*, 4603.

[119] Langer, R.; *Acc. Chem. Res.* **2000**, *33*, 94.

[120] (a) Jun, Y. K.; Kim, W. H.; Kweon, O. K.; Hong, S. H.; *Biomaterials* **2003**, *24*, 3731. (b) Hench L.L. *Bioceramics J. Am. Ceram. Soc.* **1998**, *81*, 1705.

[121] Kato, K.; Uchida, E.; Kang, E. T; Uyama, Y.; Ikada, Y. *Prog. Polym. Sci.* **2003**, *28*, 209.

[122] Panyam, J.; Labhasetwar, V. *Advanced Drug Delivery Reviews* **2003**, *55*, 329.

[123] Hersel, U.; Dahmen, C.; Kessler, H. *Biomaterials* **2003**, *24*, 4385.

[124] Xavier, S.P.; Carvalho, P. S. P.; Beloti, M. M.; Rosa, A. L. *Journal of Dentistry* **2003**, *31*, 173.

[125] Sarikaya, M. *Proc. Natl. Acad. Sci. USA* **1999**, *25*, 14183.

[126] (a) Westbroek, P.; Young, J. R.; Linschooten, K.; *J. Protozool.* **2000**, *36*, 368. (b) Riebesell. U.; Zondervan, I.; Rost, B.; Tortell, P. D.; Zeebe, R. E.; Morel, F. M. M. *Nature* **2000**, *407*, 364. (c) Gattuso, J. P.; Allemand, D.; Frankignoulle, M. *Am. Zool.* **1999**, *39*, 160. (d) Marubini, F.; Thake, B. *Limnol. Oceanogr.* **1999**, *44*, 716. (e) Langdon, C. *et al. Glob. Biogeochem. Cycles* **2000**, *14*, 639. (f) Leclercq, N.; Gattuso, J. P.; Jaubert, J. *Glob. Change Biol.* **2000**, *6*, 329.

[127] Treguer, P.; Pondaven, P. *Nature* **2000**, *406*, 358.

[128] Adour, L.; Couriol, C.; Amrane, A.; Prigent, Y. *Enzyme and MicrobialTechnology* **2002**, *31*, 533.

[129] Couriol, C.; Amrane, A.; Prigent, Y. *J. Biosci. Bioeng.* **2001**, *91*, 570.

[130] Pelczar, J.; Michael, J.; Reid, R. D. "*Microbiology*" McGraw Hill Book Company, New York, USA **2001**.

[131] Y. Okami, T. Beppu and H. Ogawara, *Biology of Actinomycetes*, Japan Scientific Societies Press: Tokyo, 1988; p 508.

[132] T. Sasaki, J. Yoshida, M. Itoh, S. Gomi, T. Shomura and M. Sezaki, *J. Antibiot.* 1988, **41**, 835.

[133] Selvakannan, PR.; Kumar, P. S.; More, A. S.; Shingte, R. D.; Wadgaonkar, P. P.; Sastry, M. *Adv. Mater.* **2004**, *16*, 966.

CHAPTER II

Characterization Techniques

The different experimental characterization techniques used during the course of the present work are discussed in this chapter.

This thesis have emphasized on the mineral growth within lipid thin films, mineral growth at a liquid-liquid interface, synthesis of mineral using aqueous foam lamellae, mineral growth on surface functionalized polymers, and biological synthesis of minerals using microorganisms. The surfactant coated minerals and the mineral-protein biocomposites produced via both chemical and biological protocols respectively have been characterized by a host of techniques such as Quartz Crystal Microgravimetry (QCM), Ellipsometry, Contact angle measurements, Fourier Transform Infrared Spectroscopy (FTIR), UV-visible Spectroscopy (UV-vis), Atomic absorption spectroscopy (AAS), Thermal Gravimetric Analysis (TGA), Isothermal Calorimetry (ITC), Scanning Electron Microscopy (SEM), Energy Dispersive Analysis of X-Rays (EDAX), Transmission Electron Microscopy (TEM), X-ray diffraction (XRD), and Gel Electrophoresis. Thin lipid films were prepared by thermally evaporating appropriate surfactants in a vacuum coating unit. This chapter is devoted in explaining the basic principles and techniques used for characterization.

2.1 Thermal evaporation of lipids

The films used for mineral synthesis in chapter 3 have been deposited using an Edwards E306 coating unit. The coating unit consists of a rotary pump, which can pump up to 10^{-3} Torr. Below this pressure, an oil diffusion pump is employed and can go up to 10^{-7} Torr [1]. Both these pumps are used in conjunction for backing and roughing the deposition chamber. A liquid nitrogen trap was also used. Deposition of organic thin films is done under vacuum due to the following reasons: a) The quality of deposition is better due to the increased mean free path of a molecule under vacuum as compared to atmosphere. This results in a linear trajectory of the thermally evaporated molecule; b) The melting point is reduced under vacuum enabling low current requirements for thermal evaporation. The amphiphilic molecules required for deposition, were taken in a molybdenum boat and subjected to a low tension DC of about 20 amperes under 10^{-7} Torr vacuum. Different substrates such as gold-coated AT-cut quartz crystals (for monitoring film thickness), Si (111) and glass were kept at a suitable distance above the molybdenum boat. The lipids were deposited by a process of sublimation in vacuum at a temperature not exceeding 80^{o} C for a period of 5 minutes. The rate of deposition was monitored by using an Edwards FTM5 quartz crystal microbalance (QCM) fitted in the

deposition chamber and crosschecked by ellipsometry measurements. FTIR analysis of the thermally evaporated surfactant films showed no evidence of thermal degradation of the surfactant molecules.

2.2 Quartz crystal microgravimetry

Quartz crystal based microgravimetry (QCM) is a powerful tool to study various adsorption processes and has been used to study adsorption of gases [2a,b] self-assembled monolayers (SAMs) [2c,d], Langmuir-Blodgett films [2e,f], nanoparticles [2e,g,h] and biomolecules [2i,j]. For the work discussed in chapter 3, QCM has been extensively used for calculating the exact amount of entrapped metal ions (both cations and anions) in thermally evaporated lipid films and also it helped in determining the actual time of immersion of surfactant deposited substrates in appropriate electrolyte solutions for reactions in order to form suitable mineral.

Basic principles. Pieree and Marie Curie showed in 1880 that when mechanical stress was applied to the surfaces of various crystals such as quartz, rochelle and tourmaline, they afford a corresponding electrical potential across the crystal whose magnitude was proportional to the applied stress [3]. This was referred to as the *piezoelectric effect*. It is characteristic of materials that are acentric, i.e. those that crystallize in non-center of symmetric space groups. A single crystal of an acentric material will possess a polar axis due to dipoles associated with the orientation of atoms in the crystalline lattice. When stress is applied across an appropriate direction, there is a shift of dipoles resulting from the displacement of atoms. This atomic displacement leads to a corresponding change in the net dipole moment. This will produce a net change in electrical charge on the faces of the crystal. The validity of the converse of this effect was also established wherein application of a voltage across these crystals afforded a corresponding mechanical strain. This inverse piezoelectric effect is the basis of the QCM technique. AT-cut quartz resonator, in which thin quartz wafer is prepared by slicing a quartz rod at an angle of 35^{o} with respect to the X-axis of the crystal, resonates in the thickness shear mode. Fig.2.1 shows a typical QCM crystal.

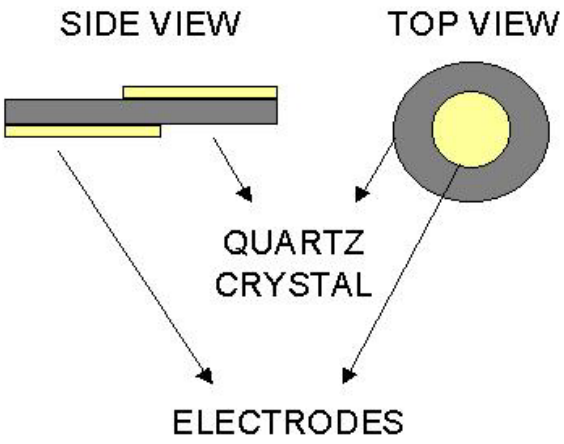

Fig.2.1: *Diagram showing details of a typical quartz resonator.*

Application of electric field across the crystal causes a vibrational motion of the quartz crystal, with amplitude parallel to the surface of the crystal [2d]. The result of the vibrational motion of the quartz crystal is the establishment of a transverse acoustic wave that propagates across the thickness of the crystal, reflecting back into the crystal at the surfaces. When a uniform layer of foreign material is added to the surface of the quartz crystal, the acoustic wave will travel across the interface, and will propagate through the layer. This leads to decrease in the frequency of the crystal. The details have been depicted in the Fig.2.2 shown below. The Frequency changes on deposition of the film can be converted to mass loading using the Saurbrey formula [4].

Saurbrey formula:

$$\Delta f = -2 f_0^2 \times \frac{\Delta m}{A \times (\mu_q \times \rho_q)^{1/2}}$$

Where Δf : frequency shift, f_0 : frequency of the crystal prior to a mass change, Δm : mass change, A : Piezo electrically active area, ρ_q : density of quartz, μ_q : shear modulus for quartz. ($\mu_q = 2.95 \times 10^{11}$ g cm^{-1} s^{-2}, $\rho_q = 2.65$ g/cm^3).

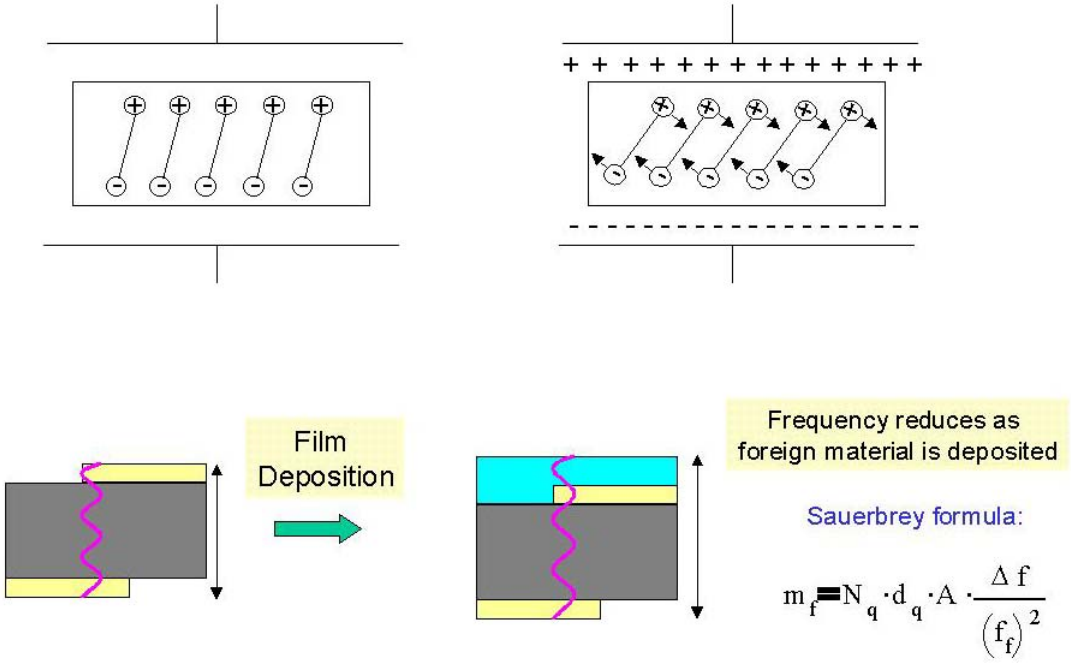

Fig.2.2: *Diagram showing the details of principles involved in QCM measurements.*

In the work described in chapter 3 we have used a gold coated AT-cut 6 MHz quartz crystal. The frequency counter used was an Edwards FTM5 instrument operating at a frequency stability and resolution of $\pm$ 1 Hz. At this resolution and the type of quartz crystal used, the mass resolution would be 12 ng/cm^2. We have used QCM technique in the following way. Different thickness films of lipids were thermally evaporated on the QCM crystals. These crystals were immersed into appropriate solutions for different time intervals and the frequency changes were measured *ex situ* after thorough washing (in deionized water) and drying (in flowing nitrogen) of the crystals. The frequency changes were converted to a mass uptake by using the standard Saurbrey formula [4].

We have observed a number of situations where entrapment of metal ions (both cationic and anionic) in thermally evaporated lipid films analyzed by QCM yields metal ion concentrations in the film much higher that expected from charge neutrality considerations. While we don't understand this fully at this stage, we believe that consequent to metal ion entrapment and formation of metal salts of the lipids, the film stiffness (acoustically) increases. In other words, there is a large change in the acoustic impedance of the film, which to our knowledge has not been determined for such lipid films after ion entrapment. Clearly, this factor is not taken into account.

2.3 Ellipsometry

Ellipsometry is a convenient and accurate technique for the measurement of thickness and refractive indexes of very thin films on solid surfaces and for the measurement of optical constants of reflecting surfaces [5]. The estimation of film thickness usually is the first characterization method used for a newly prepared film. Today, ellipsometry is the common optical technique for the determination of thickness, uniformity and refractive index of freshly prepared films. We have used ellipsometer to cross check the thickness of lipid films deposited in a vacuum coating unit as described in section 2.1 of this chapter.

Working principles: The technique is based on the principle that the state of polarization of light changes on reflection from an interface. This technique is also known as reflection polarimetry or polarimetric spectroscopy. In its broadest sense, ellipsometry is the measurement of the state of polarization of light. Paul Drude was the first to develop fundamental equations of ellipsometry, which demonstrated potential monolayer sensitivity for the detection and characterization of thin films on specular surfaces [6a].

When a polarized light beam reflects from any specular surface, changes occur in both the amplitude and phase of the oscillating parallel and perpendicular vector components of the electric field associated with the beam. The main objective of an ellipsometry experiment is to measure these amplitude and phase changes, which provide us information about the reflecting surface through the Fresnel reflection coefficients [6b]. We have used a Gaertner L 118 manually operated null ellipsometer in the polarizer-compensator-sample-analyser (PCSA) mode to measure the ellipsometric angles of thin lipid films deposited on Si (111) substrate.

2.4 Contact angle measurements

It is a method to study the wettability of solids. The quality and wetting properties of any monolayer and multilayer films can be estimated from contact angle measurements [7]. In this thesis contact angle measurements of thin lipid films before and after the mineral formation and minerals coated with surfactant molecules were carried out on a 1 μl sessile water drop using a Rame-Hart 100 goniometer on different points on the film surface. Contact angle measurements are sensitive to changes in the

surface and one can probe any changes in surface hydrophobicity by this technique. For example, Whitesides and co-workers have extensively studied the SAM formation, surface functionality etc using contact angle titrations [8].

2.5 Fourier transform infrared spectroscopy

Fourier transform infrared (FTIR) spectroscopy is a characterization method by which infrared radiation is passed through a sample. The main importance of IR spectroscopic analysis is to determine the chemical functional groups and molecular orientations in the sample. Different functional groups absorb characteristic frequencies of IR radiation. IR spectroscopy is also an important and popular tool for structural elucidation and compound identification. It is bound by the red end of the visible region at high frequencies and the microwave region at low frequencies. IR absorption positions are generally presented as wavenumbers. Samples may be prepared in a solid, liquid, or gas form. The nature of the sample determines which technique should be used. Common sample preparation methods include: the salt pellet technique (sample powder is diluted in an IR-transparent salt like KBr); Nujol Mull method (sample powder is diluted in an IR-transparent oil); thin sample technique; attenuated total reflectance (the sample is sandwiched between two IR-transparent crystals); and diffuse reflectance infrared FT (optics focus beam on the top surface of the sample) [9].

Basic principles: The principles of IR can be explained by classical as well as quantum theories [6]. The classical model considers a simple ball and spring model wherein diatomic molecule with two masses m_1 and m_2 are connected by a spring. According to Hooke's law when spring is displaced,

$$F = -kx$$

Where F = opposing restoring force; k = force constant; x = displacement from equilibrium position. This is simple harmonic equation wherein the frequency of vibration is given by the relation:

$$\nu = \frac{1}{2\pi} \cdot \sqrt{\frac{k}{\mu}}$$

Where μ is the reduced mass. Using simple laws of mechanics, a system of masses joined by springs has a number of fundamental modes of vibration each of which

has a particular natural frequency. Consider an oscillator such as the electric vector of electromagnetic radiation coupled to a system of masses such as a polyatomic molecule. By scanning through a range of frequencies some may be 'tuned' to the various fundamental modes of vibration by virtue of a change in dipole moment associated with that vibration. So, a series of absorption take place for a polyatomic molecule as we scan through a range of frequencies, radiation is absorbed each time we tune-in or come into resonance with the natural frequency of a fundamental mode which is capable of dipolar interaction [10].

Many facts cannot be explained classically (one such fact is the CO_2 splitting) and requires quantum mechanical treatment. This treatment considers the electronic change accompanied by vibration and rotation with discrete energy levels. The energy of quantised energy levels is derived by using Schrodinger wave equation. For polyatomic molecules, the position of each atoms can be described using coordinate geometry, and the degree of freedom are stated for linear molecules (3N-5) and for non-linear molecules (3N-6). N represents number of atoms [10].

All FTIR spectra shown in this thesis have been presented as obtained, except for baseline correction. Infrared spectroscopy have been used for obtaining insights into the organization of hydrophobic chain, ion exchange in lipid films, phase identifications of minerals and amide linkages between amino acid residues in polypeptides and proteins which give rise to well-known signatures in the infrared region of the electromagnetic spectrum [11]. For ion incorporation into the lipid films discussed in this thesis, 250-500 Å thick lipids were deposited onto a Si (111) wafer. For mineral phase identifications, samples were prepared in the form of pellets by dispersing powders of minerals in KBr. The FTIR measurements of these films were carried out on a Perkin Elmer Spectrum One FTIR spectrometer operated in the diffuse reflectance mode at a resolution of 4 cm^{-1}. A total of 250 scans yielded a good signal to noise ratio of the IR spectra.

2.6 UV-visible spectroscopy

Basic principles. Absorption spectroscopy in the visible region has long been an important tool to the analyst [12]. Color transitions arise due to molecular and structural changes in the substances being examined, leading to corresponding changes in the ability to absorb light in the visible region of the electromagnetic spectrum. Appearance

of color arises from the property of the colored material to absorb selectively within the visible region of the electromagnetic spectrum. Absorption of energy leads to a transition of electron from ground state to excited state. Most of the spectra are very broad, smooth curves and not sharp peaks. This is because any change in the electronic energy is accompanied by a corresponding change in the vibrational and rotational energy levels. A variety of energy absorption is possible depending upon the nature of the bonds within a molecule. For instance, strong σ bonds, in weaker π-bonds or non-bonding (n) and when energy is absorbed all of these types of electrons can be elevated to excited antibonding states represented as σ^*, π^*. Most σ to σ^* absorptions for individual bonds take place below 200 nm in the vacuum ultraviolet region and compounds containing just σ bonds are transparent in the near UV/vis region $\pi \rightarrow \pi^*$ and $n \rightarrow \pi^*$ absorptions occur in the near UV/vis region, and result from the presence in molecules of unsaturated groups known as chromophores.

The intensity of light passing through a sample is given by the relation:

$$I = I_0 \exp(-\alpha k x)$$

Where I = intensity of transmitted light; I_0 = intensity of incident light; α = molar absorption coefficient; k = constant; x = path length.

The combined Beer-Lambert law is used for quantification of exact concentration of unknown species in a mixture using UV-vis spectroscopy. This can be done by drawing a graph of intensities of absorption for different concentrations of the sample and comparing with a standard graph [12].

The Beer-Lambert law is:

$$A = \varepsilon c l$$

Where ε = proportionality constant known as the absorptivity.

These laws can easily explain the absorption of proteins in the mineral-protein composite used in this thesis. On the other hand, light absorption by gold metal nanoparticles is best described by Mie's theory [13]. The absorption spectrum of particles in a given solvent can be calculated from the optical constants of the bulk metal, although the absorption of the particles is often vastly different from that of the bulk metal itself [13]. The simplest case is when the particles are spherical and their size is small compared to the wavelength of light, and the particles are well separated in solution. At

particle sizes between about 3 and 20 nm, there is not a strong dependence of the absorption spectra on particle size. This is because the particles are below the size at which higher order terms in the Mie formula for the absorption constant become significant. Thus, one has to regard only the dipole term, which depends only on the total metal concentration in the solution and not on particle size. The absorption coefficient in mol^{-1}. L. cm^{-1} is calculated from the relation [13,14].

$$\alpha = \frac{18\,\pi}{\ln 10}\;\frac{10^5}{\lambda}\;\frac{M\,n_0^3}{\rho}\;\frac{\varepsilon_2}{(\varepsilon_1 + 2\,n_0^2) + \varepsilon_2^2}$$

where λ is the wavelength of light in nanometers, M and ρ are the molecular weight and density of the metal, n_o is the refractive index of the solvent and ε_1 and ε_2 are the real and imaginary parts of the dielectric constant of the metal. When the size of the particles becomes smaller than the mean free path of the electrons, the absorption bands are broadened; this is accounted for by using size-corrected values of ε_2 [13,14].

$$\varepsilon_2 = \varepsilon_{2(bulk)} + (\omega_p^2 / \omega^3)(V_F/R)$$

where, ω is the light frequency, ω_p is the plasmon frequency, V_F the electron velocity at the Fermi level and R the particle radius (R/V_F, mean time of the free movement of the electrons). Resonance with the incident light is reached at the wavelength, where the negative value of ε_1 of the metal is equal to twice the dielectric constant of the medium. Gold particles possess plasmon resonances in the visible range (~514 nm).

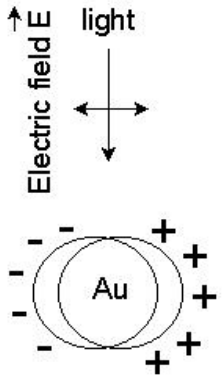

Fig.2.3: *Polarization of a spherical metal particle by the electric field vector of the incoming light.*

Resonance is produced by a collective excitation of all the free electrons in the particles. As is shown in Fig.2.3, the movement of the electrons under the influence of the electric field vector of the incoming light leads to a dipole excitation across the particle sphere, the positive polarization charge acting as a restoring force, which makes the electrons oscillate.

Thus, the electron density within a surface layer, the thickness of which is about equal to the screening length of a few angstroms, oscillate, whereas the density in the interior of the particle remains constant (surface plasmon). Therefore, any changes in the electron density of this surface layer will lead to changes in the plasmon absorption. For example, the surface sensitivity of colloidal nanoparticles has been used to study adsorption/chemisorption of thiols [15].

We have extensively used UV-visible spectroscopy for monitoring gold nanoparticles signatures and protein signatures. Noble metal particles are ideal candidates for study with UV-vis spectroscopy, since they exhibit strong surface plasmon resonance absorption in the visible region, and are highly sensitive to surface modification. Furthermore, the resonance at about 280 nm arising from the proteins is a characteristic signature. UV-visible measurements were monitored on a Jasco UV-vis spectrophotometer (V570 UV-VIS-NIR) operated at a resolution of 2 nm.

2.7 Atomic absorption spectroscopy

Atomic absorption spectroscopy (AAS) is one of the common chemical analysis methods for qualitative and quantitative determination of sample composition. We have used AAS, in order to estimate the amount of metal ions present in a sample.

Operating principles. The main parts of the AAS system are a hollow cathode lamp, nebulizer, air/acetylene flame, and optical system [16]. The jobs of each are detailed below:

The hollow cathode lamp (HCL) uses a cathode made of the element of interest with a low internal pressure of an inert gas. A low electrical current (~ 10 mA) is imposed in such a way that the metal is excited and emits a few spectral lines characteristic of that element. The light is emitted directionally through the lamp's window, a window made of a glass transparent in the UV and visible wavelengths. It provides the analytical light line for the element of interest. It also provides a constant yet

intense beam of that analytical line. The nebulizer chamber suck up liquid sample at a controlled rate and create a fine aerosol for introduction into the flame. The nebulizer mix the aerosol and fuel and oxidant thoroughly for introduction into the flame. The flame destroys any analyte ions and breakdown complexes create atoms (the elemental form) of the element of interest. The monochromator isolate analytical lines' photons passing through the flame. It also removes scattered light of other wavelengths from the flame. In doing this, only a narrow spectral line impinges on the photomultiplier tube (PMT). As a detector, PMT determines the intensity of photons of the analytical line exiting the monochromator [16].

2.8 Scanning electron microscopy

Scanning electron microscope (SEM) is designed for direct studying the surfaces of solid objects. By scanning with an electron beam that has been generated and focused by the operation of the microscope, an image is formed in much the same way as a television. SEM gives better resolution and depth of field than optical microscope. For this reason the SEM can produce an image that is a good representation of the three-dimensional sample. In this thesis we have extensively used SEM for observing the morphology of minerals synthesized via various methods described in the following chapters. SEM measurements were performed on a Leica Stereoscan-440 scanning electron microscope instrument equipped with a Phoenix EDAX attachment.

Operating principles: The instrument can be simplified into three major sections: a) electron-optical column; b) vacuum system and c) electronics and display system [17]. A tungsten filament is heated to 2700 K, which produces electrons that are accelerated towards the anode disc. Electrostatic shaping of the electron beam under vacuum gives a beam diameter of about 50 μm. Ultimate performance of the SEM is mainly limited by the diameter of the beam and hence two lenses and condensers demagnify the beam to around 5 nm. The scanning coils deflect this beam and sweep it over the specimen surface. A cathode-ray display tube is scanned synchronously with the electron beam. The brightness of the display tube is modulated by the signal, which arises from the interaction of the beam with the surface element, which is probed. The strength of this signal is translated into image contrast. Secondary electrons, which the beam probe liberates from the specimen surface, are collected and used as the contrast signal. The

yield of collected electrons depends on the nature of the specimen surface and on its inclination with respect to the probing beam. Consequently, one obtains pictures with a high perspective appearance [17].

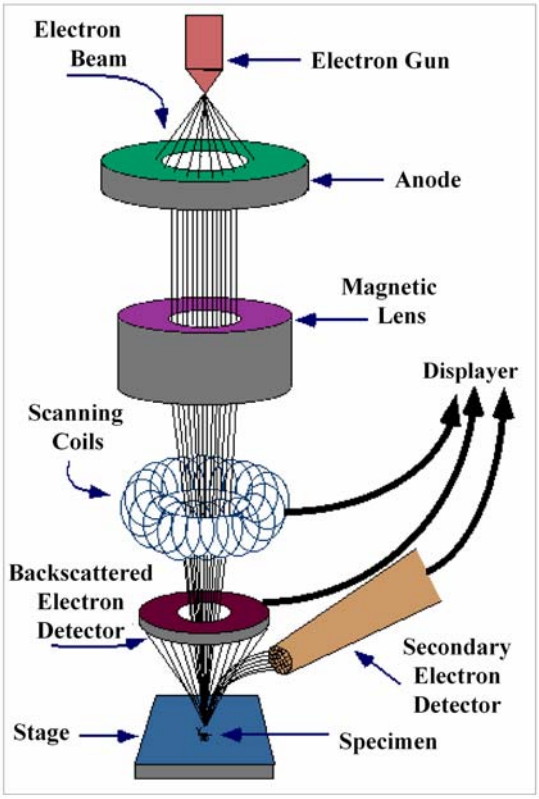

Fig.2.4: *Diagram showing different parts of a scanning electron microscope.*

Fig.2.4 shows a beam of electrons is produced at the top of the microscope by heating of a metallic filament. The electron beam follows a vertical path through the column of the microscope. It makes its way through electromagnetic lenses, which focus and direct the beam down towards the sample (Fig.2.4). Once it hits the sample, other electrons (backscattered or secondary) are ejected from the sample. Detectors collect the secondary or backscattered electrons, and convert them to a signal that is sent to a viewing screen similiar to the one in an ordinary television, producing an image (Fig.2.4).

The schematic (Fig.2.5) shows the ray traces for two probe-forming lens-focusing conditions: small working distance (left) and large working distance (right). Both

conditions have the same condenser lens strength and aperture size. However, as the sample is moved further from the lens, the following occurs: the working distance is increased, the demagnification decreases, the spot size increases and the divergence angle is decreased. The decrease in demagnification is obtained when the lens current is decreased, which in turn increases the focal length of the lens. The resolution of the specimen is decreased with an increased working distance, because the spot size is increased. Conversely, the depth of field is increased with an increased working distance, because the divergence angle is smaller.

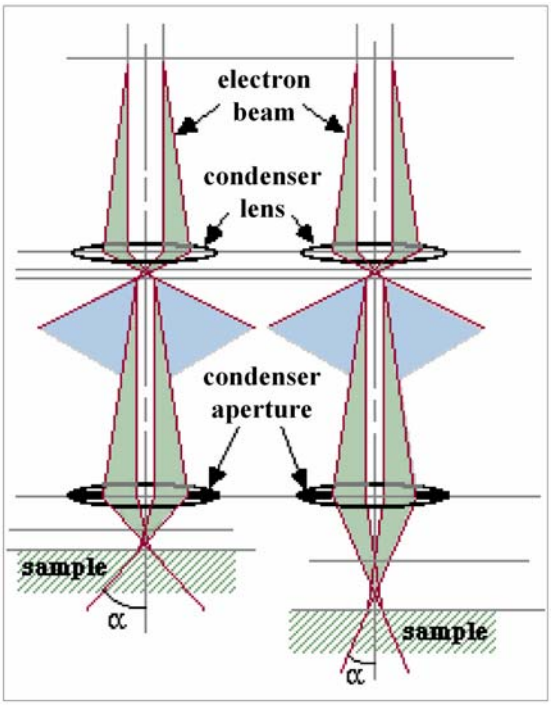

Fig.2.5: *Schematic (not to scale) of SEM ray diagram.*

Specimen-beam interaction: There are different types of interactions of the electron beam possible with the sample as shown in Fig.2.6 [17]. For thin samples (< 1μm), with electron beam energy of 20-30 keV, one can have unscattered electrons, wherein the beam just passes through and does not contain any information about the sample. Most of the electrons are scattered at large angles (from 0 to 180^{o}) when they interact with the positively charged nucleus. These elastically scattered electrons usually called

'backscattered electrons' are used for SEM imaging. Some electrons scatter inelastically due to the loss in kinetic energy upon their interaction with orbital shell electrons.

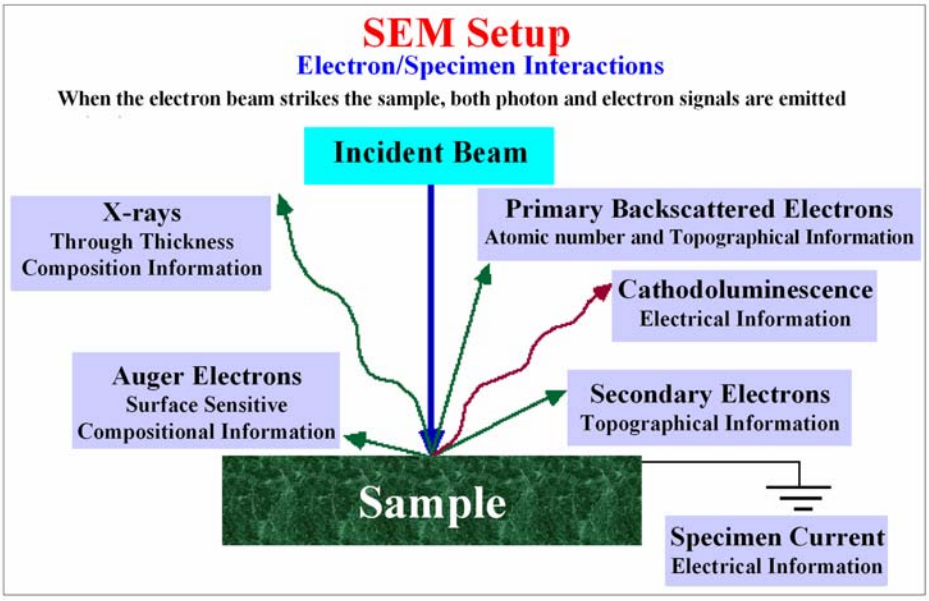

Fig.2.6: *Schematic (not to scale) showing the interaction between electron and specimen.*

Due to electron bombardment, phonons are set up in the specimen resulting considerable heating of the specimen. Incident electrons may knock off loosely bound conduction electrons out of the sample. These are secondary electrons and along with backscattered electrons are widely used for SEM topographical imaging. If the electron beam knocks off an inner shell electron, the atom rearranges by dropping an outer shell electron to an inner one. This excited or ionised atom emits an electron commonly known as the Auger electron. Recently Auger electron spectroscopy (AES) is useful to provide compositional information. Instead of excited atom releasing Auger electron, it can release a photon of electromagnetic radiation. If the amount of energy released is high, the photon will be an X-ray photon. These electrons are characteristic of the sample and can be used for analysis. This type of analysis is known as EDAX and is described in the next section. While all these signals are present in the SEM, not all of them are detected and used for information. The signals most commonly used are the secondary electrons, the backscattered electrons and X-rays.

The electron beam hits the sample, producing secondary electrons from the sample. These electrons are collected by a secondary detector or a backscatter detector, converted to a voltage, and amplified. The amplified voltage is applied to the grid of the cathode ray tube (CRT) and causes the intensity of the spot of light to change. The image consists of thousands of spots of varying intensity on the face of a CRT that correspond to the topography of the sample.

An electron detector is used with the SEM to convert the radiation of interest into an electrical signal for manipulation and display by signal processing electronics, which to you and me is much like a television. Most SEM's are equipped with an Everhart-Thornley (E-T) detector. It works in the following manner:

The scintillator material is struck by an energetic electron. This collision produces photons which are conducted by total internal reflection in a light guide to a photomultiplier. These photons are now in the form of light so they can pass through a vacuum environment and a quartz glass window. The photon is then converted back into an electron current where a positive bias can attract the electrons and collect them so that they will be detected.

2.9 Energy dispersive analysis of X-rays

Energy Dispersive analysis of X-rays (EDAX) is a chemical microanalysis technique. The technique utilizes X-rays that are emitted from the sample during bombardment by the electron beam to characterize the elemental composition of the analyzed volume. Features or phases as small as about 1 μm can be analyzed. When the sample is bombarded by the electron beam of the SEM, electrons are ejected from the atoms comprising the sample's surface. A resulting electron vacancy is filled by an electron from a higher shell, and an X-ray is emitted to balance the energy difference between the two electrons (Fig.2.6). The EDAX X-ray detector measures the number of emitted X-rays versus their energy. The energy of the X-ray is characteristic of the element from which the X-ray was emitted. A spectrum of the energy versus relative counts of the detected X-rays is obtained and evaluated for qualitative and quantitative determinations of the elements present in the sampled volume. In this thesis we have extensively used EDAX measurements in ordered to determine the chemical composition (both qualitative and quantitative) of mineral-surfactant and mineral-protein composites.

Operating principles. One of the instruments most commonly used in conjunction with the SEM is the EDAX. The X-ray spectrometer converts an X-ray photon into an electrical pulse with specific characteristics of amplitude and width. A multi-channel analyzer measures the pulse and increments a corresponding energy slot in a monitor display. The location of the slot is proportional to the energy of the x-ray photon entering the detector. The display is a histogram of the x-ray energy received by the detector, with individual peaks, the heights of which are proportional to the amount of a particular element in the specimen being analyzed.

The locations of the peaks are directly related to the particular X-ray fingerprint of the elements present. Consequently, the presence of a peak, its height, and several other factors, allows the analyst to identify elements within a sample, and with the use of appropriate standards and software, a quantitative analysis can be made of elements with atomic number of 4 (carbon) or greater.

Combining the EDAX system with the SEM allows the identification, at microstructural level, of compositional gradients at grain boundaries, second phases, impurities, inclusions, and small amounts of material. In the scanning mode, the SEM/EDAX unit can be used to produce maps of element location, concentration, and distribution.

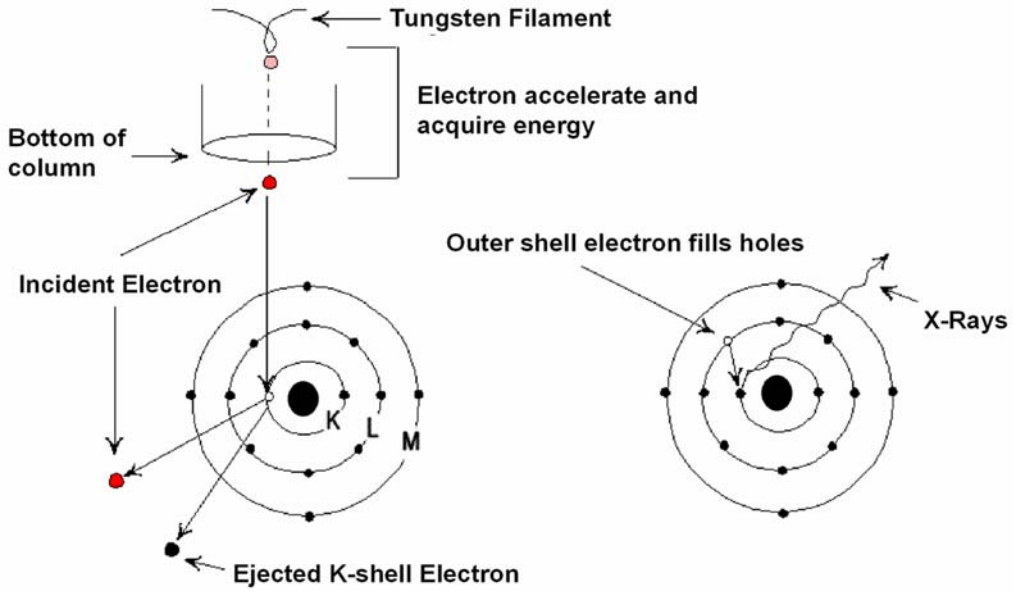

Fig.2.6: *Schematic (not to scale) showing production of X-ray for EDAX measurements.*

Electrons leave the filament and are accelerated down the column through a potential that can approach 40 kV. This gives the incident electrons enough energy to eject electrons in the sample. An X-ray is produced when an outer shell electron falls into replace the inner shell electron. In the sample, a L-shell electron replaces the missing K-shell electron. This produces a Kα X-ray at a very specific energy of 1.741 KeV [17].

Limitations of EDAX. The design of the equipment makes the technique incapable of detecting elements lighter than carbon. Sensitivity (ability to detect the presence of an element above background noise) is 0.1 wt% with the EDAX. There is also poorer sensitivity for light elements (low atomic weight) in a heavy matrix. Resolution of the x-ray energy levels limits the positive identification of certain elements (i.e. molybdenum and sulfur) due to overlapping energy slots.

Quantitative analysis is usually limited to flat, polished specimens. Unusual geometries, such as fracture surfaces, individual particles, and films on substrates can be analyzed, but with considerably greater uncertainty.

2.10 Transmission electron microscopy

This technique requires that the thickness of the films under study will be less than 300 Å; however, direct observation of one monolayer is not possible because of lack of contrast. The electron energy in TEM is very high (100 KeV) and the resolution ranges from 1000 Å in to a few tens of Angstroms. We have used TEM for observing the crystal morphologies with finer details. Samples for TEM analysis were prepared by drop-coating films of the redispersed powder in deionized water on carbon-coated copper TEM grids, allowing the grid to stand for 2 minutes following which the extra solution was removed using a blotting paper. TEM analysis was performed on a JEOL model 1200EX instrument operated at an accelerating voltage at 120 kV.

Operating principles: Diffraction camera consists of an electron gun, an aperture to define a small beam cross-section, a specimen holder, a fluorescent screen and a plate camera [18]. A technical explanation of a typical TEMs workings is as follows :

1. The virtual source that is an electron gun, producing a stream of monochromatic electrons.
2. This stream is focused to a small, thin, coherent beam by the use of condenser lenses 1 and 2. The first lens usually controlled by a spot size knob largely

determines the spot size; the general size range of the final spot that strikes the sample. The second lens usually controlled by the intensity or brightness knob actually changes the size of the spot on the sample; changing it from a wide dispersed spot to a pinpoint beam.

3. The beam is restricted by the condenser aperture, knocking out high angle electrons.
4. The beam strikes the specimen and parts of it are transmitted.
5. This transmitted portion is focused by the objective lens into an image.
6. Optional objective and selected area metal apertures can restrict the beam; the objective aperture enhancing contrast by blocking out high-angle diffracted electrons, the selected area aperture enabling the user to examine the periodic diffraction of electrons by ordered arrangements of atoms in the sample
7. The image is passed down the column through the intermediate and projector lenses, being enlarged all the way.

The image strikes the phosphor image screen and light is generated, allowing the user to see the image. The darker areas of the image represent those areas of the sample that fewer electrons were transmitted through (they are thicker or denser). The lighter areas of the image represent those areas of the sample that more electrons were transmitted through (they are thinner or less dense)

2.11 X-ray diffraction

X-ray Diffraction (XRD) is one of the primary techniques used by mineralogists and solid state chemists to examine the physico-chemical make-up of unknown solids. It is the most effective way of observing the atomic structure of crystals. X-ray diffraction is scattering of x-rays by periodic arrangement of atoms forming lattice or crystals. X-rays are only a small part of the electromagnetic spectrum with wavelengths (λ) ranging from 0.02 Å to 100 Å. X-rays used to study crystals have λ on the order of 1 to 2 Å (i.e. copper Kα = 1.5418 Å). Visible light has much larger λ's (4000-7200 Å) and thus, x-rays are much more energetic (i.e. can penetrate deeper into a material). This can easily be seen by inspection of the Einstein equation ($E = h\nu = hc/\lambda$; E is Energy, ν frequency, c speed of light which is constant for electromagnetic radiation, λ wavelength, h Plank's constant).

Diffraction and the Bragg equation. Diffraction of an x-ray beam striking a crystal occurs because the wavelength of the x-ray beam is similar to the spacing of atoms in minerals (1-10 Å). When an x-ray beam encounters the regular, 3-D arrangement of atoms in a crystal, most of the x-rays will destructively interfere with each other and cancel each other out, but in some specific directions they constructively interfere and reinforce one another. It is these reinforced (diffracted) x-rays that produce the characteristic x-ray diffraction patterns that used for mineral identifications [19].

W.L. Bragg (early 1900's) showed that diffracted x-rays act as if they were reflected from a family of planes within crystals. Bragg's planes are the planes of atoms that make up the crystal structure. These reflections were shown to only occur under certain conditions, which satisfy the equation:

$$n\lambda = 2d\sin\theta \text{ (Bragg Equation)}$$

where, n is an interger (1, 2, 3, ..., n), λ the wavelength, d the distance between atomic planes, and θ the angle of incidence of the x-ray beam and the atomic planes. $2d\sin\theta$ is the path length difference between two incident x-ray beams where one x-ray beam takes a longer (but parallel) path because it reflects off an adjacent atomic plane. This path length difference must equal an integer value of the λ of the incident x-ray beams for constructive interference to occur such that a reinforced diffracted beam is produced.

For a given λ of incident x-rays and interplanar spacing (d) in a mineral, only specific θ angles will satisfy the Bragg equation. Example: focus a monochromatic x-ray beam (x-rays with a single λ) on a cleavage fragment of calcite and slowly rotate crystal. No reflections will occur until the incident beam makes an angle θ that satisfies the Bragg equation with n = 1. Continued rotation leads to other reflections at higher values of λ and correspond to when n = 2, 3, ... etc.; these known as 1st, 2nd, 3rd order, etc., reflections.

Operating principles. Photographic plates were traditionally used to record the intensity and position of diffracted x-rays. Modern systems use diffractometers, which are electronic x-ray counters (detectors) that can measure intensities much more accurately.

There are two main techniques used in x-ray diffraction measurements, such as single-crystal methods (x-ray beam is focused on a single crystal) and powder methods (x-ray beam focused on a powder pellet or powder smeared on a glass slide). In this thesis, we have mainly used the powder x-ray diffraction studies of minerals.

Powder methods. Essential for minerals that do not form large crystals and eliminates the problem of precise orientation necessary in single-crystal methods. Primary application is for mineral identification. Also can be used to determine mineral compositions (if d-spacing is a function of mineral chemistry) and to determine relative proportions of minerals in a mixture.

Monochromatic x-rays are focused on pellet or slide mounted on rotating stage. Since sample is powder, all possible diffractions are recorded simultaneously from hypothetical randomly oriented grains. Mount is then rotated to ensure all diffractions are obtained. Older methods used photographic techniques. Most modern applications employ X-ray powder diffractometers [19].

X-ray powder diffractometry. The XRD technique takes a sample of the material and places a powdered sample in a holder or powder mounted on glass slide, then the sample is illuminated with x-rays of a fixed wave-length and the intensity of the reflected radiation is recorded using a goniometer. The diffracted x-rays are detected electronically and recorded on an inked strip chart. The detector rotates simultaneously with the stage, but rotates through angles = 2θ. The strip chart also moves simultaneously with the stage and detector at a constant speed. The strip chart records the intensity of x-rays as the detector rotates through 2θ. Thus, the angle 2θ at which diffractions occur and the relative intensities can be read directly from the position and heights of the peaks on the strip chart. This data is then can be analyzed by using the Bragg equation to solve for the interplanar spacings (d) for all the major peaks and look up a match with standard x-ray diffraction charts.

We have used XRD for the determination of the lamellar lipid bilayer structures. The spacing between the reflections has been converted from the d values using Bragg's law. We have also used XRD for characterizing crystalline and amorphous minerals, their specific orientation, and polymorphic identifications. XRD measurements of lipid-mineral, surfactant coated minerals and mineral-protein composites obtained were prepared on glass substrates and were performed in the transmission mode on a Philips PW 1830 instrument operating at 40 kV voltages and a current of 30 mA with Cu K_{α} radiation.

2.12 Thermal gravimetric analysis

The determination of changes in chemical or physical properties of material as a function of temperature in a controlled atmosphere can be obtained by a thermal analysis. Thermal analysis is a good analytical tool to measure thermal decomposition of solids and liquids, solid-solid and solid-gas chemical reactions, material specification, purity and identification, inorganic solid material adsorption and phase transitions.

Thermogravimetric analysis (TGA) is based on the measurement of the weight loss of the material as a function of temperature. TGA operates on a null-balance principle, using an electromechanical transducer coupled to a taut-band suspension system. The sensitivity of the balance is 0.1 mg. TGA curve provides information concerning the thermal stability of the initial sample, intermediate compounds that may be formed and of the residue if any. In addition to thermal stability, the weight losses observed in TGA can be quantified to predict the pathway of degradation or to obtain compositional information. The ability to vary atmosphere during the TGA evaluation, particularly from an inert to a reactive gas, provides additional information about a material composition and its stability. The experimental data offer more sophisticated understanding of reactions occurring at materials heating. This ability to obtain measurements at higher temperatures is most useful for inorganic materials such as minerals used in this thesis.

2.13 Isothermal titration calorimetry

Every molecular interaction either generates or absorbs small amounts of heat; ultra sensitive isothermal titration calorimetry (ITC) can detect these small changes in heat [20]. Recent advances in ITC systems permit the complete characterization of molecular interactions with as little as a few nanomoles of material. An ITC experiment takes only 30–60 min to complete and is highly automated, including instrument operation and data collection and analysis. Each ITC experiment provides a complete thermodynamic profile of the interaction including the binding constant (Ka), the number of binding sites (*n*), enthalpy (ΔH), entropy (ΔS), and free energy (ΔG). Since heat is universally generated or absorbed during any molecular interaction, ITC may be viewed as a universal detector for such interactions. ITC may be used to study interactions using

native, modified, or immobilized substances and is the only bioanalytical method that directly measures enthalpy [20].

Instrument operation. The instrument utilizes a differential design with two identical cells. All binding processes occur in the sample cell, whose temperature is continuously compared to that of the reference cell, where no reaction takes place. The cells are surrounded by an inner shield, which is maintained at the same temperature as the cells in order to minimize any heat flow to or from the cells. The outer shield is also maintained at the same temperature, to compensate for any changes in room temperature. During operation, a very small constant power is supplied to a heater on the reference cell. The amount of power supplied to the sample cell (feedback power) is continuously adjusted so that its temperature is always identical to that of the reference cell. If, for example, an exothermic reaction occurs in the sample cell, then the feedback power to the sample cell will automatically be reduced to null the temperature difference caused by the heat released in the sample cell. The precise amount of heat released by the exothermic process can then be determined since it is exactly equal to the reduction in the amount of feedback heat necessary to reestablish the temperature null between the cells [20].

We have used MicroCal VP-ITC instrument, which is an ultrasensitive ITC system that requires less sample and is easier to use than preceding models. These characteristics allow ITC to be used as a routine method for studying molecular interactions. ITC is an extremely powerful thermodynamic technique that has been used with much success in understanding biomolecular binding processes [21-25]. It is widely used in biochemistry to study protein-ligand [21], protein-protein [22], DNA-RNA [23], DNA-protein [24] and protein-lipid [25] interactions. In this thesis, we have used ITC in order to understand the strength and nature of interaction of molecules during the synthesis of minerals.

2.14 Gel electrophoresis

The term electrophoresis describes the migration of a charged particle under the influence of an electric field [26]. Many important biological molecules, such as amino acids, peptides, proteins, nucleotides and nucleic acids, posses ionizable groups and, therefore, at any given pH, exist in solution as electrically charged species either as cations (+) or anions (-). Under the influence of an electric field these charged particles

will migrate either to the cathode or to the anode, depending on the nature of their net charge [26].

The equipment required for electrophoresis consists basically of two items, a power pack and an electrophoresis unit. Electrophoresis units are available for running either vertical or horizontal gel systems. In this thesis, we have used a vertical gel system. Vertical slab gel units are commercially available and routinely used to separate proteins in acrylamide gels. The gel is formed between to glass plates that are clamped together but held apart by plastic spacers. Gel dimensions are typically 12 cm x 14 cm, with a thickness of 0.5 to 1 mm. A plastic comb is placed in the gel solution and is removed after polymerization to provide loading wells for samples. When the apparatus is assembled, the lower electrophoresis tank buffer surrounds the gel plates and affords some cooling of the gel plates. The electrophoresis is carried out in an appropriate buffer, which is essential to maintain a constant state of ionization of the molecules being separated [26].

Electrophoresis of proteins

Sodium dodecyl sulphate-polyacrylamide gel electrophoresis. SDS-polyacrylamide gel electrophoresis (SDS-PAGE) is the most widely used method for analyzing protein mixtures qualitatively. It is particularly useful for monitoring protein purification and, because the method is based on the separation of proteins according to size, the method can also be used to determine the relative molecular mass of proteins. SDS (CH_3-$(CH_2)_{10}$-$CH_2OSO_3^-Na^+$) is an anionic detergent. The protein samples to be run on SDS-PAGE are firstly boiled for 5 min in sample buffer containing β-mercaptoethanol and SDS. The mercaptoethanol reduces any disulphide bridges present that are holding together the protein tertiary structure, and the SDS binds strongly to, and denatures the protein. Each protein in the protein mixture is therefore fully denatured by this treatment and opens up into a rod-shaped structure with a series of negatively charged SDS molecules along the polypeptide chain. The original negative charge on the molecule is therefore completely swamped by the negatively charged SDS molecules and hence, the polypeptide chains move in an SDS-PAGE according to their relative masses [26]. The protein fraction responsible for the control of mineral morphology was analyzed by 10 % SDS-PAGE carried out at pH 8.2 according to the procedure published by Laemmli [27].

2.15 References

[1] Maissel, L. I.; Glang, R. *Handbook of thin film technology*, McGraw Hill Book Company, NewYork, **1970**.

[2] (a) Burrell, M. C.; Armstrong, N.R. *Langmuir* **1986**, *2*, 37. (b) Cheek, G.T.; O' Grady, W.E. *J. Electroanal. Chem.*, **1990**, *277*, 341. (c) Wang, J.; Frostman, L.M.; Ward, M.D. *J. Phys. Chem.* **1992**, *96*, 5224. (d) Buttry, D. A.; Ward, M.D. *Chem. Rev.* **1992**, *92*, 1356. (e) Brust, M.; Etchonique, R.; Calvo, E.J.; Gordillo, G. J. *J.C.S. Chem. Commun.*, **1996**, 1949. (f) Patil, V.; Mayya, K. S.; Pradhan, S. D.; Sastry, M. *J. Am. Chem. Soc*., **1997**, *119*, 9281. (g) Patil, V.; Mayya, K. S.; Pradhan, S. D.; Sastry, M. *J. Am. Chem. Soc*., **1997**, *119*, 9281 (h) Sastry, M.; Patil, V.; Sainkar, S. R. *J. Phys. Chem. B*, **1998**, *102*, 1404. (i) Caruso, F.; Niikura, K.; Furlong, D. N.; Okahata, Y. *Langmuir* **1997**, *13*, 3427. (j) Gole, A.; Dash, C.; Mandale, A. B.; Rao, M.; Sastry, M. *Anal.Chem.* **2000**, *72*, 4301.

[3] Curie, P.; Curie, J. C. R. *Acad. Sci.* **1880**, *91*, 294.

[4] Sauerbrey, G. *Z.Phys. (Munich)* **1959**, *155*, 206.

[5] McCrackin, F. L.; Passaglia, E.; Stromberg, R. R.; Steinberg, H. L. *J. Res. Natl. Inst. of Stand. & Tech.* **2001**, *106*, 589.

[6] (a) Hall, A.C. *Surf. Sci*, **1969**, *16*, 1. (b) Azzam, R.M.A.; Bashara, N.M. *Ellipsometry and Polarized Light*.; **1977**, North-Holland: Amsterdam.

[7] Ulman, A. *An introduction to Ultrathin Organic Films: from Langmuir-Blodgett to Self-Assembly*, Academic Press, San Diego, CA, **1991**.

[8] Lee, T. R.; Carey, R. I.; Biebuyck, H. A.; Whitesides, G. M. *Langmuir* **1994**, *10*, 741.

[9] Condrate, R. "*Fourier transform infrared spectroscopy*" (CES 348 Spectroscopy) New York **2000**.

[10] George, W.O.; Mcintyre, P.S. *Infrared Spectroscopy: Analytical Chemistry by open learning*, John Wiley and Sons, USA, **1987**.

[11] (a) Marshbanks, T.L.; Ahn, D.J.; Franses, E.I. *Langmuir* **1994**, *10*, 276. (b) Falini, G.; Albeck, S.; Weiner, S.; Addadi, L. *Science* **1996**, *271*, 67. (c) Dong, A.; Huang, P.; Caughey, W. S. *Biochemistry* **1992**, *31*, 182.

[12] Denney, R.C; Sinclair, R. *Visible and Ultraviolet Spectroscopy*. *Analytical Chemistry by open learning series*, John Wiley and Sons, USA.

[13] Mie, G.; *Ann. Phys*., **1908**, *25*, 377.

[14] (a) Mulvaney, P. *Langmuir*, **1996**, *12*, 788. (b) Henglein, A. *J.Phys.B*., **1993**, *97*, 5457.

[15] (a) Brust, M.; Walker, M.; Bethell, D.; Schiffrin, D.J.; Whyman, R. *J.C.S. Chem Commun*., **1994**, 801; (b) Malinsky, M.D.; Kelly, K.L.; Schatz, G.C.; VanDuyne, R.P. *J.Am.Chem.Soc*., **2001**, *123*, 1471; (c) Templeton, A.C.; Wvelfing, W.P.; Murray, R.W. *Acc.Chem.Res*., **2000**, *33*, 27.

[16] Notes written by Chasteen, T. G. Department of Chemistry, Sam Houston State University, Huntsville, Texas 77341. Copyright **2000**.

[17] Lawes, G. *Scanning electron microscopy and X-ray microanalysis: Analytical chemistry by open learning*, John Wiley & sons, **1987**.

[18] Knoll, M.; Ruska, E. *Z. Phys (Munich)* **1932**, *78*, 318.

[19] Cullity, B. D. "*Elements of X-ray diffraction*" Addison-Wesley publishing company, Inc **1959**.

[20] Chellani, M. *Application Notes* **1999**, 14.

[21] Qin, K.; Srivastava, D. K. *Biochemistry* **1998**, *37*, 3499.

[22] Pierce, M. M.; Raman, C. S.; Nall, B. T. *Methods* **1999**, *19*, 213.

[23] Barbieri, C. M.; Li, T. K.; Guo, S.; Wang, G.; Shallop, A. J.; Pan, W.; Yang, G.; Gaffney, B. L.; Jones, R. A.; Pilch, D. S.; *J. Am. Chem. Soc.* **2003**, *125*, 6469.

[24] Kunne, A.; Sieber, M.; Meierhans, D.; Allemann, R. K. *Biochemistry* **1998**, *37*, 4217.

[25] Wenk, M. R.; Seelig, J. *Biochemistry* **1998**, *37*, 3909.

[26] Wilson, K.; Walker, J. "*Practical Biochemistry*" (5^{th} Edition) Cambridge University Press.

[27] Laemmli, U. K. *Nature* **1970**, *227*, 680.

CHAPTER III

Thermally Evaporated Lipid Thin Films as Templates for the Growth of Minerals

This chapter discusses the use of an anisotropic constrained environment for mineral growth by using thin films of thermally evaporated lipid bilayers as templates. The growth of minerals such as $BaSO_4$, $BaCrO_4$, $SrCO_3$ and $CaCO_3$ within thermally evaporated sodium bis-2-ethylhexyl-sulfosuccinate and stearic acid thin films were demonstrated by a process of sequential entrapment of Ba^{2+}, Sr^{2+}, Ca^{2+} followed by SO_4^{2-}, CrO_4^{2-}, CO_3^{2-} ions. The formation of the minerals is believed to occur via hydrophobic association of the respective crystallites that are covered by a monolayer of the surfactant used. The issue of crystal morphology variation, their polymorph selectivity and the kinetics of crystal growth in different thermally evaporated templating matrices were discussed.

Part of the work presented in this chapter has been published:

1) Rautaray, D.; Kumar, A.; Reddy, S.; Sainkar, S.R.; Sastry, M. *Crystal Growth & Design* **2002**, *2*, 197-203. 2) Rautaray, D.; Sainkar, S. R.; Sastry, M. *CrystEngComm* **2003**, *5*, 400-404. 3) Rautaray, D.; Sainkar, S. R.; Sastry, M. *Langmuir* **2003**, *19*, 888-892. 4) Rautaray, D.; Sainkar, S. R.; Sastry, M. *Chem. Mater.* **2003**, *15*, 2809-2814. 5) Rautaray, D.; Sinha, K.; Sainkar, S. R.; Pasricha, R.; Pavaskar, N. R.; Sastry, M. *J. Am. Ceram. Soc.* **2004**, (*In Press*).

3.1 Introduction

The use of organic compounds as templates for the generation of inorganic structures and materials has received increasing attention over the last decade [1]. Inorganic/organic hybrid films offer the possibility of combining the distinct properties of organic and inorganic components. For example, during biomineralization process, natural inorganic/organic hybrid materials are formed through a cooperative interaction of inorganic materials with organic macromolecules, where the macromolecules control the nucleation, growth, morphology, structure, and crystal orientation of the inorganic component [2].

Several emerging strategies in biomimetic research take advantage of compartmentalized and/or template chemical reactions. The natural prototype of this approach is in biomineralization [3]. Biomineralization occurs within specific subunit compartments or micro-environments, which stimulates the crystal production at certain functional sites and prevention of the process at all other sites, producing a specific mineral with defined crystal size and orientation, and packaging many incremental units together in a moving front process to form fully densified microscopic structures [3a]. There are two key structural factors in the use of organic matrices in controlled nucleation. Firstly the matrix is pre-organized with respect to nucleation through processes such as self-assembly and aggregation, which impart spatial regulation of functional groups. Secondly nucleation at the matrix surface with a limited number of sites being confined where the ion binding could result in specific conformational changes in the pre-organized matrix such that nucleation is activated within localized domains [3b]. The first known examples of organic/inorganic nano-laminate composites is the emergence of mollusks [4]; the brickwork architecture of nacre or mother-of-pearl, consisting of alternating tablets of aragonite (a few hundreds of nanometers thick) and thin organic films (a few tens of nanometers thick), imparts to the mollusk shell an exceptional strength without the brittleness associated with pure inorganic phases [4]. In analogous biomimetic approaches, synthetic organic layers have been employed to nucleate inorganic thin films and complex organic/inorganic nanolaminates at interfaces [5]. Recent developments in the synthesis and processing of inorganic thin films at organic interfaces and between organic layers include Langmuir films at the air-water

interface [6], self-assembled films on solid substrates [7], organic polymer films [8], and vesicles [9] as the nucleating templates.

Thus it is clear that the protein matrix plays a very important role in regulating biomineral formation in nature [10]. The role of a matrix is primarily to lower the activation energy of nucleation by decreasing the time between ionic collisions. In many cases, the matrix is assumed to have an orientational role such that specific molecular interactions at the nuclei-matrix interface results in crystallographic alignment of the forming crystals [10]. However there remain many unknowns as to how the matrix affects the crystallization process, especially the initial nucleation [10a]. Matrix mediated growth of inorganic materials has not been systematically investigated in vitro even though it may have applications in crystal engineering and materials science. By drawing inspiration from natural phenomenon, in this chapter we have presented a synthetic method for the synthesis of inorganic-in-organic thin films, where the inorganic phase is preformed *in-situ* in the organic thin lipid films, by using simple electrostatic interactions.

It is known that lipids play an important role in biomineralization and countless other biological processes, and they are receiving increasing attention for the synthesis of new biomimetic biomaterials [11]. In this chapter, we have used thermally evaporated lipid bilayer stacks such as sodium bis-2-ethylhexyl-sulfosuccinate ($C_{20}H_{37}NaO_7S$; aerosol OT, AOT) and stearic acid (CH_3 $(CH_2)_{16}$ COOH; StA) for the immobilization of cations such as Ba^{2+}, Sr^{2+} and Ca^{2+} prior to the formation of minerals such as $BaSO_4$, $BaCrO_4$, $SrCO_3$ and $CaCO_3$. The formation of such technologically important minerals within the thin lipid films is interesting since crystal growth occurs in a constrained environment, which is anisotropic in nature. The choice of the two surfactants for thin film formation and crystal growth was motivated by differences in their structure - StA possesses a single hydrocarbon tail and forms lamellar structures of StA bilayers arranged in a head-head and tail-tail configuration while AOT is a twin-tailed surfactant known to form reverse micelles. Our aim is also to highlight the role of the surfactant (in a thin film form) in modulating the morphology of crystals grown within the film host and to see whether significant changes occur in the morphology and assembly of mineral crystals if AOT molecules are physically constrained in the form of thin films and thus not as mobile as AOT molecules in reverse micelles [12].

3.2 Thermally evaporated lipid bilayers stacks

In this laboratory, a novel process was developed based on thermally evaporated ionizable lipid films for the electrostatic entrapment of inorganic ions [13], surface-modified nanoparticles [14], proteins/enzymes [15] and DNA [16]. This approach was based on electrostatically entrapping ions for example Cu^{2+} and Ni^{2+} within lipid matrices such as stearic acid, which thereafter can be reduced *in-situ* to yield the corresponding metal nanoparticles [17]. Interesting low-temperature alloying of the Cu and Ni nanoparticles synthesized in such lipid bilayer stacks has been observed [17]. *In situ* growth of gold and silver nanoparticles by reduction of the corresponding ions entrapped in lipid films has also been demonstrated [18]. It is clear that metal ions entrapped in such lipid bilayer stacks can be chemically reacted to yield a variety of materials within the confines of the bilayer stacks. In this chapter we have extended this protocol and studied the growth of minerals within the lipid bilayer stacks by suitable reaction of entrapped metal cations.

We have used this novel protocol for the synthesis of important minerals and the experiments were carried out as follows:

1. The formation of barium sulfate crystals in thermally evaporated AOT and StA thin films were carried out by sequential entrapments of Ba^{2+} and SO_4^{2-} ions.
2. The formation of barium chromate crystals in thermally evaporated AOT and StA thin films were carried out by sequential entrapments of Ba^{2+} and CrO_4^{2-} ions.
3. The formation of strontium carbonate crystals in thermally evaporated AOT and StA thin films were carried out by sequential entrapments of Sr^{2+} and CO_3^{2-} ions.
4. The formation of calcium carbonate crystals in thermally evaporated AOT and StA thin films were carried out by sequential entrapment of Ca^{2+} and CO_3^{2-} ions.

Thin films of anionic surfactants AOT and StA of 500 Å thickness were thermally vacuum deposited in an Edwards E306 vacuum coating unit equipped with a liquid nitrogen trap onto gold-coated AT-cut quartz crystals, glass and Si (111) substrates. The surfactant was deposited by a process of sublimation in vacuum at a temperature not exceeding 80^{o} C. The pressure during film deposition was 1 x 10^{-7} Torr and the deposition rate was 50 Å /min. FTIR analysis of the thermally evaporated AOT and StA films showed no evidence of thermal degradation of the surfactant molecules. The film

thickness was monitored using a QCM fitted to the deposition chamber and crosschecked by ellipsometry measurements.

After deposition of the AOT and StA films, the films were used to grow minerals such as $BaSO_4$, $BaCrO_4$, $SrCO_3$ and $CaCO_3$ by the immersion of the lipid films separately in electrolyte solutions such as $BaCl_2$, $SrCl_2$ and $CaCl_2$ and thereafter the subsequent reaction with respective counterions such as SO_4^{2-}, CrO_4^{2-} and CO_3^{2-}.

After deposition of the AOT and StA films, the QCM crystals were separately immersed in respective electrolyte solutions and the frequency change of the crystals were monitored *ex-situ,* as a function of time of immersion in the electrolyte solutions, taking care to wash and dry the crystals thoroughly prior to frequency measurement. Frequency measurements were made on an Edwards FTM5 frequency counter (stability and resolution of 1 Hz). For the 6 MHz crystal used in this study, the mass resolution was 12.1 ng/cm^2 and the frequency changes were converted to mass loading using the Sauerbrey equation [19]. The optimum immersion time determined from the QCM kinetics measurements were used to load the AOT and StA films on glass and Si (111) substrates with Ba^{2+}/Sr^{2+}/Ca^{2+} ions by similar immersion separately in the respective electrolyte solutions. After formation of the barium, strontium and calcium sulfosuccinate and stearate films, the films on glass were subjected to XRD analysis and the films on Si (111) substrates were subjected to FTIR measurements. Thereafter, the ion-entrapped films on the QCM crystals were reacted with the appropriate counterions by immersion in the necessary aqueous solution and the frequency changes of the crystals were monitored as a function of time of immersion of the respective QCM crystals in the electrolyte solutions. The optimum immersion time determined from the QCM kinetics measurements were used to grow the minerals within the lipid matrix on different solid substrates. The QCM measurements were thus merely used as an indicator of the optimum time of immersion in the electrolyte solutions. After the growth of minerals in the lipid films, the mineral-lipid composites were characterized by FTIR, XRD, EDAX and SEM measurements. Prior to FTIR, XRD, SEM and EDAX studies, these films were subjected to mild ultrasonic agitation in water for ca. 3-5 min to dislodge any mineral crystals that had nucleated in the solution and had bound weakly to the AOT and StA films surface. In order to determine whether the growth of these crystals were purely surface processes, contact angles were measured at various points on the films.

3.3 Crystallization of $BaSO_4$ in thermally evaporated lipid bilayers stacks

Thin films of anionic surfactants AOT and StA of 500 Å thickness were thermally vacuum deposited. After deposition of the AOT and StA films, the deposited substrates were separately immersed in 50 ml of 10^{-3} M aqueous $BaCl_2$ solution (pH 5.5) based on the optimum immersion time determined from the QCM kinetics. After formation of barium sulfosuccinate and barium stearate films, the films were immersed in 50 ml of 1.4 x 10^{-3} M Na_2SO_4 aqueous solution (pH 6) by using the optimum immersion time from QCM measurements. The growth of barium sulfate in AOT and StA thin films were characterized by FTIR, XRD, EDAX, SEM and contact angle measurements.

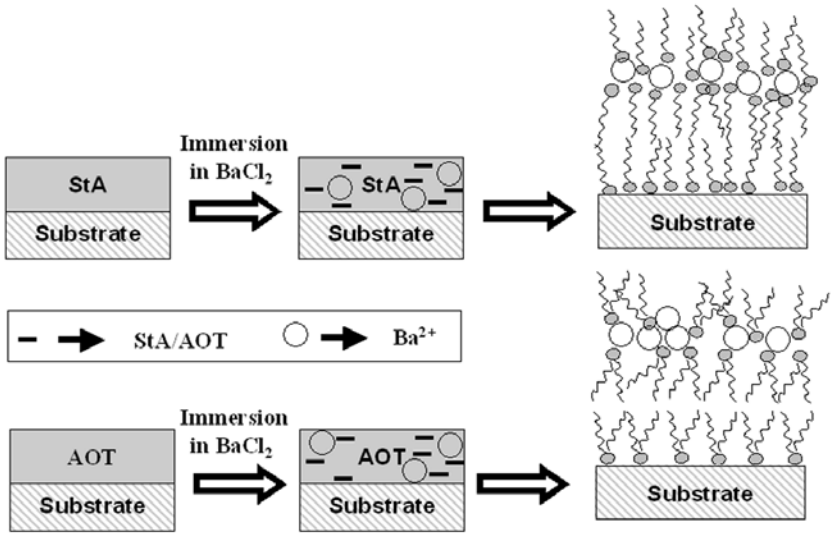

Fig. 3.1 : *Cartoon showing (not to scale) the expected organization of barium ions within thermally evaporated StA and AOT thin films after immersion in aqueous $BaCl_2$ solution.*

The scheme above (Fig.3.1) shows one bilayer of barium stearate/sulfosuccinate resting on a monolayer of StA/AOT in contact with the substrate. In reality, a 500 Å thick barium stearate/sulfosuccinate films would consist of roughly 10 such bilayers stacked one on top of the other.

3.3.1 Quartz crystal microgravimetry (QCM) Studies

The kinetics of incorporation of Ba^{2+} ions in 500 Å thick AOT and StA films were followed by QCM and the data recorded as a function of time of immersion in the $BaCl_2$ solution and thereafter in the Na_2SO_4 solution are shown in Fig.3.2A ($BaSO_4$-AOT) and Fig.3.2B ($BaSO_4$-StA). During immersion in the $BaCl_2$ solution, a fairly large

mass increase is seen in both the cases and is attributed to electrostatically controlled diffusion (and entrapment) of the Ba^{2+} ions in the AOT and StA matrix respectively. At pH 5.5, the sulfosuccinate and stearate ions of the AOT and StA matrix respectively is expected to be fully negatively charged leading to maximum attractive electrostatic interaction with the Ba^{2+} cations. It is observed that equilibration of the Ba^{2+} ion density in the film occurs within 6300 sec (for AOT) and 11268 sec (for StA) of immersion of the AOT and StA films in the $BaCl_2$ solution respectively. From the equilibrium mass uptake of Ba^{2+} ions i.e ca. 7000 ng cm^{-2} (for AOT) and ca. 40000 ng cm^{-2} (for StA) and the mass of the AOT film, a Ba^{2+} : AOT molar ratio of 7 : 1 and Ba^{2+} : StA molar ratio of 15 : 1 were calculated.

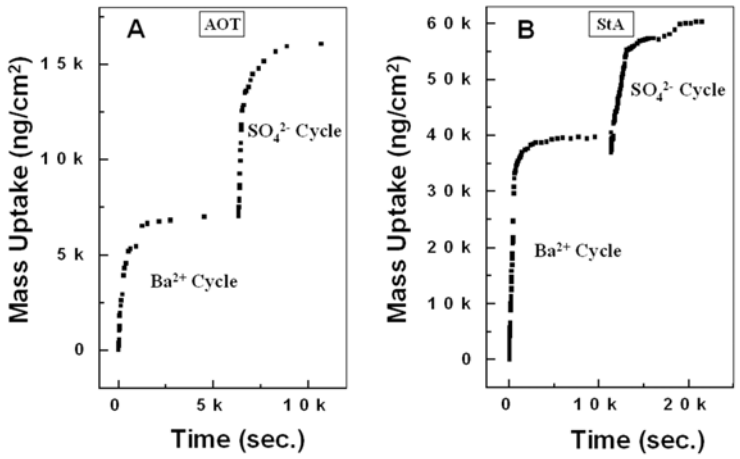

Fig. 3.2 : *(A) QCM mass uptake recorded ex-situ during immersion of a 500 Å thick AOT film sequentially in Ba^{2+} and SO_4^{2-} ion solutions. (B) QCM mass uptake recorded ex situ during Ba^{2+} and SO_4^{2-} ion incorporation in a 500 Å thick thermally evaporated StA film. The different cycles of ion exchange are indicated.*

This result indicates considerable over compensation of the negative charge in the anionic matrices by the Ba^{2+} ions. Such charge over compensation is known to occur in layer-by-layer electrostatically assembled systems [20]. However, we would like to caution here that there are number of factors that could contribute to an error in estimation of the Ba^{2+} : AOT and Ba^{2+} : StA molar ratios. One source of error could be a change in the acoustic properties of the AOT and StA films after complexations with Ba^{2+} ions. We believe binding of the Ba^{2+} ions to the AOT and StA molecules would lead to it becoming acoustically 'stiffer' and could account for (to a large extent) the seemingly unreasonable charge overcompensation observed. In thermally evaporated

surfactant films, it is likely that there are a number of defect structures such as pores in the films, which would result in creation of water channels for transport of ions into the lipid. The swelling of lamellar structure of the lipid matrix observed on immersion in water [13a] would also lead to aqueous pathways for the transport of Ba^{2+} ions into the film. Thus, the hydrocarbon layers need not necessarily be viewed as barriers to ion transport since lateral diffusion via hydrophilic water channels perpendicular to the lamellae is highly possible.

After Ba^{2+} ion entrapment within AOT and StA matrices, the Ba^{2+}-AOT and Ba^{2+}-StA covered QCM crystals were immersed in Na_2SO_4 solution (pH 6) and the frequency change of the crystals were monitored as a function of time of immersion in the electrolyte solutions. Large mass increases are observed during this cycle of immersion as well and is due to electrostatically controlled diffusion (and entrapment) of the SO_4^{2-} ions in the Ba-AOT and Ba-StA films yielded a mass uptake of ca. 16113 ng cm^{-2} (10622 sec) and ca. 60667 ng cm^{-2} (21576 sec) were measured respectively. The Ba^{2+} : SO_4^{2-} molar ratio of 1.4 : 1 (AOT) and 1.3 : 1 (StA) were calculated. The QCM measurements were purely used as an indicator of the optimum time of immersion in the $BaCl_2$ and Na_2SO_4 solutions for $BaSO_4$ formation.

3.3.2 Fourier transform infrared (FTIR) spectroscopy studies

Fig.3.3A shows FTIR spectra recorded from the as-deposited 500 Å thick AOT film on a Si (111) substrate (curve 1), the AOT film after entrapment of Ba^{2+} ions (curve 2) and the barium sulfosuccinate film after reaction with Na_2SO_4 (curve 3). Prominent absorption bands are seen at 1047, 1700, 2850 and 2920 cm^{-1} in the case of the as-deposited AOT film. The band at 1047 cm^{-1} is assigned to the S=O stretching vibration of the sulfonate group present in the AOT molecules (Fig.3.3A, curve 1) [21]. The band at 1700 cm^{-1} is due to carbonyl stretch vibrations in the AOT molecules and the two bands at 2850 and 2920 cm^{-1} have been assigned to the methylene symmetric and antisymmetric stretching vibrations in the hydrocarbon chains respectively. After entrapment of Ba^{2+} ions in the AOT thin film, the absorption band at 1047 cm^{-1} (Fig.3.3A, curve 1) has shifted to 1103 cm^{-1} (Fig.3.3A, curve 2) clearly indicating that the Ba^{2+} ions have complexed electrostatically with the sulfonate groups in the film. The FTIR spectrum

recorded from the barium sulfosuccinate film after reaction with Na_2SO_4 (Fig.3.3A, curve 3) is essentially featureless.

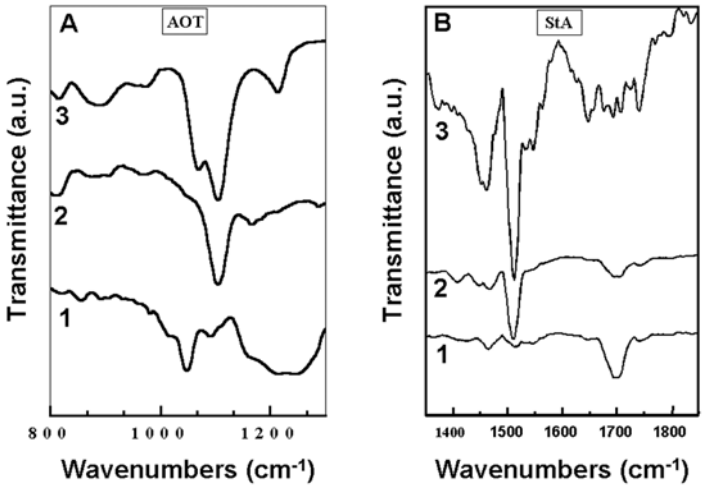

Fig. 3.3 : *The FTIR spectra recorded from a 500Å thick AOT films (A) and StA films (B) on a Si (111) substrate (curve 1), the AOT and StA films after incorporation of Ba^{2+} ions (curve 2), and the barium sulfosuccinate and stearate films after incorporation of SO_4^{2-} ions (curve 3) in a particular spectral window.*

Fig.3.3B shows FTIR spectra recorded from the as-deposited 500 Å thick StA films on a Si (111) substrate (curve 1), the StA film after immersion in $BaCl_2$ solution (curve 2) and the barium stearate film after reaction with Na_2SO_4 (curve 3). A prominent absorption is seen at 1700 cm^{-1} in the case of the as deposited StA film (curve 1) as well as with the StA film after immersion in $BaCl_2$ solution (curve 2). This band is due to excitation of carbonyl stretch vibrations in the carboxylic acid groups of the fatty acid film. In addition to this band, the barium stearate film shows an additional absorption at ca. 1515 cm^{-1} (curve 2). This band is assigned to the carbonyl stretch of the carboxylate groups of the stearic acid. The presence of a small band at 1700 cm^{-1} in the barium stearate film indicates that complete salt formation had not occurred. The FTIR spectrum recorded from the barium stearate film after reaction with Na_2SO_4 (curve 3) is essentially featureless indicating substantial reorganization of the lipid molecules around the barite crystals.

3.3.3 Lamellar ordering studies of Ba-AOT and Ba-StA films

It has been shown before in this laboratory that thermally evaporated fatty acid films when immersed in electrolyte solutions such as $PbCl_2$ and $CdCl_2$ resulted in the

electrostatic entrapment of the metal cations and the spontaneous ordering of the lipid films into a lamellar *c*-axis oriented structure [13]. We have used this approach to form barium sulfosuccinate and barium stearate films by immersion of 500 Å thick AOT and StA films in $BaCl_2$ solution. The formations of lamellar barium sulfosuccinate (curve 2, Fig.3.4A) and barium stearate (curve 2, Fig.3.4B) were ascertained by the presence of characteristic odd-even intensity oscillations in the (0 0 l) Bragg reflections in the XRD patterns of the films [13]. These Bragg reflections are not observed in the as-deposited AOT (curve 1, Fig.3.4A) and StA (curve 1, Fig.3.4B) films. The *c*-axis oriented lamellar structure of a barium sulfosuccinate and barium stearate bilayers are illustrated in the schematic in Fig.3.1.

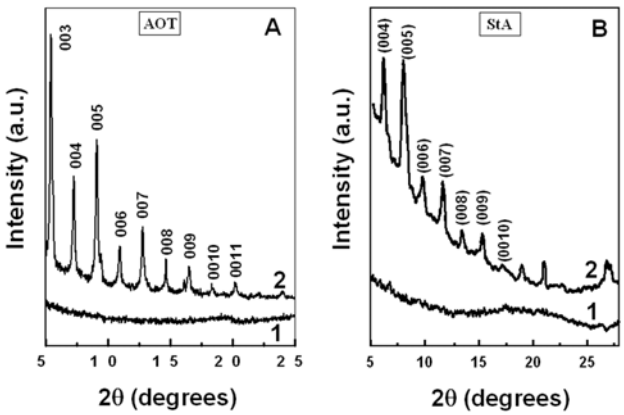

Fig. 3.4 : (A) *XRD patterns recorded from a 500 Å thick as-deposited AOT film (curve 1) and this film after entrapment of Ba^{2+} ions (curve 2). XRD pattern recorded from a 500 Å thick StA film (curve 1) and XRD pattern recorded from a 500 Å thick StA film after entrapment of Ba^{2+} ions (curve 2). The (0 0 l) Bragg reflections are identified in the figures.*

3.3.4 Scanning electron microscopy (SEM) measurements

3.3.4.1 Formation of $BaSO_4$ within AOT thin film

SEM pictures recorded from a 500 Å thick AOT film on a Si (111) substrate after formation of $BaSO_4$ are shown in Figs.3.5A, B and C at different levels of magnification. The SEM images (Fig.3.5A and B) show well-formed assembly of barite crystals organized into quasi-linear super-structures. The higher magnification SEM image (Fig.3.5C) recorded from the barite-AOT film clearly shows the presence of highly organized assemblies of mature barite crystals. The barite crystals are flat and needle-like in shape. This image also indicates two levels of hierarchy in the assembly of barite crystals. At the first level, the flat barite crystals are assembled into flower-like patterns

and later these flower-like assemblies are in turn assembled into quasi-linear superstructures of length often in excess of 20 μm.

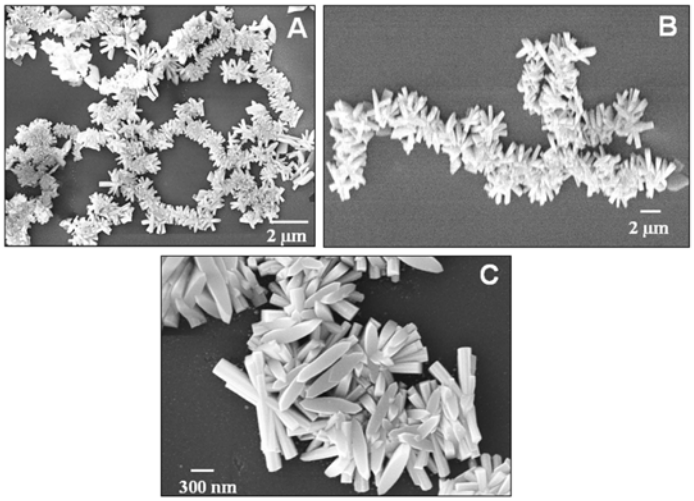

Fig. 3.5 : *Representative SEM images at different magnifications of $BaSO_4$ crystals formed in a 500 Å thick thermally evaporated AOT thin film.*

One possible method to ascertain the mechanism is to monitor the growth of the barite crystals as a function of time of immersion of Ba-AOT film in the Na_2SO_4 solution. SEM pictures recorded from a 500 Å thick barium-sulfosuccinate film on a Si (111) wafer after immersion in Na_2SO_4 solution for 30, 45, 60 and 80 minutes are shown in Fig.3.6A-D respectively.

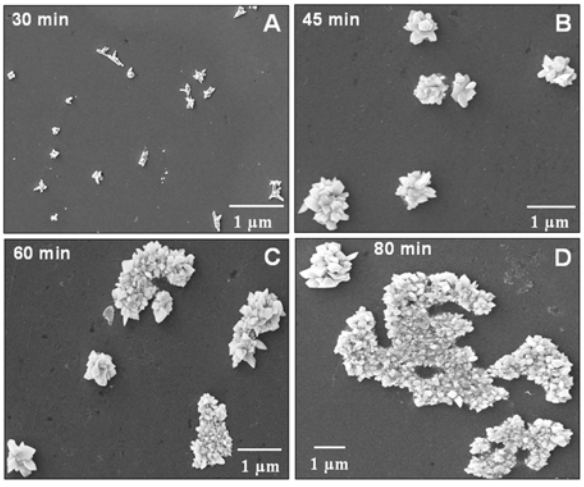

Fig. 3.6 : A–D) *Representative SEM images of $BaSO_4$ crystals grown in a 500 Å thick thermally evaporated AOT thin film as a function of time of reaction of the barium-sulfosuccinate film with SO_4^{2-} ions.*

After 30 min of reaction, the SEM image (Fig.3.6A) shows the growth of very small barite crystallites on the substrate surface. After a further 15 min of reaction, the growth of flat disk/needle like plates of $BaSO_4$ assembled in flower-like pattern is observed (Fig.3.6B). Reaction of the barium- sulfosuccinate film for 60 min leads to self-assembly of the flower-like aggregates into higher order superstructure (Fig.3.6C). Immersion of the barium-sulfosuccinate film for 80 minutes in the Na_2SO_4 solution clearly shows assembly of the barite crystals into quasi-linear superstructures (Fig.3.6D). The size of the barite crystals in Figs.3.6C and D is not very different indicating that the crystal growth is complete within 60 min of reaction and that further immersion in the electrolyte solution facilitates assembly of the barite crystals. Thus, SEM images recorded from the barium-sulfosuccinate film during growth of the barite crystals suggest that the growth process occurs within the AOT matrix and not externally by a leaching process. Such assemblies of flat, needle shaped barite crystals formed within AOT thin films as templates have not been observed in the numerous earlier studies on barite crystallization [6,12,22] including $BaSO_4$ formation in solution using AOT microemulsions [12].

3.3.4.2 Formation of $BaSO_4$ within StA thin film

SEM pictures recorded from a 500 Å thick stearic acid film after formation of $BaSO_4$ are shown in Fig.3.7A and B. The lower magnification image (Fig.3.7A) shows a number of well-formed barite crystals of fairly uniform size and with faceted surfaces.

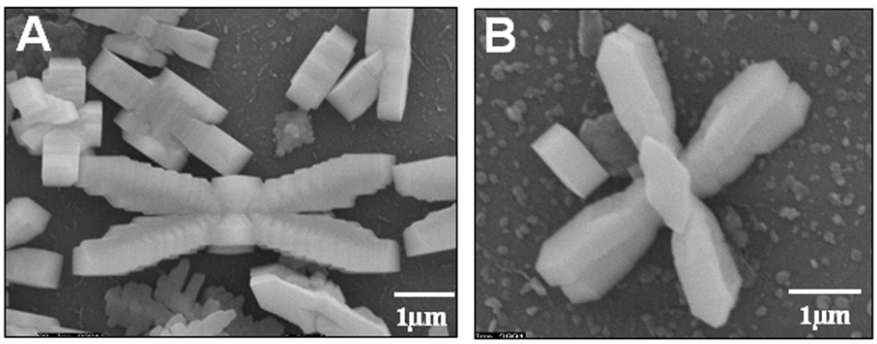

Fig. 3.7 : *SEM images of $BaSO_4$ crystals formed in a thermally evaporated StA thin film at different magnifications.*

The mature crystals exhibit an elongated hexagonal morphology similar to that obtained for barite crystals grown in solution along with block co-polymers [22b]. The two SEM

images show fortuitously a large crystal viewed edge-on (center of Fig.3.7A) and parallel to the lipid bilayer templating surface (Fig.3.7B). It is observed in the SEM images that secondary nucleation occurs around a central crystal leading to the formation of a flower-like structure with four petals. What is interesting is that the secondary crystals occur in pairs, which can be clearly seen in Fig.3.7A and to some extent in Fig.3.7B. Such a flower-like structure consisting of pairs of barite crystals in each petal have been observed by Qi *et al* [22b]. In their study, flowers consisting of up to 10 petals were formed during the growth of barite in the presence of sulfonated derivative of poly(ethyleneglycol)-block-poly(ehtyleneimine)-poly(sulfonic acid) (PED-b-PEIPSA).

3.3.4.3 Formation of $BaSO_4$ in solution

It is clear from the above SEM studies that the barite crystal morphology is a strong function of the nature of the template used (Fig.3.6 & 3.7) and that the crystal morphology is unique to a particular template. However, an important aspect to be verified is the variation in the $BaSO_4$ crystal morphology during growth in solution in the absence of any additives. In control experiments, $BaSO_4$ crystals were grown in solution without any additives and the SEM images recorded from the crystals formed are shown in Fig.3.8.

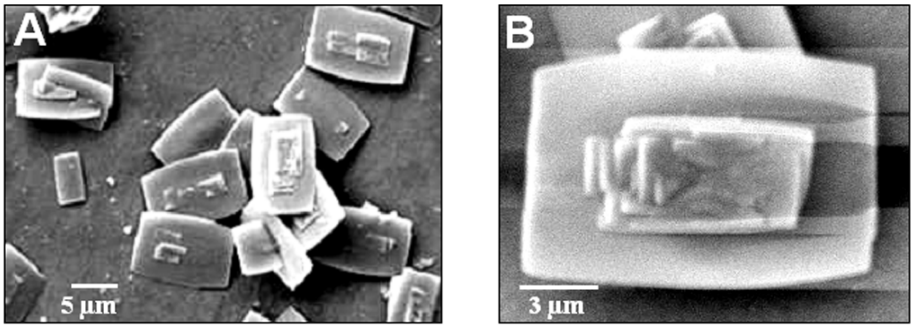

Fig. 3.8 : *SEM images of $BaSO_4$ crystals grown in solution by reaction of aqueous solutions of $BaCl_2$ and Na_2SO_4.at different magnifications.*

The crystals exhibited a plate like structure with evidence of some secondary nucleation from the center of the plates (Fig.3.8). This morphology is clearly distinct from the morphology of barite crystals grown on any of the thermally evaporated lipid thin film templates as observed above (Fig.3.6 & 3.7).

3.3.5 Energy dispersive analysis of X-rays (EDAX) measurements

A chemical analysis of the as-deposited 500 Å thick AOT film on a Si (111) substrate before and after immersion in $BaCl_2$ solution and after reaction with SO_4^{2-} ions was done using EDAX (Fig.3.9A, curves 1, 2 and 3 respectively). It is seen that the as-deposited AOT thin film shows the presence of Na, S, C and O signals (curve 1). A quantitative analysis of the Na and S components yielded a 1 : 1.22 atomic ratio for Na : S in agreement with the expected stoichiometry. After immersion of the AOT film in $BaCl_2$ solution, a strong Ba signal appears and indicates the entrapment of Ba^{2+} ions in the AOT thin film. A quantitative analysis of the Ba and S components yielded a 1 : 1.69 atomic ratio for Ba : S. This is in reasonable agreement with the expected Ba : S ratio of 1 : 2 based on charge neutrality considerations. Thereafter, immersion of Ba^{2+}-AOT film in Na_2SO_4 solution resulted in an enhancement of the S and O signals (curve 3) indicating the formation of $BaSO_4$ crystals. EDAX analysis of the $BaSO_4$ crystals yielded a Ba : S : O atomic ratio of 1 : 1.56 : 12 (curve 3 in Fig.3.9A). While the Ba : S ratio is in fair agreement with the expected stoichiometry, excess oxygen is due to sampling from the silica substrate.

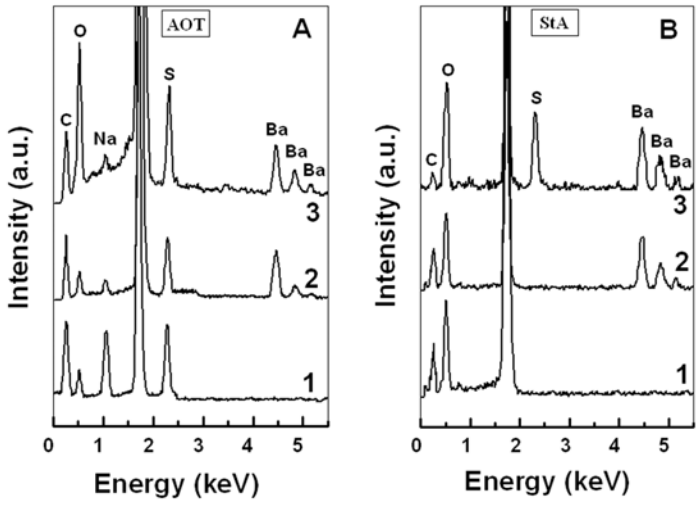

Fig. 3.9 : (A) *EDAX spectra recorded from as-deposited 500 Å thick AOT film on a Si (111) substrate (curve 1), the AOT film after incorporation of Ba^{2+} ions (curve 2) and the Ba-AOT film after reaction with SO_4^{2-} ions (curve 3).* (B) *EDAX spectra recorded from as-deposited 500 Å thick StA film on a Si (111) substrate (curve 1), the StA film after incorporation of Ba^{2+} ions (curve 2) and the Ba-StA film after reaction with SO_4^{2-} ions (curve 3).*

Similarly, a chemical analysis of the as-deposited 500 Å thick StA film on a Si (111) substrate before and after immersion in $BaCl_2$ solution and after reaction with SO_4^{2-} ions was done using EDAX (Fig.3.9B, curves 1, 2 and 3 respectively). It is seen that the as-deposited StA thin film shows the presence of C and O signals (curve 1) arising from the organic template. After immersion of the StA film in $BaCl_2$ solution, a strong Ba signal appears and indicates the entrapment of barium ions into the StA lipid matrix. Thereafter, immersion of Ba^{2+}-StA film in Na_2SO_4 solution resulted in an appearance of strong S signal and an increase in the O signal (curve 3) indicating the formation of $BaSO_4$ crystals within the StA lipid matrix.

3.3.6 X-ray diffraction (XRD) studies

The XRD patterns recorded from the $BaSO_4$ crystals shown in Fig.3.5 ($BaSO_4$-AOT) and Fig.3.7 ($BaSO_4$-StA) are displayed in curve 2 & 3 in Fig.3.10 respectively. A number of Bragg reflections are identified and have been indexed with reference to the unit cell of the barite structure (a = 8.87 Å, b = 5.45 Å, c = 7.15 Å; space group *Pnma*) [23]. For comparison, the XRD pattern recorded from barite crystals grown in solution in the control experiment (Fig3.8) is shown as curve 1 in Fig.3.10.

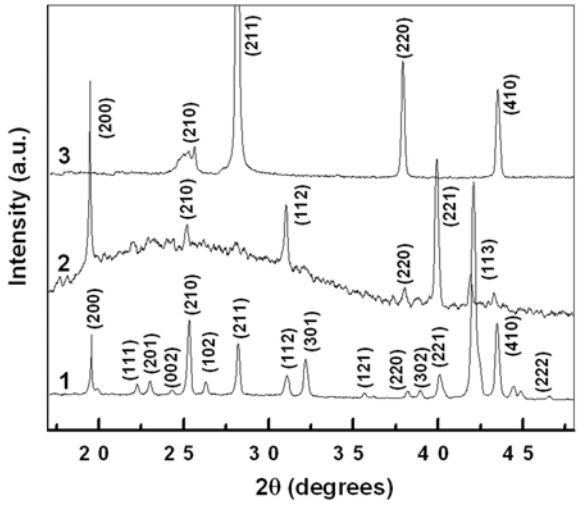

Fig. 3.10 : *XRD patterns recorded from $BaSO_4$ crystals grown in solution (curve 1), within a 500 Å thick thermally evaporated AOT film (curve 2) and StA film (curve 3). The hkl planes correspond to the Bragg reflections are identified in the figure.*

It is observed that the intensity ratios of the different Bragg reflections in the barite crystals grown in the AOT and StA films are quite different from those obtained in the

control experiment. The crystals grown in the thermally evaporated AOT thin film have pronounced orientational order, the predominant nucleating planes being (200), (112) and (221). While, the barite crystals grown in the StA thin film have orientational order along (211) and (220) planes. The presence of these intense Bragg reflections in both the XRD patterns suggests oriented growth of the barite crystals along these particular crystallographic planes and that the nature of growth in these constrained environments may play a role in face-specific nucleation of the barite crystals. We believe that favorable epitaxy between the AOT and StA molecules and the Ba^{2+} ion is responsible for the highly preferred oriented growth of barite crystals within these lipid bilayer stacks.

3.3.7 Contact angle Measurements

In order to determine whether the growth of these $BaSO_4$ crystals in the AOT thin film was purely a surface process, we measured the contact angle at various points on the film surface and found that the surface was quite hydrophobic [mean contact angle of 95^o]. This is to be contrasted with a contact angle of 65^o measured for films of barite crystals grown in solution and picked up on to a Si (111) wafer coated with a 500 Å thick AOT film. This result clearly shows that the barite aggregates observed (Fig.3.5) are covered with a monolayer of AOT, which renders them hydrophobic. Similarly, in the case of pair-coordinated petals in the flower-like barite crystals (Fig.3.7) synthesized in the StA lipid matrix indicated that the films were hydrophobic (contact angle > 90^o at all points on the film surface).

3.3.8 Summary

The crystallization of barium sulfate within thermally evaporated AOT and StA films by a process of Ba^{2+} ion entrapment and thereafter, reaction with SO_4^{2-} ions has been successfully carried out. The overall crystal morphology of barite formed within thermally evaporated AOT bilayers is very different from that of barite grown within thermally evaporated StA. Under conditions where there is good registry between the Ba^{2+} ions and the underlying lipid templates, oriented growth of barite crystals with unusual morphologies are observed. The barite crystals grown in the AOT matrix show two levels of hierarchical assembly. The first level consists of the formation of barite

flower-like structures that assemble into quasi-linear structures at the second level. The further assembly of the barite flowers into quasi-linear structures in AOT matrix may be rationalized in terms of interleaving of the petals of neighbouring flowers, this process also presumably driven by hydrophobic interactions between AOT molecules bound to the individual barite crystals. Barite crystals with elongated hexagonal morphology are observed to form within StA lipid matrix. That the assembly process does not occur for films grown in stearic acid films clearly underlines the special role of the AOT molecules in the assembly of barite crystals.

3.4 Synthesis of $BaCrO_4$ nanoparticles in thermally evaporated lipid bilayers stacks

Thin films of AOT and StA of 500 Å thickness were thermally vacuum deposited separately. After deposition of the AOT and StA films, the respective QCM crystals were immersed in 50 ml of 10^{-3} M aqueous $BaCl_2$ solution (pH 5.7) and the frequency changes of the crystals were monitored *ex-situ*. The optimum immersion time determined from the QCM kinetics measurements was used to load the AOT and StA films on glass, Si (111) substrates and on TEM grids. Thereafter, the Ba-AOT and Ba-StA films on the QCM crystals was immersed in 50 ml of 7.9 x 10^{-4} M Na_2CrO_4 aqueous solution (pH 6) and the frequency changes of the crystals were monitored as a function of time of immersion in the electrolyte solutions. The growth of barium chromate in both the lipid thin films for FTIR, XRD, SEM, EDAX and TEM studies were carried out using the optimum immersion times determined from the QCM kinetics measurements mentioned above.

3.4.1 Quartz crystal microgravimetry measurements

The kinetics of incorporation of Ba^{2+} ions in 500 Å thick AOT (curve 1 in Fig.3.11) and StA (curve 2 in Fig.3.11) films was followed by QCM measurements and the data recorded as a function of time of immersion in the $BaCl_2$ solution and thereafter in the Na_2CrO_4 solution is shown in Fig.3.11. During immersion in the $BaCl_2$ solution, a fairly large mass increase is seen and is attributed to electrostatic entrapment of Ba^{2+} ions in the AOT and StA matrices. After entrapment of the Ba^{2+} ions, the Ba-AOT and Ba-StA covered QCM crystals were immersed in Na_2CrO_4 solution (pH 6) and the frequency

change of the crystals was monitored as a function of time of immersion in the electrolyte solutions.

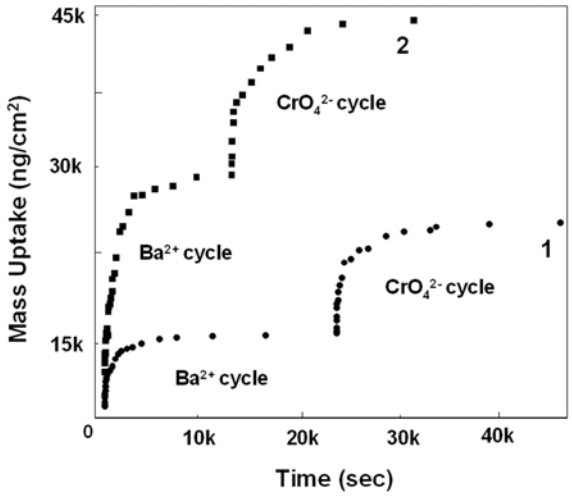

Fig. 3.11 : *QCM mass uptake recorded ex-situ after immersion of a 500 Å thick AOT (curve 1) and StA (curve 2) films sequentially in Ba^{2+} and CrO_4^{2-} ion solutions for different times.*

A large mass increase is observed during this cycle of immersion of CrO_4^{2-} ions in the Ba-AOT and Ba-StA films. From the measured Ba^{2+} and CrO_4^{2-} ion mass uptake values, the Ba^{2+} : CrO_4^{2-} molar ratios within the AOT and StA films are calculated to be 1 : 1.1 and 1 : 1.3 respectively, in reasonable agreement with the expected 1 : 1 ratio.

3.4.2 Fourier transform infrared spectroscopy studies

Fig.3.12A shows the FTIR spectra recorded from the as-deposited 500 Å thick AOT film on a Si (111) substrate (curve 1), the AOT film after entrapment of Ba^{2+} ions (curve 2) and the barium sulfosuccinate film after reaction with Na_2CrO_4 (curve 3). A prominent absorption band is seen at 1053 cm^{-1} (Fig.3.12A, curve 1), in the case of the as-deposited AOT film. The band at 1053 cm^{-1} is assigned to the S=O stretching vibration of the sulfonate group present in the AOT molecules [21]. After entrapment of Ba^{2+} ions in the AOT thin film, the absorption band at 1053 cm^{-1} has shifted to 1106 cm^{-1} (Fig.3.12A, curve 2) clearly indicating that the Ba^{2+} ions have complexed electrostatically with the sulfonate groups in the film. The FTIR spectrum recorded from the barium sulfosuccinate film after reaction with Na_2CrO_4 (Fig.3.12A, curve 3) is essentially featureless.

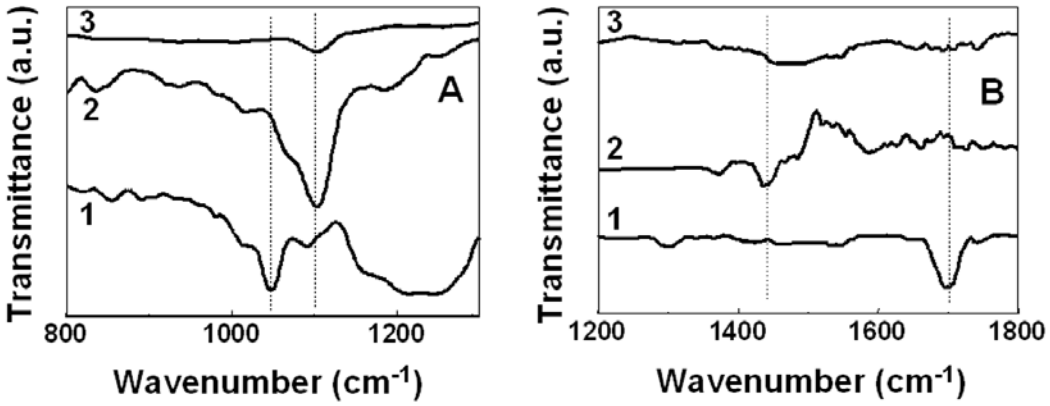

Fig. 3.12 :.(A & B) *FTIR spectra recorded from 500Å thick AOT and StA films on a Si (111) substrate (curve 1), films after incorporation of Ba^{2+} ions (curve 2), and the barium sulfosuccinate and stearate films after incorporation of CrO_4^{2-} ions (curve 3) for a particular spectral windows.*

Fig.3.12B shows the FTIR spectra recorded from the as-deposited 500 Å thick StA film on a Si (111) substrate (curve 1), the StA film after entrapment of Ba^{2+} ions (curve 2) and the barium stearate film after reaction with Na_2CrO_4 (curve 3). A prominent absorption is seen at 1700 cm^{-1} in the case of as-deposited StA film (curve 1). This band is due to excitation of carbonyl stretch vibrations in the carboxylic acid groups of the fatty acid film [13]. The FTIR spectrum recorded from the StA film after Ba^{2+} ion incorporation (Fig.3.12B, curve 2) shows a shift in the carbonyl stretch frequency from 1700 cm^{-1} to 1450 cm^{-1}. The shift in the carbonyl stretch frequency to lower wavenumbers followed by the disappearance of the 1700 cm^{-1} resonance is known to be a clear indicator of salt formation in such fatty acid films [13] and indicates complete barium stearate salt formation. The FTIR spectrum recorded from the barium stearate film after reaction with Na_2CrO_4 (Fig.3.12B, curve 3) shows no important features.

3.4.3 Lamellar ordering studies of Ba-AOT and Ba-StA films

Barium-sulfosuccinate and barium-stearate films were formed by immersion of 500 Å thick StA and AOT films in $BaCl_2$ solution separately. The formation of lamellar barium-sulfosuccinate (Fig.3.13A) and barium-stearate (Fig.3.13B) were ascertained by the presence of characteristic odd-even intensity oscillations in the (0 0 l) Bragg reflections in the XRD pattern of the film [13]. From the periodicity of the (0 0 l) Bragg reflections, the thickness of the barium stearate and barium sulfosuccinate bilayers is

calculated to be 48 Å and 49 Å respectively and is consistent with the size of StA and AOT molecules (~ 24 Å and ~ 23 Å respectively).

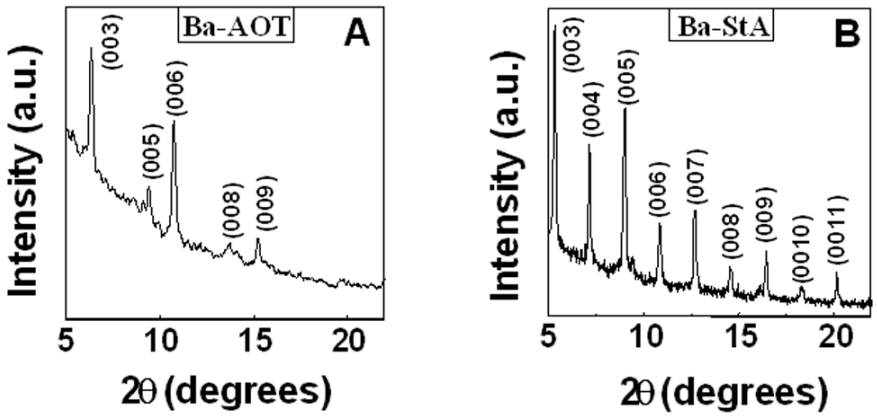

Fig.3.13 : *XRD patterns recorded from a 500 Å thick AOT film (A) and StA film (B) after entrapment of Ba^{2+} ions. The (0 0 l) Bragg reflections are indexed in both these figures.*

3.4.4 SEM and EDAX measurements

An SEM picture recorded from a 500 Å thick AOT film on a Si (111) substrate after formation of $BaCrO_4$ is shown in Fig.3.14A. The SEM image shows densely populated spherical $BaCrO_4$ structures interspersed within a filamentary network. EDAX analysis of the one of the spherical structures yielded a Ba : Cr : O atomic ratio of 1 : 1.4 : 6. The size of each spherical structure is roughly 80-100 nm. A higher magnification SEM image of one of the $BaCrO_4$ structures is shown in the inset of Fig.3.14A. The particle is roughly spherical in shape and has a size of ~ 90 nm.

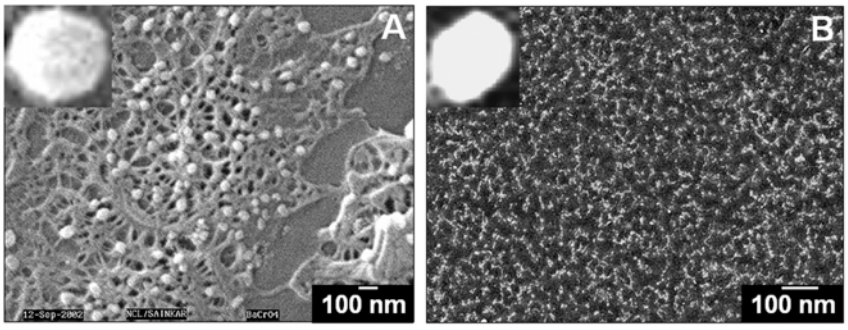

Fig. 3.14 : *(A) and (B) – SEM images of $BaCrO_4$ crystallites formed within 500 Å thick thermally evaporated AOT and StA films respectively. The inset in both A and B shows higher magnification SEM images of a single crystallite.*

After reaction of a 500 Å thick Ba-StA film on a Si (111) substrate with CrO_4^{2-} ions, SEM images were recorded from this film and one representative image is shown in Fig.3.14B. The SEM image shows densely populated, well-organized spherical $BaCrO_4$ nanocrystallites. EDAX analysis of the $BaCrO_4$ crystallites yielded a Ba : Cr : O atomic ratio of 1 : 1.2 : 8. While the Ba : Cr ratio is in fair agreement with the expected stoichiometry, excess oxygen is due to sampling from the silica substrate. The size of the crystallites determined from the SEM image was in the range 20-60 nm. The higher magnification SEM image (Fig.3.14B, inset) clearly shows one individual crystallite (size ~ 40 nm), rather similar in overall morphology to those obtained in StA thin films (Fig.3.14A, inset).

3.4.5 X-ray diffraction measurements

The XRD pattern recorded from the $BaCrO_4$ crystals grown within AOT lipid thin film is displayed in Fig.3.15, curve 1. A number of Bragg reflections are identified and indexed with reference to the unit cell of the $BaCrO_4$ structure (a = 9.105 Å, b = 5.541 Å, c = 7.343 Å; space group *Pnma*) [24].

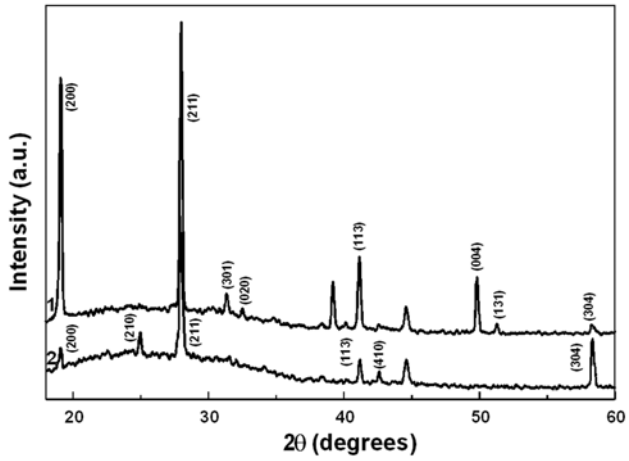

Fig. 3.15 : *XRD patterns recorded from $BaCrO_4$ crystals grown within a 500 Å thick thermally evaporated AOT film (curve 1) and StA film (curve 2).*

While, the XRD pattern recorded from the $BaCrO_4$ crystals synthesized in StA lipid matrix is displayed in Fig.3.15, curve 2. The presence of intense (200), (211), (113), (004) [$BaCrO_4$-AOT] and (211) and (304) [$BaCrO_4$-StA] Bragg reflections indicates oriented growth of the $BaCrO_4$ crystallites along these crystallographic planes. The

broadening in the Bragg reflections in the XRD data is in agreement with the small size of the $BaCrO_4$ crystals observed in the SEM images (Fig.3.14).

3.4.6 Transmission electron microscopy (TEM) measurements

A representative TEM picture recorded from a 150 Å thick AOT film on a carbon coated TEM grid after formation of $BaCrO_4$ is shown in Fig.3.16A. It is clear from the TEM images that the $BaCrO_4$ structures are spherical in shape and that the size (80-100 nm) is consistent with the SEM image. TEM result also reveals that the spherical structures are even composed of very small crystallites of $BaCrO_4$. The bigger spherical clusters of $BaCrO_4$ are made up of smaller crystallites of size ~ 10 nm.

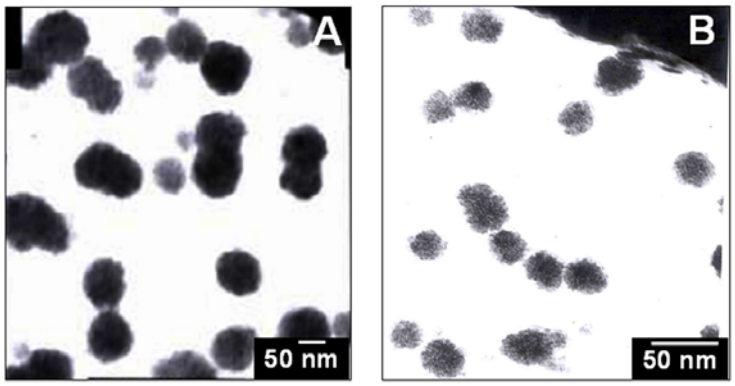

Fig. 3.16 : *(A and B) – TEM images of $BaCrO_4$ crystallites formed within 150 Å thick thermally evaporated AOT and StA films respectively.*

A TEM picture recorded from a 150 Å thick StA film on a carbon coated TEM grid after formation of $BaCrO_4$ is shown in Fig.3.16B. It is clear from the TEM image that the individual spherical structures are in turn composed of very small individual crystallites of $BaCrO_4$ by an aggregation process. An estimate of the size of the individual crystallites in one of the assemblies was made from the TEM image to be ca. 5-10 nm. Apparently, the high magnification SEM image shown in the inset of Fig.3.15B was unable to resolve the individual crystallites of $BaCrO_4$. While the overall size of the spherical aggregates in the case of AOT and StA films is different, the size of the individual $BaCrO_4$ crystallites in both cases is nearly the same. This indicates that the forces driving the assembly of the crystallites into superstructures in the two cases are different.

3.4.7 Contact angle measurements

In order to determine whether the growth of the $BaCrO_4$ crystals was purely a surface process, we measured the contact angle at various points on the AOT and StA film surface and found that the surface was hydrophobic (mean contact angle of 93^o and 89^o respectively). This result clearly shows that the spherical aggregates of $BaCrO_4$ crystallites shown in Fig.3.15 are covered with monolayers of AOT and StA, which renders them hydrophobic.

3.4.8 Summary

The synthesis of nano-scale $BaCrO_4$ crystals in thin films of water-insoluble surfactants such as AOT and StA by a process of ion entrapment has been described. The nano-crystallites of $BaCrO_4$ are observed to exist in the form of spherical assemblies of well-defined dimensions in the thin films. The assembly of the $BaCrO_4$ crystals into spherical superstructures indicates that there is sufficient mobility of the surfactant-covered crystallites even when constrained in thin film form. The assembly of the crystallites is equally facile with double-tailed and single-tailed surfactants, possibly due to a large amount of water uptake in the thermally evaporated AOT and StA thin films during immersion in the different electrolyte solutions. As the crystallites grow, they are covered by a monolayer of AOT/StA, which renders the crystallites hydrophobic. Since the crystal growth is carried out in an aqueous environment, hydrophobic interactions between surfactant-capped $BaCrO_4$ crystallites would lead to their association and formation of the spherical structures as observed.

3.5 Crystallization of $SrCO_3$ in thermally evaporated lipid bilayers stacks

Thin films of AOT and StA of 500 Å thickness were thermally vacuum deposited. After deposition of the AOT and StA films, the deposited substrates were separately immersed in 50 ml of 10^{-3} M aqueous $SrCl_2$ solution (pH 5.6) based on the optimum immersion time determined from the QCM kinetics. After formation of strontium sulfosuccinate and strontium stearate films, the films were immersed in 50 ml of 1.5×10^{-3} M Na_2CO_3 aqueous solution (pH 6.2) by using the optimum immersion time from QCM measurements. After the growth of strontium carbonate crystals in the lipid films, the $SrCO_3$-lipid composites was characterized by FTIR, XRD, EDAX and SEM.

3.5.1 Quartz crystal microgravimetry studies

The kinetics of incorporation of Sr^{2+} ions in a 500 Å thick AOT film was followed by QCM and the data recorded as a function of time of immersion in the $SrCl_2$ solution and thereafter in the Na_2CO_3 solution is shown in Fig.3.17.

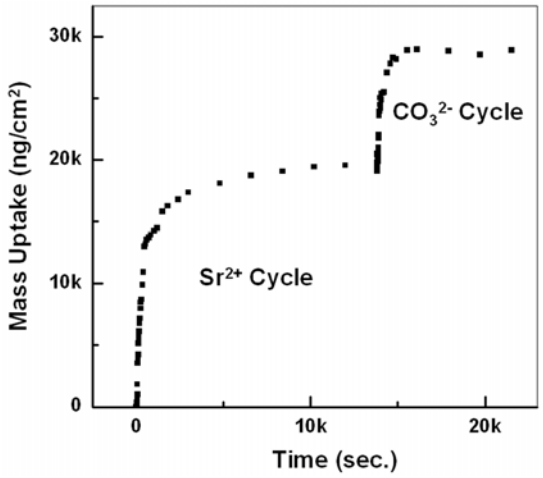

Fig. 3.17 : *QCM mass uptake recorded ex-situ during immersion of a 500 Å thick AOT film sequentially in Sr^{2+} and CO_3^{2-} ion solutions.*

During immersion in the $SrCl_2$ solution, a fairly large mass increase is seen and is attributed to electrostatically controlled diffusion and entrapment of Sr^{2+} ions in the AOT matrix. At pH 5.5, the sulfosuccinate ions of the AOT matrix are expected to be fully negatively charged leading to maximum attractive electrostatic interaction with the Sr^{2+} cations. After entrapment of the Sr^{2+} ions, the Sr-AOT covered QCM crystal was immersed in Na_2CO_3 solution (pH 6) and the frequency change of the crystal was monitored as a function of time of immersion in the electrolyte solution. A large mass increase is observed during this cycle of immersion as well and is due to electrostatically controlled entrapment of the CO_3^{2-} ions in the Sr-AOT film. From the measured Sr^{2+} and CO_3^{2-} ion mass uptake values, the Sr^{2+} : CO_3^{2-} molar ratio within the AOT film is calculated to be 1.3 : 1.

3.5.2 Fourier transform infrared spectroscopy studies

Fig.3.18 shows FTIR spectra recorded from the as-deposited 500 Å thick AOT film on a Si (111) substrate (curve 1), the AOT film after entrapment of Sr^{2+} ions (curve 2) and the strontium sulfosuccinate film after reaction with Na_2CO_3 (curve 3).

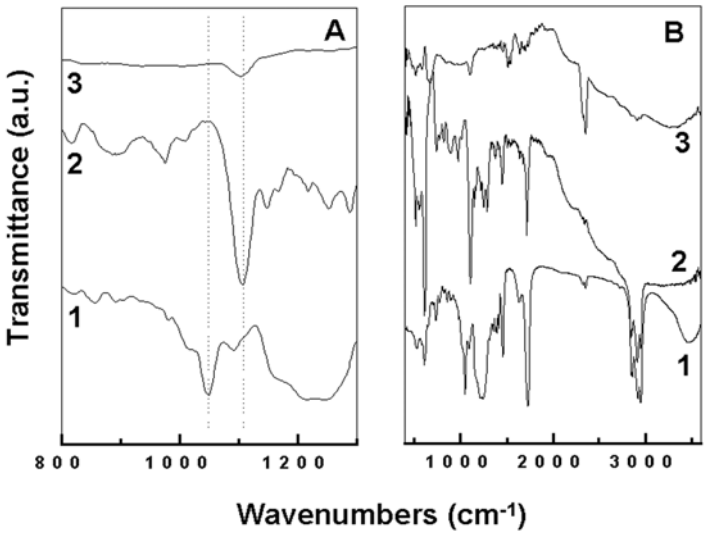

Fig. 3.18 : *A and B – FTIR spectra recorded from a 500 Å thick AOT film on a Si (111) substrate (curve 1), the AOT film after incorporation of Sr^{2+} ions (curve 2), and the strontium sulfosuccinate film after incorporation of CO_3^{2-} ions (curve 3) in different spectral windows.*

Prominent absorption bands are seen at 1049, 1700, 2850 and 2930 cm^{-1} in the case of the as-deposited AOT film (Fig.3.18, curve 1). The band at 1049 cm^{-1} is assigned to the S=O stretching vibration of the sulfonate group present in the AOT molecules [21]. The band at 1700 cm^{-1} is due to carbonyl stretch vibrations in the AOT molecules and the two bands at 2850 and 2920 cm^{-1} have been assigned to the methylene symmetric and antisymmetric stretching vibrations in the hydrocarbon chains respectively. After entrapment of Sr^{2+} ions in the AOT thin film, the absorption band at 1049 cm^{-1} (Fig.3.18A, curve 1) has shifted to 1104 cm^{-1} (Fig.3.18A, curve 2) clearly indicating that the Sr^{2+} ions have complexed electrostatically with the sulfonate groups in the AOT thin film. The FTIR spectrum recorded from the strontium sulfosuccinate film after reaction with Na_2CO_3 (Fig.3.18, curve 3) is essentially featureless.

3.5.3 Lamellar ordering studies of Sr-AOT film

The formation of lamellar strontium sulfosuccinate films by immersion of 500 Å thick AOT films in $SrCl_2$ solution was ascertained by the presence of characteristic odd-even intensity oscillations in the (0 0 l) Bragg reflections [13a] in the XRD pattern of the film (Fig.3.19). These Bragg reflections are not observed in as-deposited AOT films clearly establishing the electrostatic entrapment of Sr^{2+} ions into the AOT lipid matrix.

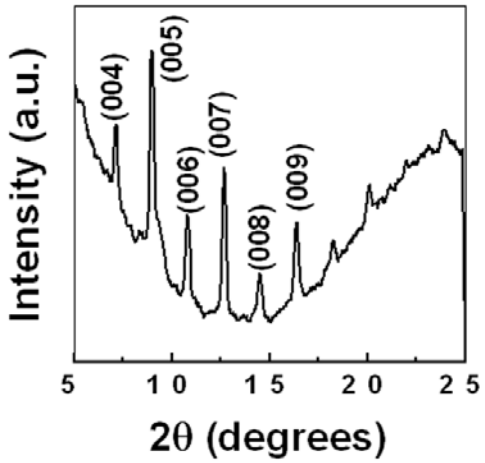

Fig. 3.19 : *XRD pattern recorded from a 500 Å thick AOT film after entrapment of Sr^{2+} ions. The (0 0 l) Bragg reflections are identified in this figure.*

3.5.4 SEM and EDAX Measurements

3.5.4.1 SEM and EDAX measurements of $SrCO_3$ grown within AOT lipid Matrix

SEM pictures recorded from a 500 Å thick AOT film on a Si (111) substrate after formation of $SrCO_3$ are shown in Fig.3.20 at different levels of magnification. The low magnification image (Fig.3.20A) shows densely populated bundles of well-formed $SrCO_3$ sheets/ribbons.

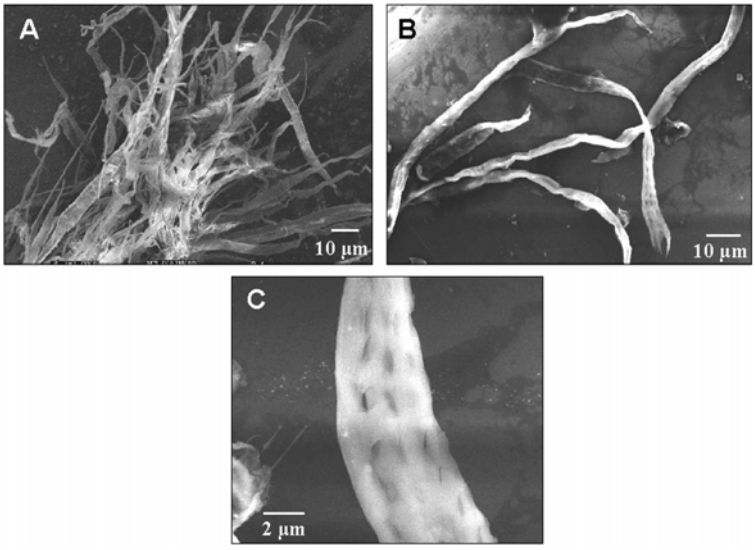

Fig. 3.20 : *SEM images of $SrCO_3$ crystals formed in thermally evaporated AOT film (500 Å thick) at different magnifications.*

EDAX analysis of the $SrCO_3$ ribbons within this bundle yielded a Sr : C : O atomic ratio of 1 : 1.4 : 9. While the Sr : C ratio is in fair agreement with the expected stoichiometry, the excess oxygen is likely to be due to from the underlying silica layer on the Si support. The length of the $SrCO_3$ ribbons is often in excess of 100 μm while the widths are typically in the range 2-7 μm (Fig.3.20B). In the higher magnification image, the texture of individual ribbons is more clearly seen (Fig.3.20C). The stronianite crystals are quite flat and less than 1 μm in thickness (Fig.3.20B & C). The surface of the crystals shows interesting texture with a number of regularly organized gaps being observed (Fig.3.20C). The interesting ribbon-like morphology of $SrCO_3$ crystals formed within AOT thin films, as templates have not been observed in the numerous earlier studies on strontianite crystallization [7d,e, 25].

3.5.4.2. SEM and EDAX measurements of $SrCO_3$ grown within StA lipid Matrix

Reaction of CO_3^{2-} ions with Sr^{2+} ions entrapped within 500 Å thick StA film leads to the growth of strontianite crystals and is shown in Fig.3.21 at different magnifications. The low magnification image (Fig.3.21A) shows beautiful, flower-like structures of close-packed needles. The strontianite needles observed to be aggregated into dense, flower-like structures. The higher magnification SEM image (Fig.3.21B) of the flower-like assembly of strontianite crystals can clearly be seen with greater details. The close packed flower like strontianite structures observed to be originated from a central nucleation point. In this case, there is no evidence of formation of strontianite sheets/ribbons as observed for AOT matrix (Fig.3.20).

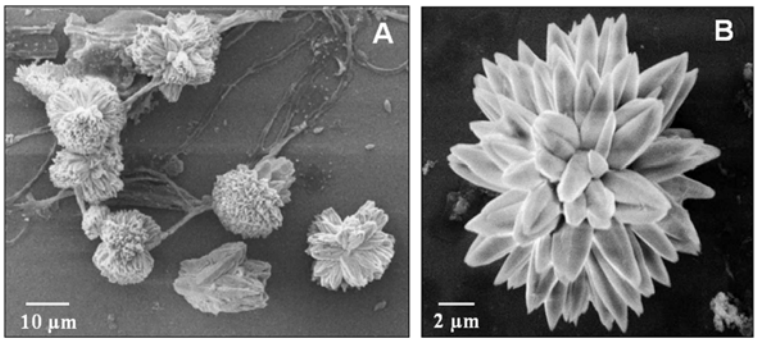

Fig. 3.21 : *SEM images at different magnification of $SrCO_3$ formed in thermally evaporated StA film.*

The kinetics of crystallization in the case of growth within the lipid matrix, are expected to be much slower than for homogeneous nucleation in solution. Kuther *et al* have observed that carrying out the growth of $SrCO_3$ crystals at reduced temperatures on self-assembled monolayer surfaces did result in some aggregation of the strontianite crystals [7e]. However, the extent of aggregation was considerably less than that observed in this study. It is possible that both hydrophobic and kinetic effects contribute to the interesting strontianite superstructures observed in the case of strontium sulfosuccinate and stearate films.

3.5.4.3 SEM studies of $SrCO_3$ crystals grown in control experiments

In order to understand better the role of the AOT and StA matrices on the strontianite morphology and assembly process, control experiments were performed wherein strontianite crystals were grown in solution both in the presence and absence of lipid molecules as an additive. The strontianite crystals grown in solution in the absence of any surfactant is shown in Fig.3.22A and in this control experiment, needle-shaped strontianite crystals are obtained. Unlike in the case of $SrCO_3$ crystals grown in the StA matrix (Fig.3.21), there is no evidence of assembly of the individual needle like crystallites in solution (Fig.3.22A). The crystallization of $SrCO_3$ was also carried out in solution in the presence of lipid molecules (10^{-3} M AOT). Fig.3.22B shows an SEM image of $SrCO_3$ crystals obtained in this control experiment wherein a number of open aggregates of the crystals are observed. The structure of the aggregates is seen to consist of quasi-linear assemblies of strontianite needles (Fig.3.22B).

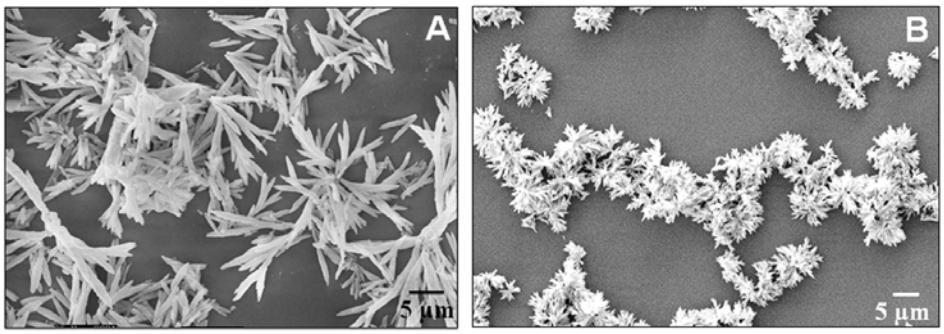

Fig. 3.22 : *A) SEM image of $SrCO_3$ crystals grown in solution by mixture of aqueous solutions of $SrCl_2$ and Na_2CO_3. and B) SEM image of $SrCO_3$ crystals grown in solution in the presence of 10^{-3} M AOT.*

It is thus clear that the AOT molecules in solution coat the strontianite needles and direct their assembly in solution. An important observation in these control experiments is that there is no evidence of formation of either strontianite sheets/ribbons or flower-like assembly of strontianite needles as observed in the case of crystals grown in thermally evaporated AOT and StA films.

3.5.5 X-ray diffraction measurements

The XRD pattern recorded from the $SrCO_3$ crystals grown in AOT matrix (shown in Fig.3.20) is displayed as curve 1 in Fig.3.23. A number of Bragg reflections are identified and have been indexed with reference to the unit cell of the strontianite structure (a = 5.107 Å, b = 8.414 Å, c = 6.029 Å; space group *Pmcn*) [7d, 25, 26]. An interesting feature of the XRD pattern of the strontianite crystals grown in AOT matrix is the presence of intense (020), (221) and (202) reflections indicating some degree of oriented growth of the strontianite sheets/ribbons. The Bragg reflections from the strontianite crystals are fairly broad (curve 1, Fig.3.23) indicates that the flat, highly textured ribbons observed in the SEM images are assemblies of smaller strontianite crystallites. Curve 2 in Fig.3.23 shows the XRD spectra recorded from $SrCO_3$ crystals synthesized within a 500 A° thick stearic acid matrix (Fig.3.21). The Bragg reflections observed from this film are corresponds to the strontianite phase and have been identified. The corresponding hkl planes are labeled in the figure.

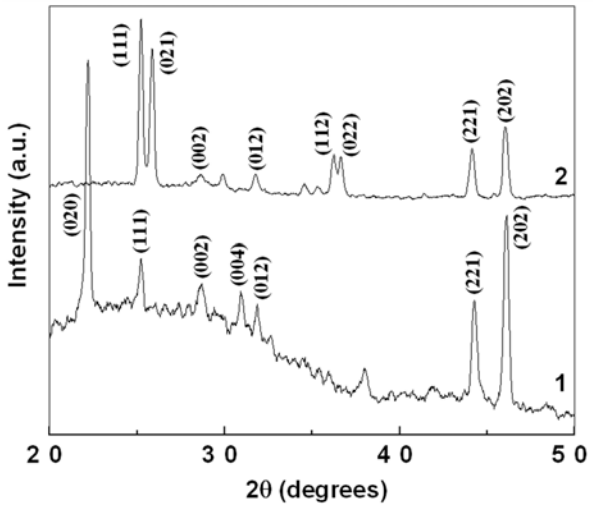

Fig. 3.23 : *XRD pattern recorded from $SrCO_3$ crystals grown within a thermally evaporated AOT (curve 1) and StA (curve 2) films*

.

The major Bragg reflections agree very well with those reported by Kuther *et al.* for strontianite crystals grown on self-assembled monolayers [7e]. XRD pattern in this case shows some degree of orientation along (111) and (021) crystallographic planes as well clearly establishing the role of specific lipid matrix on $SrCO_3$ crystal growth.

3.5.6 Contact angle measurements

To determine whether the growth of strontianite crystals within the AOT and StA matrices were purely surface processes, we measured the contact angle of a sessile water drop at various points on the $SrCO_3$–AOT/StA film surface and found that the surface was quite hydrophobic (mean contact angle of 86^o and 93^o for AOT-$SrCO_3$ and StA-$SrCO_3$ respectively). This is to be contrasted with a contact angle of 64^o and 67^o measured for films of strontianite crystals grown in solution and picked up on to a Si (111) wafer coated with a 500 Å thick AOT and StA films respectively. This result clearly shows that the ribbon and flower-like strontianite crystals of Figs.3.20 & 3.21 nucleate and grow within the AOT and StA matrix respectively and that the mature crystals are eventually covered with a monolayer of AOT and StA that renders them hydrophobic.

3.5.7 Summary

The crystallization of strontium carbonate within thermally evaporated AOT and StA films by a process of Sr^{2+} ion entrapment and thereafter, reaction with CO_3^{2-} ions have been demonstrated. While, the $SrCO_3$ structures grown in the AOT films exhibit an unusual ribbon-like morphology that possibly arises due to AOT-directed assembly of smaller strontianite crystallites, the interesting flower like superstructures of strontianite needles were observed using StA thin film. These experiments clearly underline the special role played by the thermally evaporated lipid molecules in directing the unusual morphology of the strontianite crystals obtained in this study. The morphology variation in the strontianite crystals within the AOT and StA bilayers may be a consequence of inhibition of growth along certain crystallographic directions by the anionic molecules in the respective bilayers. The hydrophobic nature of the crystallites points to a possible reason for formation of thin sheets of strontianite. Since the growth of the crystals occurs in an aqueous environment, hydrophobic forces between the AOT monolayer-covered

strontianite crystals (at least in the very early stages of crystal growth) could lead to aggregation of the crystals into sheet/ribbon-like structures as observed. It is possible that both hydrophobic and kinetic effects contribute to the interesting strontianite superstructures observed in the case of strontium stearate films.

3.6 Crystallization of $CaCO_3$ in thermally evaporated lipid bilayers stacks

Thin films of AOT and StA of 500 Å thickness were thermally vacuum deposited. After deposition of the AOT and StA thin films on Si (111) and glass substrates were immersed in 50 ml of 10^{-2} M aqueous $CaCl_2$ solution (pH 6). Thereafter, growth of calcium carbonate in the Ca-AOT and Ca-StA thin films were achieved by immersion of these films in 50 ml of 2.4 x 10^{-3} M Na_2CO_3 aqueous solution (pH 6) for 3 hours. The $CaCO_3$ crystals grown within 500 Å thick AOT and StA films were washed with double distilled water and subjected to FTIR, XRD, EDAX, SEM and contact angle measurements.

3.6.1 Quartz crystal microgravimetry measurements

The kinetics of incorporation of Ca^{2+} ions in a 500 Å thick AOT film was followed by QCM and the data recorded as a function of time of immersion in the $CaCl_2$ solution and thereafter in the Na_2CO_3 solution is shown in Fig.3.24.

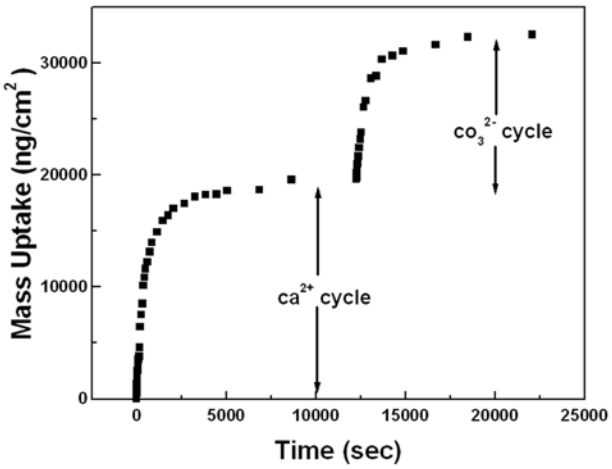

Fig. 3.24 : *QCM mass uptake recorded ex-situ during immersion of a 500 Å thick AOT film sequentially in Ca^{2+} and CO_3^{2-} ion solutions.*

During immersion in the $CaCl_2$ solution, a fairly large mass increase is seen and is attributed to electrostatically controlled entrapment of Ca^{2+} ions in the AOT matrix. At pH 6, the sulfosuccinate ions of the AOT matrix are expected to be fully negatively charged leading to maximum attractive electrostatic interaction with the Ca^{2+} cations. After entrapment of the Ca^{2+} ions, the Ca-AOT covered QCM crystal was immersed in Na_2CO_3 solution (pH 6) and the frequency change of the crystal was monitored as a function of time of immersion in the electrolyte solution. A large mass increase is observed during this cycle of immersion as well and is due to electrostatically controlled entrapment of the CO_3^{2-} ions in the Ca-AOT film. From the measured Ca^{2+} and CO_3^{2-} ion mass uptake values, the Ca^{2+} : CO_3^{2-} molar ratio within the AOT film is calculated to be 1.5 : 1.

3.6.2 Fourier transform infrared spectroscopy studies

Fig.3.25 shows the FTIR spectra recorded from the as-deposited 500 Å thick AOT film on a Si (111) substrate (curve 1), the AOT film after entrapment of Ca^{2+} ions (curve 2) and the calcium sulfosuccinate film after reaction with Na_2CO_3 (curve 3) in two different spectral windows. Prominent absorption bands are seen at 1057 (Fig.3.25A, curve 1), 1700, 2850 and 2920 cm^{-1} (Fig. 3.25B, curve 1) in the case of the as-deposited AOT film. The band at 1057 cm^{-1} is assigned to the S=O stretching vibration of the sulfonate group present in the AOT molecules [21]. The band at 1700 cm^{-1} is due to carbonyl stretch vibrations in the AOT molecules and the two bands at 2850 and 2920 cm^{-1} have been assigned to the methylene symmetric and antisymmetric stretching vibrations in the hydrocarbon chains respectively. After entrapment of Ca^{2+} ions in the AOT thin film, the absorption band at 1057 cm^{-1} has shifted to 1113 cm^{-1} (Fig.3.25A, curve 2) clearly indicating that the Ca^{2+} ions have complexed electrostatically with the sulfonate groups in the film. The methylene antisymmetric and symmetric vibrations have reduced marginally in intensity following Ca^{2+} incorporation (Fig.3.25B, curve 2).

The FTIR spectrum recorded from the calcium sulfosuccinate film after reaction with Na_2CO_3 (Fig.3.25A, curve 3) shows the presence of absorption bands at 1113 cm^{-1} and 855 cm^{-1}. Retention of the 1113 cm^{-1} band after Na_2CO_3 treatment indicates that not all of the Ca^{2+} ions have reacted with carbonate ions to form calcium carbonate. The feature centered at 855 cm^{-1} is characteristic of the aragonite polymorph [27] and shows

unequivocally formation of these crystals in the AOT matrix. There is no evidence of either calcite or vaterite polymorphs of $CaCO_3$ which are known to show strong infrared absorption bands at 712 cm^{-1}, 874 cm^{-1} and 744 cm^{-1}, 877 cm^{-1} respectively [27].

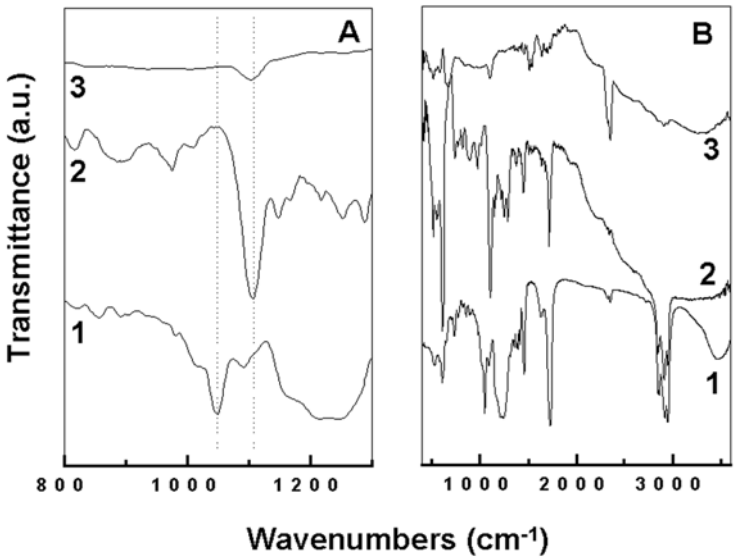

Fig. 3.25 : *A and B - FTIR spectra recorded from a 500 Å thick AOT film on a Si (111) substrate (curve 1), the AOT film after incorporation of Ca^{2+} ions (curve 2), and the calcium sulfosuccinate film after incorporation of CO_3^{2-} ions (curve 3) in different spectral regions.*

The almost complete disappearance of the methylene antisymmetric and symmetric vibration bands after aragonite formation (Fig.3.25B, curve 3) indicates considerable reorganization in the film, possibly due to randomization of AOT hydrocarbon chain orientation around the aragonite crystals.

3.6.3 Lamellar ordering studies of Ca-AOT films

Calcium sulfosuccinate film was formed by immersion of 500 Å thick AOT film in $CaCl_2$ solution. The formation of lamellar calcium sulfosuccinate was ascertained by the presence of characteristic odd-even intensity oscillations in the (0 0 l) Bragg reflections [13a] in the XRD pattern of the film (Fig.3.26A, curve 210 min.). These Bragg reflections are not observed in as-deposited AOT films (Fig.3.26A, curve 0 min.). From the periodicity of the (0 0 l) Bragg reflections, the thickness of the calcium sulfosuccinate bilayers is calculated to be 48 Å and is fairly consistent with the AOT molecular size of ~ 22 Å.

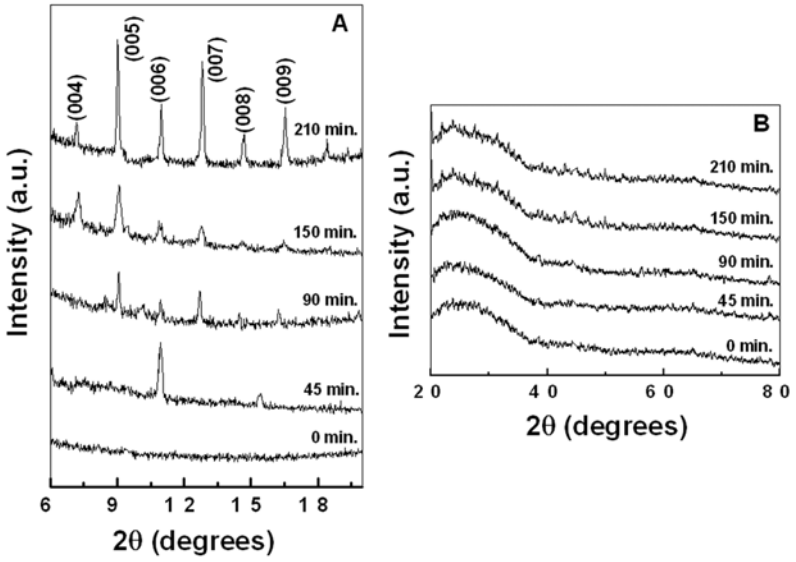

Fig. 3.26 : *(A) Small and wide angle XRD patterns recorded from a 500 Å thick AOT film after different times of reaction of calcium ions with the AOT thin film.*

In order to understand the formation of lamellar calcium sulfosuccinate with characteristic odd-even intensity oscillations in the Bragg reflections in the XRD pattern, small and wide angle XRD patterns were recorded from a 500 Å thick AOT film on a glass substrate after immersion in $CaCl_2$ solution for 45, 90, 150 and 210 min. and are shown in the Fig.3.26 A & B respectively. The curve labeled 0 min in Fig.3.26A corresponds to the small angle XRD pattern recorded from the as-deposited AOT thin film. Bragg reflections are not observed in the as deposited AOT film. As a function of time of immersion of the as-deposited AOT film in $CaCl_2$ solution, it is observed that the (0 0 l) Bragg reflections slowly grow in intensity reaching saturation within 210 min of reaction. This clearly indicates evolution of lamellar order in the AOT film as the Ca^{2+} ions diffuse into the lipid matrix. Formation of lamellar calcium sulfosuccinate was ascertained by the presence of characteristic odd-even intensity oscillations in the (0 0 l) Bragg reflections in the XRD pattern of the film (Fig.3.26A, Curve 210 min.). Bragg reflections are absent in the wide angle XRD patterns shown in Fig.3.26B for all times of immersion of the AOT film in $CaCl_2$ solution. Therefore, in-plane ordering of the AOT molecules could not be detected by wide angle XRD measurements. However, this does not rule out the possibility of short range ordering of the AOT molecules in the thermally

evaporated thin films which would be sufficient, in principle, to induce oriented growth of nuclei of aragonite as evidenced from FTIR result (curve 3 in Fig.3.25A).

3.6.4 SEM and EDAX measurements of $CaCO_3$ grown within AOT and StA lipid Matrices

SEM pictures recorded from a 500 Å thick Ca-AOT film on a Si (111) substrate after immersion in Na_2CO_3 solution for 160 min are shown in Fig.3.27 at different magnifications. The low magnification image (Fig.3.27A) shows densely populated, well-organized bundles of $CaCO_3$ needles. EDAX analysis of the $CaCO_3$ needles yielded a Ca : C : O atomic ratio of 1 : 1.3 : 8. While the Ca : C ratio is in fair agreement with the expected stoichiometry, excess oxygen is due to sampling from the silica substrate. The higher magnification SEM image (Fig.3.27B & C) recorded from the $CaCO_3$-AOT film clearly shows individual bundles of aragonite crystals with the needles nucleating from a central crystallite, which was in contact with the organic surface.

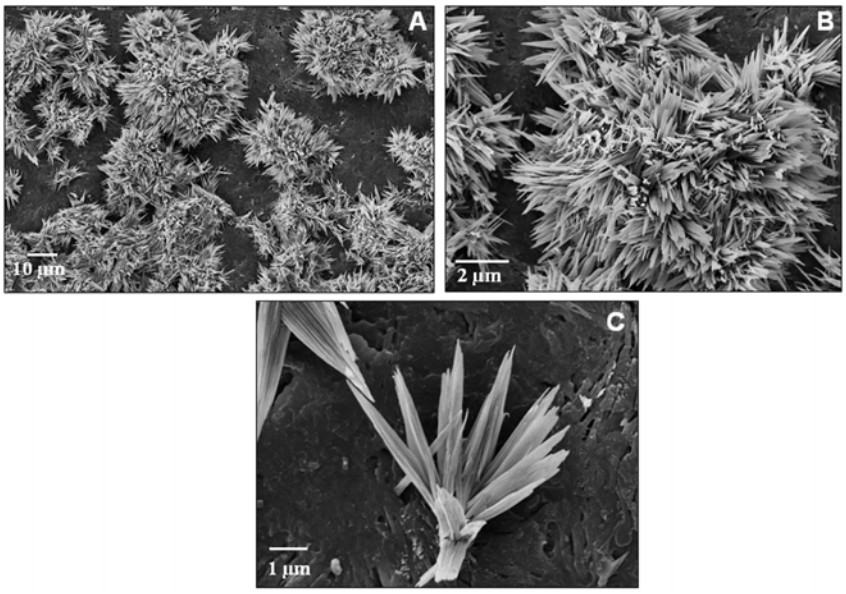

Fig.3.27 : *A, B & C – Representative SEM images of $CaCO_3$ crystals formed within a 500 Å thick thermally evaporated AOT film at different magnifications.*

It is important to mention here that previous reports on aragonite crystallization have been carried out in presence of soluble additives such as Mg^{2+} ions [28], and at elevated temperature [7e, 28c,d] with the exception of the reports of Litvin *et al* [6c] and Heywood *et al* [29]. In this study, we have been able to achieve phase-pure aragonite

growth at room temperature with AOT as a crystallization template in the form of thin film. It is possible that the growth of the aragonite crystals occurs in solution by a process of leaching out of Ca^{2+} ions from the calcium-sulfosuccinate film followed by reaction with carbonate ions and attachment of the crystals thus formed to the surface of the AOT film. This possibility is to be discounted before *in-situ* growth of the aragonite crystals within the AOT matrix and can be accepted as a plausible mechanism.

One possible method to ascertain the crystal formation mechanism is to monitor the growth of the aragonite crystals as a function of time of immersion in the Na_2CO_3 solution. SEM pictures recorded from a 500 Å thick calcium-sulfosuccinate film on a Si (111) wafer after immersion in Na_2CO_3 solution for 30, 60, 90, 120 and 160 minutes are shown in Figs.3.28A-E respectively. After 30 min. of reaction, the SEM image (Fig.3.28A) shows the growth of very small $CaCO_3$ crystals apparently within the AOT film.

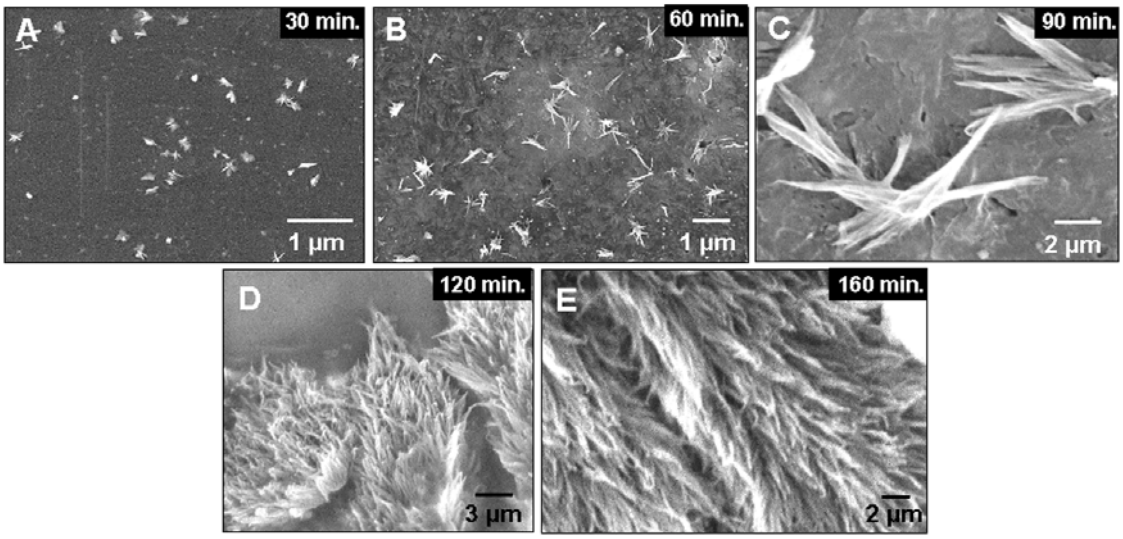

Fig. 3.28 : *A - E – Representative SEM images of $CaCO_3$ crystals grown in a 500 Å thick thermally evaporated AOT film at different time intervals of reaction of the precursor calcium-sulfosuccinate film with the CO_3^{2-} ions.*

After a further 30 min of reaction, the growth of smaller individual bundles of aragonite crystals is observed (Fig.3.28B). Reaction of the calcium-sulfosuccinate film for 90 min leads to the formation of bigger but immature bundles of aragonite crystals (Fig.3.28C). Immersion of the calcium-sulfosuccinate film for a further 30 minutes in the Na_2CO_3 solution resulted in bundles of aragonite needles branching out from a central point, which was in contact with the organic surface (Fig.3.28D). Reaction of the

calcium-sulfosuccinate film for 160 min. clearly shows assembly of individual bundles of aragonite crystals into a highly dense structure (Fig.3.28E). While the morphology of the aragonite crystals in Figs.3.28D and E is not very different, the extent of assembly of the aragonite bundles appears to proceed with time reaching saturation after 160 min of reaction.

While in the study of using stearic acid as the crystallizing template, we did not observe the growth of the aragonite phase. Fig.3.29 show SEM images of $CaCO_3$ crystals grown within a 500 Å thick stearic acid film under conditions identical to that adopted for AOT studies above, wherein oriented growth of rhombohedral calcite crystals (at pH 6) can clearly be seen (Fig.3.29A).

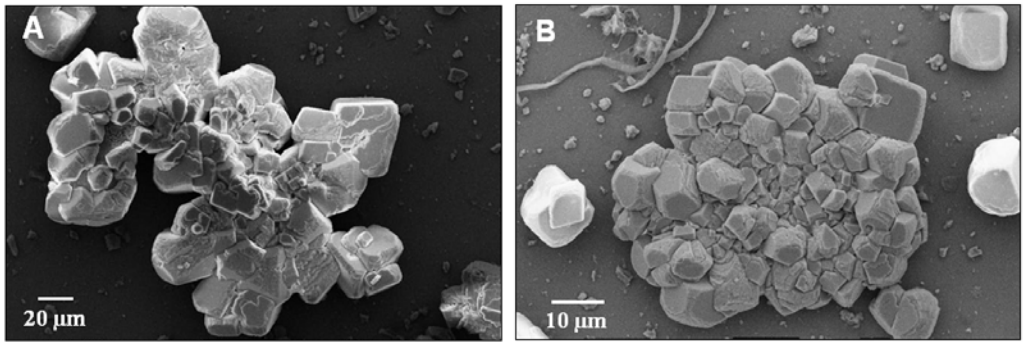

Fig. 3.29 : *SEM image of $CaCO_3$ crystals formed within a 500 Å thick thermally evaporated StA thin film.*

The calcite crystals clearly aggregate into dense structure with no relevance to the morphology and crystallography as observed in AOT matrix which clearly establish the importance of the nature of lipid matrix on $CaCO_3$ crystal growth.

3.6.5 X-ray diffraction results

The XRD pattern recorded from the $CaCO_3$ crystals shown in Fig.3.27 is shown as curve labeled 160 min. in Fig.3.30A. A number of Bragg reflections are identified and have been indexed with reference to the unit cell of the aragonite structure (a = 4.959 Å, b = 7.968 Å, c = 5.741 Å; space group *Pmcn*) [28c, 30]. For comparison, the simulated powder XRD pattern of aragonite is shown as curve 1, in Fig.3.30A. There is no evidence of either calcite or vaterite formation in the thermally evaporated AOT film. The XRD data thus provides clear support for the morphology of the $CaCO_3$ crystals seen in the SEM images – such well-defined needles are known to be characteristic of the aragonite

polymorph [28c, 7e]. Additionally, the presence of intense (0 0 2) and (2 2 1) reflections indicates oriented growth of the aragonite needles along these crystallographic planes.

The evolution of XRD patterns recorded as a function of time of reaction of Ca-AOT with carbonate ions is shown in Fig.3.30A and correspond to the SEM images shown in Fig.3.28A-E. As expected, the Ca-AOT film before initiation of reaction shows no Bragg reflections in the region of interest (Fig.3.30A, 0 min curve). As $CaCO_3$ growth proceeds, the Bragg reflections characteristic of aragonite grow in intensity reaching saturation after 160 min of reaction. It is observed that at the initial growth stage (30 min of reaction), the aragonite crystals show preferred orientation along the (002) direction. We have observed in the SEM images that further reaction leads to considerable assembly of the aragonite bundles (Figs.3.28C-E) and the possibility of reorientation of the crystallites. However, in the XRD spectra we observe that the (002) Bragg reflection remains the most intense even after 160 min of reaction. This indicates that the aragonite needle assembly proceeds without significant reorientation of the crystallites.

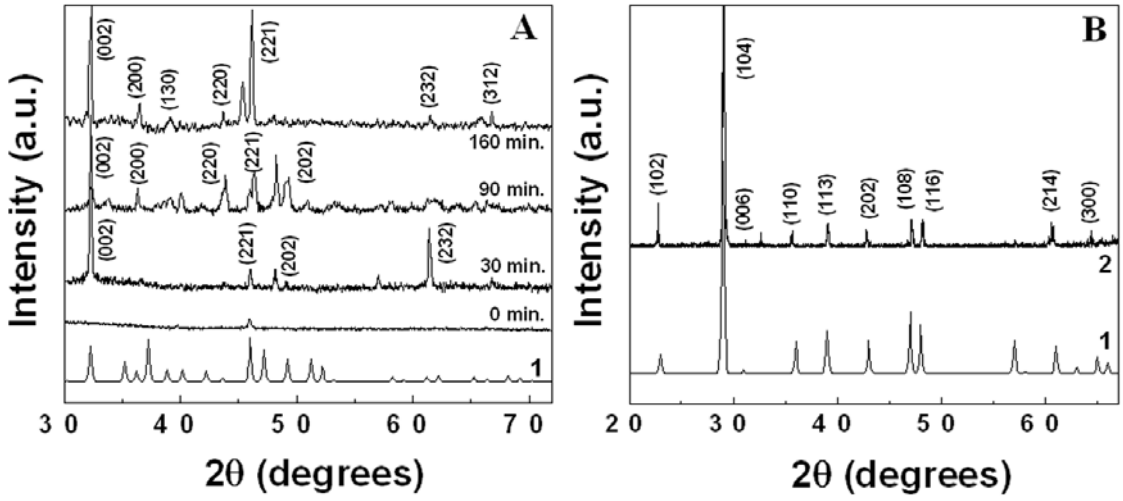

Fig. 3.30 : *(A) Simulated powder XRD pattern of aragonite crystals (Curve 1) and XRD pattern recorded from $CaCO_3$ crystals grown within a 500 Å thick thermally evaporated AOT film at different time interval of crystal growth. (B) Simulated powder XRD pattern of calcite crystals (Curve 1) and XRD pattern recorded from $CaCO_3$ crystals grown within a 500 Å thick thermally evaporated StA film.*

Curve 2 in Fig.3.30B shows the XRD spectra recorded from a 500 Å thick $CaCO_3$-StA film. A number of Bragg reflections are observed, and those corresponding to the calcite phase have been identified and labeled. For comparison, the simulated powder XRD pattern of calcite is shown as curve 1, in Fig.3.30B. It is clear that calcium carbonate

crystallizes into calcite when the crystallization occurs in StA matrix while aragonite polymorph is stabilized in AOT matrix. The major Bragg reflections for calcite agree very well with those reported in the literature [7a, 30]. It is observed that the calcite crystals nucleated in StA matrix have pronounced orientational uniformity, the predominant nucleating planes being (104) and (102). These dramatic changes in the crystallization of $CaCO_3$ further highlight the role played by the different nature of lipid matrix in the nucleation of calcite and aragonite crystals. This is an important result of the work and indicates that the nature of growth in constrained environments may play a role in face-specific nucleation of the $CaCO_3$ crystals.

3.6.6 Contact angle measurements

Contact angle measurements carried at various points on the $CaCO_3$-AOT/StA films surface at various stages of reaction and found that the surface was quite hydrophobic at all stages of reaction. The contact angles were measured on at least 10 different points on the film surface. The mean contact angles of the as deposited AOT and StA films were observed to be 95^o and 92^o respectively. The mean contact angles of the Ca-AOT and Ca-StA films were 92^o and 87^o. The contact angles after the formation of the $CaCO_3$ crystals did not show any drastic change. Thus, the SEM images and contact angle measurements obtained from the Ca-AOT and Ca-StA films during growth of the aragonite and calcite crystals suggest that the growth process occurs within the lipid matrix and not externally by a leaching process.

3.6.7 Summary

The crystallization of calcium carbonate within thermally evaporated AOT and StA films by a process of Ca^{2+} ion entrapment and thereafter, reaction with CO_3^{2-} ions has been demonstrated. Under conditions where there is good registry between the Ca^{2+} ions and the underlying AOT and StA templates, oriented growth of predominantly aragonite crystals is observed in the AOT template at room temperature whereas rhombohedral calcite is observed with a StA template. The crystallography of $CaCO_3$ crystals is observed to be strongly dependent on the nature of the lipid in the thermally evaporated matrices. The formation of large bundles of aragonite needles is an interesting

feature of this study. The hydrophobic nature of the crystallites points to a possible reason for formation of needle like aragonite.

3.7 Discussion

It is possible that the growth of the minerals as shown above may occur in solution by a process of ions leaching out of the thin lipid films and attachment of the crystals thus formed in the surface of the lipid films. To discount this possibility a simple calculation has been performed to show that the formation of minerals within lipid matrix is not mediated through ions leaching process followed by their reaction to form the respective mineral. The experiment was carried out for the $BaSO_4$-AOT system. The barium-sulfosuccinate films used in this study were typically of 1 cm x 1 cm dimensions. Assuming that the QCM mass loading in these films is reasonable at ca. 7000 ng cm^{-2} (Fig.3.2A) and if all the barium ions in this film are leached out into the 50 ml 1.4 x 10^{-3} M Na_2SO_4 solution, it can easily be calculated that the concentration of the barium ions in this solution would be nearly 1.02 x 10^{-6} M. Clearly, this would lead to a supersaturation ratio far too small to yield nucleation and growth of $BaSO_4$ crystals in solution. Together with the SEM studies on the kinetics of growth presented above (Fig.3.6), these calculations show that growth of the crystals occurs within the lipid matrix. The likely mechanism is therefore the nucleation and growth of the mineral crystals within the nanoscale hydrophilic regions of the bilayers in the lamellar ordered films accompanied by expansion of the lipid matrix (and consequent surface coating) to accommodate the large crystals. As the crystallites grow, they are covered by a monolayer of lipid, which renders the crystallites hydrophobic. The hydrophobic nature of the crystallites points to a possible reason for formation of superstructures of $BaSO_4$, $BaCrO_4$, $SrCO_3$ and $CaCO_3$. Since the growth of the crystals occurs in an aqueous environment, hydrophobic forces between the lipid monolayer-covered mineral crystals in the very early stages of crystal growth could lead to assembly of the crystals into higher ordered structures as observed. A similar mechanism has been implicated in the assembly of prismatic, rectangular super lattices and long filaments of $BaCrO_4$ crystals into linear superstructures grown in AOT microemulsions by Mann and co workers [12a]. The fact that AOT molecules in a highly condensed solid thin film state result in similar hydrophobic association-driven assembly indicates considerable swelling of the mineral-

AOT films during immersion in water. The overall crystal morphologies of minerals formed within thermally evaporated AOT bilayers are very different from that of minerals grown within thermally evaporated StA films.

The morphology variation of the minerals within the lipid bilayers may be a consequence of inhibition of growth along certain crystallographic directions by the respective anionic molecules in the bilayer; another factor that could contribute is the kinetics of crystal growth and the built-in anisotropy of the bilayer geometry. This is not difficult to understand given that the size of the carboxylic acid and sulfonate headgroups in StA and AOT molecules respectively is very different. The difference in periodicity of the carboxylate ions in StA and AOT would clearly affect face-specific nucleation of the mineral in both cases. It is possible that the bulky nature of the AOT headgroup forces it to pack in a rectangular pattern whereas stearic acid with smaller carboxylic acid headgroups would pack hexagonally in the thermally evaporated thin films. This would satisfactorily explain the difference in morphology and crystallography observed for $BaSO_4$, $BaCrO_4$, $SrCO_3$ and $CaCO_3$ grown in the different templates. While the exact packing of the AOT and StA molecules in the thermally evaporated bilayer stacks is not known, we expect that it may not be significantly different for Langmuir monolayers or SAMs bearing similar polar functional groups [6, 7]. Litvin *et al* have reported that aragonite needle growth occurs under Langmuir monolayers of 5-hexadecyloxyisophthalic acid where each molecule resides in a rectangular lattice and interacts with two neighbors through hydrogen bonding [6c]. Kuther and co-workers also observed growth of aragonite needles on SAMs when the terminal functionality of the self-assembling molecule (anthracene terminated thiol, ANTH) was changed to force assembly into a rectangular lattice [7e]. $CaCO_3$ crystals grown on otherwise hexagonally packed SAMs yielded calcite crystals [12c].

3.8 Conclusions

In this chapter, we have presented a new method to grow minerals using thermally evaporated lipid thin films, mimicking a general model for biomineralization. It is clear from this study that the lipid matrix that acts as the host for crystal growth plays a significant role in not only determining the morphology of the minerals, but also their crystallography. Epitaxy between the nucleating crystal face and underlying template is

possibly determining the morphology and crystallography of the mineral. Since the spatial arrangement of stearic acid and AOT molecules within the thermally evaporated lipid bilayers is significantly different, this approach is successful in controlling the nucleation and the inhibition induced by the lipid films on oriented crystal growth as observed above. We expect that these organic/inorganic composites can be used as novel materials that will exhibit high mechanical strength and other unique physical properties. The ability to control not only crystal habit and morphology, but also their spatial organization opens ways towards more intricate architectures that approach the complexity found in nature and might lead to functional materials with properties comparable to those found in nature. It is understandable that the lipid envelope is able to increase its surface, as the crystal within it grows, as it is not a rigid structure.

3.9 References

[1] (a) Bommel, K. J. C. V.; Friggeri, A.; Shinkai, S. *Angew. Chem. Int. Ed.* **2003**, *42*, 980. (b) Mann, S.; Burkett, S. L; Davis, S. A.; Folwer, C. E.; Mendelson, N. H.; Sims, S. D.; Walsh, D.; Whilton, N. T.; *Chem. Mater.* **1997**, *9*, 2300. (c) Estroff, L. A.; Hamilton, A. D.; *Chem. Mater.* **2001**, *13*, 3227. (d) Davis, S. A.; Breulmann, M.; Rhodes, K. H.; Zhang, B.; Mann, S. *Chem. Mater.* **2001**, *13*, 3218.

[2] (a) Berman, A.; Hanson, J.; Leiserowitz, L.; Koetzle, T. F.; Weiner, S.; Addadi, L. *Science*, **1993**, *259*, 776. (b) Xu, X.; Han, J. T.; Cho, K. *Chem. Mater.* **2004**, *16,* 1740. (c) Weiner, S.; Addadi, L. *J. Mater. Chem.* **1997**, *7*, 689. (d) Simkiss, K.; Wilbur, K. *Biomineralization*; Academic Press: New York, **1989**. (e) Mann, S. *Biomimetic Materials Chemistry*; John Wiley & Sons Publishers: **1995**. (f) Zaremba, C. M.; Morse, D. E.; Mann, S.; Hansma, P. K.; Stucky, G. D. *Chem. Mater.* **1998**, *10*, 3813.

[3] (a) Lowenstam, H. A. *Science* **1981**, *211*, 1126. (b) Heuer, A. H.; Fink, D. J.; Laraia, V. J.; Arias, J. L.; Calvert, P. D.; Kendall, K.; Messing, G. L.; Blackwell, J.; Rieke, P. C.; Thompson, D. H.; Wheeler, A. P.; Veis, A.; Caplan, A. I. *Science* **1992**, *255*, 1098.

[4] (a) Addadi, L.; Weiner, S. *Angew. Chem.* **1992**, *104*, 159. (b) Addadi, L.; Weiner, S. *Angew. Chem. Int. Ed. Engl.* **1992**, *31*, 153. (c) Lowenstam, H. A.; Weiner, S. *On Biomineralization*, Oxford Univ. Press, New York, 1989, 324 pp. (d) Addadi, L.;

Weiner, S. *Nature* **1997**, *389*, 912. (e) Kuhn-Spearing, L. T.; Kessler, H.; Chateau, E.; Bllarini, R.; Heuer, A. *J. Mater. Sci.* **1996**, *31*, 6583. (f) Mann, S. *Nature* 1993, *365*, 499.

[5] (a) Berman, A.; Ahn, D. J.; Lio, A.; Salmeron, M.; Reichert, A.; Charych, D. *Science* **1995**, *269*, 515. (b) Archibald, D. D.; Quadri, S. B.; Gaber, B. P. *Langmuir* **1996**, *12*, 538.

[6] (a) Xu, G.; Yao, N.; Aksay, I. A.; Groves, J. T. *J. Am. Chem. Soc.* **1998**, *120*, 11977. (b) Heywood, B. R.; Mann, S. *Adv. Mater.* **1994**, *6*, 9. (c) Litvin, A. L.; Valiyaveettil, S.; Kaplan, D. L.; Mann, S. *Adv. Mater.* **1997**, *9*, 124. (d) Heywood, B. R.; Mann, S. *Langmuir* **1992**, *8*, 1492. (e) Heywood, B. R.; Mann, S. *J. Am. Chem. Soc.* **1992**, *114*, 4681. (f) Buijnsters, P. J. J. A.; Donners, J. J. J. M.; Hill, S. J.; Heywood, B. R.; Nolte, R. J. M.; Zwanenburg, B.; Sommerdijk, N. A. J. M. *Langmuir* **2001**, *17*, 3623.

[7] (a) Aizenberg, J.; Black, A. J.; Whitesides, G. M. *J. Am. Chem. Soc.* **1999**, *121*, 4500. (b) Travaille, A. M.; Kaptijn, L.; Verwer, P, Hulsken, B.; Elemans, J. A. A. W.; Nolte, R. J. M.; Kempen, H. V. *J. Am. Chem. Soc.* **2003**, *125*, 11571. (c) Travaille, A. M.; Donners, J. J. J. M.; Gerritsen, J. W.; Sommerdijk, N. A. J. M.; Nolte, R. J. M.; Kempen, H. V. *Adv. Mater.* **2002**, *14*, 492. (d) Kuther, J.; Bartz, M.; Seshadri, R.; Vaughan, G. B. M.Tremel, W. *J. Mater. Chem.* **2001**, *11*, 503. (e) Kuther, J.; Nelles, G.; Seshadri, R.; Schaub, M.; Butt, H. J.; Tremel, W. *Chem. Eur. J.* **1998**, *4*, 1834.

[8] Hosoda, N.; Kato, T. *Chem. Mater.* **2001**, *13*, 688. (b) Kato, T; Suzuki, T.; Irie, T. *Chem. Lett.* **2000**, 186.

[9] (a) Mann, S.; Hannington, J. P.; Williams, R. J. P. *Nature* **1986**, *324*, 565. (b) Mann, S.; Hannington, J. P. *J. Coll. Interf. Sci.* **1987**, *122*, 326.

[10] (a) Mann, S. *Nature* **1988**, 332, 119. (b) Calvert, P.; Mann, S. *J. Mater. Sci.* **1988**, *23*, 3801. (c) Albeck, S.; Aizenberg, J.; Addadi, L.; Weiner, S.; *J. Am. Chem. Soc.* **1993**, *115*, 11691. (d) Grassmann, O.; Muller, G.; Lobmann, P. *Chem. Mater.* **2002**, *14*, 4530. (e) Fallini, G.; Fermani, S.; Gazzano, M.; Ripamonti, A. *Chem. Eur. J.* **1997**, *3*, 1807.

[11] (a) Lochhead, M. J.; Letellier, S. R.; Vogel, V. *J. Phys. Chem. B.* **1997**, *101*, 10821. (b) Messersmith, P. B.; Vallabhaneni, S.; Nguyen, V.; *Chem. Mater.* **1998**, *10*, 107.

(c) Messersmith, P. B.; Starke, S. *Chem. Mater.* **1998**, *10*, 117. (d) Khan, S. R.; Whalen, P. O.; Glenton, P. A. *J. Cryst. Growth* **1993**, *134*, 211.

[12] (a) Li, M.; Schnablegger, H.; Mann, S. *Nature* **1999**, *402*, 393. (b) Hopwood, J. D.; Mann, S. *Chem. Mater.* **1997**, *9*, 1819. (c) Li, M.; Mann, S. *Langmuir* **2000**, *16*, 7088. (d) Mann, S. *Angew. Chem. Int. Ed.* **2000**, *39*, 3392.

[13] (a) Ganguly, P.; Sastry, M.; Pal, S.; Shashikala, M. N. *Langmuir* **1995**, *11*, 1078. (b) Patil, V.; Malvankar, R. B.; Sastry, M. *Langmuir* **1999**, *15*, 8197.

[14] Sastry, M.; Rao, M.; Ganesh, K.N. *Acc.Chem.Res.* **2002**, *35*, 847.

[15] (a) Gole, A.; Vyas, S.; Sainkar, S. R.; Lachke, A.; Sastry, M. *Langmuir* **2001**, 17, 5964. (b) Sastry, M. *Trends Biotech.* **2002**, *20*, 185.

[16] Ramakrishnan, V.; Sable, M.; D'Costa, M.; Ganesh, K. N.; Sastry, M. *Chem.Commun.* **2001**, 2622.

[17] Damle, C.; Kumar, A.; Sastry, M. *J. Mater. Chem.* **2002**, *12*, 1860.

[18] (a) Mandal, S.; Sainker, S.R.; Sastry, M. *Nanotechnology*, **2001**, *12*, 358. (b) Mandal, S.; Sainker, S.R.; Sastry, M. *Mater.Res.Bull.* **2002**, *37*, 1613.

[19] Sauerbrey, G. *Z.Phys.(Munich)* **1959**, *155*, 206.

[20] (a) Cuvillier, N.; Rondelez, F. *Thin Solid Films*, **1998**, *19*, 327. (b) Decher, G. *Science* **1997**, *277*, 1232.

[21] Spectrometric Identification of Organic Compounds (Silverstein R. M.; Webster F. X.) *John Wiley & Sons, Inc*.(Sixth Edition, P-107).

[22] (a) Bromley, L. A.; Cottier, D.; Davey, R. J.; Dobbs, B.; Smith, S.; Heywood, B. R. *Langmuir* **1993**, *9*, 3594. (b) Qi, L.; Coffen, H.; Antonietti, M. *Angew. Chem. Intl. Ed.* **2000**, *39*, 604. (c) Uchida, M.; Sue, A.; Yoshioka, T.; Okuwaki, A. *CrystEngComm* **2001**, 5. (d) Hopwood, J. D.; Mann, S. *Chem. Mater.* **1997**, *9*, 950.

[23] Hill, R. J. *Can. Mineral.* **1977**, *15*, 522.

[24] The XRD patterns were indexed with reference to the unit cell of the $BaCrO_4$ structure from *ASTM* chart (a = 9.105 Å, b = 5.541 Å, c = 7.343 Å; space group *Pnma*, *ASTM* chart card no. 15-376).

[25] (a) Kuther, J.; Seshadri, R.; Tremel W. *Angew. Chem. Int. Ed.* **1998**, *37*, 3044. (b) Wang, L.; Zhu, Y. *Chem. Lett.* **2003**, *32*, 594. (c) Kuther, J.; Seshadri, R.; Nelles, G.; Assenmacher, W.; Butt, H. J.; Mader, W.; Tremel, W. *Chem. Mater.* **1999**, *11*, 1317. (d) Sondi, I.; Matijevic, E. *Chem. Mater.* **2003**, *15*, 1322.

[26] The XRD patterns were indexed with reference to the unit cell of the strontianite structure from *ASTM* chart (a = 5.107 Å, b = 8.414 Å, c = 6.029 Å; space group *Pmcn*, ASTM chart card no. 5-0418).

[27] (a) Nassrallah-Aboukais, N.; Boughriet, A.; Laureyns, J.; Aboukais, A.; Fischer, J. C.; Langelin, H. R.; Wartel, M. *Chem. Mater.* **1998**, *10*, 238. (b) Falini, G.; Albeck, S.; Weiner, S.; Addadi, L. *Science* **1996**, *271*, 67.

[28] (a) Sugawara, A.; Kato, T. *Chem. Commun.* **2000**, 487-488. (b) Walsh, D.; Mann, S. *Nature* **1995**, *377*, 320. (c) Ota, Y.; Inui, S.; Iwashita, T.; Kasuga, T.; Abe, Y. *J. Am. Ceram. Soc.* **1995**, *78*, 1983. (d) Kuther, J.; Tremel, W. *Chem. Commun.* **1997**, 2029.

[29] Heywood, B. R.; Mann, S. *Chem. Mater.* **1994**, *6*, 311.

[30] The XRD patterns were indexed with reference to the unit cell of the calcite and aragonite structure from *ASTM* chart card nos. 5-0586 and 5-0453 respectively.

CHAPTER IV

Mineral Growth at a Liquid-Liquid Interface

This chapter discusses the synthesis of minerals at a charged liquid-liquid (static and dynamic) interface. The dynamic charged interface was realized using a Hele-Shaw cell where the synthesis of $BaSO_4$, $SrCO_3$ and $CaCO_3$ crystals was accomplished by the reaction of appropriate metal cations electrostatically complexed with surfactant molecules pinned to the interface with corresponding counterions present in the aqueous part of the biphasic reaction medium. We show that polymorph selectivity, morphology and assembly of the minerals can be modulated by varying the experimental conditions such as the nature of the surfactant, the plate separation, the supersaturation ratio, and the viscosity between the liquids in the Hele-Shaw cell. The importance of a dynamic charged liquid-liquid interface in controlling mineral growth is highlighted with various control experiments as well as with the mineral growth at a static liquid-liquid interface.

Part of the work presented in this chapter has been published and patented:

1) Rautaray, D.; Kumar, A.; Reddy, S.; Sainkar, S.R.; Pavaskar, N.R.; Sastry, M. *CrystEngComm* **2001**, *45*,1-4. 2) Reddy, S.; Rautaray, D.; Sainkar, S.R.; Sastry, M. *Bull. Mater. Sci.* **2003**, *26*, 283-288. 3) Rautaray, D.; Banpurkar, A.; Sainkar, S.R.; Limaye, A. V.; Ogale, S.; Sastry, M. *Crystal Growth & Designi* **2003**, *3*, 449-452. 4) Rautaray, D.; Banpurkar, A.; Sainkar, S.R.; Limaye, A. V.; Pavaskar, N.R.; Ogale, S.; Sastry, M. *Adv. Mater.* **2003**, *15*, 1273-1278. 5) Rautaray, D.; Kavathekar, R.; Sastry, M. *Faraday Discuss.* **2004**, (*In Press*). 6) Murali Sastry, Debabrata Rautaray; *US Patent Filed* (NCL/28/2003).

4.1 Introduction

Interfaces play a key role in modern science and technology and the unique features and phenomena induced in them have attracted the interest of researchers in many different fields. In particular, liquid-liquid interfaces have drawn much attention; not only do these interfaces have structural and dynamical nonlinear properties which are not observed in bulk liquids, but also they are integral to many chemical, physical and biological systems [1-4]. In this respect, substantial research effort has been aimed at developing a detailed understanding of interfacial interactions associated with biomineralization [5,6] and surface- or template-directed crystallization [7,8]. In particular, electrostatic interactions at charged interfaces are widely recognized as significant in surface-directed mineralization [6].

There is growing interest in the two- and three-dimensional organization of inorganic nanoparticles such as metals [4], oxides [9] and ceramics [10]. The main challenge in this area is to develop protocols for the organization of crystalline arrays of nanoparticles wherein both the size and separation between the nanoparticles in the arrays can be tailored. Application based on the collective properties of the organized particles requires flexibility in controlling the nanoarchitecture of the film [11]. It is clear from above that a relatively unexplored aspect of research in this area concerns the assembly of individual crystallites into highly ordered superstructures, such superstructures often determining the mechanical, optical and other properties of inorganic nanoparticles.

The liquid-liquid interface has been extensively investigated in the synthesis of advanced materials. In this context, a number of templating interfaces have been used in the growth of inorganic crystals, but very little work has been done on crystal growth at the liquid-liquid interface using suitably immobilized templating molecules at the interface. However, in all these above studies, the interface (often charged due to the presence of ionizable surfactants) was static [1-10] and other than providing a scaffold on which material growth could take place, was more or less passive. The idea of generating expanding liquid-liquid interfaces and investigating their role in modulating the morphology/crystallography of inorganic materials grown at these interfaces is a relatively new one developed in this laboratory. In order to achieve controllable

expanding liquid-liquid interfaces for growth of materials, we have used a Hele-Shaw cell [12] commonly used to study the phenomenon of viscous fingering [12-13]. The displacement of a viscous fluid constrained between two parallel plates by a less viscous one leads to the formation of finger-like patterns known as 'viscous fingering' [12,13]. The morphology of the viscous-finger patterns generated is a function of many parameters such as the flow rate, difference in viscosities of the two fluids and the interfacial tension. Thus, the Hele-Shaw cell has been invaluable in the study of dynamic instabilities at interfaces and in the study of viscous finger pattern formation. However, the potential of the Hele-Shaw cell in carrying out reactions at the interface between the two fluids leading to the formation of inorganic materials has been largely unrecognized and underexploited. Realizing that the dynamic liquid-liquid interface in a Hele-Shaw cell would provide opportunities to control a variety of time-scales associated with material formation, we have used the Hele-Shaw cell in mineral synthesis.

In our first set of experiments we have studied the growth of the minerals $BaSO_4$, $SrCO_3$ and $CaCO_3$ in a radial Hele-Shaw cell. This was accomplished by taking fatty acids such as stearic acid/AOT in the organic phase and carrying out reaction of the appropriate metal ions ($Ba^{2+}/Sr^{2+}/Ca^{2+}$) with the corresponding counterions (SO_4^{2-}/CO_3^{2-}) present in the aqueous phase (injected phase). The reaction lead to mineral formation occurs at the interface due to strong complexation of the metal cations with the charged fatty acid/AOT. The role of viscosity in determining the morphology and assembly of $CaCO_3$ crystals grown in a radial Hele-Shaw cell was also studied.

In order to understand the importance of the dynamic charged liquid-liquid interface, we investigate the growth of $BaSO_4$, $SrCO_3$ and $CaCO_3$ crystals at static charged liquid-liquid interface between an aqueous solution of $Ba^{2+}/Sr^{2+}/Ca^{2+}$ ions and organic solutions containing surfactant molecules by reaction with Na_2SO_4/Na_2CO_3. The process is seemingly similar to the growth of $BaSO_4/SrCO_3/CaCO_3$ crystals at the air-water interface with anionic Langmuir monolayers as the template [14] with the following important differences. The magnitude of the dielectric discontinuity between water-organic solution and water-air would be different and could lead to important differences in the electrostatics of complexation of the Ba^{2+} ions with the anionic surfactant molecules at the interface. Furthermore, the finite solubility of the two solutions would lead to a region of the interface with a much broader gradation in the

dielectric function which would in turn influence the electrostatics of the metal ion complexation with the lipid molecules as well as the organization of the templating lipid molecules in the interfacial region. The solvation of the hydrocarbon chains in the organic phase would also contribute to disruption in the ordering of the surfactant molecules at the water-organic solution interface with important consequences in the epitaxy associated with crystal nucleation processes.

4.2 Mineral growth at the liquid-liquid interface

The crystallization of minerals at the charged liquid-liquid (both dynamic and static) interfaces were realized with the following set of experiments:

1. The synthesis of $BaSO_4$ crystals was accomplished at the static and dynamic charged interfaces between two liquids (aqueous solution of $BaCl_2$ and Na_2SO_4 and chloroform solution containing StA/AOT).
2. The synthesis of $SrCO_3$ crystals was accomplished at the static and dynamic charged interfaces between two liquids (aqueous solution of $SrCl_2$ and Na_2CO_3 and chloroform solution containing StA/AOT).
3. The synthesis of $CaCO_3$ crystals was accomplished at the static and dynamic charged interfaces between two liquids (aqueous solution of $CaCl_2$ and Na_2CO_3 and chloroform solution containing StA/AOT). The role of variation of viscosity in determining the morphology and assembly of $CaCO_3$ crystals grown in a radial Hele-Shaw cell was also studied.

4.2.1 Mineral growth at a dynamic charged liquid-liquid interface

In order to realize a dynamic liquid-liquid interface, we have used a Hele-Shaw cell to study the mineral growth. The Hele-Shaw cell used in this study comprised of two 1 cm thick, 30 x 30 cm^2 float-glass plates. Spacers of size ranging b = 200 - 400 μm were used between the top and bottom glass plates. The viscous fluid (mixed aqueous solution of $BaCl_2/SrCl_2/CaCl_2$ and Na_2SO_4/Na_2CO_3) was placed in the cell gap and thereafter, chloroform containing stearic acid [$CH_3(CH_2)_{16}COOH$; StA,]/sodium bis-2-ethylhexyl-sulfosuccinate [($C_{20}H_{37}NaO_7S$; aerosol OT, AOT] was injected through a hole (0.5 mm diameter) drilled at the center of the top glass plate using an automated fluid delivery system (Fig.4.1).

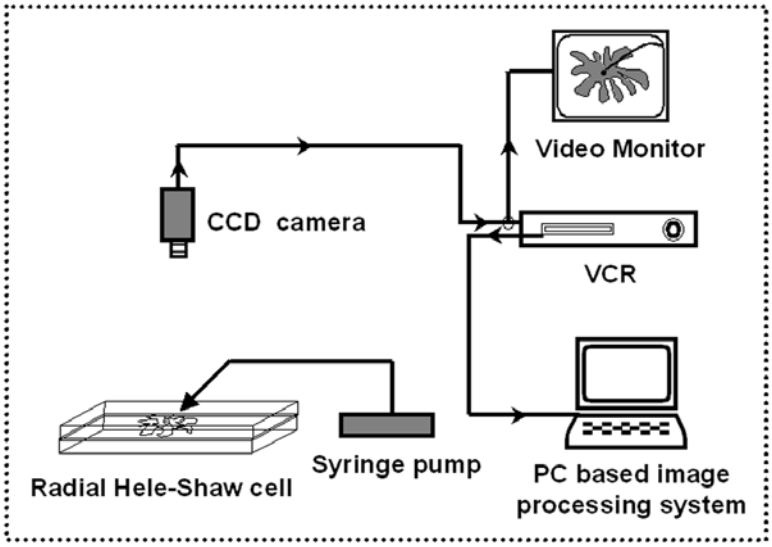

Fig.4.1 *Schematic showing the various elements in the radial Hele-Shaw experiment.*

Two experiments were performed in salt solutions as the displaced fluid of supersaturations (S_R) of ca. 30 and ca. 50. A small amount of dye was added to the chloroform to yield sufficient contrast between the aqueous and organic solvent phases for easy capture of the images with the CCD (charge-coupled device) camera (Fig.4.1). The experiments were performed at a constant volumetric flow rate (VFR) of chloroform into the aqueous phase (mixed electrolytes solutions) at 0.5 ml/min. The evolution of the finger pattern with time was followed for the above cases using a CCD camera connected to a video recorder at an image capture rate of 25 images/sec (Fig.4.1). On completion of the injection process (typically 15-20 minutes), the organic solution was carefully removed and the remaining aqueous precipitate was washed with copious amounts of double distilled water and transferred to Si (111) and glass substrates for SEM, EDAX, FTIR and XRD measurements.

4.2.2 Mineral growth at a static charged liquid-liquid interface

In this part of experiments, $BaSO_4$, $SrCO_3$ and $CaCO_3$ crystallization were achieved at a static liquid-liquid interface (Fig.4.2). In this experiment, a solution of fatty acid/AOT in organic solvent (chloroform) was taken in a separating funnel and aqueous solution of $BaCl_2$/$SrCl_2$/$CaCl_2$ was added to it. The biphasic mixture was allowed to rest

for 30 minutes following which aqueous solution of Na_2SO_4/Na_2CO_3 was injected slowly into the aqueous side of the liquid-liquid interface (solubility of $CHCl_3$ in water is 0.08 $^{w}/_{w}$ %; dielectric constant = 4.8; density = 1.47 g/ml).

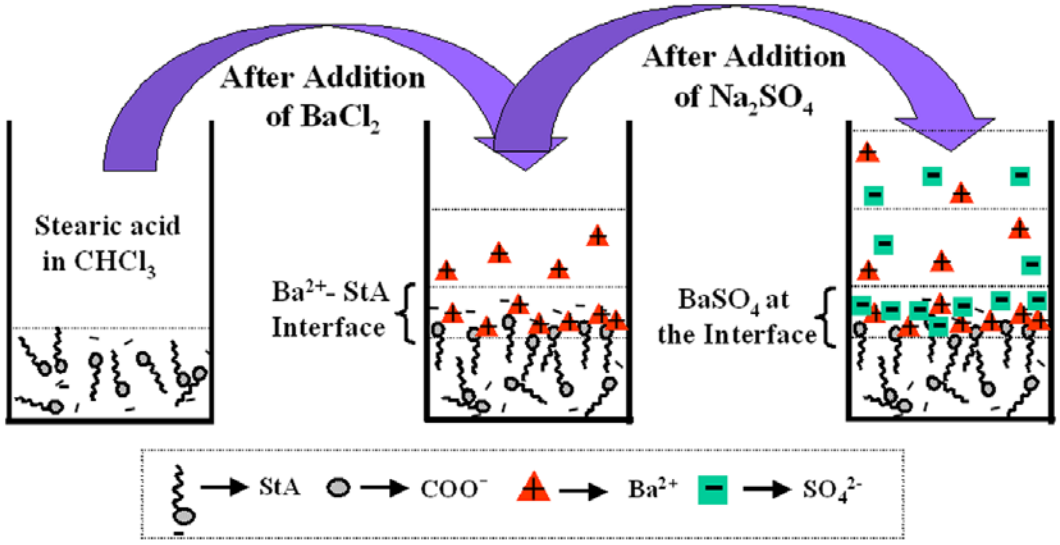

Fig.4.2 A typical s*chematic showing the process of mineral ($BaSO_4$) growth at a static liquid-liquid interface.*

The concentrations of the respective salts were adjusted to yield an S_R of 30. As the injection of Na_2SO_4/Na_2CO_3 progressed, the interface turned turbid and after some time it was noticed that crystals of $BaSO_4$, $SrCO_3$ and $CaCO_3$ were formed at the liquid-liquid interface (Fig.4.2). Apart from the interface, the organic and aqueous phases were clear. The organic solution was carefully removed from the separating funnel and the crystals separated by filtration, washed with copious amounts of double distilled water and placed on Si (111) substrates for SEM, EDAX and XRD measurements.

4.3 Crystallization of $BaSO_4$ at the liquid-liquid interface

The synthesis of $BaSO_4$ crystals was accomplished at a steadily expanding interface between two liquids (aqueous solution of $BaCl_2$ and Na_2SO_4 and chloroform solution containing StA/AOT) in a radial Hele-Shaw set up. Spacers of size b = 300 µm was used between the top and bottom glass plates. The experiments were performed in salt solutions as the displaced fluid of S_R of ca. 30 (5 ml of 1 x 10^{-3} M aqueous $BaCl_2$ and 5 ml of 3.564 x 10^{-4} M aqueous Na_2SO_4) and ca. 50 (5 ml of 1 x 10^{-3} M aqueous $BaCl_2$

and 5 ml of 9.9 x 10^{-4} M aqueous Na_2SO_4). The experiments were performed at a constant VFR of chloroform into the aqueous phase (mixed aqueous solutions of $BaCl_2$ and Na_2SO_4) at 0.5 ml/min. The flow rate was decided based upon the induction time observed for initiation of crystal nucleation. The growth of $BaSO_4$ crystals was also carried out at the static liquid-liquid interface between an aqueous solution of Ba^{2+} ions and organic solution containing StA/AOT molecules by reaction with sodium sulfate at an S_R of 30. The aqueous precipitates obtained in all the experiments were washed and placed on Si (111) and glass substrates for SEM, EDAX and XRD measurements.

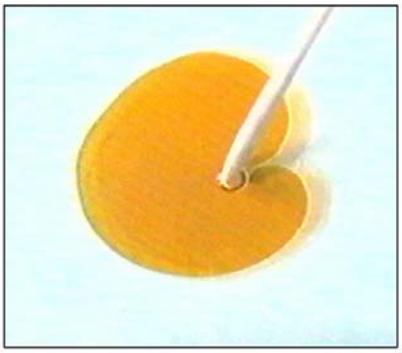

Fig.4.3: *Image of the viscous fingering pattern formed at a particular instant during injection of chloroform containing stearic acid (colored phase) into an aqueous solution of $BaCl_2$ and Na_2SO_4.*

Fig.4.3 shows a representative image recorded during injection of chloroform containing StA into the electrolyte solution. The interface between the two liquids is very uniform, with no evidence of finger formation. Therefore, on the scale of 10-100 μm, the interface may be considered to be essentially flat. The slow VFR coupled with the small difference in viscosities of the two fluids [13] is responsible for the smooth interface and thus provides a simplified model system for understanding the crystal growth process.

4.3.1 SEM and EDAX measurements

4.3.1.1 $BaSO_4$ crystals grown at a dynamic charged liquid-liquid interface in the presence of StA

SEM images recorded from $BaSO_4$ crystals grown in the Hele-Shaw cell at an S_R of 30 are shown in Figs.4.4A, B and C at different magnifications. The representative low magnification SEM image in Fig.4.4A shows that the substrate is covered with a fairly

large density of extremely straight $BaSO_4$ filaments. Fig.4.4B shows some such $BaSO_4$ filaments (often of lengths in excess of 200-300 μm) criss-crossing the substrate surface. A small percentage of nearly spherical, individual crystallites can also be seen (Fig.4.4B). At higher magnification, one of the long filaments is observed to consist of assemblies of individual crystallites (Fig.4.4C). Other smaller filaments at different stages of aggregation are also observed in this image. EDAX analysis of the $BaSO_4$ fibers yielded a Ba : S : O atomic ratio of 1 : 1.2 : 7.5. While the Ba : S ratio is in fair agreement with the expected stoichiometry, excess oxygen is due to sampling from the silica substrate.

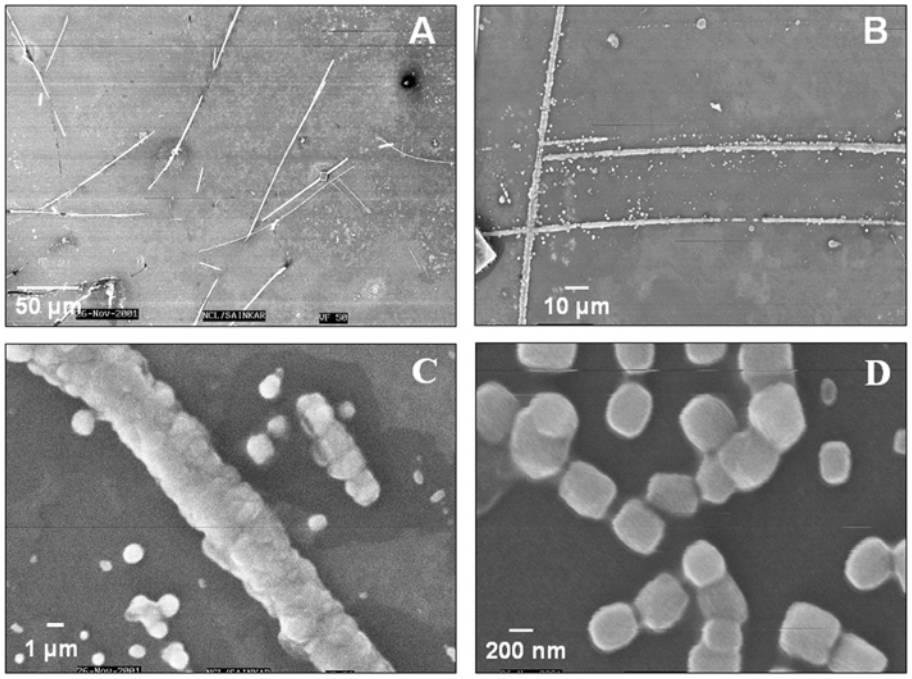

Fig.4.4: *A, B and C) Low and high magnification SEM images respectively of $BaSO_4$ crystals grown in the Hele-Shaw cell using StA in the organic phase at an S_R of 30. and D) SEM image of $BaSO_4$ crystals grown in the Hele-Shaw cell using StA in the organic phase at an S_R of 50.*

The SEM picture of $BaSO_4$ crystals grown in the Hele-Shaw cell at an S_R of 50 is shown in Fig.4.4D. While a number of very regular, rectangular $BaSO_4$ crystals densely populating the substrate surface can be seen, the formation of extended linear assemblies of crystallites has not occurred. However, some degree of incipient localized ordering of the rectangular particles can be observed (Fig.4.4D). EDAX analysis of the $BaSO_4$ rectangular crystals confirms the expected composition.

4.3.1.2 $BaSO_4$ crystals grown at a dynamic charged liquid-liquid interface in the presence of AOT

In order to understand the role of surfactant in directing the crystal morphology at the dynamic liquid-liquid interface, $BaSO_4$ crystals were grown in the Hele-Shaw cell using another surfactant AOT in the chloroform phase. Representative SEM pictures at different magnifications of $BaSO_4$ crystals grown at the dynamic liquid-liquid interface at an S_R of 30 in the presence of AOT are shown in Figs.4.5A & B.

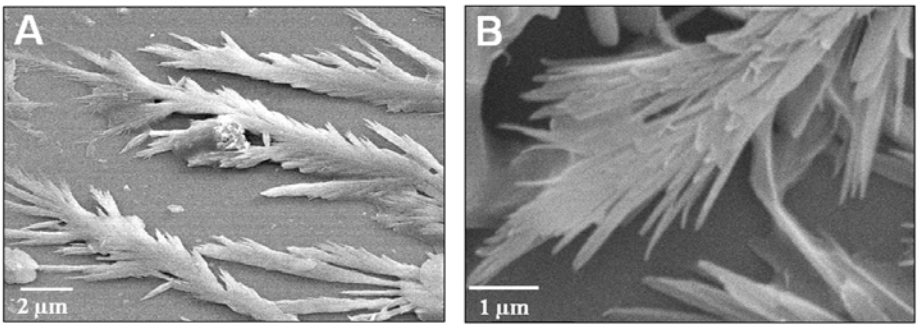

Fig.4.5: *A & B) Representative SEM images at different magnifications of $BaSO_4$ crystals grown in the Hele-Shaw cell using AOT in the organic phase at an S_R of 30.*

The $BaSO_4$ crystals do assemble into extended linear structures (Figs.4.5A) with the difference that the assemblies are more branched than in the experiment involving the surfactant StA (Figs.4.4A-C). There is no evidence of individual barite crystallites were observed in the AOT experiment. The higher magnification SEM image (Fig.4.5B) clearly shows the branched barite superstructures in greater details. The surface of these extended linear structures is observed to be very solid in nature rather than any assembly of individual crystallites. It is clear from the Hele-Shaw experiments that the expanding liquid-liquid interface plays an important role in assembling the barite crystallites and that the nature of the surfactants modulates the morphology and the assembly.

4.3.1.3 $BaSO_4$ crystals grown in control experiments

By choosing a fixed VFR but different S_R values in a range where supersaturation variation is not expected to lead to significant differences in the morphology of the barite crystals, we expect to understand better growth of the crystals at the expanding interface (S_R = 30) versus that occurring in the bulk solution (S_R = 50). We believe the linear filaments of barite crystals observed in the S_R = 30 Hele-Shaw experiment (Figs.4.4A,B

and C) correspond to crystals grown at the expanding interface while the crystals obtained in the S_R = 50 experiment are those grown predominantly in the bulk of the electrolyte solution (Fig.4.4D). In order to test this hypothesis, control experiments were performed where we did observe barite growth in solution at S_R = 50 within 6 minutes (less than the time-scale of the Hele-Shaw experiment) while no growth in solution was seen at S_R = 30 within the same experimental time-scale.

To differentiate between the ordering influence of an expanding liquid-liquid interface and the presence of surfactant molecules at the interface, another control experiment was performed wherein crystallization of $BaSO_4$ was accomplished in the Hele-Shaw cell at an S_R of 30 in the absence of any surfactant in the chloroform phase. The representative SEM image recorded from $BaSO_4$ crystals grown in this experiment is shown in Fig.4.6 and clearly shows the formation of plate-like $BaSO_4$ crystals. There is no evidence for assembly of the barite crystallites into higher order structures.

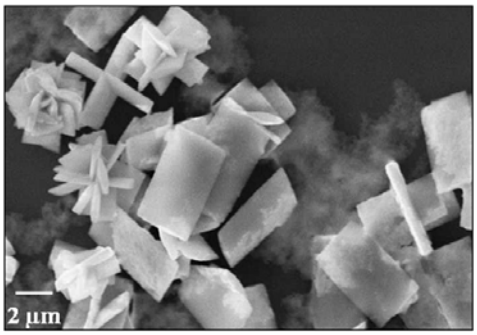

Fig.4.6: *Representative SEM image of $BaSO_4$ crystals grown in the Hele-Shaw cell at an S_R of 30 in the absence of a surfactant.*

4.3.1.4 $BaSO_4$ crystals grown at the static charged liquid-liquid interface

SEM micrographs at different magnifications obtained from the $BaSO_4$ crystals grown at the static liquid-liquid interface with StA in the organic phase is shown in Fig.4.7. At lower magnification (Fig.4.7A), a number of plate shaped $BaSO_4$ crystals of uniform size are observed. Spot profile EDAX measurements taken from within one of the crystals yielded a Ba : S : O ratio of 1 : 1.45 : 9 which is in excellent agreement with that expected for barite. The excess oxygen in the EDAX measurements is due to sampling from the silica substrate. The higher magnification SEM image clearly shows the formation of flat rectangular barite crystals with smooth edges (Fig.4.7B). It is clear from this image that the particles are extremely thin and plate-like in overall morphology.

Fig.4.7C shows a representative SEM image of $BaSO_4$ crystals grown at the static liquid-liquid interface with AOT in the organic phase. The crystals exhibited plate-like structures; rather similar in morphology to that observed for barite crystals grown in the presence of StA at the liquid-liquid interface with the only difference is that the plate like barite crystals in this case are sintered with each other.

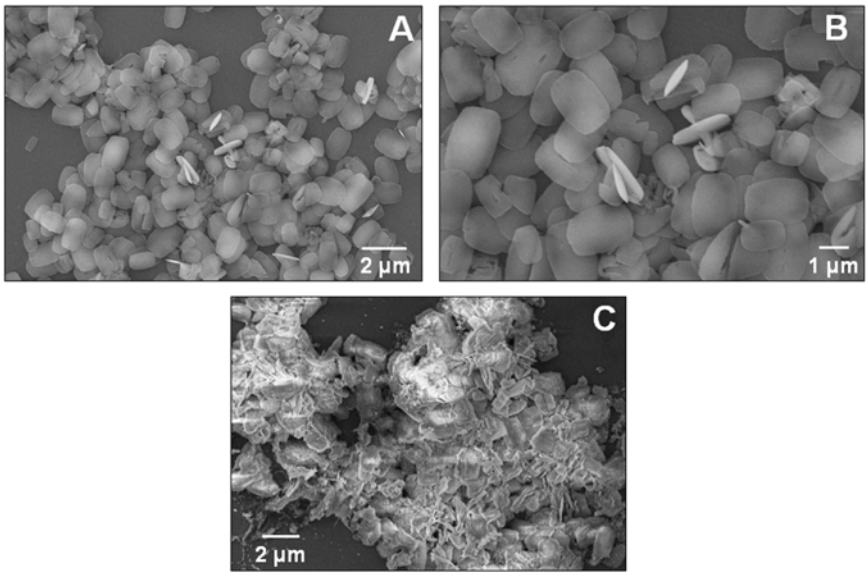

Fig.4.7: *A and B – SEM micrographs at different magnifications recorded from $BaSO_4$ crystals grown at the aqueous-organic interface with StA molecules in the organic phase. C – A representative SEM micrograph recorded from $BaSO_4$ crystals grown at the aqueous-organic interface with AOT molecules in the organic phase.*

The morphology of the barite crystals of this study grown in the presence of the surfactant more closely resembles barite crystals grown in solution in the presence of crystallization inhibitors possessing (iminodimethylene) phosphonate motifs [15] and inhibitors such as aminocarboxylate chelating precursors (nitrilotriacetic acid, to be more specific) [16]. It appears that the surfactant molecules at the liquid-liquid interface behave similarly to such crystal growth inhibitors.

4.3.2 X-ray diffraction studies

The XRD pattern recorded from the $BaSO_4$ crystals shown in Fig.4.4A is displayed as curve 2 in Fig.4.8. A number of Bragg reflections are identified and have been indexed with the reference to the unit cell of the barite structure {a = 8.8701 Å, b = 5.4534 Å, c = 7.1507 Å; space group V_h^{16} (*Pnma)*} [17]. For comparison, the simulated powder XRD pattern of barite crystals is shown as curve 1 in Fig.4.8. An interesting

feature of the diffraction pattern of the barite filaments grown in the Hele-Shaw cell is the intense (2 0 0) Bragg reflection from the crystals indicating oriented growth of the barite crystals in this experiment (Fig.4.8, curve 2).

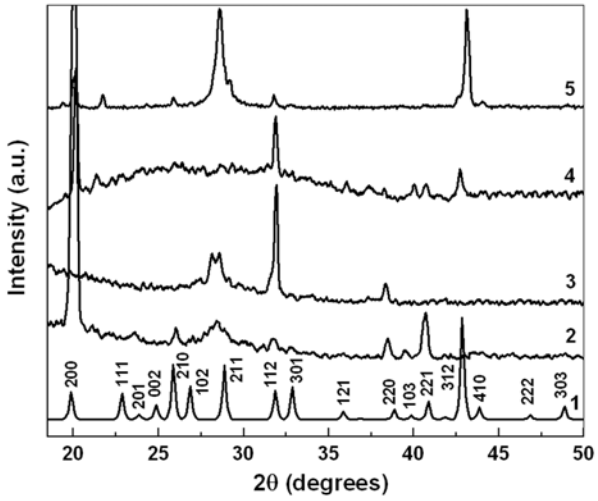

Fig.4.8: *Curve 1 : simulated powder XRD pattern of barite crystals; curves 2 and 3 : XRD patterns recorded from $BaSO_4$ crystals synthesized in the radial Hele-Shaw cell in the presence of StA at S_Rs of 30 and 50 respectively; curve 4 : XRD pattern from $BaSO_4$ crystals grown in the Hele-Shaw cell at an S_R of 30 in the presence of AOT and curve 5, XRD pattern from $BaSO_4$ crystals grown in the Hele-Shaw cell at an S_R 30 in the absence of a surfactant.*

The XRD pattern recorded from the barite crystals grown at S_R = 50 is shown as curve 3 in Fig.4.8. The Bragg reflections for barite crystals are observed in this experiment as well. The (2 0 0) Bragg reflection is absent while the (1 1 2) reflection is most intense indicating that oriented growth of the crystals in this case is considerably different from that observed in the previous experiment (S_R = 30). The XRD pattern recorded from the $BaSO_4$ crystals grown in the Hele-Shaw cell at an S_R of 30 in the presence of AOT shown in Fig.4.5 is displayed in Fig.4.8, curve 4. As in the case of barite crystals grown in the Hele-Shaw cell in the presence of StA, an intense (2 0 0) Bragg reflection is observed indicating that oriented growth of the barite crystals is a feature characteristic of nucleation and growth at an expanding liquid-liquid interface. The XRD pattern recorded from the $BaSO_4$ crystals grown in control experiment shown in Fig.4.6 is displayed as curve 5 in Fig.4.8. These barite crystals exhibited intense (2 1 1) Bragg reflections while the (2 0 0), (2 1 0) and (1 1 2) reflections were comparatively less intense. There are two important observations based on $BaSO_4$ crystal growth in solution and in the Hele-Shaw cell. The barite crystals that grow at the dynamic liquid-

liquid interface in the presence of StA and AOT are not only organized into quasi-linear superstructures (Figs.4.4A-C and Fig.4.5) but they also show preferred orientation along the (200) direction (Fig.4.8, curves 2 and 4). This preferred orientation is absent in the barite crystals grown in the Hele-Shaw cell in the presence of StA but at a higher S_R of 50 (Fig.4.8, curve 3) and in the crystals grown in the cell in the absence of a surfactant (Fig.4.8, curve 5). The absence of (200) orientation in the crystals grown in the presence of StA at an S_R of 50 can be rationalized in terms of the fact that at this supersaturation value, growth takes place predominantly in the bulk of the solution and not at the interface.

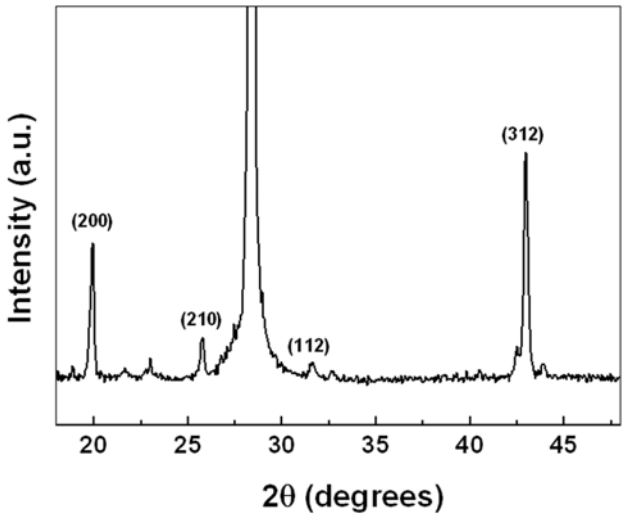

Fig.4.9: *XRD patterns recorded from $BaSO_4$ crystals grown at the static liquid-liquid interface with StA in the organic phase.*

The XRD pattern recorded from barite crystals grown at a static liquid-liquid interface in the presence of StA is shown in Fig.4.9. The (3 1 2) Bragg reflection is most intense in the XRD spectrum indicating that the flat rectangular $BaSO_4$ crystals are fortuitously oriented along this crystallographic direction. We did not see any significant difference in the XRD pattern for $BaSO_4$ grown at a static liquid-liquid interface in the presence of AOT compared to the StA experiment. The (2 0 0) Bragg reflection in the XRD pattern (Fig.4.9) is considerably less intense compared to that observed for barite crystals grown in the Hele-Shaw experiments. The Bragg reflection at $2\theta = 28.30^{o}$ is from the Si (111) substrate used in this particular experiment. The fact that oriented growth of the barite crystals occurs in the Hele-Shaw cell under conditions where crystal nucleation and growth occurred primarily at the interface indicates epitaxy between the

ordering surfactant monolayer at the interface and the (200) face of barite. The observation that preferential growth along the (200) plane occurs both in the case of StA and AOT is surprising given that the headgroup packing at the interface would be expected to be different in both cases.

4.3.3 Summary

$BaSO_4$ crystals grown at a steadily expanding liquid-liquid interface in a radial Hele-Shaw cell populated by stearate and AOT ions spontaneously organize themselves into highly linear superstructures over large length-scales. The barite crystals show growth along a preferred crystallographic direction suggesting epitaxy between the surfactant monolayer at the interface and the crystal. On the other hand barite crystals grown at a static liquid-liquid interface with suitable surfactants adsorbed at the interface resulted in the formation of individual flat rectangular barite crystals with no evidence of their assembly into extended dimensions, as observed in the Hele-Shaw experiments.

4.4 Crystallization of $SrCO_3$ at the liquid-liquid interface

The synthesis of $SrCO_3$ crystals was accomplished at the steadily expanding interface between two liquids (aqueous solution of $SrCl_2$ and Na_2CO_3 and chloroform solution containing StA/AOT) in radial Hele-Shaw set up. Spacers of size b = 300 and 400 μm were used between the top and bottom glass plates. The experiments were performed in salt solutions as the displaced fluid of S_R of ca. 30 (5 ml of 1 x 10^{-3} M aqueous $SrCl_2$ and 5 ml of 9.9 x 10^{-5} M aqueous Na_2CO_3) and ca. 50 (5 ml of 1 x 10^{-3} M aqueous $SrCl_2$ and 5 ml of 3 x 10^{-4} M aqueous Na_2CO_3). The experiments were performed at a constant volumetric flow rate (VFR) of chloroform into the aqueous phase (mixed aqueous solutions of $SrCl_2$ and Na_2CO_3) at 0.5 ml/min.

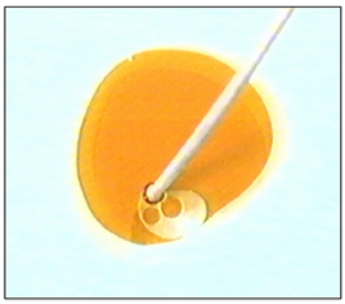

Fig.4.10: *Image of the viscous fingering pattern formed at a particular instant during injection of chloroform containing AOT (colored phase) into an aqueous solution of $SrCl_2$ and Na_2CO_3.*

Fig.4.10 shows a representative image recorded during injection of chloroform containing AOT into the electrolyte solution. The interface is observed to be extremely flat and uniform between the two liquids, with no evidence of finger formation in this case as well.

The growth of $SrCO_3$ crystals was also carried out at the static liquid-liquid interface between an aqueous solution of Sr^{2+} ions and organic solution containing surfactant molecules by reaction with sodium carbonate. The aqueous precipitates obtained in all the experiments were washed and placed on Si (111) and glass substrates for SEM, EDAX and XRD measurements.

4.4.1 SEM and EDAX measurements

4.4.1.1 $SrCO_3$ crystals grown at a dynamic charged liquid-liquid interface in the presence of AOT

SEM images at different magnifications of $SrCO_3$ crystals grown in the Hele-Shaw cell using AOT in the organic phase at an S_R of 30 with an S_P of 300 μm are shown in Figs.4.11A and B. The substrate was populated with dense assemblies of $SrCO_3$ needle-like crystallites (Fig.4.11A).

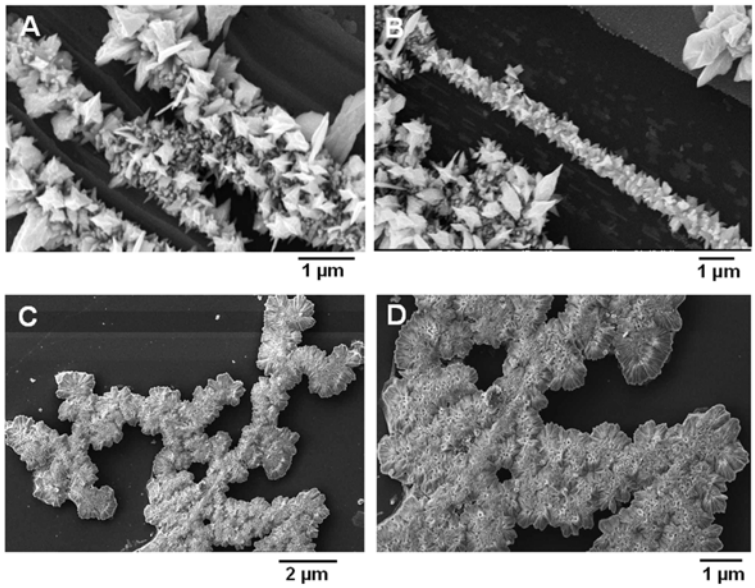

Fig.4.11: *A and B - Low and high magnification SEM images respectively of $SrCO_3$ crystals grown in the Hele-Shaw cell using AOT in the organic phase at an S_R of 30 and an S_P of 300 μm. C and D - Low and high magnification SEM images respectively of $SrCO_3$ crystals grown in the Hele-Shaw cell using AOT in the organic phase at an S_R of 50 and an S_P of 300 μm.*

EDAX analysis of the $SrCO_3$ assemblies yielded a Sr : C : O atomic ratio of 1 : 1.36 : 11. In addition to Sr, C, and O, the presence of Na and S signals was also observed in the EDAX spectrum, which is coming from the template AOT. It is observed that the dense assemblies are made up of sharp needle like strontianite crystallites (Fig.4.11B). The length of the $SrCO_3$ superstructures is in excess of 50 μm while the widths are typically in the range 0.5 – 1 μm. SEM pictures at different magnifications of $SrCO_3$ crystals grown in the Hele-Shaw cell using AOT in the organic phase at an S_R of 50 and S_P of 300 μm are shown in Figs.4.11C and D. Extremely flat strontianite assemblies are observed, spread all over substrate surface (Fig.4.11C). The strontianite assemblies in this case are made up of flat crystallites rather than the sharp needles that observed in case of S_R of 30 experiments. EDAX analysis of the structures shown in Figs.4.11C and D yielded a Sr : C : O atomic ratio is in fair agreement with the expected stoichiometry along with signals of Na and S coming from the AOT template.

In order to understand the role of plate separation in modulating the morphology of $SrCO_3$ crystals, crystal growth in the Hele-Shaw cell was attempted at an S_R of 30 with a higher plate separation of 400 μm. SEM pictures at different magnifications recorded from $SrCO_3$ crystals grown in the Hele-Shaw cell at an S_R of 30 and with an S_P of 400 μm are shown in Figs.4.12A and B.

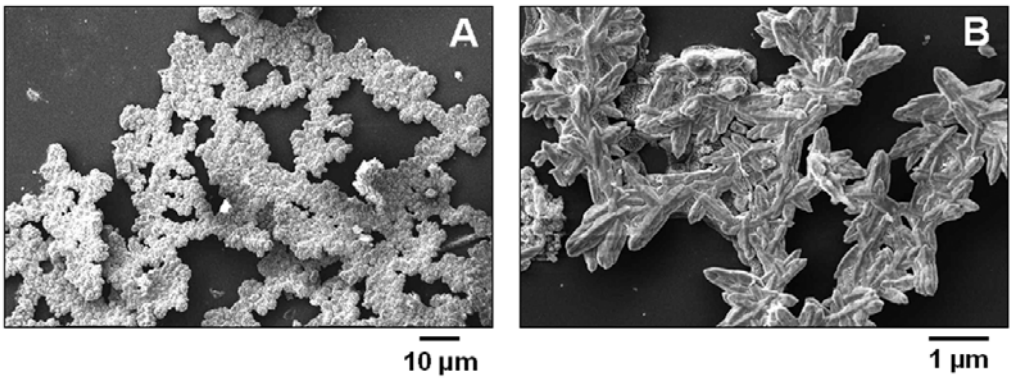

Fig.4.12: *A and B - Low and high magnification SEM images respectively of $SrCO_3$ crystals grown in the Hele-Shaw cell using AOT in the organic phase at an S_R of 30 with an S_P of 400 μm.*

Fig.4.12A shows higher order assembly of $SrCO_3$ crystals populating the substrate surface. EDAX analysis of the strontianite assemblies shown in Figs.4.12A and B yielded a Sr : C : O atomic ratio in fair agreement with the expected stoichiometry along with

signals of Na and S coming from the AOT template. At a higher magnification (Fig.4.12B), the strontianite assemblies are clearly observed to be made up of individual needle-like crystallites. As can be seen in these images, changing the plate separation from 300 to 400 μm lead to a significant change in morphology of individual $SrCO_3$ crystallites, which thereafter assembled at the expanding liquid-liquid interface. The individual strontianite needles in this case (Fig.4.12B) are not much sharper than those observed in the lower plate separation experiments (Fig.4.11B), clearly establishing the role of plate separation on the morphology of $SrCO_3$ crystals.

4.4.1.2 $SrCO_3$ crystals grown at a dynamic charged liquid-liquid interface in the presence of StA

In order to understand the role of the nature of the surfactant at the expanding liquid-liquid interface, $SrCO_3$ crystallization was carried out in the presence of the anionic surfactant stearic acid. SEM pictures at different magnifications of $SrCO_3$ crystals grown in the Hele-Shaw cell at an S_R of 30 and S_P of 300 μm with StA in the organic phase is shown in Figs.4.13A & B. Fig.4.13A clearly shows the formation of branched assembly of $SrCO_3$ crystals where the assembly is appear to be originated from a central nucleating point. The higher magnification SEM image (Fig.4.13B) shows the strontianite assembly in greater detail, which indicates the formation of very fine $SrCO_3$ fiber like structures. EDAX analysis of the $SrCO_3$ fine fibers yielded a Sr : C : O atomic ratio of 1 : 1.12 : 5.

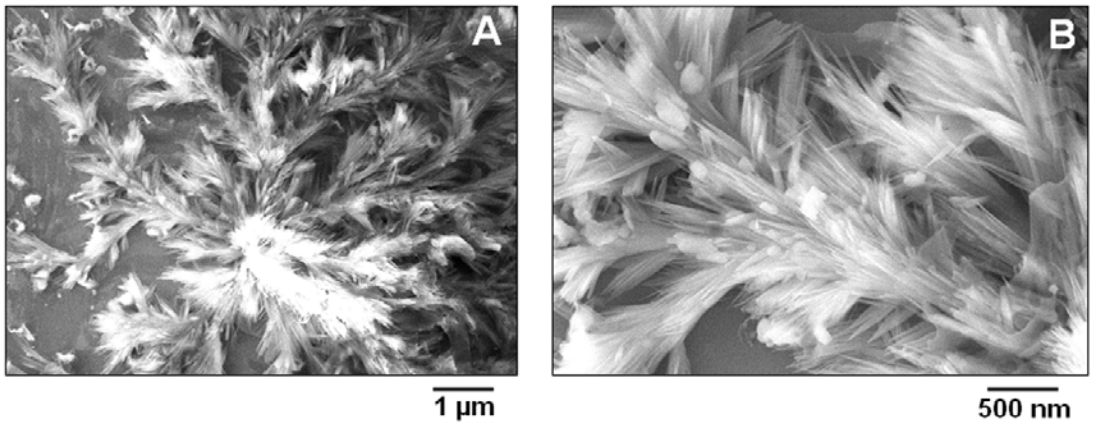

Fig.4.13: *A and B - Low and high magnification SEM images respectively of $SrCO_3$ crystals grown in the Hele-Shaw cell using StA in the organic phase at an S_R of 30 with an S_P of 300* μm.

4.4.1.3 $SrCO_3$ crystals grown at a static charged liquid-liquid interface

SEM images recorded at different magnifications of $SrCO_3$ crystals grown at the static liquid-liquid interface at an S_R of 30 with AOT molecules in the organic phase are shown in Fig.4.14. The low magnification SEM image in Fig.4.14A shows that the substrate is covered with a large density of needle like $SrCO_3$ crystals. Furthermore, on higher magnification it is observed that the individual needles possess $SrCO_3$ crystals with spherical crystallites arranged around central needles (Fig.4.14B).

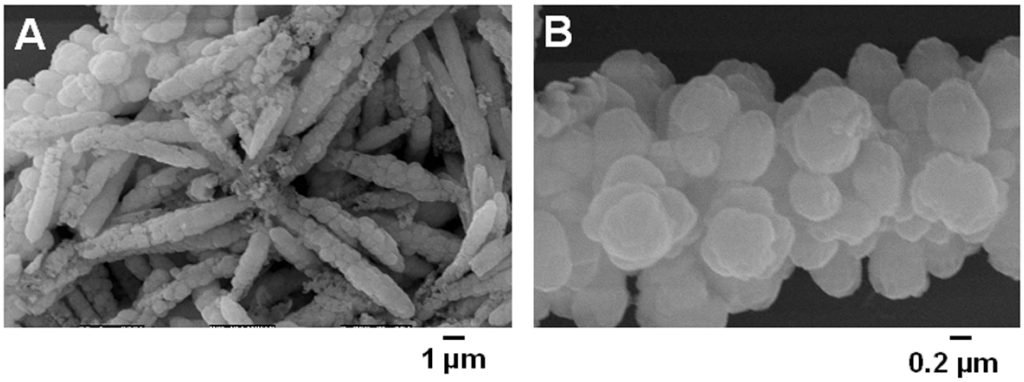

Fig.4.14: *A and B – SEM micrographs at different magnifications recorded from $SrCO_3$ crystals grown at the static liquid-liquid interface with surfactant (AOT) molecules in the organic phase.*

The strontianite needles grown appear to consist of aggregates of very uniform smaller spherical crystallites (Fig.4.14B) appeared to be due to secondary nucleation around the core needle structures.

4.4.2 X-ray diffraction studies

The XRD pattern recorded from the $SrCO_3$ crystals grown at an S_R of 30 and S_P of 300 µm is displayed as curve 1 in Fig.4.15. A number of Bragg reflections are identified and have been indexed with reference to the unit cell of the strontianite structure (a = 5.107 Å, b = 8.414 Å, c = 6.029 Å; space group *Pmcn*) [18]. The interesting feature of the diffraction pattern of the strontianite assemblies grown in the Hele-Shaw cell is the intense (1 1 1) (1 2 0) (2 4 1) Bragg reflections indicating oriented growth of the strontianite crystals along these crystallographic directions. The XRD pattern recorded from the $SrCO_3$ crystals grown at an S_R of 50 and S_P of 300 µm did not show any significant difference from that shown in curve 1. The XRD pattern recorded from the $SrCO_3$ crystals grown at an S_R of 30 and S_P of 400 µm is shown as curve 2 in

Fig.4.15. The (1 1 1) Bragg reflection is most intense in this case indicating oriented growth of the $SrCO_3$ crystals along this direction. The XRD pattern recorded from the $SrCO_3$ crystals grown in the Hele-Shaw cell at an S_R of 30 and S_P of 300 μm in the presence of StA shown in Fig.4.13 is displayed as curve 3 in Fig.4.15. As in the case of $SrCO_3$ crystals grown in the Hele-Shaw cell in the presence of AOT, an intense (1 1 1) Bragg reflection is observed in this case as well along with intense (1 3 0) and (2 2 1) reflections. The (1 1 1) Bragg reflection is observed in all the Hele-Shaw experiments indicating that the strontianite assembly preferably oriented along this crystallographic direction.

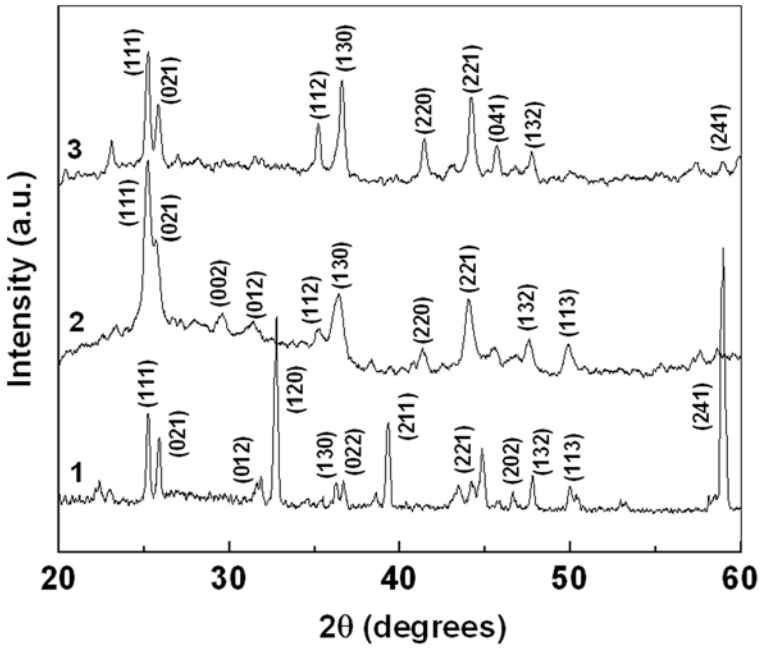

Fig.4.15: *XRD patterns recorded from $SrCO_3$ crystals synthesized in the radial Hele-Shaw cell in the presence of AOT. Curve 1: S_R of 30 with an S_P of 300 μm, Curve 2: S_R of 30 with an S_P of 400 μm, Curve 3: XRD pattern recorded from $SrCO_3$ crystals synthesized in the radial Hele-Shaw cell in the presence of StA with an S_R of 30 and an S_P of 300 μm.*

The XRD pattern recorded from $SrCO_3$ crystals grown at a static liquid-liquid interface is shown in Fig.4.16. The Bragg reflections in this spectrum could be indexed based on the strontianite structure with broader peaks indicating the formation of smaller crystallites. The (111) Bragg reflection is most intense in this case as well along with intense (012), (022) and (221) reflections.

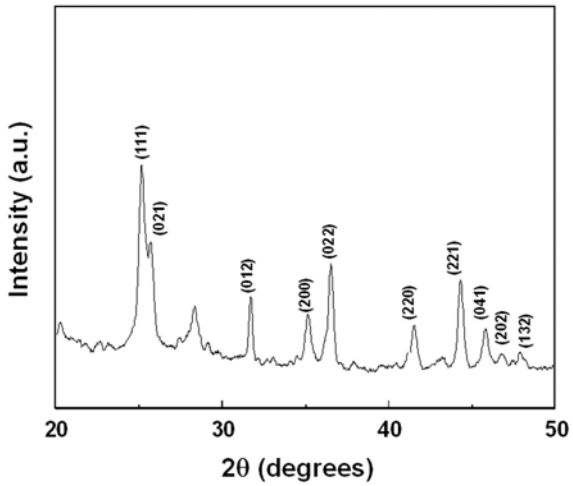

Fig.4.16: *XRD patterns recorded from $SrCO_3$ crystals grown at the static liquid-liquid interface with the surfactant in the organic phase.*

4.4.3 Summary

The morphology of the $SrCO_3$ crystals grown at the dynamic and static charged interfaces are completely different from each other clearly indicating the importance of the nature of the interface on strontianite crystal growth. $SrCO_3$ crystals grown at a steadily expanding liquid-liquid interface populated by StA and AOT molecules in a radial Hele-Shaw cell resulted in the assemblies of individual strontianite needles into higher order superstructures. Where as, $SrCO_3$ crystals grown at the static liquid-liquid interface with suitable surfactants adsorbed at the interface resulted in the formation of unusual strontianite needles with spherical aggregates, clearly establishing the role of a interface in directing the morphology and assembly of $SrCO_3$ crystals.

4.5 Crystallization of $CaCO_3$ at the liquid-liquid interface

The synthesis of calcium carbonate crystals in the Hele-Shaw cell was accomplished by the reaction of Ca^{2+} ions electrostatically complexed with AOT/StA ions pinned to the interface with carbonate ions present in the aqueous part of the biphasic reaction medium. The viscous fluid (mixed aqueous solution of $CaCl_2$ and Na_2CO_3) was taken in the cell gap and thereafter, chloroform containing AOT/StA (1 x 10^{-3} M) was injected through the hole of the top glass plate. Separate experiments were performed at salt solution S_R of 30 (10 ml of 1 x 10^{-2} M aqueous $CaCl_2$ and 10 ml of 1.368 x 10^{-3} M aqueous Na_2CO_3) and 50 (10 ml of 1 x 10^{-2} M aqueous $CaCl_2$ and 10 ml of 3.8 x 10^{-3} M aqueous Na_2CO_3) as the displaced fluid with S_P of 200, 300 and 400 μm

and VFR of 0.1 and 0.5 ml/min. The synthesis of $CaCO_3$ crystals was also carried out at a static liquid-liquid interface between an aqueous solution of Ca^{2+} ions and organic solutions containing AOT molecules by reaction with sodium carbonate at an S_R of 30. The crystals obtained in all the experiments were washed and placed on Si (111) and glass substrates for SEM, EDAX and XRD measurements.

Fig.4.17: *Image of the pattern formed at a particular instant during injection of chloroform containing AOT (colored phase) into an aqueous solution of $CaCl_2$ and Na_2CO_3 (transparent phase).*

Fig.4.17 shows a representative image recorded during injection of chloroform into the electrolyte solution. The interface between the two liquids is very uniform, with no evidence of finger formation. The relatively slow VFR coupled with the small difference in viscosities of the two fluids [13] is responsible for the smooth interface and thus provides a simplified model system for understanding the crystal growth process.

4.5.1 SEM and EDAX measurements

4.5.1.1 $CaCO_3$ crystals grown at a dynamic charged liquid-liquid interface in the presence of AOT

SEM images at different magnifications of $CaCO_3$ crystals grown in the Hele-Shaw cell at an S_R of 30 with an S_P of 300 μm are shown in Figs.4.18A and B. The substrate was densely populated with extremely thin $CaCO_3$ needle-like fibers (Fig.4.18A) arranged in the form of bundles. These fibers are similar to the aragonite fibers obtained by Ota *et al*. wherein crystallization of $CaCO_3$ was carried out in the presence of Mg^{2+} ions [19]. The higher magnification SEM image (Fig.4.18B) shows the $CaCO_3$ fibers in greater detail. The length of the $CaCO_3$ fibers is often in excess of 10 μm while the widths are typically in the range 0.1 – 0.5 μm. EDAX analysis of the $CaCO_3$ fibers yielded a Ca : C : O atomic ratio of 1 : 1.6 : 15. While the Ca : C ratio is in fair

agreement with the expected stoichiometry, excess oxygen may have been sampled from the silica overlayer on the Si (111) substrate. An important feature of our approach based on the Hele-Shaw cell is that we have been able to achieve aragonite growth at room temperature using AOT molecules bound to the expanding liquid-liquid interface. The $CaCO_3$ polymorph aragonite, is known to have very high mechanical strength and is metastable under ambient conditions [14a]. A classical example is that of nacre in which growth of plate-like aragonite crystals occur within a complex organic matrix [14a]. The laboratory synthesis of aragonite at room temperature has been very difficult to achieve without the use of soluble additives such as small organic molecules or Mg^{2+} ions [19,20] but has been achieved at slightly elevated temperatures.[19,21] with exception of the reports of Litvin *et al* [14a] and Heywood *et al* [22] where the formation of aragonite crystals at the air-water interface using compressed monolayers of 5-hexadecyloxyisophthalic acid[14a] and under monolayers of eicosanoic acid and n-eicosyl sulfate has been demonstrated.[22] Another important report on the room temperature synthesis of aragonite crystals is that of Falini *et al*. who have shown that this polymorph may be grown *in vitro* by treatment of layers of aragonite-associated glycoproteins assembled on β-chitin-silk fibroin substrates [23].

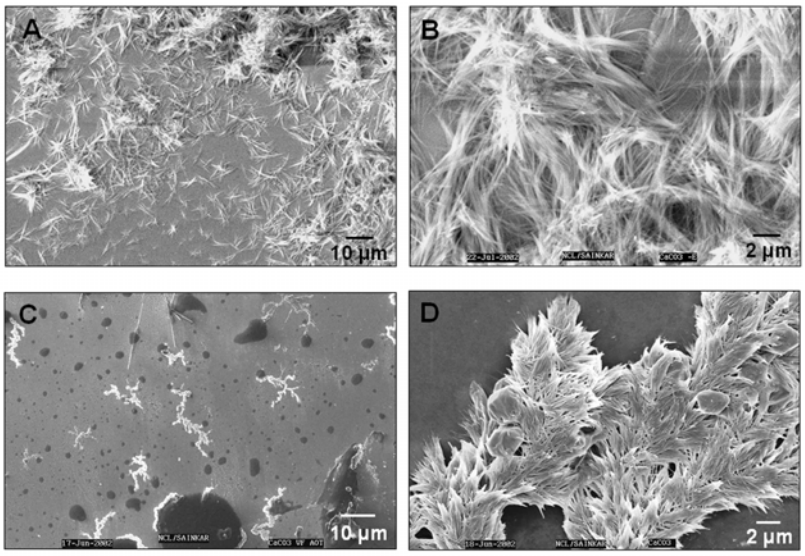

Fig.4.18: *A and B - Low and high magnification SEM images respectively of $CaCO_3$ crystals grown in the Hele-Shaw cell using AOT in the organic phase at an S_R of 30 and an S_P of 300 μm. C and D - Low and high magnification SEM images respectively of $CaCO_3$ crystals grown in the Hele-Shaw cell using AOT in the organic phase at an S_R of 50 and an S_P of 300 μm.*

SEM pictures at different magnifications of $CaCO_3$ crystals grown in the Hele-Shaw cell at an S_R of 50 and S_P of 300 μm are shown in Figs.4.18C and D. The substrate was populated with densely packed assemblies of $CaCO_3$ crystals in highly branched superstructures (Fig.4.18C). At higher magnification, the morphology and constitution of individual assemblies is clearly visible (Fig.4.18D). It is observed that the branched aggregates consist of fibrous crystallites assembled into tree-like superstructure. The $CaCO_3$ fibers appear to be thicker than in the lower S_R case (Fig.4.18B) and are in morphology characteristic of the aragonite polymorph [21a,19]. Some well-defined and fairly large (ca. 2.5 μm) rhombohedral crystals are also observed in Fig.4.18D which resemble the morphology normally obtained for the calcite polymorph [24]. EDAX analysis of the structures shown in Figs.4.18C and D yielded a Ca : C : O atomic ratio is in fair agreement with the expected stoichiometry.

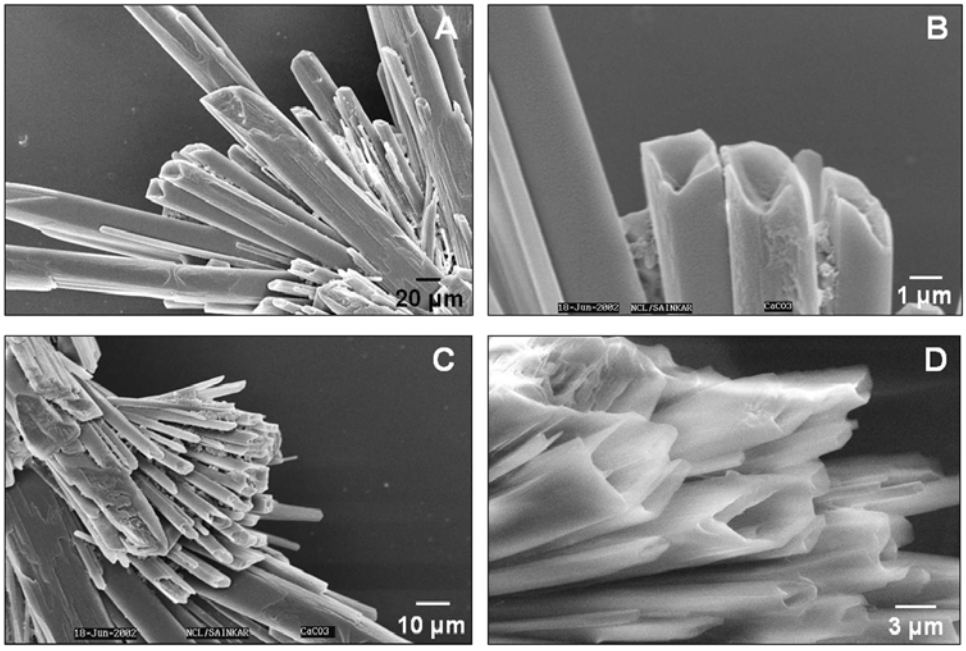

Fig.4.19: *A and B - Low and high magnification SEM images respectively of $CaCO_3$ crystals grown in the Hele-Shaw cell using AOT in the organic phase at an S_R of 30 with an S_P of 400 μm. C and D - Low and high magnification SEM images respectively of $CaCO_3$ crystals grown in the Hele-Shaw cell using AOT in the organic phase at an S_R of 50 with an S_P of 400 μm.*

In order to understand the role of plate separation in modulating the morphology of $CaCO_3$ crystals, crystal growth in the Hele-Shaw cell was attempted at the two different supersaturations of 30 and 50 but with a higher plate separation of 400 μm.

SEM pictures at different magnifications recorded from $CaCO_3$ crystals grown in the Hele-Shaw cell at an S_R of 30 and with an S_P of 400 μm are shown in Figs.4.19A and B. Fig.4.19A shows quasi-linear assembly of $CaCO_3$ crystals in the form of elongated needles. The length of the $CaCO_3$ needles is in excess of 400-500 μm while the widths are typically in the range 4-10 μm. At higher magnification, the SEM image of the linear assemblies shows that are actually hollow cylindrical structures with a rhombic cross-section. SEM pictures at different magnifications of $CaCO_3$ crystals grown in the Hele-Shaw cell at an S_R of 50 and an S_P of 400 are shown in Figs.4.19C & D. As can be seen in these images, changing the S_R value from 30 to 50 while maintaining the plate separation at 400 μm does not lead to a significant change in morphology of the $CaCO_3$ crystals. Fig.4.19C shows bundles of hollow cylinders of $CaCO_3$ crystals apparently branching out from a central point. At higher magnification, the cross-section of the hollow $CaCO_3$ cylinders is more clearly seen (width of cylinders is ~ 9-10 μm with internal dimensions of ~ 6-7 μm). EDAX analysis of the $CaCO_3$ crystals yielded Ca : C : O atomic ratio is in fair agreement with the expected stoichiometry.

4.5.1.2. $CaCO_3$ crystals grown at a dynamic charged liquid-liquid interface in the presence of StA

There are two factors that appear to control the morphology and crystallography of the $CaCO_3$ crystals grown in the Hele-Shaw cell, that is the nature of the surfactant at the expanding liquid-liquid interface and as mentioned above, the plate separation. The role of the surfactant may be determined by carrying out $CaCO_3$ crystallization in the presence of the anionic surfactant stearic acid.

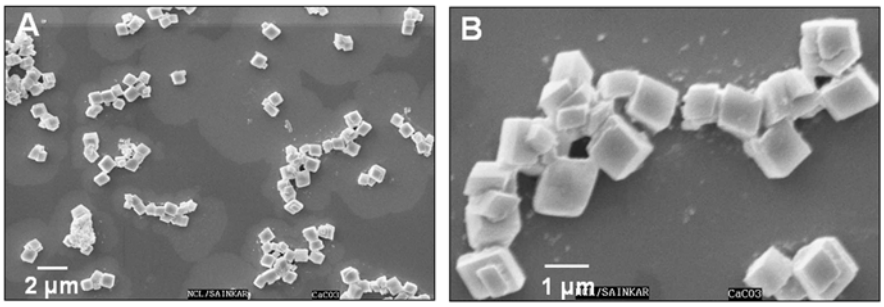

Fig.4.20: *A and B - Low and high magnification SEM images respectively of $CaCO_3$ crystals grown in the Hele-Shaw cell using StA in the organic phase at an S_R of 30 with an S_P of 300 μm.*

SEM pictures at different magnifications of $CaCO_3$ crystals grown in the Hele-Shaw cell at an S_R of 30 and S_P of 300 μm with StA in the organic phase are shown in Figs.4.20A and B. Fig.4.20A clearly shows formation of rhombohedral calcite crystals. The higher magnification SEM image (Fig.4.20B) shows the rhombohedral calcite crystals in greater detail with indications of some kind of assembly of the calcite crystals.

4.5.1.3. $CaCO_3$ crystals grown at a dynamic charged liquid-liquid interface in control experiments

Increasing the plate separation from 300 to 400 μm while maintaining the volumetric flow rate and other conditions constant essentially means that the liquid-liquid interface expands less rapidly in the higher plate separation experiment. As described earlier, the formation of hollow cylindrical crystals at higher plate separations consisting of both aragonite and calcite polymorphs may be due to dissolution of the aragonite phase and recrystallization into the calcite phase. This process would presumably be more facile if the time available for the recrystallization to occur at the liquid-liquid interface was enhanced as occurs by increasing the plate separation. By the same token, reducing the plate separation under constant VFR should lead to stabilization of the aragonite phase. Fig.4.26A shows a representative SEM picture of $CaCO_3$ crystals grown at an S_R of 30, S_P of 200 μm and VFR of 0.5 ml/min. It is seen that the crystals form as dense bundles of whiskers characteristic of aragonite crystals (Fig.4.26A).

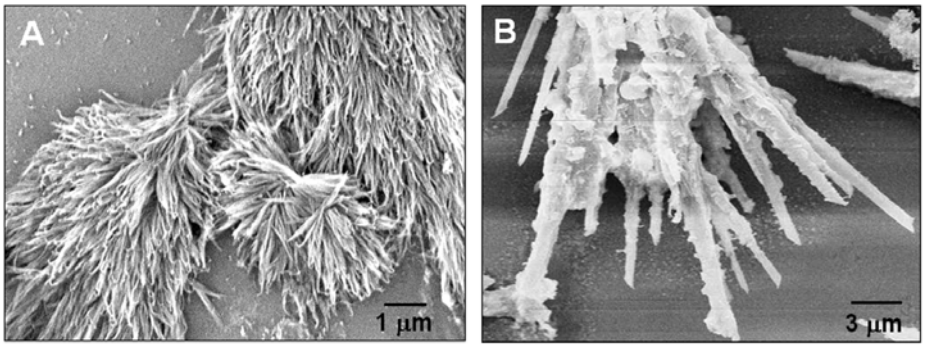

Fig.4.21: *SEM images respectively of $CaCO_3$ crystals grown in the Hele-Shaw cell. A) at an S_R of 30, an S_P of 200 μm and VFR of 0.5 ml/min, B) at an S_R of 30, an S_P of 200 μm and VFR of 0.1 ml/min.*

Another control experiment was performed wherein $CaCO_3$ crystallization was carried out at an S_R = 30, S_P = 200 μm but the VFR was reduced by 80 % to 0.1 ml/min. Fig.4.21B shows a representative SEM picture of the $CaCO_3$ crystals obtained in this

experiment. While hollow cylinders are not observed in this case, the crystals are elongated and rather thick, unlike the whisker-like morphology observed in the higher VFR experiment (Fig.4.21A). The organization of the linear structures is similar to that observed in the experiments carried out at higher plate separations (Fig.4.19A). The surface of the linear structures is covered with what appear to be small, secondary nuclei. It is possible that under these slow interfacial expansion conditions, the aragonite crystals dissolve and recrystallize as calcite secondary nuclei.

4.5.1.4 $CaCO_3$ crystals grown at a static charged liquid-liquid interface

SEM images recorded at different magnifications of $CaCO_3$ crystals grown at the static liquid-liquid interface with AOT molecules in the organic phase are shown in Fig.4.22. The low magnification SEM image in Fig.4.22A shows a number of $CaCO_3$ crystallites of flat disc-like morphology with regular uneven edges on their surface. Such morphology of $CaCO_3$ crystals is indicative of the formation of the highly unstable vaterite polymorph [23]. The higher magnification SEM image (Fig.4.22B) of the disc shaped $CaCO_3$ crystallites clearly show the structure in greater details with the evidence of the presence of some rhombohedral $CaCO_3$ crystallites indicative of calcite polymorph.

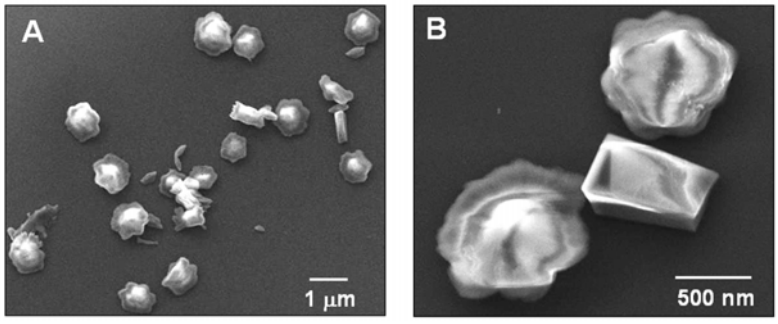

Fig.4.22: *A and B – SEM micrographs at different magnifications recorded from $CaCO_3$ crystals grown at the static liquid-liquid interface with surfactant molecules in the organic phase.*

4.5.2 X-ray diffraction studies

The XRD pattern recorded from the $CaCO_3$ crystals grown in the Hele-Shaw cell at an S_R of 30 with an S_P of 300 μm shown in Fig.4.18A, is displayed as curve 3 in Fig.4.23. For comparison, the simulated powder XRD patterns of calcite (curve 1, a = b = 4.989 Å, c = 17.062 Å, space group $D^6_{3D} – R3^*c$) [25] and aragonite crystals (curve 2, a =

4.959 Å, b = 7.968 Å, c = 5.741 Å; space group *Pmcn*) [19,26] are shown in the figure and have been used to identify the different crystallographic phases of $CaCO_3$ obtained in this study (Bragg reflections identified by 'A' for aragonite and 'C' for calcite). It is observed that the $CaCO_3$ crystals in this experiment consist of a mixed phase of aragonite and calcite with aragonite being the dominant phase. The XRD data thus provides clear support for the morphology of the $CaCO_3$ crystals seen in the SEM images (Fig.4.18A & B) – such well-defined needles are known to be characteristic of the aragonite polymorph [19,21]. The XRD pattern recorded from $CaCO_3$ crystals grown in the Hele-Shaw cell at an S_R of 50 and S_P of 300 μm shown in Figs.4.18C and D is shown as curve 4 in Fig.4.23. The XRD data clearly shows that the crystals formed in this experiment consist of a mixed phase of the calcite and aragonite crystallographic structures. Thus, the rhombohedral structures seen in Fig.4.18D are now unambiguously identified as calcite crystals while the fibrous assemblies in which calcite is embedded is the aragonite phase.

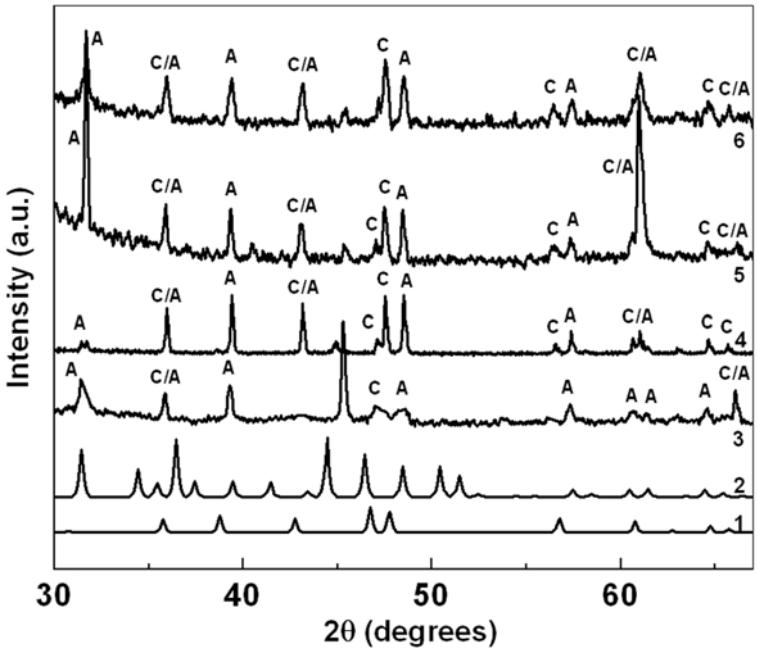

Fig.4.23: *Curve 1 : simulated powder XRD pattern of calcite crystals, Curve 2 : simulated powder XRD pattern of aragonite crystals. XRD patterns recorded from $CaCO_3$ crystals synthesized in the radial Hele-Shaw cell. Curve 3: S_R of 30 with an S_P of 300 μm, Curve 4: S_R of 50 with an S_P of 300 μm, Curve 5: S_R of 30 with an S_P of 400 μm, Curve 6: S_R of 50 with an S_P of 400 μm (A – stands for aragonite and C – stands for calcite).*

The XRD patterns recorded from the $CaCO_3$ crystals grown in the Hele-Shaw cell at an S_R of 30 and with an S_P of 400 μm and S_R of 50 and with an S_P of 400 μm shown in

Figs.4.19 are shown as curves 5 and 6 in Fig.4.23 and in both cases, the diffraction pattern is fairly similar. The XRD data thus shows the formation of a mixed phase of calcite and aragonite crystallographic structures. It is thus possible that the cylindrical structures of rhombic cross-section observed in Fig.4.19 are composites of aragonite needles that are in the process of dissolution at the interface between chloroform and water and recrystallization into the calcite polymorph. Apparently, this process of assembly of aragonite crystals, dissolution and recrystallization is favored at higher plate separations. In the case of the $CaCO_3$ crystals grown at an S_R of 30 and S_P of 400 μm (Figs.4.19A and B), the (002) and (214) Bragg reflections of aragonite and calcite respectively (Fig.4.23, curve 5) are quite intense relative to the other reflections indicating oriented growth of these two polymorphs along these directions.

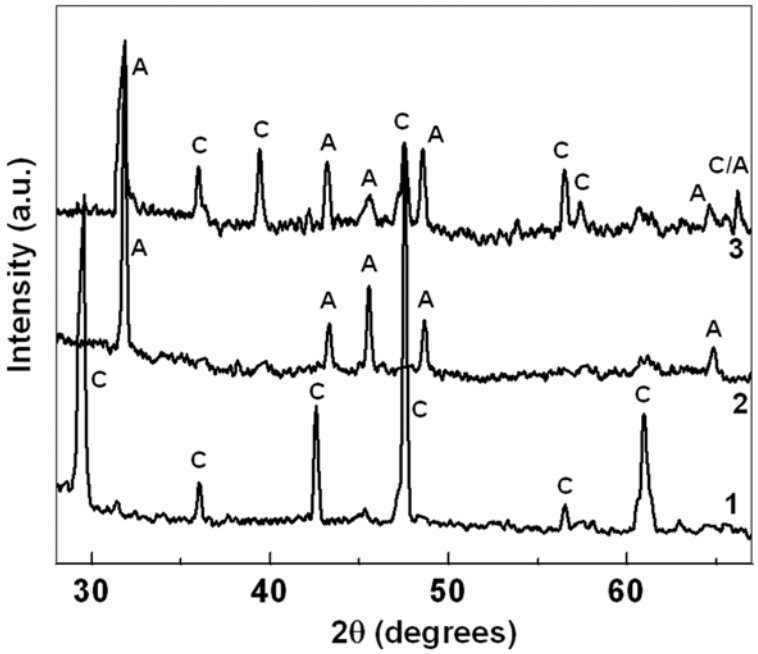

Fig.4.24: *Curve 1 : XRD pattern recorded from $CaCO_3$ crystals synthesized in the radial Hele-Shaw cell using stearic acid at an S_R of 30 with an S_P of 300 μm. Curve 2 & 3 : XRD pattern recorded from $CaCO_3$ crystals synthesized in the radial Hele-Shaw cell using AOT at an S_R of 30, S_P of 200 μm and VFR of 0.5 ml/min (curve 1), at an S_R of 30, S_P of 200 μm and VFR of 0.1 ml/min (curve 2).*

The XRD data recorded from $CaCO_3$ crystals grown in the Hele-Shaw cell at an S_R of 30 and S_P of 300 μm with StA in the organic phase shown in Figs.4.20A and B is shown as curve 1 in Fig.4.24. The Bragg reflections correspond to the calcite polymorph and have been indexed accordingly. There is no indication of aragonite formation in this

experiment. This clearly establishes the important role played by AOT in stabilizing the aragonite phase in the Hele-Shaw experiments as described above.

The XRD pattern recorded from $CaCO_3$ crystals grown at an S_R of 30, S_P of 200 μm and VFR of 0.5 ml/min is shown as curve 2 in Fig.4.24. The Bragg reflections could be indexed on the basis of the aragonite structure with no evidence of peaks corresponding to calcite. While the morphology of the $CaCO_3$ crystals obtained in the S_R = 30, VFR = 0.5 ml/min and S_P = 200/300 μm experiments is roughly the same (compare Figs.4.18A,B with Fig.4.21A), it is observed that recrystallization of the aragonite phase to calcite is reduced when the expansion rate of the liquid-liquid interface is enhanced (lower plate separation). The XRD pattern recorded from $CaCO_3$ crystals grown in a control experiment which was performed at an S_R = 30, S_P = 200 μm but at VFR that was reduced by 80 % to 0.1 ml/min. showed the presence of Bragg reflections characteristic of both the aragonite and calcite polymorphs (curve 3, Fig.4.24).

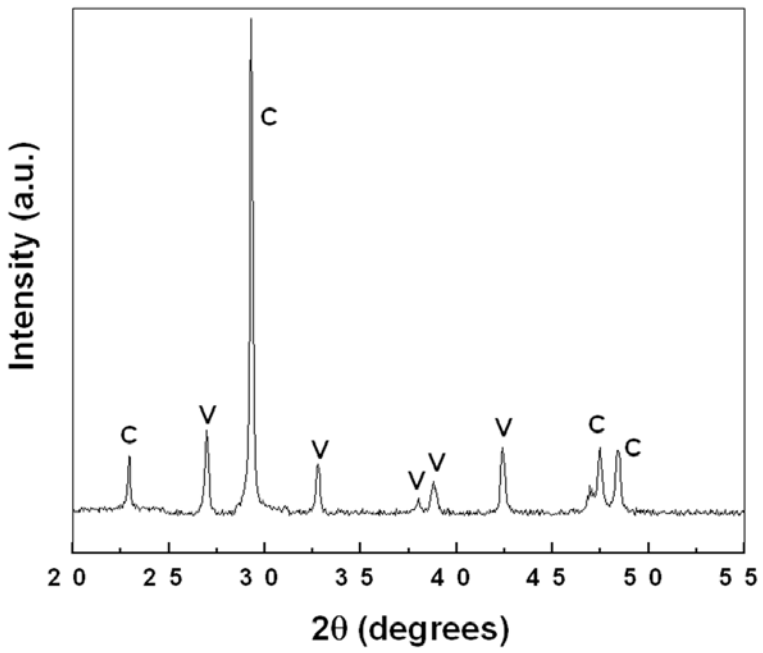

Fig.4.25: *XRD pattern recorded from $CaCO_3$ crystals grown at the static liquid-liquid interface with the surfactant in the organic phase.*

The XRD pattern recorded from $CaCO_3$ crystals grown at a static liquid-liquid interface in the presence of AOT shown in Fig.4.22 is displayed in Fig.4.25. As evident from the SEM results (Fig.4.22), a number of Bragg reflections are observed in the XRD

spectrum and could be indexed with the reference to the unit cell of the calcite and vaterite structures [23,25]. The XRD result clearly indicates the formation of a mixed polymorph of calcite and vaterite. Thus, the disc-shaped structures seen in Fig.22 are now unambiguously identified as vaterite crystals while the rhombohedral structures correspond to the calcite phase.

4.5.3 Summary

The room temperature synthesis of almost phase-pure aragonite needles in a radial Hele-Shaw cell has been achieved. The selection of this polymorph for growth at the interface has been shown to be due to AOT molecules present in the organic phase. By judicious choice of the experimental parameters in the Hele-Shaw cell, it is possible to control the degree of recrystallization of aragonite to calcite and thus, obtain crystals with hollow, cylindrical morphology.

4.6 Role of viscosity on the crystallization of $CaCO_3$ at the dynamic charged liquid- liquid interface

In this part of the study, we investigate the role of viscosity of the displaced phase in modulating the morphology of $CaCO_3$ crystals grown at the dynamic liquid-liquid interface. The $CaCO_3$ crystals are grown by reaction of an injected aqueous solution of $CaCO_3$ into a viscous chloroform-paraffin mixture containing the surfactant AOT. The viscous fluid [mixture of a solution of chloroform containing AOT (1×10^{-3} M) and paraffin] was taken in the cell gap and thereafter, an aqueous solution containing $CaCl_2$ and Na_2CO_3 at salt solution supersaturation (S_R) of 30 (10 ml of 1×10^{-2} M aqueous $CaCl_2$ and 10 ml of 1.36×10^{-3} M aqueous Na_2CO_3) was injected through the hole of the top glass plate. Experiments were performed at five different solution viscosities by varying the AOT-chloroform solution : paraffin ratios of 4 : 1 (viscosity, $\eta = 0.002678$ Pa-s), 1.5 : 1 ($\eta = 0.003434$ Pa-s), 1 : 1 ($\eta = 0.00412$ Pa-s), 1 : 1.5 ($\eta = 0.00488$ Pa-s) and 1 : 4 ($\eta = 0.046$ Pa-s) as the displaced fluid at a constant plate separation (S_P) of 300 μm. The aqueous $CaCO_3$ precipitate obtained was washed with copious amounts of double distilled water and placed on Si (111) wafers and on glass substrates for SEM, EDAX, FTIR and XRD analysis.

4.6.1 Viscous fingering patterns formed during $CaCO_3$ crystallization

Fig.4.26, clips 1-9 shows the evolution of the finger patterns with time recorded in the Hele-Shaw cell during the injection of an aqueous solution of $CaCl_2$ and Na_2CO_3 into the AOT-chloroform-paraffin mixture (η = 0.046 Pa-s).

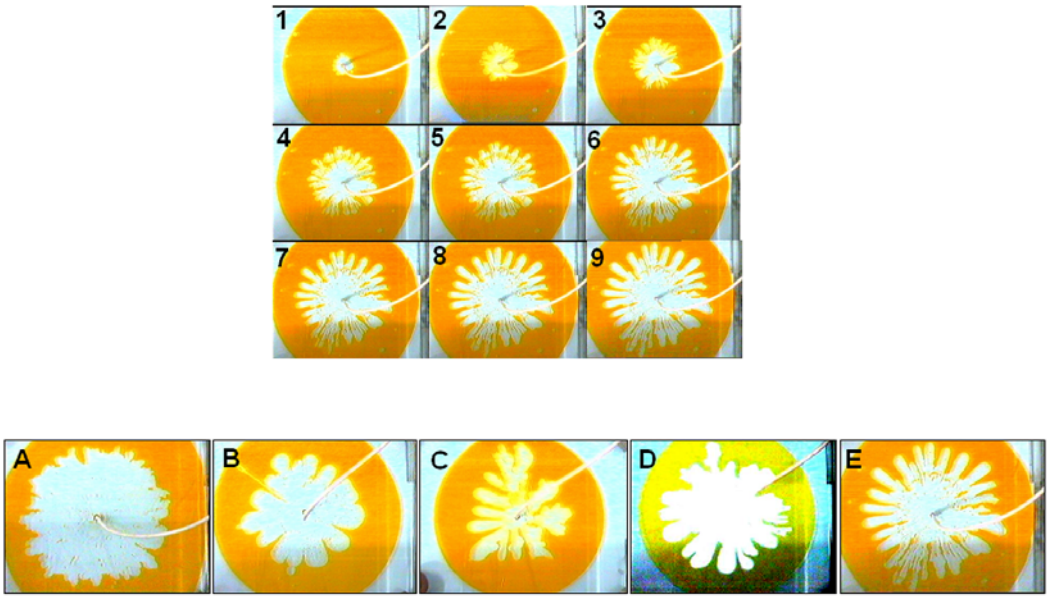

Fig.4.26: *Images (1-9) of the patterns recorded at different times during injection of aqueous solution of $CaCl_2$ and Na_2CO_3 (transparent phase) into the AOT-chloroform-paraffin solution (colored phase). (A – E) Images of the patterns formed at the end of injection of aqueous solution of $CaCl_2$ and Na_2CO_3 (transparent phase) into the AOT-chloroform-paraffin phase of different viscosities : A - 0.002678 Pa-s; B - 0.003434 Pa-s, C - 0.00412 Pa-s D - 0.00488 and E - 0.046 Pa-s.*

As can be seen in the clips 1-9 in Fig.4.26, the viscous fingering pattern evolves as the injection of the aqueous phase into the organic phase proceeds (time of injection increasing from 1-9). At completion of the injection, the highly branched viscous fingering pattern is clearly seen. The flow rate was decided based upon the induction time observed for initiation of crystal nucleation. The slow VFR coupled with the difference in viscosities of the two fluids [13b] is responsible for the complex, branched interface and thus provides a model system for understanding crystal growth processes at such dynamic liquid-liquid interfaces. The viscous fingering patterns obtained in separate experiments where the viscosity of the organic phase was varied is shown in Figs.4.26A – E [η = 0.002678 Pa-s (A); 0.003434 Pa-s (B); 0.00412 Pa-S (C); 0.00488 Pa-s (D) and 0.046 Pa-s (E)]. One can clearly notice the significant variation in the morphologies of

the branched patterns for the different viscosities of the displaced fluid used. As the viscosity increases, the morphology of the patterns become progressively more branched (Figs.4.26A – E).

The fractal dimensions of the patterns have been determined for the different viscosities used and are listed in Table 1. It is observed that there is an increase in the fractal dimensions (Table 1) on increasing the viscosity of the displaced organic phase supporting the increase in the complexity of the patterns observed (Figs.4.26A – E).

Obs No.	**Mixture of Chloroform: Paraffin**	**Viscosity (Pa S)**	**Fractal dimension (FD)**	**Morphology of $CaCO_3$ crystals formed**
1	4 : 1	0.002678	1.88 (+/- 0.03)	Flower like calcite with two/four petals
2	1.5 : 1	0.003434	1.91 (+/- 0.01)	Flower like calcite as well as patterned structures
3	1 : 1	0.00412	1.94 (+/- 0.01)	Patterned calcite with regular steps
4	1 : 1.5	0.00488	1.97 (+/- 0.02)	Patterned calcite with smaller and sharper crystallites
5	1 : 4	0.046	1.99 (+/- 0.01)	Patterned calcite assemblies

Table1: *Details of the fractal dimensions of the finger patterns, viscosity of the organic phase and observed morphology of $CaCO_3$ crystals in the Hele-Shaw cell experiments.*

4.6.2 Scanning electron microscopy studies

Representative SEM images at different magnifications of the $CaCO_3$ crystals grown in the Hele-Shaw cell during displacement of the AOT-chloroform-paraffin organic phase (η = 0.002678 Pa-s) by an aqueous solution of $CaCl_2$ and Na_2CO_3 at an S_R of 30 are shown in Figs.4.27A and B. The substrate was densely populated with flower like $CaCO_3$ crystals (Fig.4.27A). The inset of Fig.4.27A shows a magnified view of a few of the crystallites in greater detail showing that most of the flower-like $CaCO_3$ crystals

consist of either four or six petals and that the petals originate from a central point. Fig.4.27B shows the flower-like $CaCO_3$ crystals consisting of six petals in finer detail. The petals of the $CaCO_3$ crystals appear to be extremely thin and flat. The inset of Fig. 4.27B clearly shows the flatness of the $CaCO_3$ crystals. The length of the $CaCO_3$ petals in the flower-like assemblies is in the range of 300 – 600 nm while the widths are typically in the range of 200 – 300 nm. From the SEM images, we are unable to estimate the thickness of the $CaCO_3$ petals.

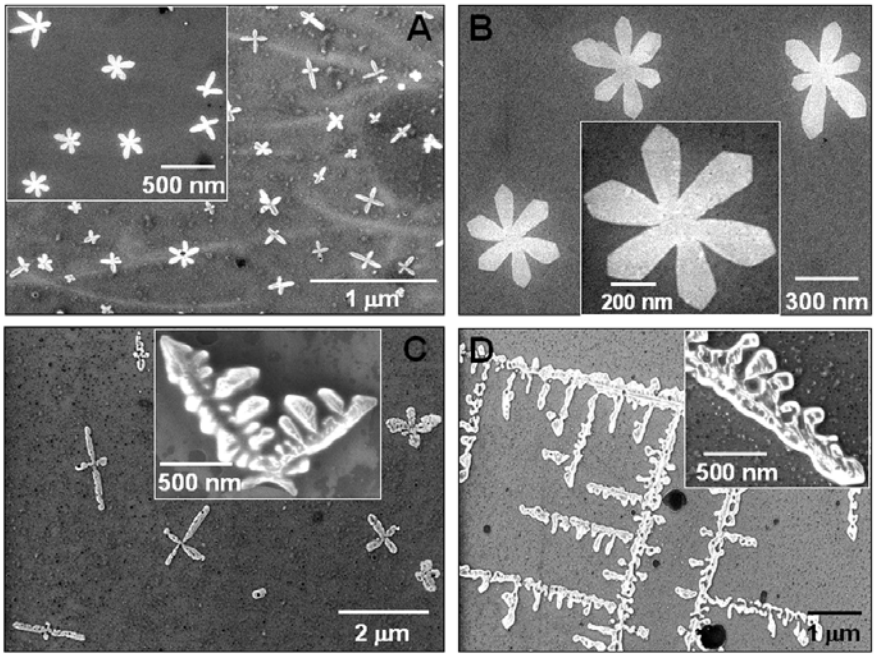

Fig.4.27: *(A and B) – Low and high magnification SEM images respectively of $CaCO_3$ crystals grown in the Hele-Shaw cell with an organic phase viscosity of 0.002678 Pa-s. (C and D) – Low and high magnification SEM images respectively of $CaCO_3$ crystals grown in the Hele-Shaw cell with an organic phase viscosity of 0.003434 Pa-s. The insets in the all the figures show magnified views of representative $CaCO_3$ crystals in the main part of the figure.*

Figs.4.27C and D show SEM images at different magnifications of $CaCO_3$ crystals grown in the Hele-Shaw cell during the displacement of AOT-chloroform-paraffin organic solution (η = 0.003434 Pa-s) by an aqueous solution of $CaCl_2$ and Na_2CO_3 at an S_R of 30. In this experiment we observe both $CaCO_3$ crystals with flower-like morphology (Fig.4.27C) as well as more extended, quasi-linear superstructures of $CaCO_3$ crystals (Fig. 4.27D). The $CaCO_3$ flowers shown at the lower magnification (Fig. 4.27C) appear on a gross scale to be quite similar to those obtained in the lower viscosity experiment (Fig. 4.27A). At higher magnification, however (inset of Fig. 4.27C)

differences are observed. The petals in the $CaCO_3$ flowers are not smooth and flat as in the earlier experiment. Furthermore, the presence of the highly branched linear structures of the crystals appears to be related to an increase in viscosity of the displaced fluid which, as seen in the images of the patterns formed for different viscosities of the organic phase (Figs.4.26 A-E), can be correlated with increasing complexity of the viscous-fingering patterns during the injection process. The inset in Fig. 4.27D shows a high magnification SEM image of a particular region of the quasi-linear $CaCO_3$ crystals clearly revealing the branched nature of the $CaCO_3$ structures.

Figs.4.28A and B show SEM images at different magnification of $CaCO_3$ crystals grown in the Hele-Shaw cell during the displacement of AOT-chloroform-paraffin (η= 0.00412 Pa-s) by an aqueous solution of $CaCl_2$ and Na_2CO_3 at an S_R of 30.

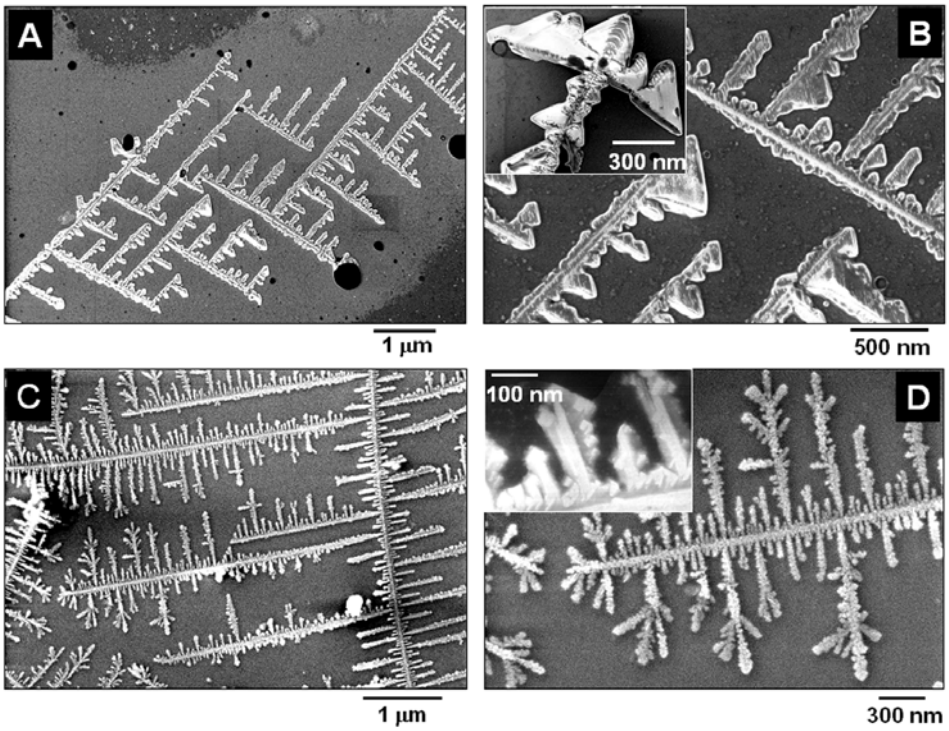

Fig.4.28: *(A and B) – Low and high magnification SEM images respectively of $CaCO_3$ crystals grown in the Hele-Shaw cell with an organic phase viscosity of 0.00412 Pa-s. (C and D) – Low and high magnification SEM images respectively of $CaCO_3$ crystals grown in the Hele-Shaw cell with an organic phase viscosity of 0.00488 Pa-s. The insets in B and D show magnified view of representative crystals shown in the main part of the figure.*

In gross detail, the $CaCO_3$ structures that are formed are similar to those synthesized in the Hele-Shaw cell at an organic solution viscosity of 0.003434 Pa-s. The $CaCO_3$ crystals in this experiment exhibit a highly branched morphology, with evidence of secondary

nucleation and growth around a linear 'core' (Fig. 4.28A). The higher magnification SEM image (Fig. 4.28B) shows that the edges of the $CaCO_3$ crystals are very sharp with steps observed regularly on the $CaCO_3$ super structures (inset of Fig. 4.28B). Similar steps have been observed previously on calcite crystals [27,28]. Orme *et al* have observed such steps in calcite crystals where they have found that site-specific binding of amino acid residues to surface steps changes the step-edge free energies, thereby giving rise to modifications that propagate from atomic length scales to macroscopic length scales [27]. Sugawara *et al* have succeeded in preparing periodically patterned $CaCO_3$ films with regular surface relief structures on a thin matrix of cholesterol-modified pullulan (soft gel matrix) from an aqueous solution containing poly(acrylic acid) [28].

Figs.4.28C and D show SEM images of $CaCO_3$ crystals grown in the Hele-Shaw cell during the displacement of AOT-chloroform-paraffin (η = 0.00488 Pa-s) by an aqueous solution of $CaCl_2$ and Na_2CO_3 under conditions identical to the other experiments. In keeping with the trend, an increase in viscosity leads to an enhancement of the branched calcite structures, as observed in Fig.4.28C. The individual crystallites in the branched assemblies are thinner and finer than those observed in the lower viscosity experiments. There also appears to be more secondary crystal growth on both sides of the linear axis. The higher magnification SEM image (inset of Fig.4.28D) clearly shows that the branches are in turn made up of smaller crystallites with sharp edges.

At the highest viscosity studied (η = 0.046 Pa-s), the fingers formed in the radial Hele-Shaw cell are at their narrowest (Fig.4.26E) and the corresponding fractal dimension is the highest (Table1). Figs.4.29A – D show SEM images at different magnification of $CaCO_3$ crystals grown in the Hele-Shaw cell involving the experiment in the organic phase being of this viscosity. The increase in complexity of the finger patterns seen in Fig.4.26E has clearly translated into the formation of quasi-linear, patterned assemblies of $CaCO_3$ crystals of very large length scales (Figs. 4.29A and B) densely populating the substrate surface. In some regions, the growth of the calcite crystals is very irregular (Fig. 4.29C). The higher magnification SEM image of one of the ordered assemblies (Fig. 4.29D) clearly shows that the $CaCO_3$ crystals are in fact assemblies of smaller $CaCO_3$ crystallites and also that in this case, growth of the secondary crystals proceeds out of the plane of the substrate as well (inset, Fig. 4.29D).

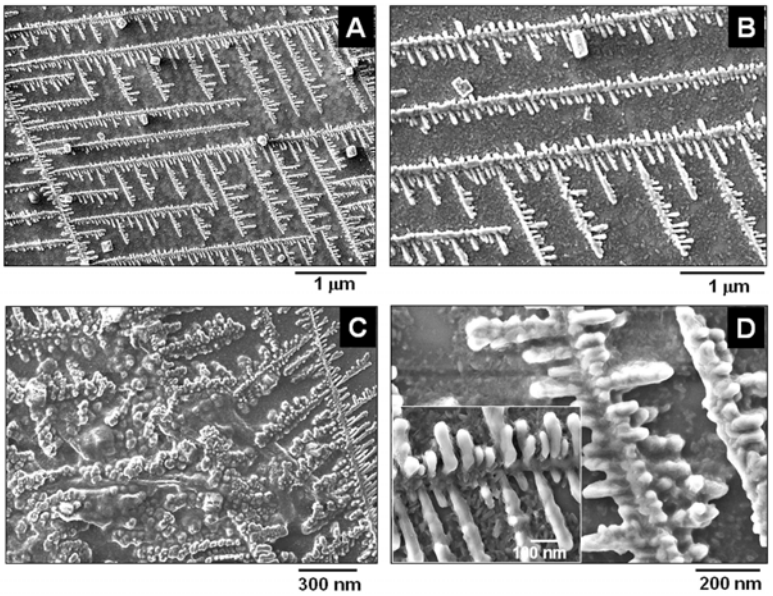

Fig.4.29: *(A – D) SEM images of $CaCO_3$ crystals at different magnifications, grown in the Hele-Shaw cell with an organic phase viscosity of 0.046 Pa-s. The inset in D shows a magnified view of the main image with a scale bar of 100 nm.*

4.6.3 Energy dispersive analysis of X-rays studies

The EDAX measurements of the $CaCO_3$ crystals grown at the dynamic liquid-liquid interface at different viscosities are shown in Fig.4.30.

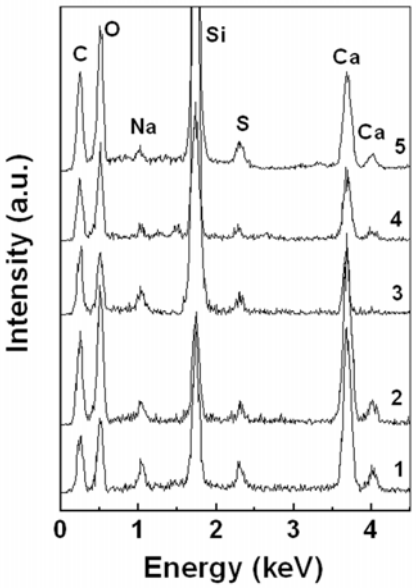

Fig.4.30 : *Spot-profile EDAX spectra recorded from the films of $CaCO_3$ crystals grown in the Hele-Shaw cell with organic phase viscosities of 0.002678 Pa-s (curve 1); 0.003434 Pa-s (curve 2); 0.00412 Pa-s (curve 3); 0.00488 Pa-s (curve 4) and 0.046 Pa-s (curve 5).*

EDAX analysis of the $CaCO_3$ crystals obtained in different viscosity experiments yielded a Ca : C : O atomic ratio close to the expected stoichiometric ratios. Along with expected Ca, C and O, strong signals of Na and S components from the surfactant AOT are observed indicating the surface binding of the AOT molecules to the $CaCO_3$ crystallites.

4.6.4 Fourier transform infrared spectroscopy measurements

The FTIR measurements of the $CaCO_3$ crystals grown at the dynamic liquid-liquid interface at different viscosities are shown as curves 1-5 in Fig.4.31. The FTIR spectra recorded from the $CaCO_3$ crystals obtained in different viscosity experiments showed absorption bands at 712 and 872 cm^{-1}, which are characteristic of calcite [23]. In addition to absorption bands for calcite, prominent absorption bands are seen at 1056, 1700, 2850 and 2950 cm^{-1}. The band at 1056 cm^{-1} is assigned to the S=O stretching vibration of the sulfonate group present in the surface-bound AOT molecules [29]. The band at 1700 cm^{-1} is due to carbonyl stretch vibrations in the AOT molecules and the two bands at 2850 and 2950 cm^{-1} have been assigned to the methylene symmetric and antisymmetric stretching vibrations in the hydrocarbon chains respectively.

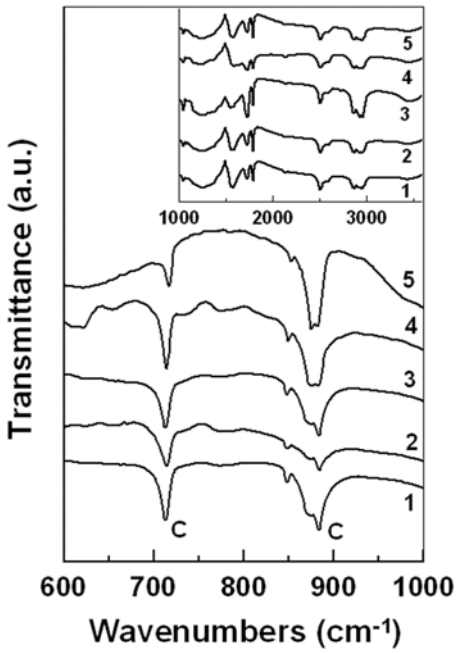

Fig.4.31 : *FTIR spectra in different spectral windows recorded from : $CaCO_3$ crystals grown in the Hele-Shaw cell with organic phase viscosities of 0.002678 Pa-s (curve 1); 0.003434 Pa-s (curve 2); 0.00412 Pa-s (curve 3); 0.00488 Pa-s (curve 4) and 0.046 Pa-s (curve 5).*

4.6.5 X-ray diffraction studies

The XRD measurements of the $CaCO_3$ crystals grown in the Hele-Shaw experiments at different viscosities are shown as curves 2-6 in Fig.4.32.

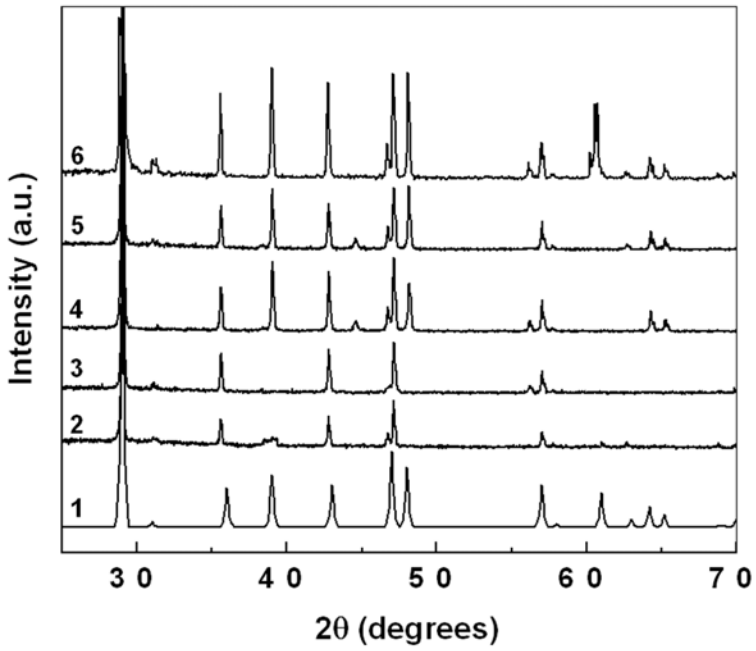

Fig.4.32: *XRD patterns recorded from $CaCO_3$ crystals synthesized in the radial Hele-Shaw cell with organic phase viscosities of 0.002678 Pa-s (curve 1); 0.003434 Pa-s (curve 2); 0.00412 Pa-s (curve 3); 0.00488 Pa-s (curve 4) and 0.046 Pa-s (curve 5).*

A number of Bragg reflections are identified and could be indexed with the reference to the unit cell of the calcite polymorph. For comparison, the simulated powder XRD patterns of calcite (curve 1, a = b = 4.989 Å, c = 17.062 Å, space group $D^6_{3D} - R3^*c$) [25] is shown in the figure and have been used to identify the calcite phase of $CaCO_3$ obtained in these studies. The XRD spectra recorded from the $CaCO_3$ crystals obtained in all viscosity experiments consist of predominantly the calcite polymorph [25]. One interesting observation in all the XRD spectra (curve 2 – 6 in Fig.4.32) is the gradual appearance of new Bragg peaks as the organic phase viscosity increases.

4.6.6 Summary

The change in viscosity of the organic phase at a dynamic liquid-liquid interface and thereby the nature of the viscous fingering interfacial structures obtained indeed lead to differences in the morphology of the calcite crystals as well as their assembly at the

interface. While the complexity of the interface does play an important role, it is possible that the hydrodynamic flows affect the reaction rate of the ions (calcium ions and carbonate ions) at the interface leading to such interesting calcite assemblies.

4.7 Discussion

A number of physical processes would contribute to crystal growth at the advancing liquid-liquid interface in the Hele-Shaw experiment. The rate of creation of fresh surface, rate of arrival of surfactant molecules to the fresh interface, rate of binding of counterions to the surfactant molecules at the interface etc [13b] would influence the nature of minerals grown at the interface. The crystal growth process in Hele-Shaw cell is similar, in principle, to that reported for minerals grown at the air-water interface in the presence of anionic Langmuir monolayers [14] with the difference that the charged interface is now expanding bringing into play the associated time-scale issues mentioned above. The assembly of $BaSO_4$, $SrCO_3$ and $CaCO_3$ crystals into higher ordered superstructures is due to dynamic processes at the interface that are not possible at a static interface such as that provided by a static liquid-liquid interface and Air-water interface [14].

A possible mechanism for the assembly of mineral crystallites in the Hele-Shaw cell in the presence of surfactant molecules could be the following. It is possible that during movement of the interface localized hydrodynamic flow effects lead to complete capping of the crystallites nucleated and grown at the interface. Formation of a monolayer of surfactant molecules surrounding the mineral crystallites could then lead to water-mediated interdigitation of the hydrocarbon chains surrounding the crystallites and association into linear superstructures as observed. That this is indeed a likely mechanism is underlined by the control experiments where such assembly was not observed either at a static liquid-liquid interface or in control experiments performed in solution and in the Hele-Shaw cell in the absence of an ordering surfactant. A similar mechanism has been put forward for the assembly of $BaCrO_4$ crystallites grown in microemulsions by Mann and co-workers [10a].

The formation of aragonite and calcite crystals in the Hele-Shaw cell experiments could be explained in terms following mechanism. The initial crystalline phase nucleated near the AOT monolayer at the liquid-liquid interface is aragonite. This aspect may be

understood in analogy with earlier studies on aragonite growth on SAMs. Kuther and co-workers have shown that aragonite needles may be grown on SAMs of anthracene-terminated thiol molecules at slightly elevated temperatures, these molecules packing in rectangular lattices due to the bulky terminal group [21a]. On the other hand, the use of methyl-terminated SAMs of thiols yielded calcite crystals due to epitaxy with the underlying template that assembled in a hexagonal close-packed structure [21a]. We believe a similar mechanism is operative here – the AOT molecules with their bulky headgroups pack into rectangular structures at the expanding liquid-liquid interface in the Hele-Shaw cell leading to epitaxy with the aragonite polymorph and selection of this phase. Thereafter, the metastable aragonite phase dissolves and recrystallizes as calcite, this process being dependent on the rate of expansion of the liquid-liquid interface. The formation of hollow cylindrical structures during recrystallization of calcite is not clear at the moment. It is possible that hydrodynamic flows at the expanding liquid-liquid interface result in the assembly of the recrystallized calcite phase in the form of hollow cylinders, the hollow centers arising due to depletion of the aragonite whiskers bundles as the calcite phase is formed. While, by increasing the viscosity of the organic phase and thereby the nature of the viscous fingering interfacial structures lead to differences in the morphology and assembly of the calcite crystals grown at the interface.

The morphology of $BaSO_4$, $SrCO_3$ and $CaCO_3$ crystals grown at the static liquid-liquid interface studies are markedly different from those observed at the dynamic liquid-liquid interface as well as at the air-water interface [14]. At a static liquid-liquid interface it may initially appear that the organization of surfactant molecules at the liquid-liquid interface is similar to that of the fatty lipids at the air-water interface but with the following important differences. The finite solubility of the two solutions leads to a fairly broad interfacial region where the surfactant molecules are relatively evenly distributed. This would enable the surfactant molecules to bind to nascent crystals growing at the interface and thereby, control the growth of specific crystallographic faces and the crystal morphology. The electrostatic interaction between the counterions and the surfactant molecules would also be modulated by the lower dielectric constant of the organic component within the interfacial region and could tailor the growth mode of crystals.

4.8 Conclusions

In this chapter, we have shown that a dynamic liquid-liquid interface is a highly versatile medium for growing and assembling minerals. The use of the liquid-liquid interface throws open the exciting possibility of tailoring the physical and chemical properties of the interface and thereby, modifying the morphology of the crystals nucleating and growing at the interface. These results demonstrate the versatility of the expanding liquid-liquid interface in a Hele-Shaw cell in designing new materials and suggests high potential for development. It also throws up a number of fundamental issues related to the interface and how they may influence the inorganic structures formed. Rational design of the interface together with a better understanding of hydrodynamic flow issues and diffusion time scales of reacting species can add value to this method for materials design and synthesis.

4.9 References

[1] (a) Selzer, Y.; Mandler, D. *J. Phys. Chem. B* **2000**, *104*, 4903. (b) Krueger, J. J.; Amiridis, M. D.; Ploehn, H. J. *Ind. Eng. Chem. Res.* **2001**, *40*, 3158. (c) Dang, L. X. *J. Phys. Chem. B,* **1999**, *103*, 39. (d) Uchiyama, Y.; Tsuyumoto, I.; Kitamori, T.; Sawada, T. *J. Phys. Chem. B* **1999**, *103,* 4663. (e) Yadav, G. D.; Reddy, C. A. *Ind. Eng. Chem. Res.* **1999**, *38*, 2245. (f) Wu, H. S. *Chem. Eng. Sci.* **1996**, *51*, 827. (g) Bhattacharya, A. *Ind. Eng. Chem. Res.* **1996**, *35*, 645. (h) Chen, Y.; Gao, Z.; Li, F.; Ge, L.; Zhang, M.; Zhan, D.; Shao, Y. *Anal. Chem.* **2003**, *75*, 6593. (i) Starks, C. M. *J. Am. Chem. Soc.* **1971**, *93*, 195. (j) Zhang, Z.; Tsuyumoto, I.; Takahashi, S.; Kitamori, T.; Sawada, T. *J. Phys. Chem. A* **1997**, *101*, 4163. (k) Zhang, Z.; Tsuyumoto, I.; Takahashi, S.; Kitamori, T.; Sawada, T. *J. Phys. Chem. B* **1998**, *102*, 10284.

[2] (a) Pieranski, P.; *Phys. Rev. Lett.* **1980**, *45*, 569. (b) Mayya, K. S.; Sastry, M. *Langmuir* **1999**, *15*, 1902. (c) Velev, O. D.; Furusawa, K.; Nagayama, K. *Langmuir* **1996**, *12*, 2374. (d) Lin, Y.; Skaff, H.; Emrick, T.; Dinsmore, A. D.; Russell, T. P. *Science* **2003**, *299*, 226.

[3] (a) Gajraj, A. ; Ofoli, R. Y. *Langmuir* **2000**, *16,* 4279. (b) Dickinson, E.; Euston, S. R.; Woskett, C. M. *Prog. Colloid Polym. Sci.* **1990**, *82*, 65.

[4] (a) Wyrwa, D.; Beyer, N.; Schmid, G. *Nano Lett.* **2002**, *2*, 419. (b) Selvakannan, PR.; Mandal, S.; Pasricha, R.; Adyanthaya, S. D.; Sastry, M. *Chem. Commun.* **2002**, 1334. (c) Selvakannan, PR.; Mandal, S.; Pasricha, R.; Sastry, M. *J .Colloids and Interface Sci.* **2004**, *279*, 124. (d) Yogev, D.; Efrima, S. *J. Phys. Chem.* **1988**, *92*, 5754. (e) Schwartz, H.; Harel, Y.; Efrima, S. *Langmuir* **2001**, *17*, 3884. (f) Dinsmore, A. D. ; Hsu, M. F. ; Nikolaides, M. G. ; Marquez, M. ; Bausch, A. R. ; Weitz, D. A. S*cience* **2002**, *298*, 1006. (g) Lin, Y.; Skaff, H.; Boker, A.; Dinsmore, A. D.; Emrick, T.; Russell, T. P. *J. Am. Chem. Soc.* **2003**, *125*, 12690. (h) Selvakannan, PR.; Kumar, P. S.; More, A. S.; Shingte, R. D.; Wadgaonkar, P .P.; Sastry, M. *Adv. Mater.* **2004**, *16*, 966. (i) Selvakannan, PR.; Kumar, P. S.; More, A. S.; Shingte, R. D.; Wadgaonkar, P .P.; Sastry, M. *Langmuir* **2004**, *20*, 295. (j) Kumar, A.; Mandal, S.; Mathew, S. P.; Selvakannan, PR.; Mandale, A. B.; Chaudhari, R. V.; Sastry, M. *Langmuir* **2002**, *18*, 6478.

[5] (a) Lowenstam, H. A.; Weiner, S. *On Biomineralization*; Oxford: New York, **1989**. (b) Addadi, L.; Weiner, S. *Angew. Chem., Int. Ed. Engl.* **1992**, *31*, 153. (c) Addadi, L.; Moradian, J.; Shay, E.; Maroudas, N. G.; Weiner, S. *Proc. Natl. Acad. Sci. U.S.A.* **1987**, *84*, 2732. (d) Belcher, A. M.; Wu, X. H.; Christensen, R. J.; Hansma, P. K.; Stucky, G. D.; Morse, D. E. *Nature* **1996**, *381*, 65.

[6] (a) Lochhead, M. J.; Letellier, S. R.; Vogel, V. *J. Phys.Chem. B.* **1997**, *101*, 10821. (b) Addadi, L.; Weiner, S. *Proc. Natl. Acad. Sci. U.S.A.* **1985**, *82*, 4110. (c) Mann, S.; Archibald, D. D.; Didymus, J. M.; Douglas, T.; Heywood, B. R.; Meldrum, F. C.; Reeves, N. J. *Science* **1993**, *261*, 1286.

[7] (a) Landau, E. M.; Levanon, M.; Leiserowitz, L.; Lahav, M.; Sagiv, J. *Nature* **1985**, *318*, 353. (b) Heywood, B. R.; Mann, S. *Ad*V. *Mater.* **1994**, *6*, 9. (c) Bunker, B. C.; Rieke, P. C.; Tarasevich, B. J.; Campbell, A. A.; Fryxell, G. E.; Graff, G. L.; Song, L.; Liu, J.; Virden, J. W.; McVay, G. L. *Science* **1994**, *264*, 48. (d) Calvert, P.; Rieke, P. *Chem. Mater.* **1996**, *8*, 1715. (e) Fendler, J. H. *Chem. Mater.* **1996**, *8*, 1616.

[8] (a) Feng, S.; Bein, T. *Nature* **1994**, *368*, 834. (b) Archibald, D. D.; Qadri, S. B.; Gaber, B. P. *Langmuir* **1996**, *12*, 538. (c) Berman, A.; Ahn, D. J.; Lio, A.; Salmeron, M.; Reichert, A.; Charych, D.; *Science* **1995**, *269*, 515. (d) Li, J.; Liang, K. S.;

Scoles, G.; Ulman, A. *Langmuir* **1995**, *11*, 4418. (e) Ma, C. L.; Lu, H. B.; Wang, R. Z.; Zhou, L. F.; Cui, F. Z.; Qian, F. *J. Cryst. Growth* **1997**, *173*, 141.

[9] (a) Lao, J. Y.; Huang, J. Y.; Wang, D. Z.; Wen, J. G.; Ren, Z. F. *Nano Lett.* **2003**, *3*, 235. (b) Sharma, S.; Sunkara, M. K. *J. Am. Chem. Soc.* **2002**, *124*, 12288. (c) Jensen, H.; Fermyn, D. J.; Moser, J. E.; Girault, H. H. *J. Phys. Chem. B* **2002**, *106*, 10908. (d) Fermyn, D. J.; Jensen, H.; Moser, J. E.; Girault, H. H. *ChemPhysChem* **2003**, *4*, 85.

[10] (a) Li, M.; Schnablegger, H.; Mann, S. *Nature* **1999**, *402*, 393. (b) Hopwood, J. D.; Mann, S. *Chem. Mater.* **1997**, *9*, 1819. (c) Li, M.; Mann, S. *Langmuir* **2000**, *16*, 7088. (d) Summers, M.; Eastoe, J.; Davis, S. *Langmuir* **2002**, *18*, 5023.

[11] Collier, C.P.; Saykally, R. J.; Shiang, J. J.; Henriches, S. E.; Heath, J. R. *Science* **1997**, *277*, 1978.

[12] (a) Ben-Jacob, E.; Garik, P. *Nature* **1990**, *343*, 523. (b) Sastry, M.; Gole, A.; Banpurkar, A. G.; Limaye, A. V.; Ogale, S. B. *Current Science* **2001**, *81*, 191.

[13] (a) Guo, H.; Hong, D. C.; Kurtze, D. A. *Phys. Rev. E.* **1995**, *51*, 4469. (b) Bonn, D.; Kellay, H.; Ben Amar, M.; Meunier, J. *Phys. Rev. Lett.* **1995**, *75*, 2132. (c) Banpurkar, A. G.; Ogale, A. S.; Limaye, A. V.; Ogale, S. B. *Phys. Rev. E.* **1999**, *59*, 2188.

[14] (a) Litvin, A.L.; Valiyaveettil, S.; Kaplan, D.L.; Mann, S. *Adv. Mater.* **1997**, *9*, 124. (b) Heywood, B.R.; Mann, S. *J. Am. Chem. Soc.* **1992**, *114*, 4681. (c) Heywood, B.R.; Mann, S. *Langmuir* **1992**, *8*, 1492. (d) Buijnsters, P.J.J.A.; Donners, J.J.J.M.; Hill, S.J.; Heywood, B. R.; Nolte, R. J. M.; Zwanenburg, B.; Sommerdijk, N.A.J.M. *Langmuir* **2001**, *17*, 3623.

[15] Bromley, L.A.; Cottier, D.; Davey, R.J.; Dobbs, B.; Smith S.; Heywood, B.R. *Langmuir* **1993**, *9*, 3594.

[16] Uchida, M.; Sue, A.; Yoshioka, T.; Okuwaki, A. *CrystEngComm* **2001**, 5.

[17] (a) Hill, R. J. *Can. Mineral.* **1977**, *15*, 522. (b) Redfern, S.E.; Parker, S.C. *J. Chem. Soc. Faraday Trans.* **1998**, *94*, 1947.

[18] The XRD patterns were indexed with reference to the unit cell of the strontianite structure from *ASTM* chart (a = 5.107 Å, b = 8.414 Å, c = 6.029 Å; space group *Pmcn*, ASTM chart card no. 5-0418).

[19] Ota, Y.; Inui, S.; Iwashita, T.; Kasuga, T.; Abe, Y. *J. Am. Ceram. Soc.* **1995**, *78*, 1983.

[20] (a) Lee, I.; Han, S. W.; Choi, H. J.; Kim, K. *Adv. Mater.* **2001**, *13*, 1617. (b) Sugawara, A.; Kato, T. *Chem. Commun.* **2000**, 487. (c) Walsh, D.; Mann, S. *Nature* **1995**, *377*, 320.

[21] (a) Kuther, J.; Nelles, G.; Seshadri, R.; Schaub, M.; Butt, H. J.; Tremel, W. *Chem. Eur. J.* **1998**, *4*, 1834. (b) Kuther, J.; Tremel, W. *Chem. Commun.* **1997**, 2029.

[22] Heywood, B. R.; Mann, S. *Chem.Mater.* **1994**, *6*, 311.

[23] Falini, G.; Albeck, S.; Weiner, S.; Addadi, L. *Science* **1996**, *271*, 67.

[24] Aizenberg, J.; Black, A. J.; Whitesides, G. M. *J. Am. Chem. Soc.* **1999**, *121*, 4500.

[25] (a) Aizenberg, J.; Black, A. J.; Whitesides, G. M. *J. Am. Chem. Soc.* **1999**, *121*, 4500. (b) The XRD patterns were indexed with reference to the unit cell of the calcite structure (a = b = 4.989 Å, c = 17.062 Å, space group D_{3D}^{6} – R3*c, *ASTM* chart card no. 5-0586) from *ASTM* chart.

[26] The XRD patterns were indexed with reference to the unit cell of the aragonite structure (a = 4.959 Å, b = 7.968 Å, c = 5.741 Å; space group *Pmcn*, *ASTM* chart card no. 5-0453) from *ASTM* chart.

[27] Orme, C. A.; Noy, A.; Wierzbicki, A.; McBride, M. T.; Grantham, M.; Teng, H. H.; Dove, P. M.; DeYoreo, J. J. *Nature* **2001**, *411*, 775.

[28] Sugawara, A.; Ishii, T.; Kato, T. *Angew. Chem. Int. ed.* **2003**, *42*, 5299.

[29] Spectrometric Identification of Organic Compounds (R. M. Silverstein, F. X. Webster) *John Wiley & Sons, Inc.* (Sixth Edition, P-107).

CHAPTER V

Aqueous Foams as Templates for the Synthesis of Minerals

This chapter discusses the synthesis of $CaCO_3$ crystals in aqueous foams stabilized by the surfactant AOT by a method of ion entrapment. This is accomplished by first electrostatically complexing Ca^{2+} ions with AOT molecules at the air-bubble solution interface followed by reaction with Na_2CO_3 solution in the final step. The crystallization of $CaCO_3$ was also performed wherein the structure of the foam was modulated by varying the drainage time of the foam as well as by creating foams with different bubble sizes. The effect of crystal growth inhibitors such as magnesium ions in controlling the morphology of $CaCO_3$ crystals in the aqueous foam was also studied.

Part of the work presented in this chapter has been published and patented:

1) Rautaray, D.; Sinha, K.; Shiv Shankar, S.; Adyanthaya, S. D.; Sastry, M. *Chem. Mater.* **2004**, *16*, 1356-1361. 2) Rautaray, D.; Sastry, M. *CrystEngComm* **2004** (Communicated). 3) Murali Sastry, Debabrata Rautaray, Kaustav Sinha, *US Patent Filed* (CSIR308fn2003).

5.1 Introduction

Development of experimental strategies for the synthesis of inorganic materials with controllable shape, size and crystallography is important in crystal engineering [1] and consequently, there is much current interest in the growth of morphologically complex mineral crystals and their morphogenesis. Many living organisms contain biominerals and composites with finely tuned properties, reflecting a remarkable degree of control over nucleation, growth and shape of the constituent crystals [2]. Such morphologically complex, three-dimensional structures, if produced synthetically, could find important applications as light weight ceramics, catalyst supports, biomedical implants, hybrid materials and cosmetic formulations [1]. Thus, an essential objective of biomimetic materials science is to develop new synthetic strategies capable of synthesizing materials and composites with complex morphologies that exhibit organizational and multifunctional specificity [3].

Recent applications of various in situ techniques have dramatically improved our understanding of the self-organization process of adsorbed molecular monolayers. The adsorption of amphiphilic surfactant molecules at interfaces is a well-known phenomenon that is at the heart of all detergency applications. A single molecular layer (monolayer) of surfactant stabilizes oil droplets and gas bubbles in an aqueous environment, enhancing the stability of emulsions and foams [4].

An exciting and considerably underexploited dynamic biomimetic template for crystal growth is foam lamellae [5]. Davey and co-workers first showed that stabilizing surfactants at the air-bubble/solution interface in foams could be used as nucleation centers for the growth of various inorganic crystals [5]. Liquid foams provide an extremely high concentration of gas bubbles dispersed in a liquid and as a result, yield large interfacial areas populated by the stabilizing surfactant. The bubble-stabilizing surfactants are amphiphiles that assemble at the gas/liquid interface and essentially form extended monolayers akin to Langmuir monolayers that are juxtaposed parallel to each other and separated by a region of water with the polar groups facing inwards. These regions occur between two neighboring bubbles and are called the plateau borders while the regions where such plateau borders meet are called the plateau junctions. The close-packed arrangement of polar groups at the gas-liquid interface offers the possibility of

using foams as a template for binding different charged ions along the plateau borders and junctions and growing a range of inorganic materials by novel chemistry. The aqueous foam-based method have been utilized in this laboratory for synthesizing metal nanoparticles such as gold [6a] and silver [6b], magnetic nanomaterials such as Co, Ni and their subsequent conversion into Co-Ag and Co-Ni core shell nanoparticles respectively [6c,d] and iron oxyhydroxide nanoparticles [6e].

There is growing demand for large-scale synthesis of nanoparticles for a variety of large-volume applications (for example, calcite nanoparticles in paper and polymer industries) and we believe the large interfacial area provided by bubbles in a foam could help realize scale-up. In this chapter, we have described the synthesis of $CaCO_3$ crystals in aqueous foams stabilized by the surfactant AOT. This is accomplished by first electrostatically complexing Ca^{2+} ions with AOT molecules at the air-bubble solution interface followed by reaction with Na_2CO_3 solution in the final step. These studies indicate that the calcite crystals of flat, plate-like morphology are formed within the plateau borders following which they assemble into spheroaggregates within the plateau junctions by hydrophobic association. To understand the process of formation of spherical $CaCO_3$ particles better, experiments were performed wherein the structure of the foam was modulated by varying the drainage time of the foam and by creating foams with different bubble sizes. We further exploit this novel procedure for controlling the mineral morphology by adding crystal growth inhibitors such as magnesium ions and study the effect of Mg^{2+} in controlling the morphology of $CaCO_3$ crystals in the aqueous foam.

5.2 Aqueous foams as templates for mineral growth

1. The synthesis of $CaCO_3$ crystals in aqueous foams stabilized by the surfactant AOT was accomplished by first electrostatically complexing Ca^{2+} ions with AOT molecules in the foam lamellae followed by reaction with Na_2CO_3 solution.
2. The effect of crystal growth inhibitors such as Mg^{2+} ions in controlling the morphology of $CaCO_3$ crystals in the aqueous foam was accomplished by first making foams of aqueous mixture of $CaCl_2$ + $MgCl_2$ + AOT followed by reaction with Na_2CO_3 solution.

In the first set of experiments, a rectangular column of 50 cm height and a square base of 10 x 10 cm^2 with sintered ceramic discs embedded in it was used for generation of the foam. An aqueous mixture of 50 ml of 5 x 10^{-3} M calcium chloride and 50 ml of 10^{-2} M AOT was taken in the rectangular column and the foam built up by injecting air at a pressure of 1-5 psig through the ceramic disc (Fig5.1, step A). Stable foams of 50 cm height could be routinely obtained. The liquid lamellae between bubbles in the foam may be considered to consist of two Langmuir monolayers of AOT electrostatically complexed with Ca^{2+} ions and therefore amenable to reaction with carbonate anions at the interface. After stabilization of the foam, the aqueous AOT + $CaCl_2$ solution was carefully drained out from below and the foam subjected to a mild and fine spray of aqueous solution of 10^{-3} M sodium carbonate (Fig.5.1, step B). The foam collapsed gradually (typically 15 to 20 min after spraying of Na_2CO_3) and the crystals of calcium carbonate were collected through the outlet provided at the bottom of the column.

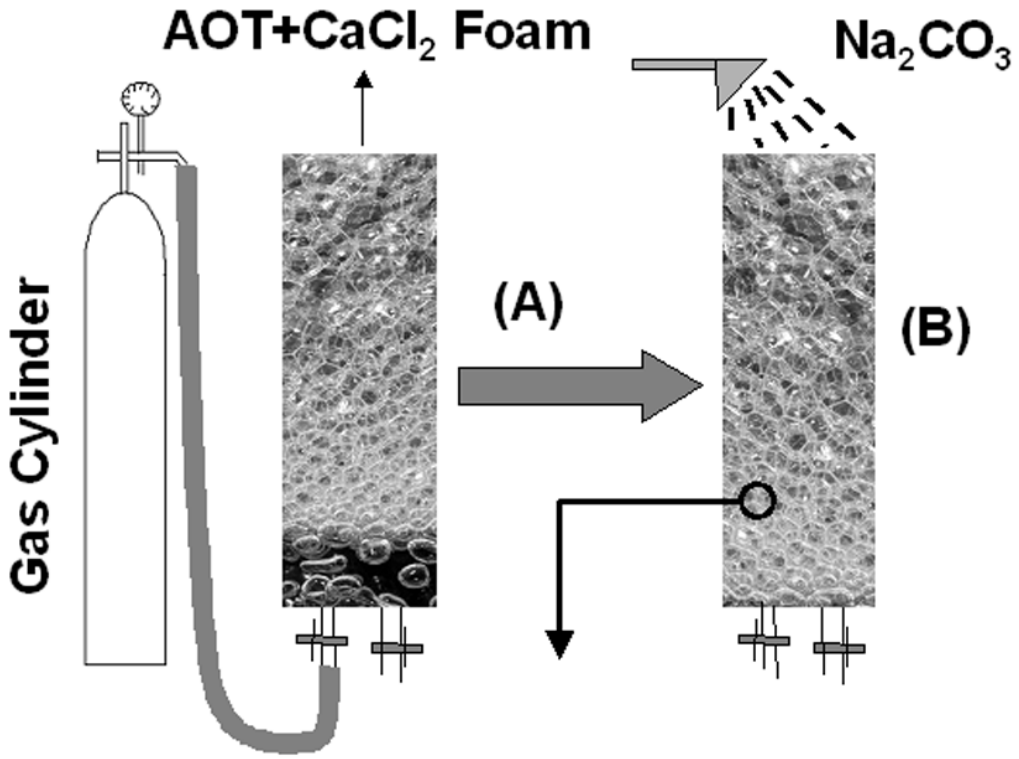

Fig.5.1 *Scheme showing the different steps involved in the synthesis of $CaCO_3$ crystals using aqueous AOT foam.*

In an separate experiment, an aqueous mixture of 100 ml of AOT (10^{-2} M) + $CaCl_2$ (10^{-2} M) + $MgCl_2$ (10^{-3} M) was taken in the rectangular column and the foam built up by injecting air at a pressure of 1-5 psig through the ceramic disc. After stabilization of the foam, the aqueous AOT + $CaCl_2$ + $MgCl_2$ solution was carefully drained out from below and the foam subjected to a mild and fine spray of aqueous solution of 10^{-2} M sodium carbonate for $CaCO_3$ crystallization. Experiments were performed with Ca : Mg in a molar ratio of 10 : 1 and 100 : 1 at two different drainage time (10 min and 5hrs) of the foam.

5.3 Synthesis of $CaCO_3$ crystals in aqueous foam lamellae

An aqueous mixture of 50 ml of 5 x 10^{-3} M $CaCl_2$ and 50 ml of 10^{-2} M AOT was taken in the rectangular column and the foam was built up. After stabilization of the foam and drainage of excess liquid, the foam was subjected to a mild and fine spray of aqueous solution of 10^{-3} M Na_2CO_3. The $CaCO_3$ crystals formed were characterized by SEM, EDAX XRD and contact angle measurements. The process of drainage of the water in the foam is expected to lead a variation in the thickness of the water channels in the foam. Similarly, the structure of the foam may also be modulated by changing the size of the bubbles in the foam. In order to understand these processes, $CaCO_3$ growth was effected in the foam at different times of drainage of the foam (10 min, 30 min, 1 hr, 2 hrs, 4hrs and 5 hrs) and with two different bubble sizes (~ 2 mm and 8 mm). The different sizes of bubbles were obtained by fitting ceramic discs of different porosity in the foam column.

5.3.1 Foam morphology

In real foams, the basic distinction is between wet foams and dry foams (Fig.5.2). In wet foam the liquid content is high (Fig.5.2A) and so the walls of the cells are thick. As a result the cells are far enough apart so that none of them is distorted by the other. Hence the cells are spherical as surface tension causes isolated bubbles to take a spherical shape, which minimizes their surface area. As the liquid leaves the foam, it becomes dry (Fig.5.2B**).** The cells, now separated by thinner walls begin to influence one another. Thus the spherical bubbles become polyhedrons [7]. A dry foam has little liquid. The films meet in lines (the edges of the polyhedra) and the lines meet at vertices.

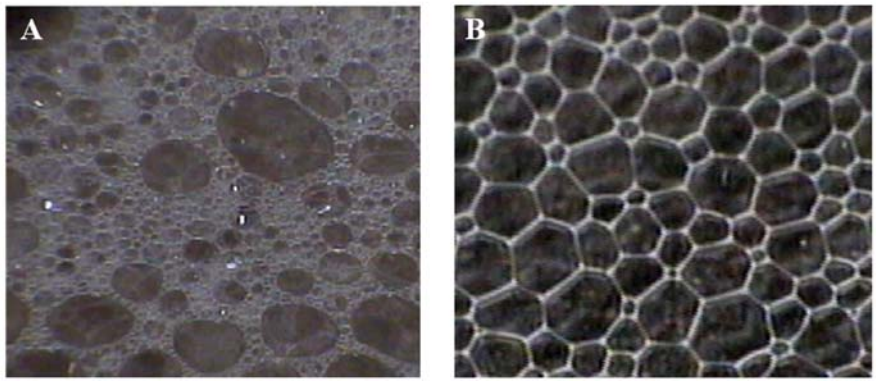

Fig.5.2: *Photograph of wet (A) and dry (B) foam.*

5.3.2 Structure of foam lamellae

Most foams owe their existence to the presence of surfactants, that is, constituents which are surface active. In the case of aqueous foam, a surfactant molecule includes two chemical groups that differ greatly in their solubility in water. One group is 'hydrophilic' or highly soluble in water and the other group is 'hydrophobic' or highly insoluble in water. A surfactant's surface activity depends on the sizes of these groups and their relative solubilities. Because of the differing solubilities, surfactants are surface active, that is, they accumulate at surfaces [7]. In particular, the hydrophobic groups on the surfactant molecules accumulate at an air-water interface (Fig.5.3). The detail descriptions of foam structure has been discussed in section 1.5.3 of chapter 1.

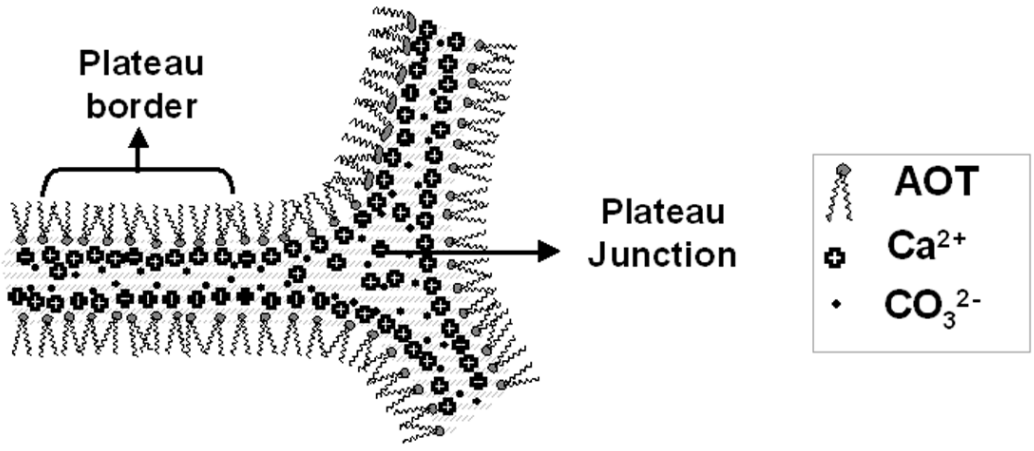

Fig.5.3: *Structure of water lamellae in the foam.*

Plateau borders are the channels that form where films meet (Fig.5.3). It tends to draw liquid out of the films. Most of the liquid in foam is in the Plateau borders and in the region where the borders meet is called the plateau junctions (Fig.5.3) [7].

5.3.3 Scanning electron microscopy and Energy dispersive analysis of X-rays studies

5.3.3.1 Formation of $CaCO_3$ crystals in aqueous foam lamellae

Fig.5.4 shows representative SEM images of $CaCO_3$ crystals synthesized by treating $CaCl_2$ – AOT foam of bubble size ~ 8 mm with Na_2CO_3 solution after allowing drainage of liquid from the foam for 10 minutes. The low magnification SEM image shows a major percentage of the structures in the form of compact spherical $CaCO_3$ particles along with a small percentage of ill-formed crystallites (Fig.5.4A). At higher magnification, the surface of the more compact spherical $CaCO_3$ assemblies appears to be made of smaller platelets in a highly close-packed assembly (Fig.5.4B). An interesting feature of the spherical crystal structures is the uniformity in shape and size (particle diameters in the range 0.6-2 μm). EDAX analysis from the crystals shown in Fig.5.4 yielded strong Ca, C and O signals together with weaker Na and S signals. This indicates the formation of $CaCO_3$ and also the presence of AOT in the spherical structures.

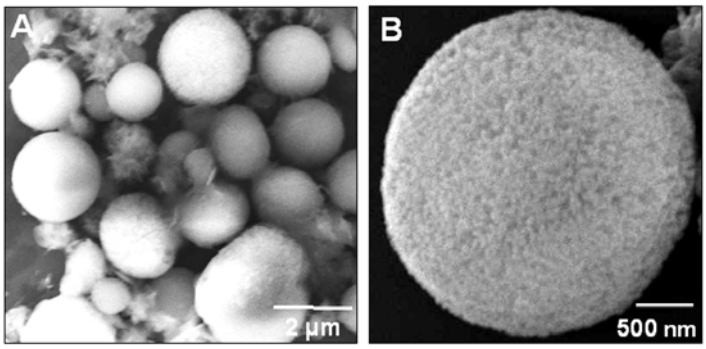

Fig.5.4: *A & B) SEM images at different magnifications of $CaCO_3$ crystals grown in a foam formed by bubbling air in an aqueous mixture of $CaCl_2$ and AOT and allowing the foam to drain for 10 min. $CaCO_3$ growth was induced by reaction with Na_2CO_3 solution. The bubble size in this experiment was ~ 8 mm.*

Figs.5.5A-E shows high magnification SEM images of some of the spherical $CaCO_3$ crystals obtained in the foam with a 10 min. of drainage. It is observed that a small percentage of the $CaCO_3$ structures were in the form of fairly open spherical

assemblies of flat, plate-like crystallites (Fig.5.5A & B). Some of the spheroaggregates are also present in different orientations on the Si (111) wafer fortuitously exposed their hollow cores (Fig.5.5C-E). The $CaCO_3$ crystallites appear to be organized in a radially oriented fashion outward from the hollow center of the spheres. Similar hollow spherical calcite/vaterite crystals have been obtained by Colfen and Antonietti during solution growth of $CaCO_3$ in the presence of suitable double hydrophilic block copolymers (DHBCs) [8,9]. It was speculated that these double-hydrophilic block copolymers, due to their strong interaction with inorganic surfaces, have the potential to control the growth of inorganic crystallites [8,9]. The formation of hollow cores in the spherical calcite/vaterite crystals were explained as it is arising due to a recrystallization process during which the core was consumed [9].

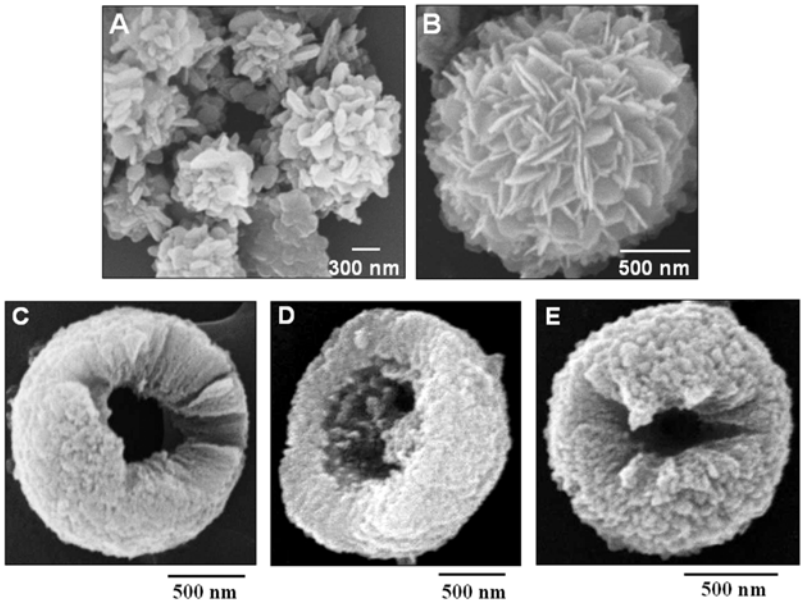

Fig.5.5: *SEM images of spherical $CaCO_3$ aggregates grown in the foam showing open spherical assemblies (A & B) and exposing their cores (C-E).*

We believe a similar process of recrystallization may be operative in this study as well. This is likely is supported by our observation that the spherical $CaCO_3$ structures in the foam are predominantly of two distinct types – one consisting of spherical assemblies of distinct plate-like crystals (Figs.5.5A and B) while the other set of spherical crystals has a very smooth surface and are made of much more compact crystals (Figs.5.4B). The set of compact, smooth spheres (with hollow cores) are possibly the spherical assembly of

plate-like $CaCO_3$ crystals at an advanced stage of recrystallization (Fig.5.5C-E). Hollow spheres with prismatic needles along the particle diameter have been observed by Kniep et al. in flourapatite-gelatin composites where growth of fluorapatite starts with formation of elongated prismatic seeds followed by self-similar branching into anisotropic spherical aggregates, this process being mediated by local electric fields [10].

5.3.3.2 Effect of varying drainage time on the $CaCO_3$ crystallization in foam lamellae

In order to understand the mechanism leading to $CaCO_3$ assembly into spherical superstructures, the effect of drainage times on the $CaCO_3$ crystal growth was studied in detail. Fig.5.6A – F show SEM images of $CaCO_3$ crystals grown in the foam for 10 min, 30 min, 1 hr, 2 hrs, 4 hrs and 5 hrs after drainage of the foam respectively. The foam was exceptionally stable even after 5 hrs of drainage with no evidence for variation in the gross structure (as seen by the naked eye).

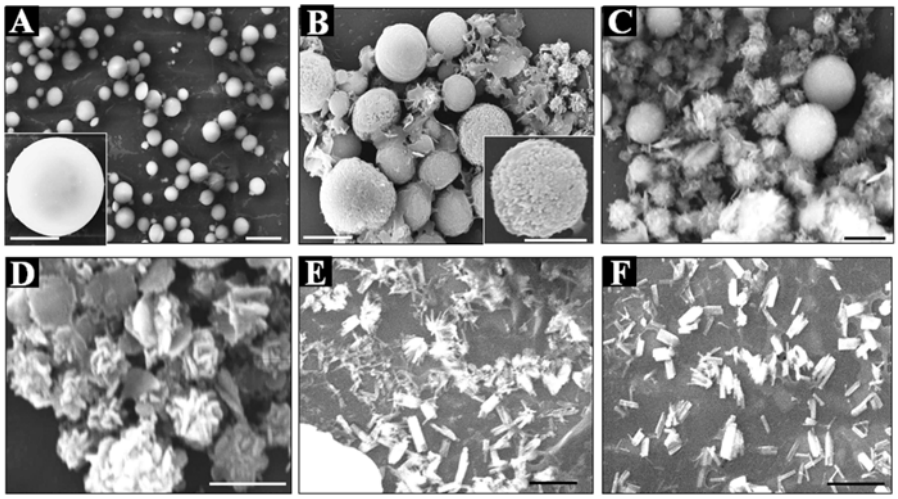

Fig.5.6: *SEM images of $CaCO_3$ crystals grown by reaction of Na_2CO_3 with the Ca^{2+}- AOT foam after different drainage times : (A) 10 min; (B) 30 min; (C) 1 hr; (D) 2 hrs; (E) 3 hrs; (E) 4 hrs and (F) 5 hrs. The scale bars in all the images correspond to 1 μm while they are 500 nm in the insets.*

The $CaCO_3$ crystals grown in the foam after 10 min of drainage (Fig.5.6A) shows well-defined spherical $CaCO_3$ structures. The inset of Fig.5.6A shows a relatively solid $CaCO_3$ spheroaggregate with a smooth surface. After 30 min of drainage, $CaCO_3$ spheroids can still be observed along with a number of ill-formed spherical aggregates (Fig.5.6B). A

magnified image of one of the spheroaggregates in this experiment is shown in the inset of Fig.5.6B revealing that they are much less compact and more porous than those formed 10 min after drainage (Fig.5.6A). On progressively increasing the drainage time, we observe that the percentage of spheroaggregates is reduced, they become more coarse and eventually, yield only flat, plate-like $CaCO_3$ crystals with no semblance of hierarchical assembly (Figs.5.6C-F). Clearly, the drainage time of the foam leads to a dramatic variation in the microscopic structure of the foam and thereby, the nature of $CaCO_3$ crystals formed in the foam.

5.3.3.3 Effect of bubble size on the $CaCO_3$ crystallization in foam lamellae

The effect of bubble size on the morphology of $CaCO_3$ crystals was also studied in foams consisting of ~ 2 mm and ~ 8 mm bubbles with a constant drainage period of 10 mins in both cases. Figs.5.7A and B show SEM images at different magnifications of $CaCO_3$ crystals grown in the foam consisting of 2 mm bubbles while Figs.5.7C and D correspond to images obtained from crystals obtained in the 8 mm foam experiment.

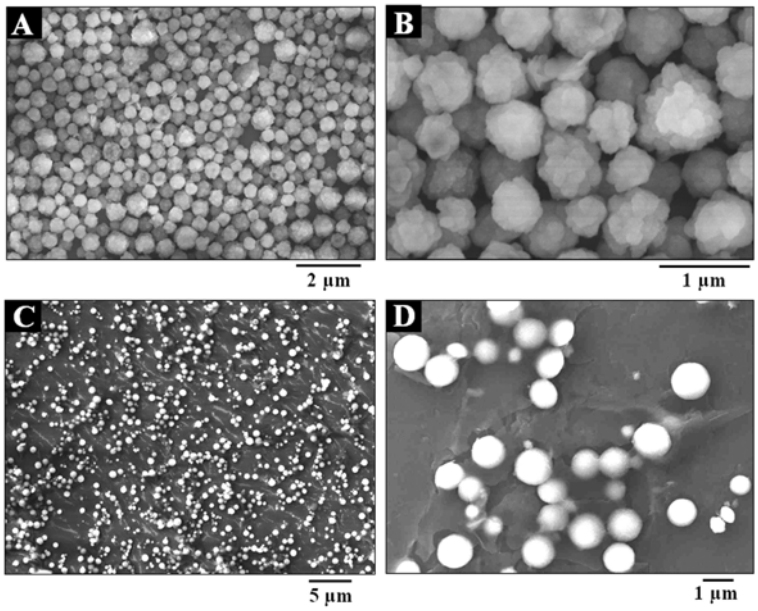

Fig.5.7: *SEM images at different magnification of $CaCO_3$ crystals grown after reaction of Na_2CO_3 with the Ca^{2+}-AOT foam consisting of different size bubbles; A,B ~2 mm and C, D ~8 mm.*

At low magnification (Figs.5.7A & C), it is apparent that the density of the $CaCO_3$ spheroaggregates is much higher in the 2 mm bubble experiment. This is understandable

given that smaller bubbles in the foam translates into more interfacial bubble area and consequently, a higher concentration of $CaCO_3$ crystals in the foam. The higher magnification SEM images (Figs.5.7B & D) show some differences in the $CaCO_3$ spheroaggregates grown in the different bubble sized foams. While the individual $CaCO_3$ crystals are clearly visible in the spherical aggregates obtained in the 2 mm foam (Fig.5.7B), the surface of the spheroaggregates in the 8 mm foam is much smoother (Fig.5.7D). It may be noted that with change in bubble size, even though the interfacial bubble area changes, there is no significant change in the thickness of the plateau borders and the cross-sectional area of the plateau junctions. The thickness of the plateau borders and the dimensions of the plateau junctions are observed to change only as a function of time of drainage of the foam and not so critically on the bubble size.

5.3.3.4 $CaCO_3$ crystallization in solution in the presence of AOT

Support for the important role played by the foam is provided by the fact that $CaCO_3$ crystals grown in solution by reaction of $CaCl_2$ and Na_2CO_3 in the presence of AOT yielded large, rhombohedral calcite particles assembled into a rudimentary close-packed structure (Fig.5.8A). The higher magnification SEM image in Fig.5.8B clearly shows one of the close packed assemblies of rhombohedral calcite crystals in a greater detail with no resemblances to the $CaCO_3$ structures observed in the foam lamellae.

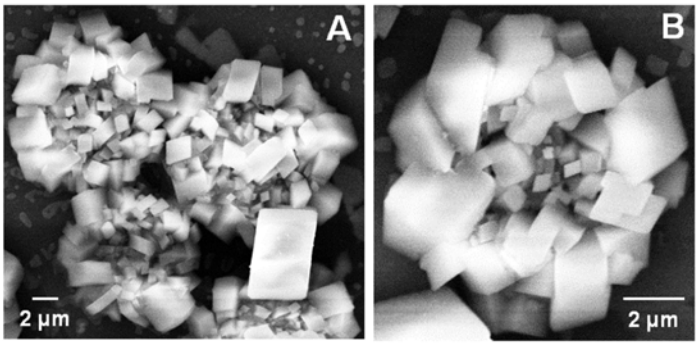

Fig.5.8: A & B) *SEM images at different magnifications of $CaCO_3$ crystals grown in solution in the presence of AOT.*

5.3.4 Contact angle measurements

Contact angle measurements at different points on the surface of drop-cast films of the $CaCO_3$ particles synthesized in AOT foam yielded an average value of 89^o. The

spherical $CaCO_3$ particles shown in Fig.5.4 are thus quite hydrophobic being enveloped by AOT molecules. The presence of AOT on the spheroaggregates suggests that sphere formation occurs through hydrophobic association of AOT-capped $CaCO_3$ platelets during growth of the crystals in the aqueous lamellae of the foam.

5.3.5 X-ray diffraction studies

The XRD pattern recorded from the spherical $CaCO_3$ crystal assemblies (Fig.5.4) cast in the form of a film on a glass substrate shows a number of Bragg reflections characteristic of the calcite polymorph along with a small percentage of aragonite (curve 1 in Fig.5.9) [11]. The Bragg reflections marked with 'A' correspond to the aragonite polymorph. The peaks are relatively broad indicating that the observed spherical micro particles of $CaCO_3$ are indeed aggregates/assembly of much smaller crystallites. The XRD results thus conclusively show that both the spherical assembly of flat, plate-shaped $CaCO_3$ crystallites (Figs.5.5A & B) and the compact, spherical particles (Figs.5.4) are predominantly of the calcite polymorph.

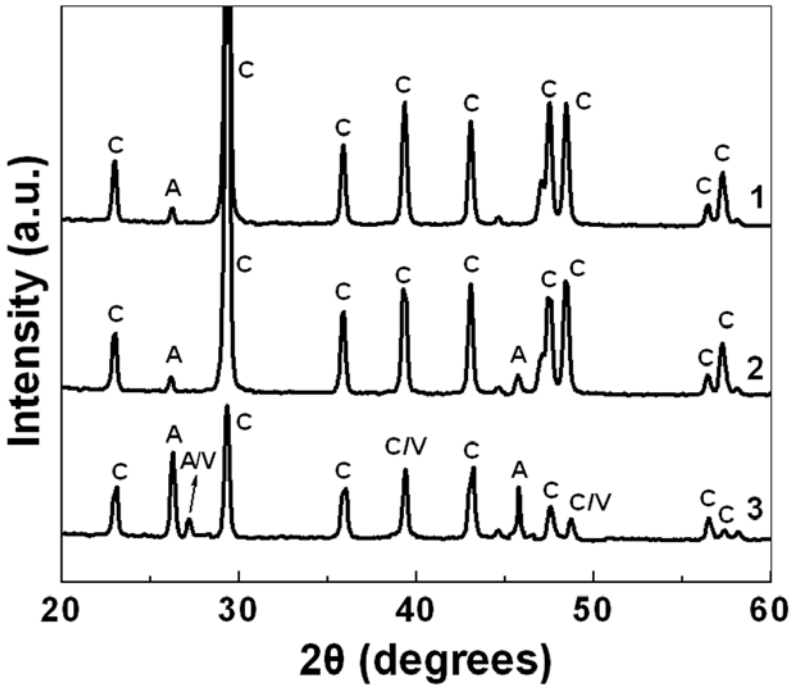

Fig.5.9: *XRD patterns recorded from $CaCO_3$ crystals grown in the aqueous AOT foam after different drainage times. Curve 1 - 10 min; curve 2 -1 hr and curve 3 - 5 hrs after drainage (peaks marked with 'C', 'A' and 'V' correspond to calcite, aragonite and vaterite Bragg reflections respectively).*

The evolution of XRD patterns recorded from the $CaCO_3$ crystals grown in the foam as a function of drainage time is shown in Fig.5.9 (curve 1 : 10 min; curve 2 : 1 hr and curve 3 : 5 hrs after drainage), these patterns corresponding to the SEM images shown in Figs.5.6A, C and F respectively. A number of Bragg reflections are identified and have been indexed with reference to the unit cells of the calcite, aragonite and vaterite structures [11]. In all the patterns, we observe the presence of calcite and aragonite polymorphs with the presence of a small percentage of vaterite at higher drainage times. The percentage contribution of aragonite appears to increase with increasing foam drainage time. From the SEM images of the $CaCO_3$ crystals grown in these experiments (Figs.5.6A, C and F), it is difficult to resolve the three phases based purely on crystal morphology considerations. It is thus possible that the $CaCO_3$ platelets observed in Fig.5.6F are composites of aragonite/vaterite and that the calcite component arises by a process of dissolution and recrystallization of aragonite/vaterite in the foam lamellae/junctions.

5.3.6 Summary

The formation of flat, plate-like calcite crystals and their hierarchical assembly into uniform spherical aggregates in an aqueous foam stabilized by the surfactant AOT, has been demonstrated. The presence of AOT on the surface of the calcite spheroaggregates inferred from the contact angle measurements indicates that hydrophobic interactions between the AOT-capped calcite platelets is responsible for such assembly.

5.4 Effect of Mg^{2+} ions in controlling $CaCO_3$ crystallization in aqueous foams

An aqueous mixture of 100 ml of AOT (10^{-2} M) + $CaCl_2$ (10^{-2} M) + $MgCl_2$ (10^{-3} M) was taken in the rectangular column and the foam built up. After stabilization of the foam, the aqueous AOT + $CaCl_2$ + $MgCl_2$ solution was carefully drained out from below and the foam subjected to a mild and fine spray of aqueous solution of 10^{-2} M sodium carbonate for $CaCO_3$ crystallization. Experiments were performed with Ca : Mg in a molar ratio of 10 : 1 and 100 : 1 at two different drainage time (10 min and 5hrs) of the foam.

5.4.1 Scanning electron microscopy measurements

5.4.1.1 $CaCO_3$ crystal growth in the presence of Mg^{2+} ions in dry foam

Fig.5.10A & B show representative SEM images at different magnifications of $CaCO_3$ crystals synthesized by treating AOT + $CaCl_2$ + $MgCl_2$ (Ca : Mg = 10 : 1) foam with Na_2CO_3 solution after allowing drainage of liquid from the foam for 5 hours. Fig.5.10A shows highly dense needle shaped $CaCO_3$ crystals populating the substrate surface. At higher magnification, the $CaCO_3$ needles are observed to have regular and uniform fractures on their surface. The width of the $CaCO_3$ needles are calculated to be in the range of 50–100 nm while the lengths are in excess of 2–5 μm. The cracks on the $CaCO_3$ needles are typically in the range of 10–20 nm in width.

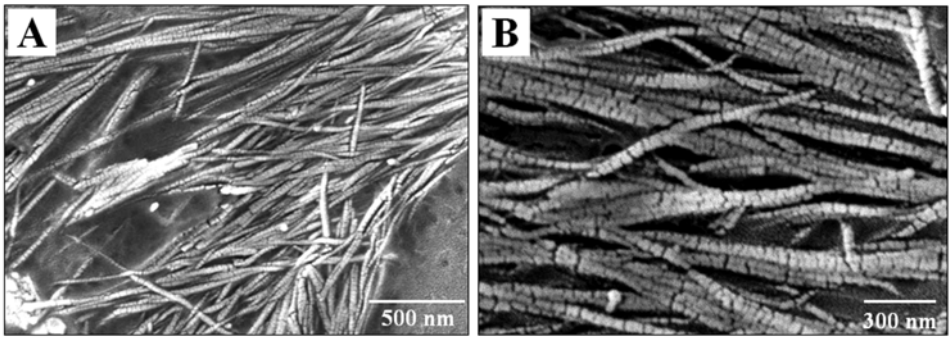

Fig.5.10: *A & B) Low and high magnification SEM images of $CaCO_3$ crystals synthesized by treating AOT + $CaCl_2$ + $MgCl_2$ (Ca : Mg = 10 : 1) foam with Na_2CO_3 solution after allowing the foam to drain for 5 hours.*

5.4.1.2 $CaCO_3$ crystal growth in the presence of Mg^{2+} ions in wet foam

The crystallization of $CaCO_3$ crystals was also achieved by treating AOT + $CaCl_2$ + $MgCl_2$ (Ca : Mg = 10 : 1) foam with Na_2CO_3 solution but with a drainage of liquid from the foam for only 10 min (to obtain a wet foam). Even with smaller drainage times, we did not observe any discernable change in the nature of the fractured needle shaped aragonite crystals (data not shown). It is clear from above that the presence of Mg^{2+} ions in the foam lamellae is responsible for the shape and polymorph control of $CaCO_3$ crystals with least contribution of the water content in the foam lamellae. Aragonite is a metastable polymorph of $CaCO_3$ and is the first phase to precipitate in this case and is stabilized with Mg^{2+} ions. The precipitation of metastable polymorph is possibly due to

the decrease in the degree of supersaturation because of the presence of Mg^{2+} ions in the crystallization solution.

Many reports have established that calcium carbonate is important in ion exchange due to its strong surface interactions with heavy metals [12]. Magnesium ions as an additive have been studied extensively [12,13], because Mg^{2+} ions are found in biological environments in high concentrations and are believed to play a critical role in the $CaCO_3$ formation [14]. Incorporation of magnesium within biological $CaCO_3$ is widespread, with many containing magnesium of different levels of concentrations leading to the control over both the shape and crystallography of $CaCO_3$ crystals depending on the extent of magnesium inclusion within the crystals [12].

5.4.1.3 Effect of Mg^{2+} ion concentration on the $CaCO_3$ crystallization in aqueous foam

The effect of magnesium ion concentration on the morphology and crystallography of $CaCO_3$ crystals was also studied using the foam template. Experiments were performed with a starting Ca : Mg molar ratio of 100 : 1 with drainage periods of 5 hours (dry foam) and 10 minutes (wet foam).

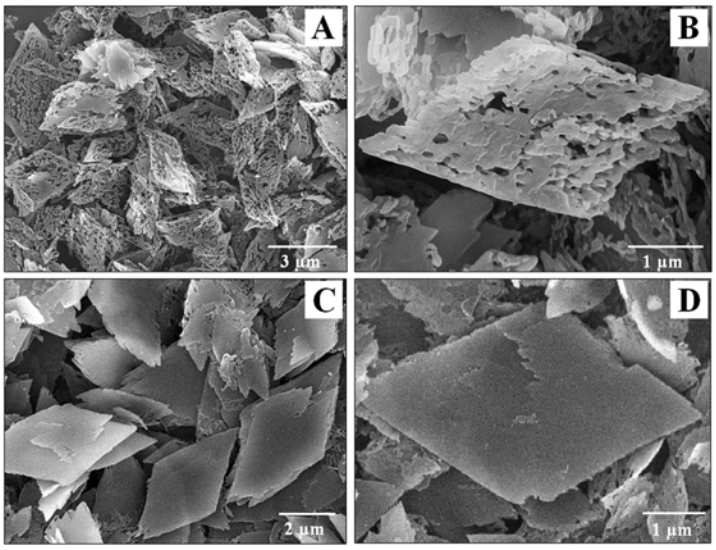

Fig.5.11: *Low and high magnification SEM images of $CaCO_3$ crystals synthesized by treating AOT + $CaCl_2$ + $MgCl_2$ (Ca : Mg = 100 : 1) foam with Na_2CO_3 solution after allowing the foam to drain for 5 hours (A & B) and 10 min (C & D).*

Fig.5.11A and B show SEM images at different magnifications of $CaCO_3$ crystals grown in the foam by treating AOT + $CaCl_2$ + $MgCl_2$ (Ca : Mg = 100 : 1) foam with Na_2CO_3 solution after allowing drainage of liquid from the foam for 5 hours. At low magnification (Fig.5.11A), a number of rhombic $CaCO_3$ crystals are observed, which are highly porous in nature. The higher magnification SEM image (Fig.5.11B) clearly shows the rhombic $CaCO_3$ crystals to be composed of a number of defects in the central part and on the edges of the crystals.

The crystallization of $CaCO_3$ crystals was also achieved by treating AOT + $CaCl_2$ + $MgCl_2$ (Ca : Mg molar ratio = 100 : 1) foam with Na_2CO_3 solution but with a lower drainage time (10 min) of liquid from the foam. The thickness of the plateau borders and the dimensions of the plateau junctions is observed to change as a function of time of drainage of the foam. Figs.5.11C and D show SEM images at different magnifications of $CaCO_3$ crystals grown in this experiment. At low magnification (Fig.5.11C), a number of rhombic $CaCO_3$ crystals are observed in this case as well but with a much reduced porosity of the crystal surface [compare with the high drainage time (5 h) experiment (Fig.5.11A)]. The high magnification SEM image (Fig.5.11D) further underlines this inference.

5.4.1.4 $CaCO_3$ crystal growth in control experiments

Support for the important role played by the Mg^{2+} ions in the AOT foam is provided by control experiments wherein, $CaCO_3$ crystal growth was effected in solution by reacting AOT + $CaCl_2$ + $MgCl_2$ mixed solution (Ca^{2+}/Mg^{2+} in a molar ratio of 10 : 1 and 100 : 1) with Na_2CO_3. The $CaCO_3$ crystals grown in solution by the reaction of $CaCl_2$ + $MgCl_2$ and Na_2CO_3 in the presence of AOT with a Ca : Mg molar ratio of 10 : 1 resulted in the formation of a mixture of fibrous as well as rhombohedral $CaCO_3$ crystals (Fig.5.12A), while a Ca : Mg molar ratio of 100 : 1 yielded stacks of calcite plates (Fig.5.12B), with no resemblance of $CaCO_3$ synthesized in the foam lamellae containing Mg^{2+} ions (Fig.5.10 and 5.11).

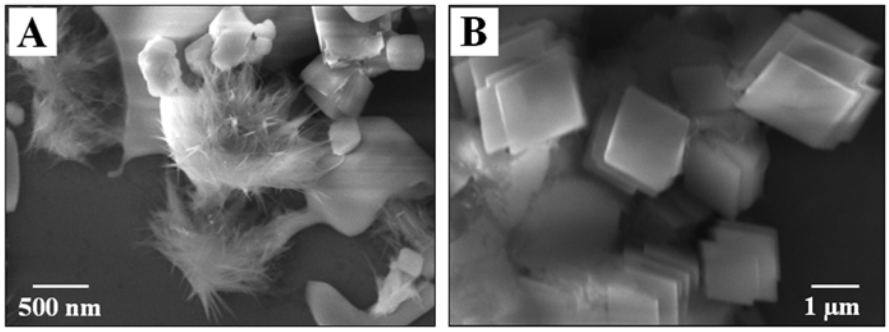

Fig.5.12: *$CaCO_3$ crystals grown in solution by the reaction of AOT + $CaCl_2$ + $MgCl_2$ mixed solution (Ca^{2+}/Mg^{2+} in a molar ratio of 10 : 1 and 100 : 1) with Na_2CO_3.*

5.4.2 Transmission electron microscopy (TEM) and Electron diffraction studies

Representative TEM images at different magnifications from the calcium carbonate crystals synthesized by using foam with a Ca : Mg in a molar ratio of 10 : 1 after allowing drainage of liquid from the foam for 5 hours are shown in Fig.5.13A & B.

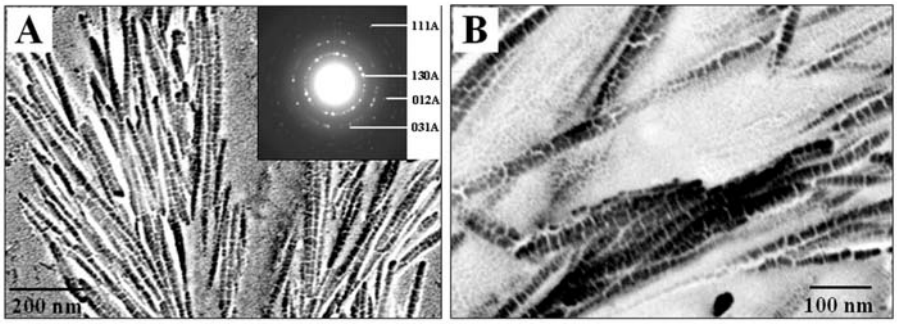

Fig.5.13: *A & B) Low and high magnification TEM images of $CaCO_3$ crystals synthesized by treating AOT + $CaCl_2$ + $MgCl_2$ (Ca : Mg = 10 : 1) foam with Na_2CO_3 solution after allowing the foam to drain for 5 hours. The inset in A shows the selected area electron diffraction pattern recorded from the crystals shown in the main part of the figure. The electron diffraction rings are indexed in the figure with 'A' stands for aragonite.*

The TEM images of the $CaCO_3$ crystals also clearly support the fractured nature of the needles as observed in the SEM images (Fig.5.10). Apparently, the high magnification TEM image (Fig.5.13B) was unable to resolve the individual crystallites of $CaCO_3$ constituting the individual needles. An estimate of the thickness of the individual cracks on the needles was made from the TEM image to be ca. 10–20 nm consistent with the SEM results. The inset of Fig.5.13A shows the selected area electron diffraction pattern

recorded from the calcium carbonate crystals shown in Fig.5.13A. The diffraction rings have been indexed in the figure based on the aragonite polymorph of $CaCO_3$ [11].

Fig.5.14A and B show TEM images at different magnifications of $CaCO_3$ crystals grown in the foam by treating AOT + $CaCl_2$ + $MgCl_2$ (Ca : Mg = 100 : 1) foam with Na_2CO_3 solution after allowing drainage of liquid from the foam for 5 hours.

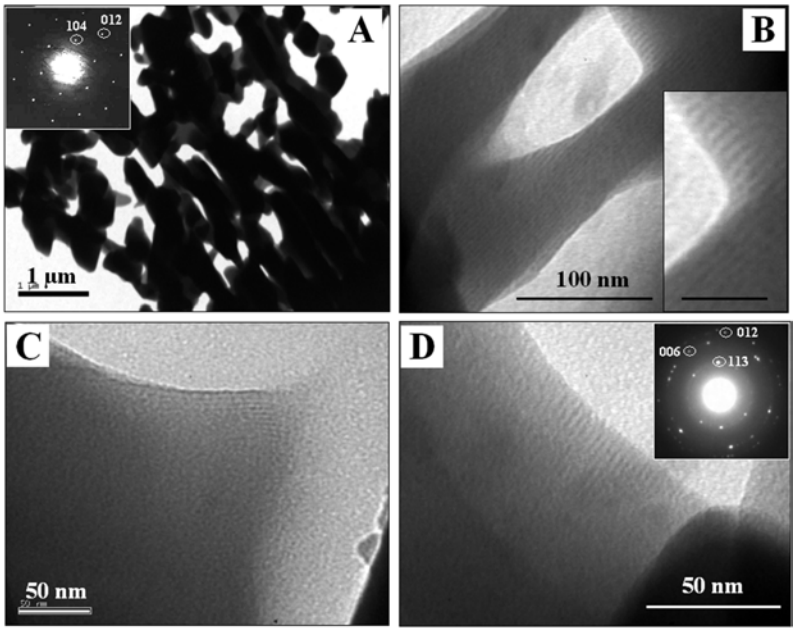

Fig.5.14: *Low and high magnification TEM images of $CaCO_3$ crystals synthesized by treating AOT + $CaCl_2$ + $MgCl_2$ (Ca : Mg = 100 : 1) foam with Na_2CO_3 solution after allowing the foam to drain for 5 hours (A & B) and 10 min (C & D).*

The porous nature of the rhombic $CaCO_3$ crystals is very prominently seen in the lower magnification TEM image shown in Fig.5.14A. The high magnification TEM image revealed that $CaCO_3$ crystals are mesoporous in nature (Fig.5.14B). The TEM image in the inset of Fig.5.14B shows the mesoporous nature of the $CaCO_3$ crystals in greater details. The inset of Fig.5.14A shows the SAED pattern from the mesoporous calcium carbonate crystals. The SAED pattern obtained is observed to be characteristic of a highly crystalline phase and has been indexed based on the calcite polymorph of $CaCO_3$ [11]. Similarly with a low drainage experiment (10 min of drainage), the TEM images recorded from the edges of the solid rhombic $CaCO_3$ crystals show the highly mesoporous nature of the crystals in this case even though the crystal porosity is much reduced (Fig.5.14C & D). The inset of Fig. 5.14D shows the SAED pattern of the

mesoporous calcium carbonate crystals. The SAED pattern obtained has been indexed in the figure based on the calcite polymorph of $CaCO_3$ [11].

5.4.3 Contact angle measurements

Contact angle measurements at different points on the surface of drop-cast films of the $CaCO_3$ crystals synthesized in the aqueous foam lamellae in the presence of Mg^{2+} ions, yielded an average value of 87^o. The needles shaped $CaCO_3$ crystals (Fig.5.10) are thus quite hydrophobic being enveloped by AOT molecules. Contact angle measurements of the porous and solid rhombic $CaCO_3$ crystals (Fig.5.11) yielded average values of 91^o and 89^o respectively. The $CaCO_3$ crystals thus obtained in this case are hydrophobic in nature due to AOT molecules surrounding the crystallites.

5.4.4 EDAX and FTIR studies

EDAX measurement from the needle shaped $CaCO_3$ crystals synthesized in the aqueous foam with a Ca : Mg ratio of 10 : 1 experiment (shown in Fig.5.10) yielded a strong Ca, C and O signals together with signals of Mg, Na, S and Cl. The EDAX spectrum after the formation of $CaCO_3$ clearly shows the presence of Mg ions as well as the Na and S signals coming from AOT (curve 1 in Fig.5.15A). The presence of Cl signal is possibly due to the $CaCl_2$ and $MgCl_2$ precursor used for initial reaction, remained even after through washing of the resulting $CaCO_3$ crystals. An analysis of the EDAX data yielded an average Ca : C : O atomic ratio of 1 : 1.7 : 4.3 with Ca : Mg in a atomic ratio of 10 : 0.89 which is approximately equal to the 10 : 1 molar ratio of the initial precursor used.

The EDAX analysis of the porous $CaCO_3$ crystals synthesized in the aqueous foam with a Ca : Mg ratio of 100 : 1 and 5 hrs of drainage experiment (shown in Fig.5.11A & B) yielded Ca, C and O with expected stoichiometric ratios along with Mg, Na, S and Cl signals as well (curve 2 in Fig.5.15A). The EDAX spectrum clearly shows the presence of Mg in this case as well with Na and S component from AOT (curve 2 in Fig.5.15A). An analysis of the EDAX data in this case yielded an average Ca : Mg in a atomic ratio of 100 : 0.83 which is approximately equal to the 100 : 1. Similarly, EDAX analysis of the $CaCO_3$ crystals synthesized in the aqueous foam with a Ca : Mg ratio of 100 : 1 and 10 min of drainage experiment (shown in Fig.5.11C & D) yielded Ca, C and

O with a expected stoichiometric ratios with Mg, Na, S and Cl signals as well (curve 3 in Fig.5.15A). The EDAX spectrum clearly shows the presence of Mg ions in this case as well with Na and S component from AOT. The EDAX data yielded an average Ca : Mg in a atomic ratio of 100 : 0.86.

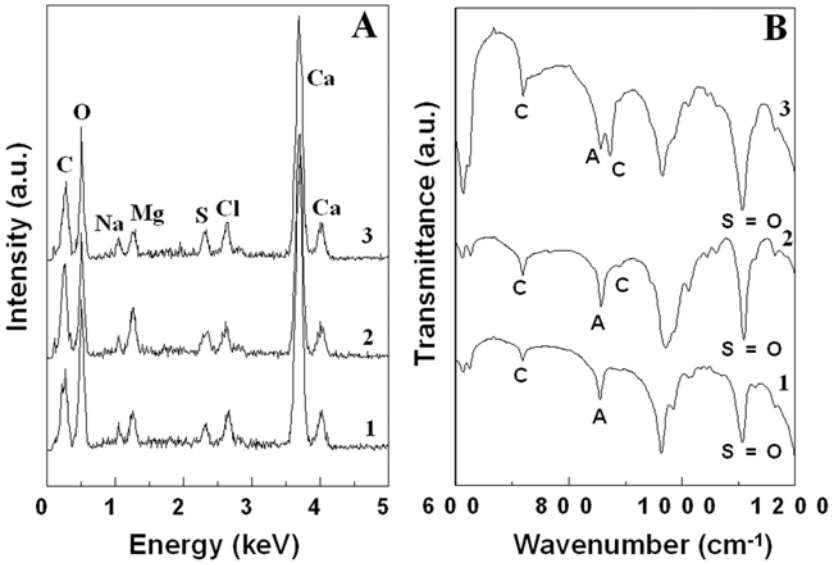

Fig.5.15: *EDAX (A) and FTIR (B) spectra recorded from $CaCO_3$ crystals synthesized by treating AOT + $CaCl_2$ + $MgCl_2$ (Ca : Mg = 10 : 1) foam with Na_2CO_3 solution after allowing the foam to drain for 5 hours (curve 1) and AOT + $CaCl_2$ + $MgCl_2$ (Ca : Mg = 100 : 1) foam with Na_2CO_3 solution after allowing the foam to drain for 5 hours (curve 2) and 10 minutes (curve 3) respectively. (In the FTIR spectra, A – stands for aragonite and C – stands for calcite).*

FTIR measurement of the needle shaped $CaCO_3$ crystals (Fig.5.10) is shown as curve 1 in Fig.5.15B, exhibited prominent absorption bands at 717, 857 and 1105 cm^{-1}. The strong absorption band at 857 cm^{-1} is characteristic of aragonite polymorph of $CaCO_3$ [15]. The weak absorption band at 717 cm^{-1} is attributed to calcite polymorph of $CaCO_3$. The characteristic IR absorption peak of aragonite at 855 cm^{-1} shifts to 857 cm^{-1} and that for calcite at 712 cm^{-1} shifts to 717 cm^{-1}. These shift to longer wavenumbers of aragonite and calcite absorption bands are due to Mg substitution in the $CaCO_3$ lattice which causes increased structural disorder [13g,h]. The characteristic IR absorption peak of S=O stretching vibration of the sulfonate group present in the AOT molecules at 1057 cm^{-1} shifts to 1105 cm^{-1} clearly indicates the electrostatic complexation of Ca^{2+} ions with the sulfonate groups of AOT [16].

FTIR measurement from the rhombic $CaCO_3$ porous plates (Fig.5.11A & B) is shown as curve 2 in Fig.5.15B. It exhibits strong absorption band at 856 cm^{-1} indicating the aragonite formation in this case as well with an increase in the absorption band for calcite at 713 cm^{-1}. A weak absorption band of calcite at 875 cm^{-1} arose in this case indicating the formation of a mixed phase of $CaCO_3$ [15]. The shifted S=O stretching vibration at 1105 cm^{-1} in the FTIR spectrum indicates the presence of AOT molecule in the $CaCO_3$ crystals formed. FTIR measurement from the solid rhombic $CaCO_3$ plates (Fig.5.11C & D) is shown as curve 3 in Fig.5.15B, exhibited strong absorption bands at 713 and 875 cm^{-1} indicating the formation calcite with a weak absorption band for aragonite at 856 cm^{-1} with a shifted S=O (1105 cm^{-1}) stretching vibration coming from AOT molecule present.

5.4.5 Atomic absorption spectroscopy (AAS) studies

The amount of metal ion uptake in the foam was estimated by a chemical analysis method of the foam by atomic absorption spectroscopy (AAS). The $CaCO_3$ crystals formed in the foam at different Mg ion concentrations were subjected to AAS measurements to estimate correctly the amount of the metal ions present in the solution obtained from foam. From AAS measurements the Ca : Mg ratios are obtained to be 10 : 1. 72 (Ca : Mg molar ratio = 10 : 1 experiment) and 100 : 2.86 (Ca : Mg molar ratio = 100 : 1 experiment). The increase in concentration of Mg^{2+} ions in the foam relative to the starting concentration in solution is possibly due to the stronger interaction of Mg^{2+} ions with AOT relative to Ca^{2+} ions.

5.4.6 X-ray diffraction measurements

The XRD pattern recorded from the needle shaped $CaCO_3$ crystals shown in Fig.5.10 cast in the form of a film on a glass substrate shows a number of Bragg reflections characteristic of the aragonite (indicated by 'A') [11] polymorph along with a small percentage of calcite (indicated by 'C') [11] and is shown as curve 1 in Fig.5.16. The broadening in the Bragg reflections in the XRD data (Fig.5.16, curve 1) is in agreement with the extremely small size $CaCO_3$ crystals observed in the SEM and TEM images. The XRD data recorded from the $CaCO_3$ crystals shown in Fig.5.11 indicate the formation of mixed phase of aragonite and calcite polymorphs (curve 2 & 3 in Fig.5.16).

It is observed that the Bragg reflections for calcite are more prominent in these cases compare to those observed with a higher magnesium concentration experiment (curve 1 in Fig.5.16). The XRD peaks are relatively broad indicating that the observed porous and solid $CaCO_3$ crystals are indeed made up of much smaller crystallites.

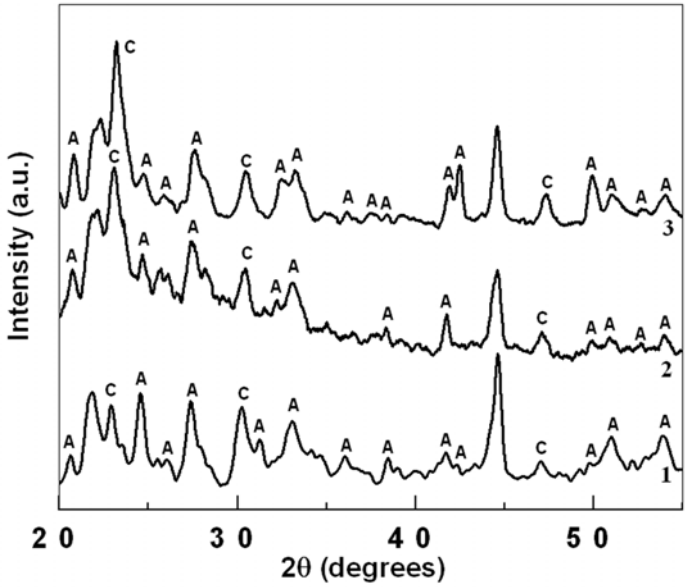

Fig.5.16: *XRD patterns recorded from $CaCO_3$ crystals grown by treating AOT + $CaCl_2$ + $MgCl_2$ (Ca : Mg = 10 : 1) foam with Na_2CO_3 solution after allowing the foam to drain for 5 hours (curve 1) and AOT + $CaCl_2$ + $MgCl_2$ (Ca : Mg = 100 : 1) foam with Na_2CO_3 solution after allowing the foam to drain for 5 hours (curve 2) and 10 minutes (curve 3) respectively (A – stands for aragonite and C – stands for calcite).*

5.4.7 Summary

We investigate the role of magnesium ions as an additive in controlling the morphology and crystallography of $CaCO_3$ in the foam lamellae. The presence of Mg^{2+} ions causes considerable changes in the morphology of $CaCO_3$ crystals in the foam. While, aragonite polymorph of $CaCO_3$ in a fractured needle like morphology was stabilized with a higher Mg^{2+} ion concentration, porous rhombic $CaCO_3$ crystals in a mixed calcite and aragonite polymorph were formed with a lower Mg^{2+} ion concentration in the aqueous foam.

5.5 Discussion

Based on the above studies, we believe the formation of $CaCO_3$ spheroids consisting of flat, plate-like calcite subunits arises from a mesoscale self-assembly process [17] as described below. The collapse of the foam consequent to Na_2CO_3

treatment and $CaCO_3$ formation is quite slow (ca. 15-20 min collapse time) and hence it may be reasonably assumed that the assembly of spheroaggregates of flat calcite platelets does not occur during collapse of the foam. The formation of the calcite platelets and assembly into spherical superstructures therefore takes place in the in-tact foam lamellae. The presence of AOT on the surface of the calcite spheroaggregates inferred from the contact angle measurements indicates that hydrophobic interactions between the AOT-capped calcite platelets is responsible for the assembly, possibly in the following manner. The plateau borders shown in Fig.5.3 provide an anisotropic confinement to the solution trapped in between them and also act as planar charged templates for immobilizing oppositely charged species. Comparatively, the plateau junctions encompass a greater volume of solution and are more isotropic in spatial extent. The thickness of both the plateau borders and the plateau junctions decreases with increasing time of drainage as the foam dries. As mirrored by the SEM images (Fig.5.5A & B), the $CaCO_3$ platelets constituting the spherical aggregates are most likely synthesized in the plateau border regions. During treatment of the foam with Na_2CO_3 solution, we believe that hydrodynamic flow of the liquid through the foam by capillary action drives the calcite platelets synthesized in the plateau border regions to the more capacious plateau junctions where they aggregate via hydrophobic association. Hydrophobic forces being non-directional, the aggregates tend to attain a spherical morphology, this structure being the most energy conserving. This is also evidenced from the morphology of the $CaCO_3$ particles synthesized in AOT foam after different times of drainage (Fig.5.6). At lower times of drainage (10 and 30 minutes), when the plateau border regions contain greater amount of entrapped water, hydrodynamic flow during treatment with Na_2CO_3 drives the platelets formed in these regions to the plateau junctions where they get aggregated. Whereas at higher drainage times, the plateau borders are thin and consequently hydrodynamic flow is minimized in the plateau border regions. Formation of the smooth surfaced compact spherical particles could be a result of further growth of calcite on the aggregated $CaCO_3$ spherical particles. It is expected that at lower drainage times, more Ca^{2+} ions are present in the foam lamellae along with water that would be available for secondary growth on the spheroaggregates. This possibly leads to the observed increase in porosity with increasing drainage time scales in the $CaCl_2$ – AOT foam and is

supported by the fact that the size of most of the spherical aggregates that are clearly visible as aggregates of platelets is less than the size of the smooth surfaced spherical particles. Thus the dynamic nature of the foam lamellae does play a crucial role in yielding spherical calcite particles since such structures have not been observed in $CaCO_3$ crystallization at static interfaces such as Langmuir monolayers [18]. It is also possible that, the formation of vaterite crystals (with spherical morphology) and aragonite crystals followed by their recrytallization into calcite could provide an alternative mechanism for the formation of spheroaggregates of calcite. Because it is known that vaterite formation in aqueous solution is favored under conditions of high HCO_3^- to Ca^{2+} ratio, whereas calcite is favored at stiochiometric proportions [19]. Under such conditions, positively charged surfaces of $CaCO_3$ are covered with carbonate anions. Thus, a high charge density at the surface could kinetically favor vaterite nuclei through stabilization of disordered clusters of excess charge. It is possible that during spraying of Na_2CO_3 into the Ca^{2+}-AOT foam, an excess of carbonate ions in comparison with calcium ions is temporarily created and thus to the stabilization of vaterite in the foam lamellae. On this basis, the formation of hollow cores in the spherical aggregates may also be explained as arising due to partial dissolution of the vaterite component and recrystallization into calcite.

The morphology of Mg^{2+} mediated $CaCO_3$ crystals in AOT foam are very different from that without Mg^{2+} ions. As mirrored by the SEM and TEM images (Figs.5.10 & 5.13), the $CaCO_3$ fine needles are most likely synthesized in the plateau border regions reflecting its narrow confinement. During treatment of the foam with Na_2CO_3 solution, we believe that even though the hydrodynamic flow of the liquid through the foam by capillary action drives the calcite needles to the more capacious plateau junctions, they do not aggregates into bigger structures at the junction because the high Mg^{2+} concentration stabilizes them. Where as with a lower Mg^{2+} concentration, rhombic porous calcite plates (Figs.5.11 & 5.14) are observed, which are bigger in size and are possibly synthesized in the plateau junction. The porous nature of calcite plates is due to the presence of Mg^{2+} ions inducing defects in the $CaCO_3$ lattice planes. It is also possible that the metastable aragonite phase form first and may subsequently transform into magnesian calcite. At lower time of drainage (10 min) when the plateau borders and

junctions contain greater amount of entrapped water, the formation of rhombic $CaCO_3$ crystals is observed with no sign of porosity, because of the high water content. It is expected that at a lower drainage time, more Ca^{2+} ions are present in the foam lamellae along with water that would be available for secondary growth on the porous calcite crystals leading to the formation of compact solid surface. Accordingly, a through understanding of the $CaCO_3$ – Mg system requires an accurate assessment of the extent to which Mg^{2+} modifies $CaCO_3$ solubility. We believe that small concentrations of additives typically affect crystallization via adsorption of the active molecules at a number of growth sites on the surface of pre-critical nuclei, which consequently prevents their growth. Incorporation of small amounts of inhibitors into a crystallite may also create internal strain, thus increases the solubility and the critical size required for a stable precipitate.

5.6 Conclusions

The crystallization of calcite in the form of spheroaggregates in aqueous foam stablilized by the surfactant AOT by a method of ion entrapment has been demonstrated. Reaction of Na_2CO_3 with Ca^{2+} ions electrostatically entrapped in the foam results in the formation of flat, plate-like calcite crystals, possibly in the plateau border regions of the foam. Hydrodynamic flow patterns in the foam are believed to transport the calcite platelets from the plateau border regions into the larger plateau junctions where they assemble into spherical structures by hydrophobic association. The presence of Mg^{2+} ions causes considerable changes in the morphology of $CaCO_3$ crystals, which may be important in the construction of architecturally complex structures produced by organisms for specific purposes. A combination of extremely large interfacial templating area provided by the liquid lamellae in foams stabilized by ionizable surfactants and the dynamic nature of the foam bubbles makes this method potentially exciting for the large-scale synthesis of important minerals.

5.7 References

[1] Matijevic, E. *Curr.Opin.Colloid Interface Sci*. **1996**, *1*, 176.

[2] (a) Orme, C. A.; Noy, A.; Wierzbicki, A.; McBride, M. T.; Grantham, M.; Teng, H. H.; Dove, P. M.; DeYoreo, J. J. *Nature* **2001**, *14*, 775. (b) Kroger, N.; Deutzman, R.;

Sumper, M. *Science* **1999**, *286*, 1129. (c) Pum, D.; Sleytr, U. B. *Trends Biotechnol.* **1999**, *17*, 8. (d) Sleytr, U. B.; Messner, P.; Pum, D.; Sara, M. *Angew. Chem. Int. Ed.* **1999**, *38*, 1034.

[3] (a) Davis, S. A.; Breulmann, M.; Rhodes, K. H.; Zhang, B.; Mann, S. *Chem. Mater.* **2001**, *13*, 3218. (b) Whitesides, G. M.; Mathias, J. P.; Seto, C. T. *Science* **1991**, *254*, 1312.

[4] Schwartz, D. K. *Annu. Rev. Phys. Chem.* **2001**, *52*, 107.

[5] Dong, B.-D.; Cilliers, J.J.; Davey, R.J.; Garside, J.; Woodburn, E.T. *J.Am.Chem.Soc.* **1998**, *120*, 1625.

[6] (a) Mandal, S.; Arumugam, S. K.; Adyanthaya, S. D.; Pasricha, R.; Sastry, M. *J. Mater. Chem.* **2004**, *14*, 43. (b) Mandal, S.; Arumugam, S. K.; Pasricha, R.; Sastry, M. *Appl. Nano Sci.* **2004** (In Press). (c) Bala, T.; Arumugam, S. K.; Pasricha, R.; Prasad, B. L. V.; Sastry, M. *J. Mater. Chem.* **2004**, *14*, 1057. (d) Bala, T.; Bhame, S. D.; Joy, P. A.; Prasad, B. L. V.; Sastry, M. *J. Mater. Chem.* **2004**, *14*, 2941. (e) Shankar, S. S.; Patil, U. S.; Prasad, B. L. V.; Sastry, M. *Langmuir* **2004**, *20*, 8853.

[7] (a) Berkman, S.; Egloff, G. "The Physical Chemistry of Foams" *Eighty Fifth Meeting of the American Chemical Society, Washington, D. C.* March **1933**. (b) Hedreul, C.; Frens, G. *Colloids and Surfaces A: Physicochem. Eng. Aspects* **2001**, *186*, 73. (c) Gardiner, B. S.; Dlugogorski, B. Z.; Jameson, G. J. *Ind. Eng. Chem. Res.* **1999**, *38*, 1099. (d) Tchoukov, P.; Mileva, E.; Exerowa, D. *Langmuir* **2003**, *19*, 1215. (e) Neethling, S. J.; Lee, H. T.; Cilliers, J. J. *J. Phys.: Condens. Matter* **2003**, *15*, 1563.

[8] (a) Colfen, H.; Antonietti, M. *Langmuir* **1998**, *14*, 582. (b) Yu, S. H.; Colfen, H.; Hartmann, J.; Antonietti, M. *Adv. Funct. Mater.* **2002**, *12*, 541.

[9] Yu, S. H. ; Colfen, H. ; Antonietti, M. *J. Phys. Chem. B*, **2003**, *107*, 7396.

[10] Busch, S.; Dolhaine, H.; Duchesne, A.; Heinz, S.; Hochrein, O.; Laeri, F.; Podebrad, O.; Vietze, U.; Weiland, T.; Kniep. R. *Eur. J. Inorg. Chem.* **1999**, 1643.

[11] The XRD patterns were indexed with reference to the unit cell of the calcite, aragonite and vaterite structure from *ASTM* chart card nos. 5-0586, 5-0453 and 2-0261 respectively.

[12] De Leeuw, N. H. *J. Phys. Chem. B* 2002, **106**, 5241-5249.

[13] (a) Rajam, S.; Mann, S. *J. Chem. Soc.*, *Chem. Commun.* **1990**, 1789. (b) Davis, K. J.; Dove, P. M.; Yoreo, J. D. *Science* **2000**, *290*, 1134. (c) Han, Y. J.; Aizenberg, J. *J. Am. Chem. Soc.* **2003**, *125*, 4032. (d) Zhang, Y.; Dawe, R. A. *Chemical Geology* **2000**, *163*, 129. (e) Sugawara, A.; Kato, T. *Chem. Commun.* **2000**, 487. (f) Meldrum, F. C.; Hyde, S. T. *J. Crystal Growth* **2001**, *231*, 544. (g) Falini, G.; Fermani, S.; Gazzano, M.; Ripamonti, A. *J. Mater. Chem.* **1998**, *8*, 1061. (h) Loste, E.; Wilson, R. M.; Seshadri, R.; Meldrum, F. C. *J. Crytal Growth* **2003**, *254*, 206.

[14] Stanley, S. M.; Ries, J. B.; Hardie, L. A. *Proc. Natl. Acad. Sci. USA* **2002**, *99*, 1523.

[15] (a) Nassrallah-Aboukais, N.; Boughriet, A.; Laureyns, J.; Aboukais, A.; Fischer, J. C.; Langelin, H. R.; Wartel, M. *Chem. Mater.* **1998**, *10*, 238. (b) Falini, G.; Albeck, S.; Weiner, S.; Addadi, L. *Science* **1996**, *271*, 67.

[16] Spectrometric Identification of Organic Compounds (Silverstein, R. M.; Webster, F. X.) *John Wiley & Sons, Inc.* (Sixth Edition, P-107).

[17] Yu, S. H.; Colfen, H.; Xu, A. W.; Dong, W. *Crystal Growth & Design* **2004**, *4*, 33.

[18] Loste, E.; Diaz-Marti, E.; Zarbakhsh, A.; Meldrum, F.C. *Langmuir* **2003**, *19*, 2830.

[19] Naka, K.; Chujo, Y. *Chem. Mater.* **2001**, *13*, 3245.

CHAPTER VI

Nano-Gold Membranes as Scaffolds for the Growth of Minerals

This chapter discusses the use of free-standing gold nanoparticle membranes to induce and support inorganic crystal growth, which has important implications in biomedical applications such as bone-implants. Calcium phosphate and carbonate crystal growth on suitably functionalized gold nanoparticle membranes was accomplished by first electrostatically complexing Ca^{2+} ions with gold nanoparticle surface-bound carboxylic acid groups and thereafter, reacting/exposing this material to $NH_4H_2PO_4/CO_2$ gas. The nature of calcium phosphate and carbonate crystals formed were found to be strong functions of the nanogold surface modifier. The control of mineralization process on the gold nanoparticles embedded in a polymeric membrane was successfully compared with the crystal growth on the amino acid protected bare gold nanoparticles. Control experiments indicated that surface modification of the gold nanoparticles is a key step to ensure efficient mineralization.

Part of the work presented in this chapter has been published and patented:

1) Rautaray, D.; Kumar, S. P.; Wadgaonkar, P.; Sastry, M.; *Chem. Mater.* **2004**, *16*, 988-993. 2) Rautaray, D.; Mandal, S.; Sastry, M. *Langmuir* **2004**, (In Press). 3) Rautaray, D.; Sastry, M. *J. Mater. Chem.* **2004**, (Accepted). 4) Murali Sastry, Debabrata Rautaray; *US Patent filed* (CSIR320fn2004).

6.1 Introduction

Inorganic composites are of special interest for biomedical applications such as in dental and bone implants wherein the ability to modulate the morphology and size of the inorganic crystals is important [1]. Current strategies for bone tissue regeneration focus on the development of implantable matrices that mimic biological tissues [2,3]. Thus, the treatment of large bone defects by composite materials combing new carrier and release systems for growth factors remain the central field of interest for researchers. Hence, it is necessary to create an artificial three-dimensional scaffold-like porous material with certain geometrical structure to induce bone growth [3].

Earlier reports on the biomineralization of bone involved the deposition of apatitic crystals on a matrix rich in collagen fibrils, the structural macromolecules that create the scaffold within which the biological mineral is formed [4]. Furthermore, the biological matrix contains acidic macromolecules rich in negatively charged groups, mainly carboxylates but also sulfates and phosphates [4,5]. These macromolecules are believed to control nucleation, polymorphism, and growth of the crystals [6]. The presence of these acidic macromolecules usually inhibits the nucleation and growth of calcium salts in aqueous solution, whereas they promote calcification when adsorbed on a substrate [7].

Calcium phosphate and carbonate minerals are classified as bioactive ceramics and have been widely used for the reconstruction of bone defects [3]. In bone implant applications, inorganic composites, mainly made of hydroxyapatite [$Ca_{10}(PO_4)_6(OH)_2$; HAP] ceramics, have attracted a great deal of attention due to their excellent biocompatibility and bioaffinity [3]. HAP is the main mineral constituent of natural bone, and holds great promise to create an excellent bond with natural tissue and may even stimulate new bone growth [8]. Many attempts have been made to fabricate well-crystallized HAP fine particles [9], but very few attempts have yet been successful. Crystallization of many sparingly soluble salts also involves in the formation of metastable precursor phases such as amorphous calcium phosphate (ACP), which subsequently dissolve and transform as the precipitation reaction proceeds to the thermodynamically more stable HAP [10].

Therefore, development of experimental processes for the synthesis of biocompatible surfaces that would induce and support mineral growth is important not

only from a fundamental point of view but also in biomedical applications such as bone implants/grafting in bone surgery [3] and manufacture of artificial tissues [11]. It is clear from the above that while a number of biocompatible surfaces do exist for mineral growth, very few of them actually present malleable/ductile materials that could be suitably molded for bone-implant applications. With this goal in mind, we have investigated the possibility of using membranes of gold nanoparticles in a polymeric background for mineral growth. There are two main reasons for using a gold nanoparticle membrane in such an application. The first is that polymeric membranes would be simple to handle and sculpt to the desired shape and size. The second is that the chemistry pertaining to surface modification of gold nanoparticles is very well understood [12]. It should therefore be relatively straightforward to derivatize the gold nanoparticle membrane with functional groups capable of inducing mineral growth. We demonstrate that a free-standing gold nanoparticle membrane synthesized at the interface between chloroform containing bis(2-(4-aminophenoxy)ethyl)ether (DAEE) and aqueous chloroauric acid solution and thereafter functionalized with the amino acids, cysteine and aspartic acid as well as the bifunctional molecule, anthranilic acid, is an excellent material for the growth of calcium carbonate and calcium phosphate. The membrane is formed spontaneously by the reduction of $AuCl_4^-$ ions by DAEE, this process leading to the formation of gold nanoparticles. The concomitant process of oxidation of DAEE leads to the creation of a polymeric matrix in which the gold nanoparticles are embedded. The gold nanoparticle membrane is extremely stable, robust, easily handled, malleable and can be grown over large areas and thickness by suitably varying the experimental conditions [13]. Calcium phosphate and carbonate crystal growth on suitably functionalized gold nanoparticle membranes was accomplished by first electrostatically complexing Ca^{2+} ions with gold nanoparticle surface-bound carboxylic acid groups (by immersion of the membrane in aqueous $CaCl_2$ solution) and thereafter, reacting/exposing this material to $NH_4H_2PO_4/CO_2$ gas. The control of mineralization process on the gold nanoparticles embedded in a polymeric membrane was successfully compared with the crystal growth on the amino acid protected bare gold nanoparticles.

6.2 Mineral growth on surface functionalized gold nanoparticles

The synthesis of calcium phosphate and calcium carbonate crystals on free-standing carboxylic acid-functionalized gold nanoparticle membranes and on amino acid-protected bare gold nanoparticles were achieved as follows:

1) Calcium phosphate crystallization on suitably functionalized gold nanoparticle membranes and on functionalized bare gold nanoparticles was accomplished by first electrostatically complexing Ca^{2+} ions with gold nanoparticle surface-bound carboxylic acid groups (by immersion of the nanoparticle membrane/nanoparticles in aqueous $CaCl_2$ solutions) and thereafter, reaction of the material with ammonium dihydrogen orthophosphate ($NH_4H_2PO_4$).
2) Calcium carbonate crystallization on suitably functionalized gold nanoparticle membranes and on functionalized bare gold nanoparticles was accomplished by first electrostatically complexing Ca^{2+} ions with gold nanoparticle surface-bound carboxylic acid groups (by immersion of the nanoparticle membrane/nanoparticles in aqueous $CaCl_2$ solutions) and thereafter, exposing this materials CO_2.

6.2.1 Mineral growth on free-standing gold nanoparticle membranes

6.2.1.1 Preparation of gold nanoparticle membrane

In a typical experiment, 30 ml of 10^{-3} M chloroauric acid ($HAuCl_4$) and 30 ml of 10^{-3} M bis(2-(4-aminophenoxy)ethyl)ether (DAEE) in $CHCl_3$ were mixed in a beaker and kept under static ambient conditions in the dark for three hours. After three hours of reaction, a purple membrane was observed to have formed at the organic/aqueous liquid-liquid interface [13].

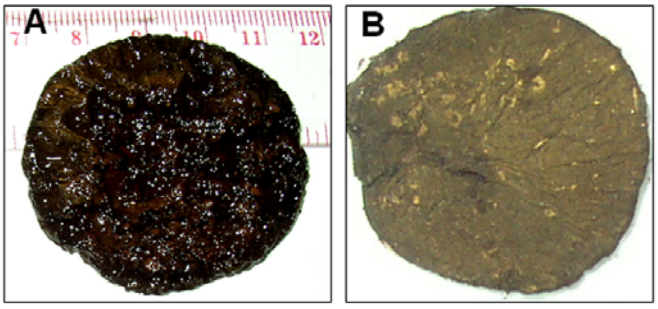

Fig.6.1: *Photographs of as prepared (A) and air-dried (B) free-standing gold nanoparticle membranes.*

Further to removal of the aqueous component of the biphasic mixture, the nanogold membrane was lifted with forceps, washed thoroughly several times with double distilled water and dried before further use (see photograph, Fig.6.1). See reference no.13 for the preparation method of nanogold membrane.

6.2.1.2 Surface modification of nano-gold membrane

The surface modification of the nanogold membranes was done by immersing the as-prepared nanogold membranes in 50 ml of aqueous solutions of 10^{-4} M aspartic acid and cysteine as well as the bifunctional molecule anthranilic acid (H_2N-C_6H_4-COOH) separately for 30 minutes. After surface functionalization, the nanogold membranes were washed thoroughly several times with double distilled water and dried before further use.

6.2.1.3 Calcium phosphate and calcium carbonate crystal growth on functionalized nano-gold membrane

The growth of calcium phosphate and calcium carbonate crystals was achieved separately by simple immersion of the aspartic acid, cysteine and anthranilic acid-functionalized nanogold membranes in aqueous $CaCl_2$ solutions. The resulting Ca^{2+}-bound gold membranes were washed with double distilled water and dried under flowing nitrogen. Thereafter, the growth of calcium phosphate crystals was achieved by immersing the different nanogold membranes in aqueous $NH_4H_2PO_4$ and the growth of calcium carbonate crystals was induced by exposing the different nanogold membranes to CO_2 atmosphere [produced by decomposition of $(NH_4)_2CO_3$)].

Fig.6.2: *A, B and C) shows photographs of $CaCO_3$ crystals grown on aspartic acid, cysteine and anthranilic acid functionalized gold nano particle membranes respectively (Scale bar is same for all).*

Consequent to formation of calcium phosphate and carbonate crystals, the color of the membrane changed from purple to a dull/dark grey. Photographs A-C in Fig.6.2 shows

$CaCO_3$ crystals grown on aspartic acid, cysteine and anthranilic acid functionalized gold nanoparticle membranes respectively. Upon formation of $CaCO_3$ crystals on the functionalized gold nanoparticle membranes, lots of white bright spots can clearly be seen (Fig.6.2A, B & C) attributed to $CaCO_3$ crystal growth, in contrast to the as-prepared nano-gold membrane (purple in color, Fig.6.1B). The resultant calcium phosphate/carbonate-nanogold membranes were washed with double distilled water prior to FTIR, XRD, SEM and EDAX analysis.

6.2.2 Mineral growth on functionalized bare gold nanoparticles

In this part of experiments, 100 ml of 10^{-4} M aqueous solution of $HAuCl_4$ was reduced by 0.01 gm of sodium borohydride ($NaBH_4$) at room temperature to yield colloidal gold particles. This procedure results in a ruby red solution (pH 8.5) containing gold nanoparticles of diameter 6.5 ± 1 nm. The colloidal gold particles were capped by addition of 10 ml of an aqueous solution of 10^{-3} M aspartic acid to 90 ml of the gold hydrosol and then the solution was allowed to age for 12 h. Uncoordinated aspartic acid in solution was removed by thoroughly dialyzing the aspartic acid-capped gold nanoparticle solution against distilled water for 2 days, using a 12 kDa cutoff dialyzing bag. The dialyzed solution was extremely stable over time. To 18 ml of the dialyzed aspartic acid-capped gold nanoparticle solution, 2 ml of 10^{-2} M aqueous solution of $CaCl_2$ was added under continuous stirring for 10 minutes and then allowed to age for 1 h. The solution changed color from ruby red to blue indicating slight aggregation of gold nanoparticles. Even though aggregation of the gold nanoparticles was indicated, the blue solution was exceptionally stable over a period of several weeks. Isothermal titration calorimetric (ITC) measurements were carried out to characterize the interaction between aspartic acid-capped gold nanoparticles and calcium ions. UV-vis spectroscopy measurements were carried out of the aspartic acid-capped gold nanoparticle solution at different stages of treatment. Thereafter, to the Ca^{2+}-aspartic acid-capped gold nanoparticle solution, 2 ml of 10^{-2} M aqueous solution of $NH_4H_2PO_4$ was added and as the reaction proceeded, an insoluble precipitate was formed. The overall reaction took place within 1 h and removal of the solvent (water) by rotovapping resulted in a dry, grey powder of calcium phosphate crystals. To remove the non-reacted Ca^{2+} and PO_4^{3-} ions,

the powder was repeatedly washed with distilled water and then redispersed in deionized water and undergone FTIR, XRD, TEM, SEM and EDAX analysis.

6.3 Calcium phosphate crystal growth on functionalized nano-gold membrane

The growth of calcium phosphate crystals on free-standing carboxylic acid-functionalized gold nanoparticle membranes was accomplished by simple immersion of the aspartic acid, cysteine and anthranilic acid-functionalized nanogold membranes in 50 ml of 10^{-3} M aqueous $CaCl_2$ (pH – 6.2) solutions for 12 hours. The resulting Ca^{2+}-bound gold membranes were immersed in 50 ml of 10^{-3} M aqueous $NH_4H_2PO_4$ (pH – 7.6).

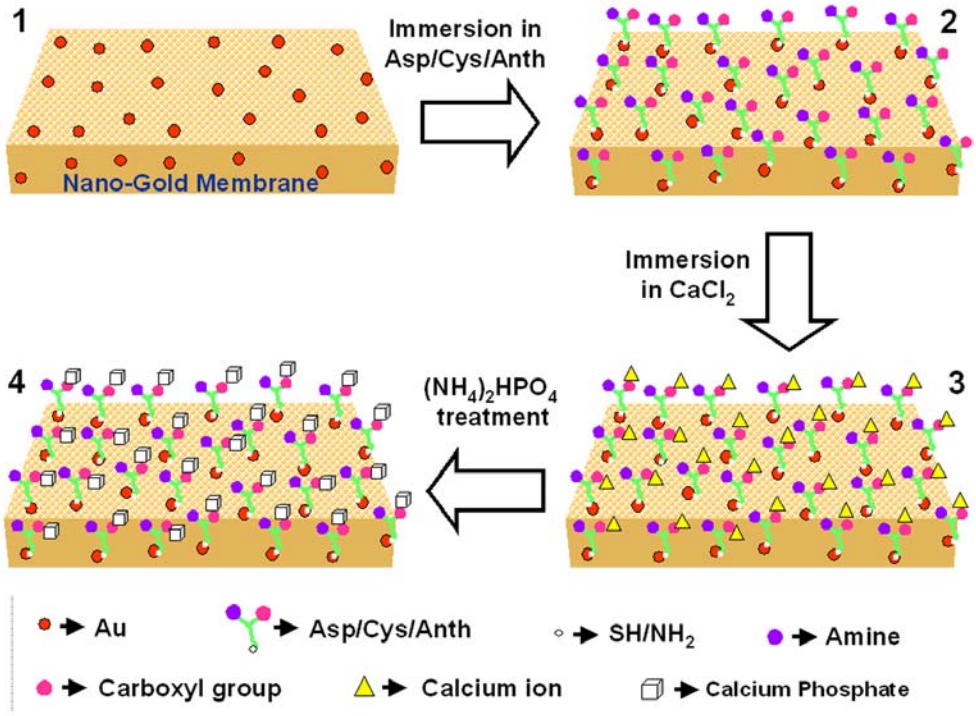

Fig.6.3: *Scheme showing different steps involved during the growth of calcium phosphate crystals on free standing gold nanoparticle membrane. Step 1 – shows as prepared gold nanoparticle membrane. Step 2 – Functionalization of the gold nanoparticle membrane by aspartic acid, cysteine and anthranilic acid respectively. Step 3 – Immobilization of Ca^{2+} ions to the functionalized gold nanoparticle membrane. Step 4 – Ca^{2+} – nano-gold membrane after reaction with $(NH_4)_2HPO_4$.*

Scheme in Fig.6.3 shows the different steps involved during the growth of calcium phosphate crystals by using free-standing gold nanoparticle membrane as a scaffold. The first step in our study is the preparation of nano-gold membrane (step 1) followed by the functionalization of the nano-gold membrane by carboxyl terminated aspartic acid,

cysteine and anthranilic acid respectively (step 2), which then were separately subjected to Ca^{2+} ions immobilization (step 3). Thereafter, the reaction of Ca^{2+}-nanogold membrane with $NH_4H_2PO_4$ resulted in the formation of calcium phosphate crystals (step 4).

6.3.1 Scanning electron microscopy (SEM) measurements

6.3.1.1 Formation of nano-gold membrane

The purple gold nanoparticle membrane formed at the interface between chloroform and water was free-standing and could easily be handled using forceps indicating its robust character (Photographs in Fig.6.1). Fig.6.4A and B show representative SEM images at different magnification of the as-prepared gold nanoparticle membrane. The membrane shows a very highly irregular, polymeric background (A) in which gold nanoparticles are embedded (B) and is hydrophilic in nature (a contact angle of 43^o was measured). The gold nanoparticles themselves appear as bright, spherical structures. The size of the gold nanoparticles in the membrane was estimated to be in the range 60 to 300 nm. The weight percentage contribution of the gold component in the membrane was estimated by thermogravimetric analysis to be ca. 35 %.

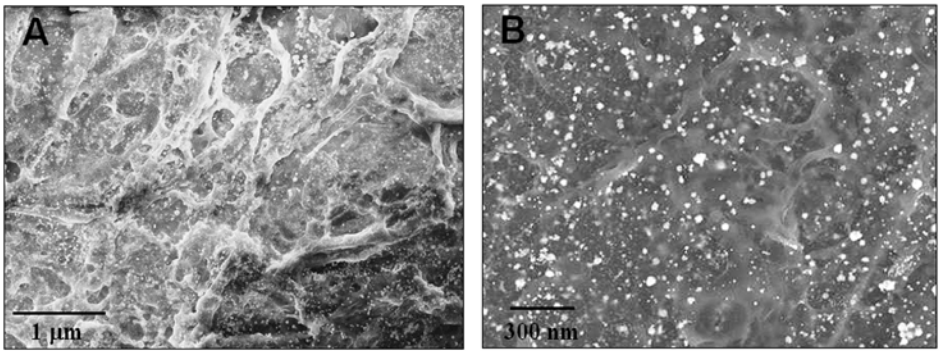

Fig.6.4: *A & B) Low and high magnification SEM micrographs of the as-prepared free-standing gold nanoparticle membrane.*

6.3.1.2 Calcium phosphate growth on aspartic acid functionalized nano-gold membrane

In order to understand the calcium phosphate growth on the aspartic acid functionalized nano-gold membrane better, the kinetics of crystallization was studied by immersion of Ca^{2+}-nano-gold membrane in aqueous $NH_4H_2PO_4$ solution for 6 h and 12 h.

Figs.6.5A & B show representative SEM images of the Ca^{2+}-nano-gold membrane upon immersion in $NH_4H_2PO_4$ solution for 6 h. At low magnification, it is seen that the membrane is very uniformly and densely covered with calcium phosphate (Fig.6.5A). The calcium phosphate crystals are quasi-spherical in morphology and fairly porous. At higher magnification (Fig.6.5B), the calcium phosphate crystals appear to be made up of open, spherical aggregates of needle-like calcium phosphate crystallites.

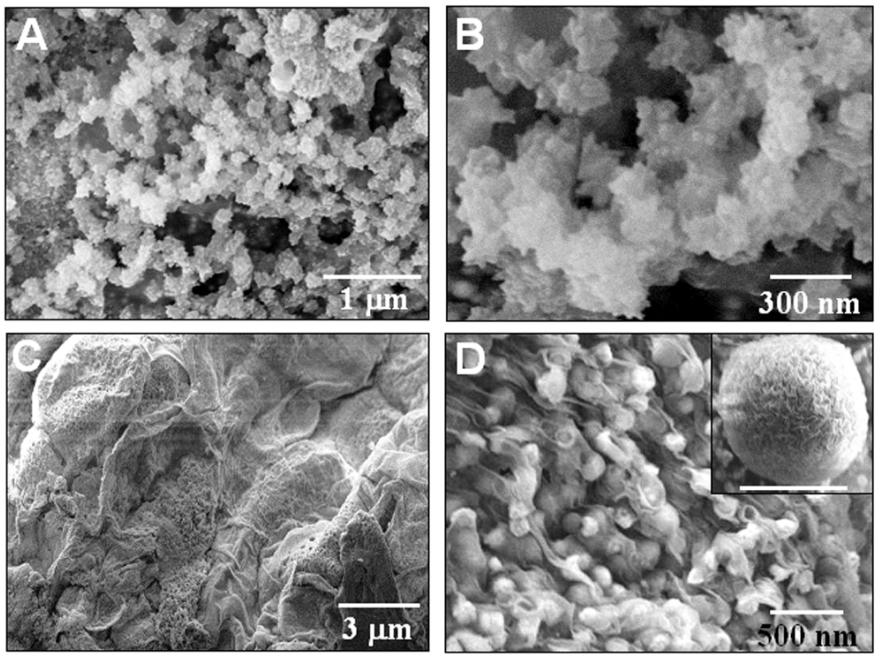

Fig.6.5: *Representative SEM micrographs recorded at different magnifications from calcium phosphate crystals grown after immersion of Ca^{2+}-aspartic acid modified nano-gold membrane in aqueous $NH_4H_2PO_4$ solution for 6 h (A and B) and 12 h (C and D). The inset in D shows a high magnification SEM picture of one of the spherical calcium phosphate crystals shown in the main image (scale bar = 150 nm).*

Figs.6.5C & D show representative SEM images of Ca^{2+}-nano-gold membrane upon immersion in $NH_4H_2PO_4$ solution for 12 h. At low magnification, the membrane is observed to be uniformly bright and covered by a dense assembly of calcium phosphate crystals in very close contact (Fig.6.5C). At higher magnification (Fig.6.5D), clearly formed highly spherical calcium phosphate crystallites bound to the membrane are observed. It is clear that as the time of reaction of the Ca^{2+}-nano-gold membrane with aqueous $NH_4H_2PO_4$ solution increases, the aggregates of needle like calcium phosphate crystals close up (possibly due to secondary nucleation) to yield highly compact spherical aggregates. An interesting feature of the spherical crystal structures is the uniformity in

their shape and size (particle diameters in the range 80-200 nm). At higher magnification (inset of Fig.6.5D), the surface of one of the compact spherical calcium phosphate assemblies appears to be made of smaller platelets/needles in a highly close-packed assembly.

6.3.1.3 Calcium phosphate growth on cysteine-functionalized nano-gold membrane

Figs.6.6A & B show SEM images of calcium phosphate grown on the cysteine-functionalized gold nanoparticle membrane after complexation with Ca^{2+} ions and reaction with $NH_4H_2PO_4$ solution for 12 h. As in the case of the aspartic acid-modified nanogold membrane, the low magnification SEM image (Fig.6.6A) shows extremely dense coverage of calcium phosphate crystals over the membrane surface and within pores of the membrane.

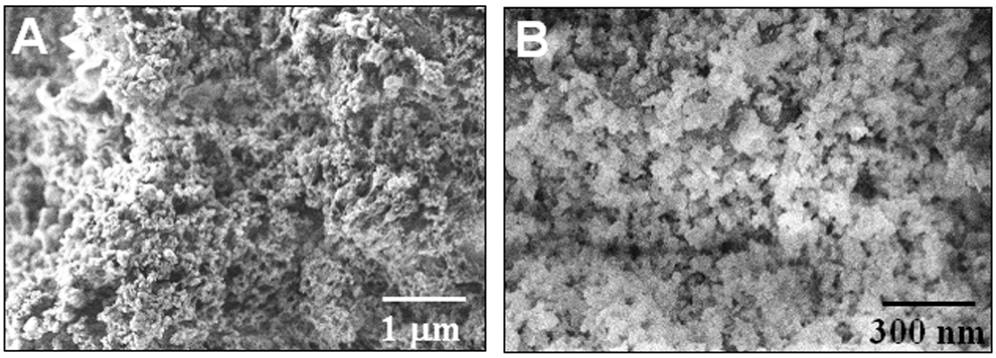

Fig.6.6: *(A & B) Representative SEM micrographs at different magnifications of calcium phosphate crystals grown after immersion of Ca^{2+}-cysteine modified nano-gold membrane in aqueous $NH_4H_2PO_4$ solution for 12 h.*

At higher magnification (Fig.6.6B), the membrane surface is seen clearly to be composed of extremely irregular shaped calcium phosphate crystals. While the morphology of the calcium phosphate crystals grown on the aspartic acid modified gold nanomembrane was predominantly spherical (Figs.6.5C and D), the crystallites are much smaller in the case of cysteine-modified gold nanomembrane and of a more irregular shape. Clearly, the nature of chemical modification of the gold nanoparticle membrane plays an important role in modulating the morphology of the calcium phosphate crystals.

6.3.1.4 Calcium phosphate growth on anthranilic acid functionalized nano-gold membrane

The crystallization of calcium phosphate was also studied using the bifunctional molecule anthranilic acid used as a surface modifier for the nanogold membrane. This molecule is expected to bind to gold nanoparticles through the amine functionality thus exposing carboxylic acid groups on the surface of the membrane. In addition, anthranilic acid possesses an aromatic group and it would be interesting to study the effect of this group on the morphology of the calcium phosphate crystals. The kinetics of crystallization of calcium phosphate on the anthranilic acid modified membrane was studied by immersion of Ca^{2+}-nano-gold membrane in aqueous $NH_4H_2PO_4$ solution for 6 h and 12 h.

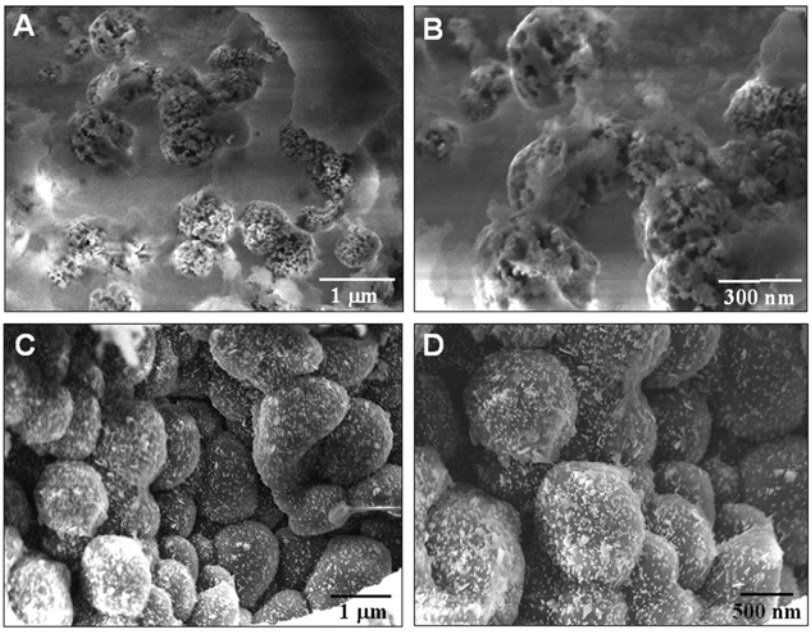

Fig.6.7: *Representative SEM micrographs recorded at different magnifications from calcium phosphate crystals grown after immersion of the Ca^{2+}-anthranilic acid modified nano-gold membrane in aqueous $NH_4H_2PO_4$ solution for 6 h (A and B) and for 12 h (C and D).*

Figs.6.7A & B show representative SEM images of the calcium phosphate crystals grown on the anthranilic acid-functionalized gold nanoparticle membrane after immersion of Ca^{2+}-nano-gold membrane in aqueous $NH_4H_2PO_4$ solution for 6 h. The low magnification SEM image (Fig.6.7A) shows calcium phosphate in a spherical porous structure populating the nanogold membrane surface at relatively low coverage. At higher

magnification (Fig.6.7B), the porous nature of the spherical aggregates can be observed in greater detail. Figs.6.7C & D show low and high magnification SEM images respectively of calcium phosphate crystals grown on the anthranilic acid-functionalized gold nanoparticle membrane after immersion of Ca^{2+}-nano-gold membrane in aqueous $NH_4H_2PO_4$ solution for 12 h. The low magnification SEM image (Fig.6.7C) clearly shows that while the overall morphology of the calcium phosphate crystals is similar to that obtained in the 6 h reaction, the surface coverage is considerably enhanced. Indeed, the underlying membrane cannot be seen in the low magnification SEM image. At higher magnification (Fig.6.7D), the individual spherical crystals are observed to be extremely dense with evidence of secondary nuclei growth on the surface of the crystals. The dense coverage of HAP deposition can be attributed to the porosity of the nanogold membrane, through which a very large fraction of the gold nanoparticles within the membrane are accessible to surface modification by the amino acids and anthranilic acid.

6.3.1.5 Formation of calcium phosphate crystals on non-functionalized nano-gold membrane

In order to understand better the role played by the surface functionality of the nanogold membrane in calcium phosphate crystallization, a control experiment was performed wherein the crystal growth was achieved on the as-prepared nano-gold membrane without prior surface functionalization.

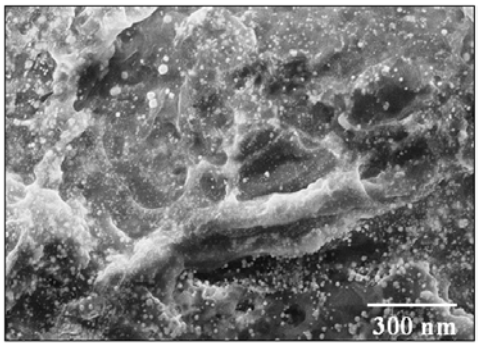

Fig.6.8: *SEM micrograph of calcium phosphate crystals grown on the as-prepared gold nanoparticle membrane without any surface modification.*

Fig.6.8 shows the SEM picture of the nano-gold membrane in this control experiment after calcium phosphate growth. There is no evidence for the presence of calcium phosphate crystals on the surface of the membrane. It is thus evident that modification of

the membrane with functional groups capable of binding Ca^{2+} ions is an essential prerequisite for the formation of calcium phosphate on the gold nanoparticle membrane.

6.3.2 Leaching of the Au nanoparticles from the nano-gold membrane

The gold nanoparticle aggregates in the membrane may be leached out without disturbing the stability and integrity of the polymeric component of the membrane, thus providing an additional degree of freedom in varying the porosity of the membrane. Fig.6.9A shows a photograph of the as-prepared gold nanoparticle membrane, which exhibits a golden luster. It is known that gold can be oxidized into Au^{3+} ions using a saturated I_2 solution in KI and therefore, a simple experiment based on leaching of the Au nanoparticles using I_2 was carried out. The gold nanoparticle membrane was kept in the iodine solution for 6 h. During leaching out of Au nanoparticles, the membrane was observed to change from a golden color to black (photograph in Fig.6.9B). A blackish and highly stable membrane that was amenable to lifting, folding etc. was obtained after complete removal of gold nanoparticles.

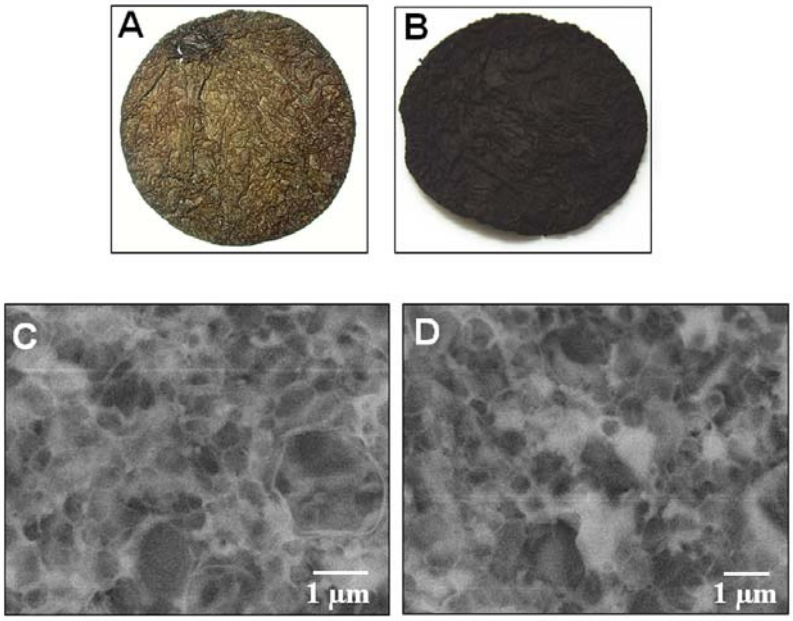

Fig.6.9: *(A) Photographs of the air-dried, as prepared free-standing gold nanoparticle membrane and (B), this membrane after complete leaching out of the gold nanoparticles by iodine treatment. (C) SEM micrograph of the structurally intact porous membrane after complete leaching out of the gold nanoparticles by iodine treatment. (D) SEM micrograph of calcium phosphate grown on the membrane minus the gold nanoparticles.*

Fig.6.9C shows an SEM image of the membrane after removal of the gold nanoparticles by iodine treatment. A comparison of the SEM images of the membrane before (Fig.6.4B) and after gold nanoparticle removal (Fig.6.9C) indicates that the membrane becomes more porous after gold removal. The polymeric network is clearly seen with gaps where the gold nanoparticles were originally embedded. The sizes of the hollow structures are comparable to the size of the gold nanoclusters. The membrane minus the gold nanoparticles would provide an ideal model system to establish the role of the gold component and surface modifiers in directing mineral growth in the nanogold membrane. Accordingly, another control experiments were performed wherein calcium phosphate crystallization was attempted on the membrane after gold leaching (before and after immersion in aspartic acid, cysteine and anthranilic acid solutions separately) as a crystallizing template. Fig.6.9D shows the SEM image of the membrane after gold leaching in one of the above control experiments after calcium phosphate growth. There is no evidence for the presence of calcium phosphate crystals on the surface of the membrane (Fig.6.9D).

6.3.3 Quantitative estimation of calcium phosphate on the nano-gold membrane

After the formation of calcium phosphate crystals on the surface functionalized nanogold membranes, the membranes were immersed in acidic solution to dissolve the calcium phosphate component. From the difference in weight of the membranes before and after calcium phosphate removal, the weight percentage contributions of calcium phosphate to the nanogold membranes were estimated to be 1.62, 1.49 and 2.12 weight % for calcium phosphate crystals growth on aspartic acid, cysteine and anthranilic acid-functionalized nanogold membranes respectively.

6.3.4 Energy dispersive analysis of X-rays (EDAX) analysis

Selected area EDAX measurements carried out on the as-prepared membrane (curve 1 in Fig.6.10A) indicated that polymeric membrane indeed contained a large concentration of gold nanoparticles. Along with a prominent Au peak, N, C and O signals are also observed in the EDAX spectrum of the nanogold membrane (curve 1 in Fig.6.10A) and is consistent with the chemical composition of the DAEE precursor used

in the membrane formation. Spot profile EDAX analysis of the Ca^{2+}-nanogold membrane before (curve 2) and after formation of calcium phosphate crystals (curves 3, 4 & 5) are shown in Fig.6.10A. Apart from the originally present Au, C, N, and O signals (compare with curve 1), a strong Ca signal can be seen in the Ca^{2+}-nanogold membrane (curve 2, Fig.6.10A). Spot-profile EDAX analysis after formation of calcium phosphate crystals on Ca^{2+}-nanogold membranes clearly show the appearance of P signal along with an increase in the O signal (curve 3, 4 & 5 in Fig.6.10A) along with strong Au and N signals from the underlying membrane, the nanoparticles and the surface modifier respectively.

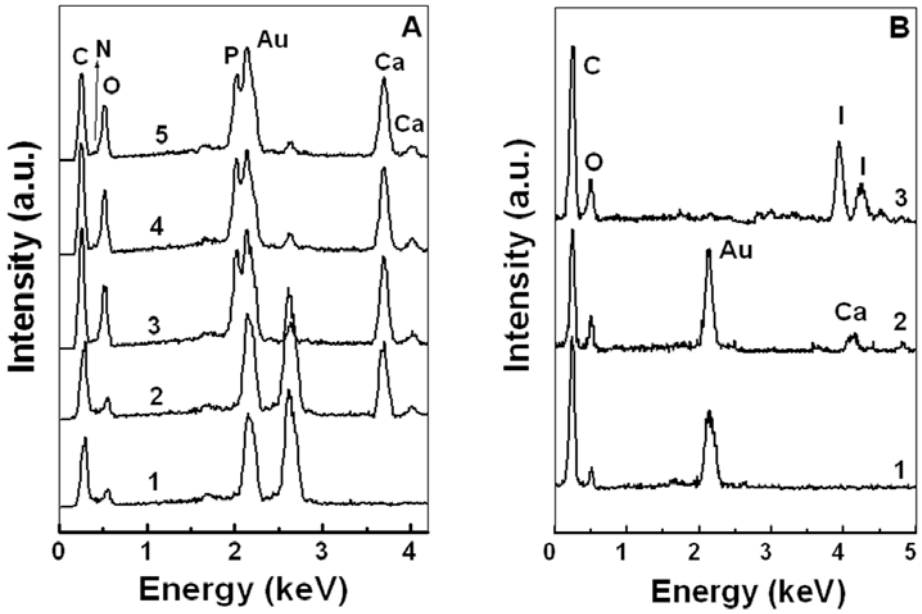

Fig.6.10: *(A) Spot-profile EDAX spectra recorded from the as-prepared gold nanoparticle membrane before (curve 1), after immobilization of Ca^{2+} ions on the aspartic acid-functionalized gold nanoparticle membrane (curve 2), after formation of calcium phosphate crystals on aspartic acid (curve 3), cysteine (curve 4) and anthranilic acid (curve 5) functionalized gold nanoparticle membranes. (B) Spot-profile EDAX spectra recorded from the as-prepared gold nanoparticle membrane before (curve 1), after immobilization of Ca^{2+} ions without prior surface modification (curve 2), and after complete leaching out of the gold nanoparticles by iodine treatment (curve 3).*

Spot profile EDAX analysis of the nanogold membrane before and after immersion in $CaCl_2$ solution (without any surface functionalization of the membrane) is shown as curves 1 and 2 respectively in Fig.6.10B. Apart from the expected presence of Au, C, N, and O signals in both spectra, a very weak Ca signal was observed after the immersion of non-functionalized nanogold membrane in $CaCl_2$ solution. This signal is considerably less intense than that recorded from functionalized membranes that have

been immersed in $CaCl_2$ solution (curve 2 in Fig.6.10A) thus highlighting the important role of the surface modifiers in immobilizing Ca^{2+} ions in the membrane and the subsequent formation of the calcium phosphate mineral. In the gold nanoparticle leaching experiment, the complete removal of the gold component in the membrane is clearly indicated in the EDAX spectra recorded from the iodine treated membrane (curve 3, Fig.6.10B) that shows complete absence of the Au signal.

6.3.5 Fourier transform infrared spectroscopy (FTIR) studies

The FTIR spectra recorded from calcium phosphate crystals grown on the aspartic acid, cysteine and anthranilic-derivatized nanogold membrane are shown as curves 2, 3 & 4 respectively in Fig.6.11. The absorption bands centered at 520, 601 cm^{-1} and 1060 cm^{-1} are characteristic of acidic phosphates, $-PO_4^{3-}$ (520 & 601 cm^{-1}) and P=O (1060 cm^{-1}) vibration modes respectively [14,15].

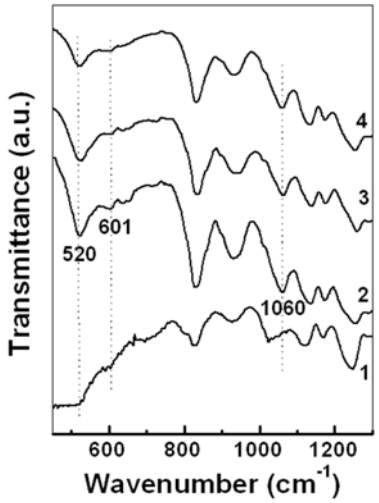

Fig.6.11: *FTIR spectra recorded from the as-prepared gold nanoparticle membrane (curve 1), and the aspartic acid (curve 2), cysteine (curve 3) and anthranilic acid-functionalized (curve 4) gold nanoparticle membranes after formation of calcium phosphate.*

6.3.6 X-ray diffraction (XRD) measurements

The XRD patterns recorded from calcium phosphate crystals grown on the aspartic acid, cysteine and anthranilic-derivatized nanogold membrane are shown as curves 2, 3 & 4 respectively in Fig.6.12. Curve 1 in Fig.6.12 shows the XRD pattern recorded from the gold nanoparticle membrane. The Bragg reflections in the as-prepared

gold nanoparticle membrane clearly correspond to the fcc crystalline structure of gold [16]. The XRD pattern recorded from the calcium phosphate crystals grown on the aspartic acid-derivatized nanogold membrane is shown as curve 2 in Fig.6.12. A number of Bragg reflections are identified and agree excellently with those reported for hydroxyapatite (peaks assigned with a '*') [15]. The XRD data thus provides clear support for the formation of HAP crystals seen in the SEM images (Fig.6.5).

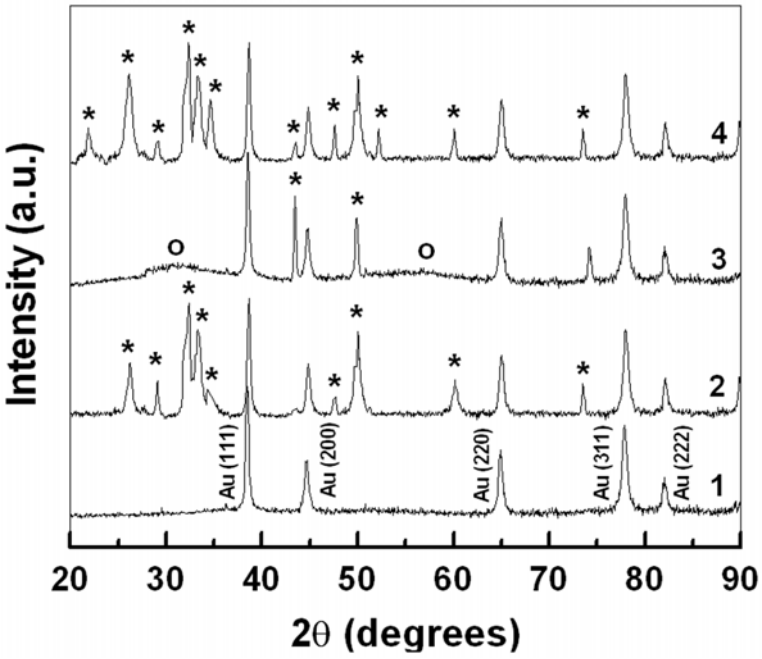

Fig.4.12: *XRD patterns recorded from the as-prepared gold nanoparticle membrane (curve 1), calcium phosphate crystals grown on aspartic acid (curve 2), cysteine (curve 3) and anthranilic acid-functionalized (curve 4) gold nanoparticle membranes. The Bragg reflections have been indexed ('*'-stands for hydroxyapatite and 'o' -stands for amorphous calcium phosphate).*

The XRD pattern recorded from the calcium phosphate crystals grown on the cysteine-functionalized nanogold membrane shown in Fig.6.6A & B is shown as curve 3 in Fig.6.12. The extremely broad Bragg reflections identified by 'o's' in the figure agree with those reported for ACP [15a]. There is also evidence for a small percentage of hydroxyapatite formation on the cysteine - modified membrane (peaks identified by '*'). The XRD pattern recorded from the calcium phosphate crystals grown on the anthranilic acid-functionalized nanogold membrane shown in Fig.6.7 is shown as curve 4 in Fig.6.12. A number of Bragg reflections are identified in this case as well and have been indexed with reference to the hydroxyapatite structure (peaks identified by '*') [15].

6.3.7 Conductivity measurements

To understand the binding of the surface modifiers with the gold nanoparticles embedded in the polymeric membrane prior to Ca^{2+} binding, the conductivity of aqueous solutions of anthranilic acid, aspartic acid and cysteine as a function of time of immersion of the nanogold membrane was monitored. Fig.6.13 shows plots of the solution conductivity with time from anthranilic acid (solid triangles), aspartic acid (solid circles) and cysteine (diamonds). The solution conductance decreases clearly with time in all these cases establishing the binding of the surface modifier molecules with the nanogold membrane.

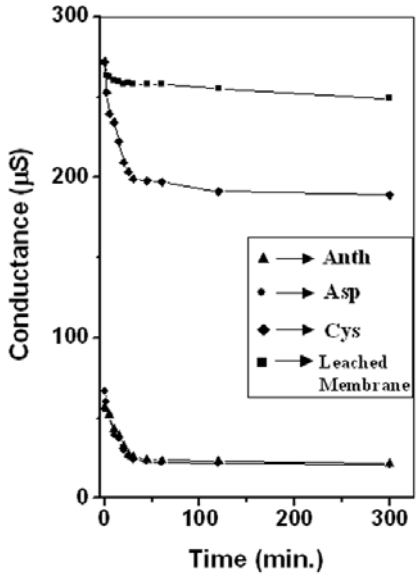

Fig.6.13: *Solution conductivity measurements as a function of time of immersion of the gold nanoparticle membrane in anthranilic acid (triangles), aspartic acid (solid circles) and cysteine (diamonds). The data obtained during immersion of the membrane minus gold nanoparticles by iodine treatment in cysteine solution is also shown (solid squares).*

Similar conductivity measurements carried out during immersion of the membrane minus gold nanoparticles by iodine treatment in cysteine solution (solid squares, Fig.6.13) shows a fall in conductivity that is much smaller that than observed for the nanogold membrane in cysteine (diamonds, Fig.6.13). This clearly establishes that the presence of gold is extremely important for efficient functionalization of the membrane. That this is a key step in Ca^{2+} ion immobilization and thus, facile formation of the calcium hydroxyapatite mineral and has been established above.

6.3.8 Summary

We have demonstrated the growth of HAP and stabilization of the unstable ACP phase on the surface of carboxylic acid-functionalized gold nanoparticle membranes. The nanogold membrane was formed spontaneously by the reaction of bis(2-(4-aminophenoxy)ethyl)ether with aqueous chloroaurate ions at the liquid-liquid interface and thereafter surface-modified with the amino acids aspartic acid and cysteine as well as the bifunctional molecule anthranilic acid. Calcium phosphate growth was achieved by binding Ca^{2+} ions to the nanogold surface-bound carboxylic acid followed by reaction with $NH_4H_2PO_4$. The nature of calcium phosphate crystals formed was found to be a strong function of the nanogold surface modifier.

6.4 Calcium phosphate crystal growth on functionalized bare gold nanoparticles

The growth of calcium phosphate crystals on aspartic acid-functionalized bare gold nanoparticles was accomplished first by the addition of 2 ml of 10^{-2} M aqueous solution of $CaCl_2$ to 18 ml of aspartic acid-capped gold nanoparticle solution under continuous stirring conditions and thereafter, the addition of 2 ml of 10^{-2} M aqueous solution of $NH_4H_2PO_4$ to Ca^{2+}-aspartic acid-capped gold nanoparticle solution.

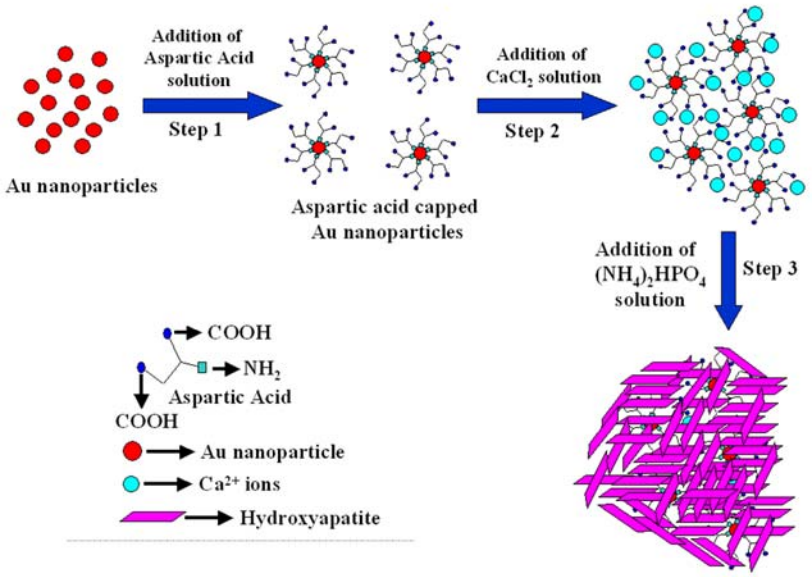

Fig.6.14: *Scheme showing different steps involved during the growth of calcium phosphate crystals on aspartic acid capped gold nanoparticles. Step 1 – Functionalization of Au nanoparticles with aspartic acid, Step 2 – Addition of $CaCl_2$ solution to the aspartic acid functionalized gold nanoparticles. Step 3 – Formation of hydroxyapatite crystals after reaction with ($NH_4H_2PO_4$) solution.*

The scheme in Fig.6.14 illustrates a possible process operative for the growth of calcium phosphate crystals on the aspartic acid capped gold nanoparticles. Step 1 in Fig.6.14 shows the derivatization of gold nanoparticles with amino acid aspartic acid. From earlier study it has been observed that aspartic acid binds with gold nanoparticles through amine group [12c] leaving the carboxylic acid groups free to complex with metal ions. Step 2 in Fig.6.14 shows the probable aggregate structures of aspartic acid capped gold nanoparticles complexed with Ca^{2+} ions after addition of $CaCl_2$ solution into aspartic acid capped gold nanoparticles solution. Step 3 in Fig.6.14 shows the possible growth of calcium phosphate crystals on the calcium bound nano-gold superstructures after reaction with $NH_4H_2PO_4$ solution.

6.4.1 UV-Visible (UV-vis) spectroscopy studies

Fig.6.15 shows the UV-vis spectra of the aspartic acid-capped gold hydrosol at different stages of preparation. Curve 1 in the figure corresponds to the spectrum of gold colloidal solution obtained by borohydride reduction of aqueous chloroauric acid; curve 2 is the spectrum of gold colloidal solution after capping with aspartic acid and curve 3 is the spectrum of aspartic acid capped gold colloidal solution after adding $CaCl_2$ solution.

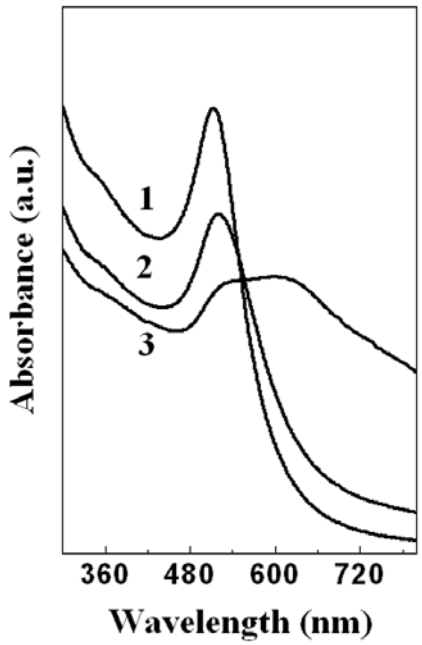

Fig.6.15: *UV-vis spectra recorded from : curve 1– borohydride reduced gold nanoparticles; curve 2– aspartic acid-capped gold nanoparticles; curve 3 – after addition of 10^{-2} M aqueous $CaCl_2$ into the aspartic acid-capped gold nanoparticle solution.*

A strong absorption in curve 1 at ca. 520 nm is observed that corresponds to excitation of surface plasmon vibrations in the gold nanoparticles [17]. When the gold nanoparticles are capped with aspartic acid, a slight broadening and red shift of the surface plasmon band is observed (curve 2) indicating some aggregation of the gold nanoparticles consequent to surface modification. However, the aspartic acid-capped gold nanoparticle solution was stable for months with little evidence of further aggregation. After addition of $CaCl_2$ solution to the aspartic acid capped gold nanoparticle solution, the absorption spectrum changes significantly with the appearance of an additional absorption band centered at ca. 620 nm (curve 3). This is a strong signature of aggregation of the particles into open structures and arises due to excitation of longitudinal (in-plane) plasmon vibrations from the aggregates. It is known that amine groups bind to gold nanoparticles [12] and in the case of aspartic acid, this leads to the presence of free carboxylic acid groups on the gold surface. It is clear that Ca^{2+} ions bind strongly to the exposed $–COO^-$ groups present in the aspartic acid (solution pH 8.5, pI of aspartic acid ~ 2.7) and that this process leads to screening of the repulsive electrostatic interaction between the negatively charged aspartic acid-capped gold nanoparticles and therefore, to aggregation of the particles. Before addition of $CaCl_2$ solution to aspartic acid capped gold nanoparticle solution, the nanoparticles are stable due to electrostatic repulsion between negatively charged aspartic acid-capped gold nanoparticles.

6.4.2 Isothermal titration calorimetric (ITC) measurements

Isothermal titration calorimetric (ITC) measurements were performed to estimate the strength of the interaction between Ca^{2+} ions and aspartic acid bound to the surface of gold nanoparticles. Fig.6.16A shows the ITC titration data recorded during injection of 10 μl of aqueous $CaCl_2$ from a syringe into 1.47 ml of aspartic acid-capped gold nanoparticle solution taken in the sample cell. It is seen from the figure that the reaction is endothermic, where each peak is the result of a single injection. The endothermicity of the first few injections is roughly the same since during the initial stages of reaction between Ca^{2+} and gold nanoparticle bound-aspartic acid; a number of binding sites (free carboxylate ions) are available for complexation. As the injections progress, the number of binding sites decreases continuously until saturation occurs and is mirrored as a

monotonic fall in the endothermic calorimetric response (Fig.6.16A). Interestingly, a second maximum in the calorimetric response is observed (arrow, Fig.6.16A), and is interpreted below. The plot shown in Fig.6.16B is the binding isotherm determined from the raw data, where the total heat per injection (in kcal per mole of $CaCl_2$ injected) is plotted against the total volume of $CaCl_2$ solution added to the cell. We note here that in reactions where the concentrations of the reactants are known, the calorimetric data is normally plotted against the molar ratio of the reactants. In this study, the concentration of aspartic acid is not known accurately due to potential errors in estimating the total gold nanoparticle surface area, area occupied by surface-bound aspartic acid molecules etc. We have used the calorimetric response merely to characterize the nature of reaction and have refrained from deriving thermodynamic parameters from the binding isotherms due to the above errors.

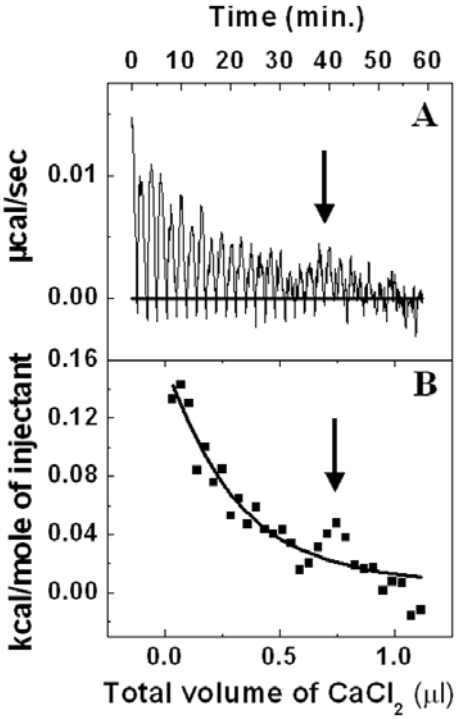

Fig.4.16: *(A) Isothermal titration calorimetric data recorded during successive injections of 10 µl aqueous $CaCl_2$ solution into the titration cell containing 1.47 ml of aqueous aspartic acid-capped gold nanoparticle solution. (B) Shows the binding isotherm obtained by integration of the raw data shown in the A plotted as a function of total volume of aspartic acid solution injected.*

The fact that the calorimetric response during the entire titration cycle of Ca^{2+} ions against aspartic acid-capped gold nanoparticles is endothermic (which opposes the

reaction) implies that the reaction is an entropically driven one. The first monotonic decrease in the binding isotherm (Fig.6.16B) is attributed to Ca^{2+} binding with the gold nanoparticle bound-aspartic acid where neutralization of the negative charge of the carboxylate ions in aspartic acid occurs. The second enthalpic maximum (Fig.6.16B and C) is attributed to aggregation of the aspartic acid capped gold nanoparticles as a consequence of neutralization of the negative surface charge by the Ca^{2+} ions. Bloomfield and co-workers have observed a similar two-step enthalpic binding isotherm in their ITC study of DNA binding and condensation with the trivalent cations cobalt hexamine and spermidine [18]. The aggregation of aspartic acid-capped gold nanoparticles in the presence of Ca^{2+} ions inferred from the ITC binding isotherms (arrow, Fig.6.16B) is good agreement with the UV-vis data (curve 3, Fig.6.15).

6.4.3 Scanning electron microscopy measurements

6.4.3.1 Calcium phosphate growth on the aspartic acid capped gold nanoparticles

Fig.6.17A & B show representative SEM images recorded at different magnifications from a drop-coated film of calcium phosphate crystals grown on aspartic acid-capped gold nanoparticles as a template. The images show the presence of quasi-spherical structures of calcium phosphate crystals with sizes ranging from 1-5 μm. At higher magnification (Fig.6.17B) the texture of the spherical particles is seen more clearly to be composed of thin platelets in a highly compact configuration.

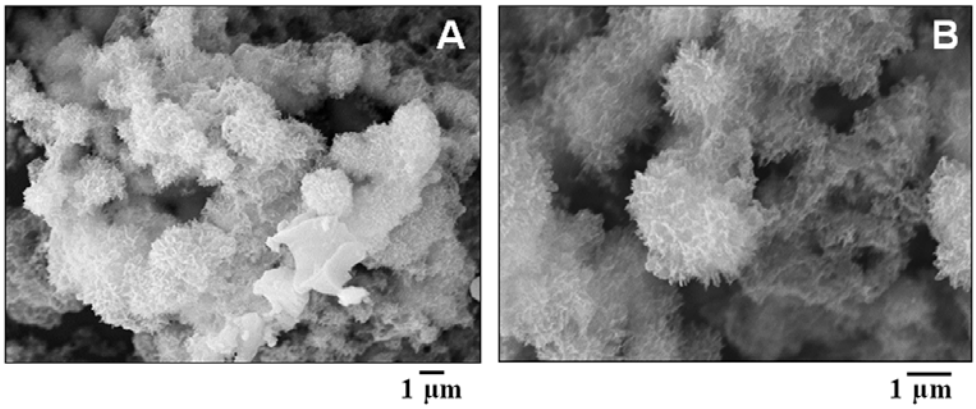

Fig.6.17: *(A) and (B) - Representative SEM images recorded at different magnifications from drop-cast films of calcium phosphate crystals grown on aspartic acid-capped gold nanoparticles.*

The calcium phosphate platelets appear to self-assemble into spheroidal structures. Such types of assemblies have been observed by Colfen and Antonietti during solution growth of $CaCO_3$ in the presence of suitable double hydrophilic block copolymers (DHBCs) [19]. It was observed that these double-hydrophilic block copolymers, due to their strong interaction with inorganic surfaces resulted in the formation of spherical assembly of plate-like calcite crystals. Spheroidal fluorapatite with prismatic needles have been observed by Kniep *et al* [20] in flourapatite-gelatin composites where growth of fluorapatite starts with formation of elongated prismatic seeds followed by self-similar branching into anisotropic spherical aggregates, this process being mediated by local electric fields.

6.4.3.2 Calcium phosphate growth in control experiments

The templating action of aspartic acid-capped gold nanoparticles was evaluated in two control experiments wherein, 1) Ca^{2+} ions were added to the borohydride reduced gold nanoparticle solution without surface modification and 2) Ca^{2+} ions were added to the aspartic acid solution without gold nanoparticles. The two solutions were aged for 1 h followed by the addition of $NH_4H_2PO_4$ solution, under the conditions described above. Fig.6.18A and B show representative SEM images recorded from a drop-coated film of the calcium phosphate crystals grown in the presence of uncapped gold nanoparticles and pure aspartic acid respectively. The overall morphology of the crystals in the control experiments (Fig.6.18) is quite different from the highly regular, spherical assemblies observed with aspartic acid-capped gold nanoparticles (Fig.6.17) as a template.

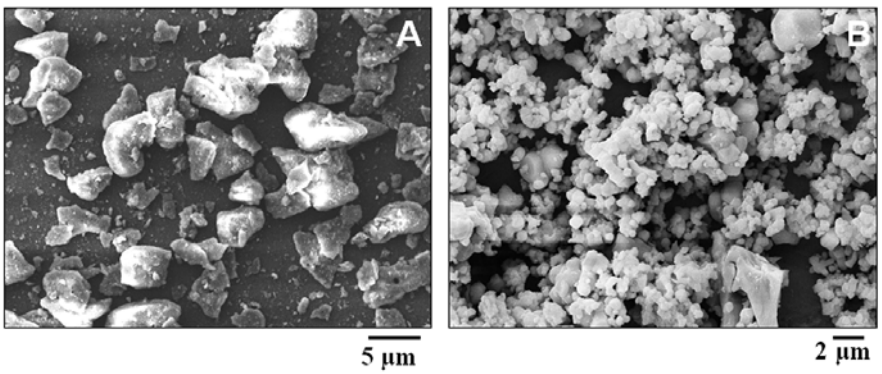

Fig.6.18: *Representative SEM images from drop-cast films of calcium phosphate crystals grown in the presence of uncapped borohydride reduced gold nanoparticles (A) and pure aspartic acid (B).*

In the case of calcium phosphate growth in the presence of uncapped gold nanoparticles, the calcium phosphate crystals are precipitated in the form of irregular prismatic crystals (Fig.6.18A) while aspartic acid induces growth of highly irregular crystals with no particular morphology (Fig.6.18B). It is clear from the above that aspartic acid bound to the surface of gold nanoparticles plays an important role in promoting the growth of crystalline calcium phosphate with a well-defined spherical morphology.

6.4.4 EDAX and FTIR studies

Fig.6.19A shows the spot-profile EDAX spectra recorded from specific regions of the calcium phosphate crystals grown on aspartic acid-capped gold nanoparticles (curve 1), on the uncapped borohydride reduced gold nanoparticles (curve 2) and in the presence of pure aspartic acid (curve 3). The presence of strong Ca, P and O signals is clearly observed in all the EDAX spectra indicating the formation of calcium phosphate. An Au signal from the gold nanoparticles in curves 1 and 2 are clearly observed and is absent as expected in curve 3 where calcium phosphate growth was attempted with pure aspartic acid. A quantitative analysis of the calcium phosphate crystals was carried out from the Ca and P signals in the EDAX spectra and yielded values of Ca : P ratios of 1.7 : 1, 1.5 : 1 and 1.5 : 1 for the aspartic acid capped nanogold, uncapped nanogold and pure aspartic acid samples respectively. These values are in good agreement with the expected stoichiometry based on the chemical structure of HAP [$Ca_{10}(PO_4)_6(OH)_2$].

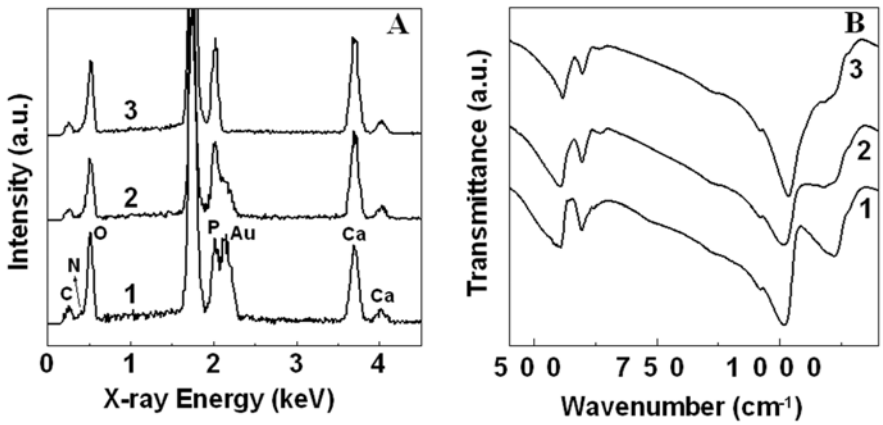

Fig.6.19: *(A) EDAX profiles recorded from calcium phosphate crystals grown on aspartic acid-capped gold nanoparticles (curve 1), on uncapped borohydride reduced gold nanoparticles (curve 2) and pure aspartic acid (curve 3). (B) FTIR spectra recorded from calcium phosphate crystals grown on aspartic acid capped gold nanoparticles (curve 1); calcium phosphate crystals grown on borohydride reduced gold nanoparticles (curve 2) and in the presence of pure aspartic acid (curve 3).*

FTIR spectra recorded from calcium phosphate crystals grown on aspartic acid-capped gold nanoparticles (curve 1), in the presence of uncapped gold nanoparticles (curve 2) and pure aspartic acid (curve 3) showed the presence of absorption bands centered at 1115, 1010 and 960 cm^{-1} and are assigned to ν_3 and ν_1 stretching modes of PO_4^{3-} respectively [14] (Fig.6.19B). In all cases, an additional band at 602 cm^{-1} was also observed which arises due excitation of the ν_4 mode of PO_4^{3-} groups. The FTIR results indicate the presence of phosphate groups in the powder, but further evidence is required to establish the formation of crystalline calcium phosphate.

6.4.5 X-ray diffraction measurements

The X-ray diffraction pattern recorded from a drop-coated film of the calcium phosphate crystals grown on aspartic acid-capped gold nanoparticles is shown as curve 1 in Fig.6.20. The peaks at 32.8°, 33.1°, 47° and 53° 2θ values (indicated by "*") are consistent with the (112), (300), (132) and (004) Bragg reflections of hydroxyapatite, respectively [15].

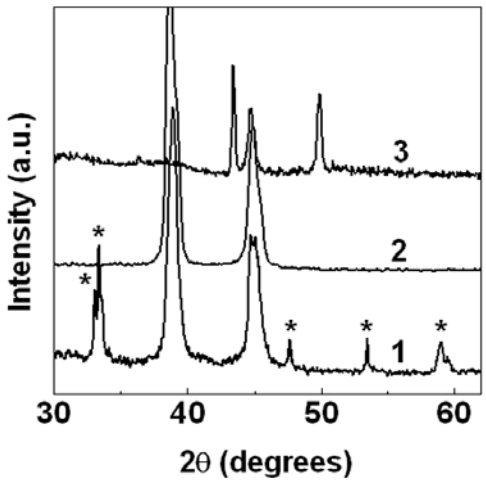

Fig.6.20: *XRD patterns recorded from calcium phosphate crystals grown on aspartic acid-capped gold nanoparticles (curve 1), on uncapped borohydride reduced gold nanoparticles (curve 2) and in pure aspartic acid solution (curve 3).*

Curves 2 and 3 correspond to XRD patterns recorded from the powders obtained in solutions containing uncapped borohydride reduced gold nanoparticles (curve 2) and pure aspartic acid (curve 3). Bragg reflections characteristic of HAP are not seen in the powders obtained in the presence of uncapped gold nanoparticles (curve 2) and the

material obtained in the presence of pure aspartic acid (curve 3). The peak at 44^{o} arises from the sample holder of the instrument. The Bragg reflections in curve 3 (calcium phosphate crystals obtained using pure aspartic acid) show peaks that are characteristic of the other form of calcium phosphate (tricalcium phosphate). As shown by the XRD data, in the two control experiments, the crystalline HAP phase was not nucleated. It is clear from that HAP crystallization is promoted by the aspartic acid monolayer present on the surface of the gold nanoparticles. This correlates well with the nature of crystallites observed in the microscopy analysis. The additional Bragg reflections (peaks not marked) in curves 1 and 2 are from the gold nanoparticles in the crystals.

6.4.6 Transmission electron microscopy (TEM) and Electron diffraction studies

Fig.6.21A & B show representative TEM images recorded at different magnifications from the calcium phosphate crystals grown on aspartic acid-capped gold nanoparticles. At low magnification, the quasi-spherical morphology of the crystallite assemblies is clearly seen as the individual platelets (Fig.6.21A). At higher magnification, the calcium phosphate crystals are observed in much greater detail (Fig.6.21B). The individual platelets themselves are not very smooth and present an irregular, corrugated surface. Gafni and co-workers have previously observed a similar morphology of HAP crystals in their study of the effect of chondroitin sulfate and biglycan on the crystallization of hydroxyapatite under physiological conditions [21].

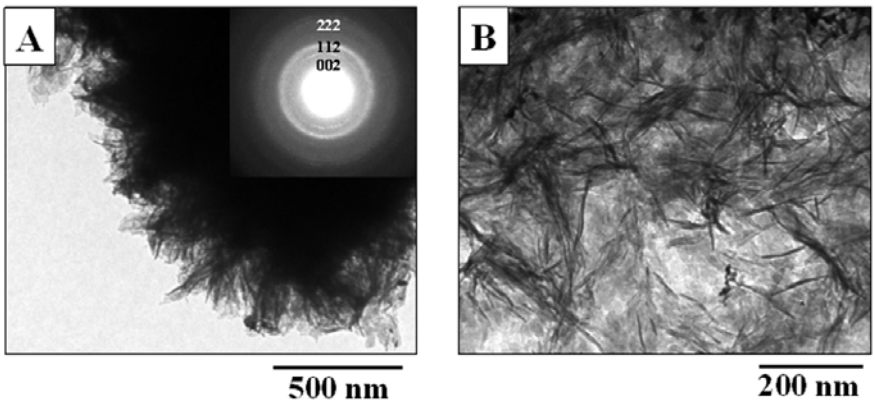

Fig.6.21: *(A & B) TEM micrographs recorded at different magnifications from drop-cast films of calcium phosphate crystals grown on aspartic acid-capped gold nanoparticles. The inset in A shows the selected area electron diffraction pattern recorded from the crystals shown in the main part of the figure.*

The inset of Fig.6.21A shows the selected area electron diffraction pattern of the calcium phosphate crystals shown in Fig.6.21A. The diffraction rings have been indexed in the figure based on the hydroxyapatite form structure of the crystals [15]. The electron beam for the diffraction pattern was focused only on the edges of the quasi-spherical plate like hydroxyapatite crystals, thus shows the diffraction rings for hydroxyapatite crystals only. Because of the higher thickness of the hydroxyapatite on Au aggregated superstructure, the electron beam penetration was not possible to get electron diffraction from the core-gold nanoparticle-nucleating center.

6.4.7 Summary

The crystallization of hydroxyapatite in the presence of aspartic acid-capped gold nanoparticles has been demonstrated. Calcium phosphate crystal growth was achieved by the binding of Ca^{2+} ions to the carboxylate ions of the nanogold surface-bound aspartic acid molecules followed by reaction with $NH_4H_2PO_4$. Plate-like hydroxyapatite crystals were observed to form in well-defined spherical assemblies. Based on the ITC and UV-vis spectroscopy measurements, it is believed that addition of Ca^{2+} ions to the aspartic acid-capped gold nanoparticle solution results in aggregation of the nanoparticles and that it is these aggregates that serve as a template for the growth of hydroxyapatite crystals.

6.5 $CaCO_3$ crystal growth on functionalized nano-gold membrane and on functionalized bare gold nanoparticles

The growth of $CaCO_3$ crystals on free-standing carboxylic acid-functionalized gold nanoparticle membranes was accomplished by simple immersion of the aspartic acid, cysteine and anthranilic acid-functionalized nanogold membranes in 50 ml of 10^{-3} M aqueous $CaCl_2$ (pH – 6.2) solutions for 12 hours. Thereafter, the growths of $CaCO_3$ crystals were induced by exposing the different nanogold membranes to CO_2 atmosphere for 1 hour. Similarly, the growth of $CaCO_3$ crystals on aspartic acid-functionalized bare gold nanoparticles was accomplished first by the addition of 2 ml of 10^{-2} M aqueous solution of $CaCl_2$ to 18 ml of aspartic acid-capped gold nanoparticle solution and thereafter, by exposing it to CO_2 atmosphere for 1 hour. The crystals formed were characterized by SEM, EDAX, FTIR and XRD measurements.

6.5.1 Scanning electron microscopy measurements

6.5.1.1 $CaCO_3$ crystal growth on amino acid functionalized nano-gold membrane

Figs.6.22A and B show representative SEM images of $CaCO_3$ crystals grown on the aspartic acid-functionalized gold nanoparticle membrane. At low magnification, it is seen that the membrane is very uniformly and densely covered with $CaCO_3$ (Fig.6.22A). At higher magnification (Fig.6.22B), the $CaCO_3$ component is clearly seen to be made up of aggregates of quasi-spherical $CaCO_3$ crystals.

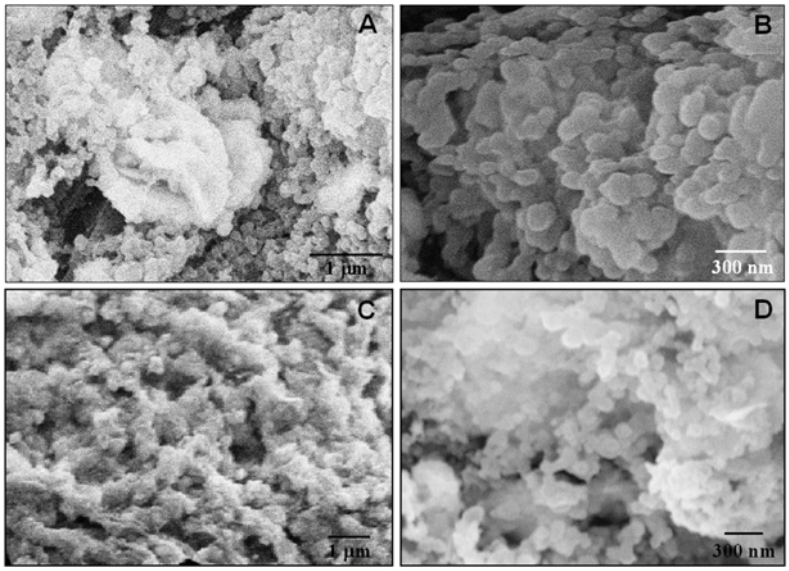

Fig.6.22: *A and B) SEM micrographs at different magnifications of $CaCO_3$ crystals grown on aspartic acid-functionalized gold nanoparticle membrane. C and D) SEM micrographs at different magnifications of $CaCO_3$ crystals grown on cysteine-functionalized gold nanoparticle membrane.*

Figs.6.22C and D show SEM images of $CaCO_3$ crystals grown on the cysteine-functionalized gold nanoparticle membrane. As in the case of the aspartic acid-modified nanogold membrane, the low magnification SEM image (Fig.6.22C) shows extremely dense coverage of $CaCO_3$ crystals over the membrane surface and within pores of the membrane. At higher magnification (Fig.6.22D), the crystals are seen clearly to be composed of spherical $CaCO_3$ crystals similar to those observed in the aspartic acid-modified nanogold membrane (Fig.6.22A and B) with the only difference being that the

crystals are smaller and apparently more uniform in size in the case of the aspartic acid-modified nanogold membrane.

6.5.1.2 $CaCO_3$ crystal growth on anthranilic acid functionalized nano-gold membrane

The crystallization of $CaCO_3$ was also studied using the bifunctional molecule anthranilic acid as a surface modifier for the nanogold membrane. This molecule binds to nanogold through the amine functionality thus exposing carboxylic acid groups on the surface of the nanoparticles. Anthranilic acid possesses an aromatic group and it would be interesting to study the effect of this group. Figs.6.23A–D shows representative SEM images of the $CaCO_3$ crystals grown on anthranilic acid-functionalized gold nanoparticle membrane.

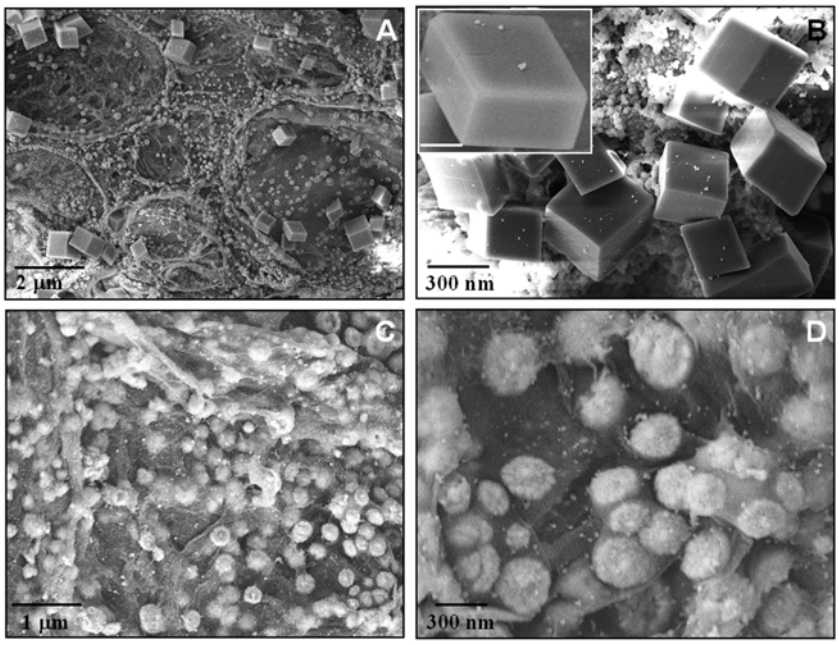

Fig.23: *A – D) SEM micrographs recorded at different magnifications of $CaCO_3$ crystals grown on anthranilic acid-functionalized gold particle membrane. The inset in B shows a higher magnification SEM micrograph of one of the rhombohedral $CaCO_3$ crystals in greater detail (scale bar is 100 nm).*

The low magnification SEM image (Fig.6.23A) shows $CaCO_3$ crystals densely populating the nanogold membrane surface. The $CaCO_3$ crystals are composed of spherical and rhombohedral structures. At higher magnification (Fig.6.23B), highly faceted rhombohedral $CaCO_3$ crystals are observed. The inset in Fig.6.23B clearly shows

one of the faceted rhombohedral $CaCO_3$ in greater detail. Figs.6.23C and D show low and high magnification SEM images of spherical $CaCO_3$ crystals present along with the rhombohedral shaped $CaCO_3$ crystals grown on the anthranilic acid-functionalized nano-gold membrane shown in Fig.6.23A. The low magnification SEM image (Fig.6.23C) clearly shows spherical $CaCO_3$ crystals populating the membrane surface along with rhombohedral crystals. The higher magnification SEM image (Fig.6.23D) clearly reveals that the individual spherical structures are in turn composed of very small individual crystallites of $CaCO_3$ by an aggregation process.

6.5.1.3 $CaCO_3$ crystal growth on aspartic acid capped bare gold nanoparticles

Fig.6.24A–D show representative SEM images recorded at different magnifications from a drop-coated film of $CaCO_3$ crystals grown on aspartic acid-capped gold nanoparticles as a template. The representative low magnification SEM image in Fig.6.24A shows that the substrate is covered with a fairly large density of spherical $CaCO_3$ crystallites. Fig.6.24B shows some degree of surface design on the spherical $CaCO_3$ crystals. The higher magnification SEM images (Fig.6.24C & D) show one of the spherical $CaCO_3$ crystals in greater details. The surface of the $CaCO_3$ crystal consists of very sharp and regular steps of faceted plate/rhombohedral $CaCO_3$ crystallites. This morphology reflects the symmetry of calcite polymorph of $CaCO_3$, indicating that they are calcite single crystals evolved from typical rhombohedral calcite crystals.

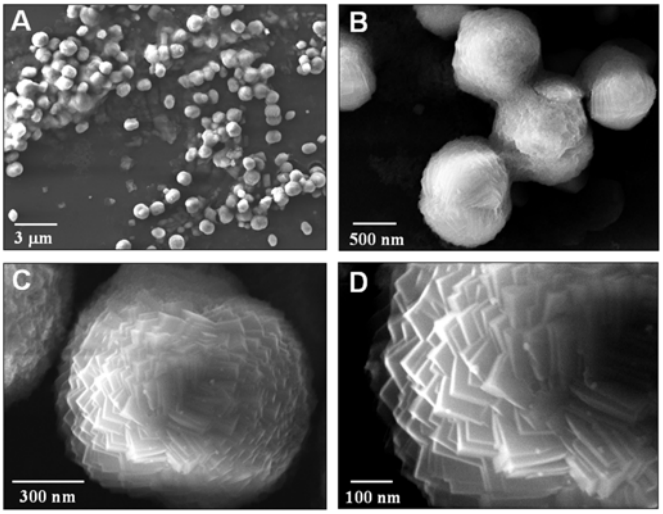

Fig.6.24: *A – D) Representative SEM images recorded at different magnifications from drop-cast films of $CaCO_3$ crystals grown on aspartic acid-capped gold nanoparticles.*

Similar steps have been observed previously on calcite crystals [22-24]. Orme *et al* have observed such steps in calcite crystals where they have found that site-specific binding of amino acid residues to surface steps changes the step-edge free energies, thereby giving rise to modifications that propagate from atomic length scales to macroscopic length scales [22]. Sugawara *et al* have succeeded in preparing periodically patterned $CaCO_3$ films with regular surface relief structures on a thin matrix of cholesterol-modified pullulan from an aqueous solution containing poly(acrylic acid) [23]. Similar calcite steps were seen when crystallization of $CaCO_3$ was effected in agarose gels [24]. Previously in an analogous study Kim and co-worker have grown spherical vaterite crystals on 4-mercaptobenzoic acid monolayers-protected gold nanoparticles [25]. They have also shown the cooperative effect between Mg^{2+} and nanoparticles can lead to aragonite in a needle-like morphology [25].

6.5.2 Quantitative estimation of $CaCO_3$ on the nano-gold membrane

After the formation of $CaCO_3$ crystals on the surface derivatized nanogold membranes, the membranes were immersed in alkali solution to dissolve the $CaCO_3$ component. From the difference in weight of the membranes before and after $CaCO_3$ removal, the weight percentage contributions of $CaCO_3$ to the nanogold membranes were estimated to be ca.2.11, 2.19 and 2.32 weight % for $CaCO_3$ crystals growth on aspartic acid, cysteine and anthranilic acid-functionalized nanogold membranes respectively.

6.5.3 EDAX and FTIR measurements

Spot profile EDAX analysis carried out on the as-prepared membrane (curve 1 in Fig.6.25A) indicated that polymeric membrane contained a large concentration of gold nanoparticles. Along with a prominent Au peak, N, C and O signals are also observed in the EDAX spectrum of the nanogold membrane (curve 1). Spot profile EDAX analysis of the Ca^{2+}-nanogold membrane before (curve 2) and after formation of $CaCO_3$ crystals (curves 3, 4 & 5) are shown in Fig.6.25A. The EDAX analysis of the Ca^{2+}- aspartic acid functionalized nanogold membrane and after formation of $CaCO_3$ crystals is shown as curves 2 and 3 in Fig.6.25A respectively. Along with Au, C, N, and O, a strong Ca signal can be seen in the Ca^{2+}-nanogold membrane (curve 2). The EDAX spectrum after the formation of $CaCO_3$ crystals clearly shows an increase in the C and O signals upon

reaction with CO_2 indicating the formation of $CaCO_3$ crystals. The analysis of the EDAX data yielded an average Ca : C : O atomic ratio of 1 : 2.3 : 3.6, 1 : 2.7 : 3.35 and 1 : 2.8 : 3.7 for $CaCO_3$ crystals growth on aspartic acid, cysteine and anthranilic acid-functionalized nanogold membranes respectively. The excess C and O in the elemental ratio is attributed to contribution from the underlying polymer membrane. Strong Au and N signals were also observed from the membrane and arise due to the nanoparticles and surface modifier respectively.

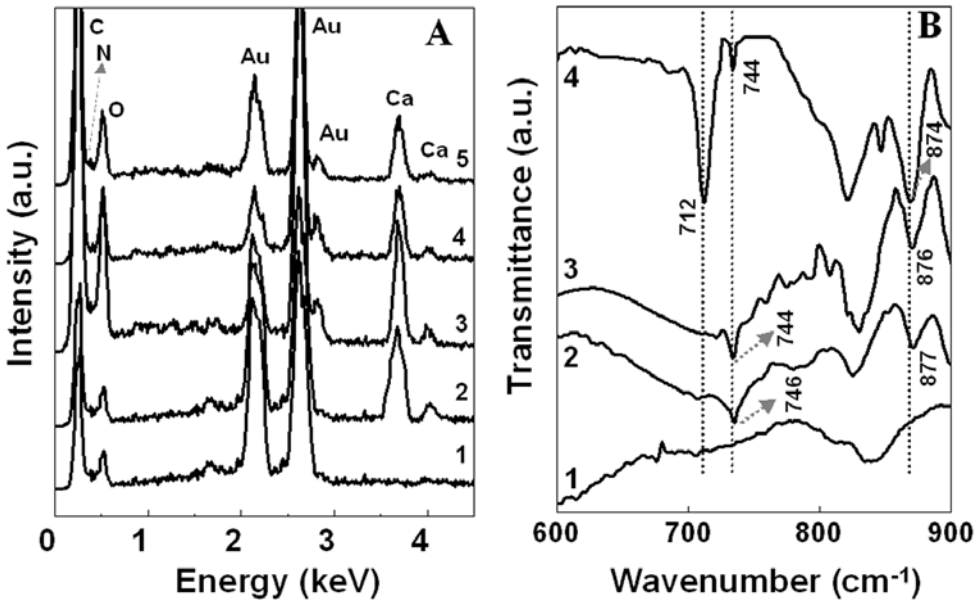

Fig.6.25: *(A) EDAX spectra recorded from the as-prepared gold nanoparticle membrane (curve 1), after immobilization of Ca^{2+} ions to the functionalized gold nanoparticle membrane (curve 2), after formation of $CaCO_3$ crystals on aspartic acid (curve 3), cysteine (curve 4) and anthranilic acid (curve 5) functionalized gold nanoparticle membranes. (B) FTIR spectra recorded from the as-prepared gold nanoparticle membrane (curve 1), and the aspartic acid (curve 2), cysteine (curve 3) and anthranilic acid (curve 4) functionalized gold nanoparticle membranes after formation of $CaCO_3$.*

The FTIR spectra recorded from $CaCO_3$ crystals grown on the aspartic acid, cysteine and anthranilic-derivatized nanogold membrane are shown as curves 2, 3 & 4 respectively in Fig.6.25B. The FTIR analysis of the $CaCO_3$-aspartic acid nanogold membrane (curve 2, Fig.6.25B) show absorption bands centered at 877 and 746 cm^{-1} which are characteristic of vaterite polymorph of $CaCO_3$ [26]. Along with the absorption bands for vaterite, a very weak absorption band can be seen at 712 cm^{-1} and is attributed to the small percentage of calcite present in the sample. The FTIR analysis of the $CaCO_3$-cysteine nanogold

membrane (curve 3, Fig.6.25B) show absorption bands centered at 876 and 744 cm^{-1} clearly indicates the formation of vaterite without any evidence of calcite polymorph. The FTIR analysis of the $CaCO_3$-anthranilic acid functionalized nanogold membrane (curve 4, Fig.6.25B) show the formation of both calcite and vaterite crystals with absorption bands centered at 874 and 712 cm^{-1} (characteristic of calcite) [26] and 744 cm^{-1} (characteristic of vaterite) [26]. The FTIR spectrum recorded from as prepare gold nanoparticle membrane did not show any distinct absorption band in the spectral window shown in Fig.6.25B.

6.5.4 X-ray diffraction studies

The XRD pattern recorded from the as-prepared gold nanoparticle membrane shows Bragg reflections correspond to the fcc crystalline structure of gold (curve 1 in Fig.6.26) [16].

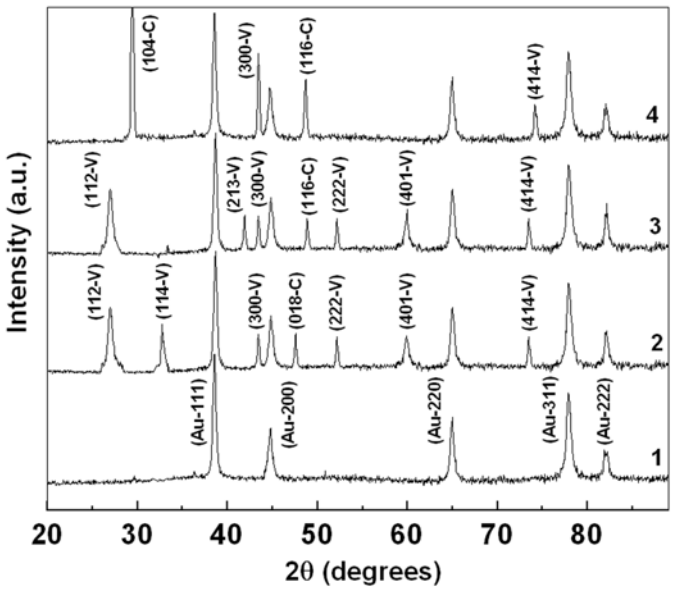

Fig.6.26: *XRD patterns recorded from the as-prepared gold nanoparticle membrane (curve 1), $CaCO_3$ crystals grown on aspartic acid (curve 2), cysteine (curve 3) and anthranilic acid (curve 4) functionalized gold nanoparticle membrane. The Bragg reflections have been indexed (C-stands for calcite and V-stands for vaterite).*

The XRD pattern recorded from the $CaCO_3$ crystals grown on the aspartic acid derivatized nanogold membrane is shown as curve 2 in Fig.6.26. A number of Bragg reflections are identified and agree excellently with those reported for vaterite (peaks designated with a 'V') [27]. A very small calcite contribution is also observed (peaks

designated with a 'C'). The XRD data thus provides clear support for the morphology of the $CaCO_3$ crystals seen in the SEM images (Fig.6.22B) – such well-defined spherical structures are known to be characteristic of the vaterite polymorph [26]. The XRD pattern recorded from the $CaCO_3$ crystals grown on the cysteine functionalized nanogold membrane also resulted in the formation of vaterite polymorph of $CaCO_3$ (curve 3 in Fig.6.26). The XRD pattern recorded from the $CaCO_3$ crystals grown on anthranilic acid derivatized nanogold membrane shown in Fig.6.23 is shown as curve 4 in Fig.6.26. A number of Bragg reflections are identified and have been indexed with reference to the unit cell of the calcite [27,28] and vaterite structure [27]. The XRD results suggest some oriented growth of the rhomobohedral calcite crystals along the (104) direction. The SEM and XRD results clearly show that in the case of anthranilic acid-functionalized nanogold membrane, $CaCO_3$ crystals of mixed polymorphs (calcite and vaterite) were nucleated and grown on the membrane.

6.5.5 Summary

The oriented growth of calcite and stabilization of the unstable polymorph vaterite on surface of carboxylic acid-functionalized gold nanoparticle membrane is described. $CaCO_3$ growth was achieved by binding Ca^{2+} ions to the nanogold surface-bound carboxylic acid followed by reaction with CO_2. The nature of $CaCO_3$ crystals formed was found to be a strong function of the nanogold surface modifier.

6.6 Discussion

The need of surface modification and the chemical binding process of the nano-gold membrane prior to mineralization is discussed below. We have chosen aspartic acid and cysteine to modify the surface of the gold nanoparticle membrane for the following reasons : a) the use of an amino acid would more closely approximate a biological surface; b) aspartic acid and cysteine molecules contain amine/thiol groups that are known to bind strongly with gold nanoparticles and therefore free carboxylic acid groups in the amino acids would be present at the surface of the nano-gold membrane during immersion in $CaCl_2$ solution thus facilitating complexation of Ca^{2+} ions. Anthranilic acid was chosen to see if the presence of an aromatic group in the molecule would affect the crystallography and morphology of calcium phosphate and carbonate crystals grown on the membrane scaffold. Even though all three surface modifiers studied would expose

carboxylic acid groups on the nanoparticle/membrane surface and thus would all bind Ca^{2+} ions, the stereochemistry of the exposed functional groups, their packing on the gold nanoparticle surface, registry with respect to the nucleating calcium phosphate and carbonate phase and relation to the polymeric backbone would all determine the nature and morphology of calcium phosphate and carbonate crystals grown on the surface. It is clear that the nature of surface modification through the carboxylic acid functional groups determines the nature of calcium phosphate and carbonate crystals grown on the surface of the nanogold membrane. The stabilization of unstable polymorphs of calcium phosphate and carbonate crystals may be due to the carboxylic acid-terminated surface modifier molecules that prevent their phase transformation to the thermodynamically more stable polymorphs.

The quasi-spherical assemblies of calcium phosphate and carbonate crystals on amino acid capped bare gold nanoparticles are mostly rely on hydrophobicity-driven association of individual crystallites into spheroidal structures. Isothermal titration calorimetry studies of Ca^{2+} ion binding with aspartic acid-capped gold nanoparticles indicates that the process is entropically driven and that screening of the negative charge by the metal ions leads to their aggregation. The aggregates of gold nanoparticles are believed to be responsible for assembly of the plate-like hydroxyapatite crystals into quasi-spherical superstructures. Thus, the spherical morphology of the HAP crystals assemblies is not due to crystal growth on individual nanoparticles but more likely to be due to crystal nucleation and growth on the Ca^{2+} ion-mediated assemblies of aspartic acid-capped gold nanoparticles.

6.7 Conclusions

The ability to grow free-standing, robust and malleable nanogold membranes that may be derivatized to induce and support inorganic crystal growth which has important implications in biomedical applications such as bone-implants as well as in nanocomposites has been demonstrated in this chapter. The nanogold membrane was formed spontaneously by the reaction of bis(2-(4-aminophenoxy)ethyl)ether with aqueous chloroaurate ions at the liquid-liquid interface and thereafter surface-modified with the amino acids aspartic acid and cysteine as well as the bifunctional molecule

anthranilic acid. Calcium phosphate/carbonate crystal growths were achieved by binding Ca^{2+} ions to the nanogold surface-bound carboxylic acid followed by reaction with $NH_4H_2PO_4/CO_2$. The nature of calcium phosphate and carbonate crystals formed were found to be strong functions of the nanogold surface modifier. The control of mineralization process on the gold nanoparticles embedded in a polymeric membrane was successfully compared with the crystal growth on the amino acid protected bare gold nanoparticles. The morphology of the calcium phosphate/carbonate crystals is found to be entirely different in both the above cases. Important control experiments indicated that surface modification of the gold nanoparticles is a key step to ensure efficient mineralization. The nanogold membrane thus suggests potential biomedical application as biocompatible implants.

6.8 References

[1] (a) Dorozhkin, S. V.; Epple, M. *Angew. Chem. Int. Ed.* **2002**, *41*, 3130. (b) Koutsopoulos, S.; Dalas, E. *Langmuir* **2000**, *16*, 6739. (c) Koutsopoulos, S.; Dalas, E. *J. Colloid Interface Sci.* **2000**, *231*, 207. (d) Koutsopoulos, S.; Dalas, E. *Langmuir* **2001**, *17*, 1074.

[2] (a) Ooms, E. M.; Wolke, J. G. C.; Heuvel, M. T. V.; Jeschke, B.; Jansen, J. A. *Biomaterials* **2003**, *24*, 989. (b) Jun, Y. K.; Kim, W. H.; Kweon, O. K.; Hong, S. H.; *Biomaterials* **2003**, *24*, 3731. (c) Lucke, M.; Schmidmaier, G.; Sadoni, S.; Wildemann, B.; Schiller, R.; Haas, N. P.; Raschke, M. *Bone* **2003**, *32*, 521. (d) Suzuki, Y. *Nucl. Instr. and Meth. in Phys. Res. B* **2003**, *206*, 501.

[3] (a) Schnettler, R.; Alt, V.; Dingeldein, E.; Pfefferle, H. J.; Kilian, O.; Meyer, C.; Heiss, C.; Wenisch, S. *Biomaterials* **2003**, *24*, 4603. (b) Kim, H. W.; Lee, S. Y.; Bae, C. J.; Noh, Y. J.; Kim, H. E.; Kim, H. M.; Ko, J. S. *Biomaterials* **2003**, *24*, 3277.

[4] Bigi, A.; Boanini, E.; Panzavolta, S.; Roveri, N. *Biomacromolecules* **2000**, *1*, 752.

[5] (a) Shenton, W.; Pum, D.; Sleytr, U. B.; Mann, S. *Nature* **1997**, *389*, 585. (b) Vaucher, S.; Dujardin, E.; Lebeau, B.; Hall, S. R.; Mann, S. *Chem.Mater.* **2001**, *13*, 4408. (c) Zaremba, C. M.; Belcher, A. M.; Fritz, M.; Li, Y.; Mann, S.; Hansma, P. K.; Morse, D. E.; Speck, J. S.; Stucky, G. D. *Chem. Mater.***1996**, *8*, 679.

[6] (a) Wu, W.; Nancollas, G. H. *Langmuir* **1997**, *13*, 861. (b) Dalas, E.; Kallitsis, J. K.; Koutsoukos, P. G. *Langmuir* **1991**, *7*, 1822. (c) Addadi, L.; Moradian, J.; Shai, E.; Maroudas, N.; Weiner, S. *Proc. Natl. Acad. Sci. USA*. **1987**, *84*, 2732. (d) Albeck, S.; Aizenberg, J.; Addadi, L.; Weiner, S. *J. Am. Chem. Soc.* **1993**, *115*, 11691. (e) Lowenstam, H. A.; Weiner, S. *On Biomineralization*; Oxford University Press: Oxford, England, **1989**. (f) Dalas, E.; Ioannou, P. V.; koutsoukos, P. *Langmuir* **1989**, *5*, 157.

[7] Huer, A. H.; Fink, D. J.; Laraia, V. J.; Arias, J. L.; Calvert, P. D.; Kendal, K.; Messing, G. L. ; Blackwell, J.; Rieke, P. C.; Thompson, D. H.; Wheeler, A. P.; Veis, A.; Caplan, A. I. *Science* **1992**, *255*, 1098.

[8] Hirai, T.; Hodono, M.; Komasawa, I. *Langmuir* **2000**, *16*, 955.

[9] (a) Isobe, T.; Nakamura, S.; Nemoto R.; Senna, M. *J. Phys. Chem. B* **2002**, *106*, 5169. (b) Akao, M.; Aoki, H.; Kato, K. *J. Mater. Sci.* **1981**, *16*, 809. (c) Yang, X.; Wang, Z. *J. Mater. Chem.* **1998**, *8*, 2233. (d) Hata, K.; Kokubo, T.; Nakashi, N.; Yamamuro, T. *J. Am. Ceram. Soc.* **1995**, *78*, 1049. (e) Rodriguez-Lorenzo, L. M.; Vallet-Regi, M. *Chem. Mater.* **2000**, *12*, 2460. (f) Furozono, T.; Walsh, D.; Sato, K.; Sonoda, K.; Tanaka, J. *J. Mater. Sci. Lett.* **2001**, *20*, 111. (g) Walsh, D.; Kingston, J. L.; Heywood, B. R.; Mann, S. *J. Cryst. Growth* **1993**, *133***,** 1.

[10] Liu, Y.; Nancollas, G. H. *J. Phys. Chem. B* **1997,** *101*, 3464.

[11] Dolder, J. V. D.; Farber, E.; Spauwen. P. H. M.; Jansen, J. A. *Biomaterials* **2003**, *24*, 1745.

[12] (a) Kumar, A. ; Mandal, S. ; Selvakannan, PR. ; Pasricha, R.; Mandale, A. B.; Sastry, M. *Langmuir* **2003**, *19*, 6277. (b) Selvakannan, PR.; Mandal, S.; Phadtare, S.; Pasricha, R.; Sastry, M. *Langmuir* **2003**, *19*, 3545. (c) Mandal, S.; Selvakannan, PR.; Phadtare, S.; Pasricha, R.; Sastry, M. *Proc. Indian Acad. Sci. (Chem. Sci.)* **2002**, *114*, 513. (d) Gole, A.; Dash, C.; Ramakrishnan, V.; Sainkar, S. R.; Mandale, A. B.; Rao, M.; Sastry, M. *Langmuir* **2001**, *17*, 1674. (f) Keating, C. D.; Kovaleski, K. M.; Natan, M. J. *J. Phys. Chem. B* **19** *102*, 9404. (g) Park, S.; Taton, T. A.; Mirkin, C. A. *Science* **2001**, *295*, 1503.

[13] Selvakannan, PR.; Kumar, P. S.; More, A. S.; Shingte, R. D.; Wadgaonkar, P. P.; Sastry, M. *Adv. Mater.* **2004**, *16*, 966.

[14] (a) Pretto, M.; Costa, A. L.; Landi, E.; Tampieri, A.; Galassi, C. *J. Am. Ceram. Soc.* **2003**, *86*, 1534. (b) Joshi, V. S.; Joshi, M. J. *Cryst. Res. Technol.* **2003**, *38*, 817. (c) Ngankam, P. A.; Lavalle, Ph.; Voegel, J. C.; Szyk, L.; Decher, G.; Schaaf, P.; Cuisinier, F. J. G. *J. Am. Chem. Soc.* **2000,** *122,* 8998.

[15] (a) Xu, G.; Aksay, I. A.; Groves, J. T. *J. Am. Chem. Soc.* **2001**, *123*, 2196. (b) Cabanas, M. V.; Vallet-Regi, M. *J. Mater. Chem.* **2003**, *13*, 1104.

[16] (a) Brust, M.; Walker, M.; Bethell, D.; Schiffrin, D. J.; Whymann, R. *Chem. Commun.* **1994**, 801. (b) Leff, D. V.; Ohara, P. C.; Heath, J. R. Gelbart, W. M. *J. Phys. Chem.* **1995**, *99*, 7036. (c) Selvakannan, PR.; Mandal, S.; Pasricha, R.; Adyanthaya, S.D.; Sastry, M. *Chem.Commun.* **2002**, 1334.

[17] Link, S.; Wang, Z. I.; El-Sayed, M. A. *J. Phys. Chem. B* **1999**, *103*, 3529.

[18] Matulis, D.; Rouzina, I.; Bloomfield, V. A. *J. Mol. Biol*., **2000,** *296*, 1053.

[19] (a) Colfen, H.; Antonietti, M. *Langmuir* **1998**, *14*, 582. (b) Yu, S. H.; Colfen, H.; Hartmann, J.; Antonietti, M. *Adv. Funct. Mater.* **2002**, *12*, 541. (c) Yu, S. H. ; Colfen, H.; Antonietti, M. *J. Phys. Chem. B*, **2003**, *107*, 7396.

[20] Busch, S.; Dolhaine, H.; Duchesne, A.; Heinz, S.; Hochrein, O.; Laeri, F.; Podebrad, O.; Vietze, U.; Weiland, T.; Kniep. R. *Eur. J. Inorg. Chem.* **1999**, 1643.

[21] Gafni, G.; Septier D.; Goldberg, M. *J. Crystal Growth* **1999**, *205*, 618.

[22] Orme, C. A.; Noy, A.; Wierzbicki, A.; McBride, M. T.; Grantham, M.; Teng, H. H.; Dove, P. M.; DeYoreo, J. J. *Nature* **2001**, *411*, 775.

[23] Sugawara, A.; Ishii, T.; Kato, T. *Angew. Chem. Int. ed.* **2003**, *42*, 5299.

[24] Yang, D.; Qi, L.; Ma, J. *Chem. Commun.* **2003**, 1180.

[25] Lee, I.; Han, S. W.; Choi, J.; Kim, K. *Adv. Mater.* **2001**, *13*, 1617.

[26] Falini, G.; Albeck, S.; Weiner, S.; Addadi, L. *Science* **1996**, *271*, 67.

[27] Nassrallah-Aboukais, N.; Boughriet, A.; Laureyns, J.; Aboukais, A.; Fischer, J.C.; Langelin, H.R.; Wartel, M. *Chem.Mater.* **1998**, *10*, 238.

[28] Kuther, J.; Nelles, G.; Seshadri, R.; Schaub, M.; Butt, H.-J.; Tremel, W. *Chem. Eur. J.* **1998**, *4*, 1834.

CHAPTER VII

Biological Synthesis of Minerals using Microorganisms

This chapter discusses the biological synthesis of metal carbonates by the reaction of different metal cations with microorganisms such as fungi and actinomycetes. Many fungi and actinomycetes are known to produce reasonable amounts of CO_2 during growth. We show that CO_2 and characteristic proteins released from the fungi and actinomycetes can be reacted with appropriate aqueous metal cations to produce truly biogenic minerals such as $CaCO_3$, $BaCO_3$ and $SrCO_3$ crystals. The control experiments involving proteins secreted by fungi and actinomycetes, clearly established the important role played by the proteins in dictating morphology and polymorph control in the mineral synthesis. The fact that these microorganisms act as a source of CO_2 makes this a truly biogenic method for the synthesis of minerals and is thus not merely biomimetic.

Part of the work presented in this chapter has been published and patented:

1) Rautaray, D.; Ahmad, A.; Sastry, M. *J. Am. Chem. Soc.* **2003**, *125*, 14656-14657. 2) Ahmad, A.; Rautaray, D.; Sastry, M. *Adv. Funct. Mater.* **2004**, *14*, 1075-1080. 3) Rautaray, D.; Ahmad, A.; Sastry, M. *J. Mater. Chem.* **2004**, *14*, 2333-2340. 4) Rautaray, D.; Sanyal, A.; Adyanthaya, S. D.; Ahmad, A.; Sastry, M. *Langmuir* **2004**, *20*, 6827-6833. 5) Absar Ahmad, Debabrata Rautaray and Murali Sastry; *US Patent filed* (NCL/42/2003).

7.1 Introduction

Nature provides numerous examples of organisms that directly generate intricate mineralized structures with micro-to-nanoscale features. The presence of inorganic materials in organisms has broad implications in guiding specific functions in their body [1,2]. For example, highly photosensitive brittlestars (marine animals) possess regular arrays of single calcite crystal microlenses that focus light onto underlying nerve bundles [3]. Aquatic algae known as diatoms assemble amorphous silica microshells into a variety of shapes [1]. Biomacromolecules are known to be involved in controlling the nucleation, growth, size, and shape of these mineral phases.

Crystallization is observed in many organisms and is a genetically regulated process. Biomineralization refers to protein-mediated deposition of crystalline materials both within and outside the cell [4]. This highly complex process involves a series of molecular events such as selective recognition and deposition of inorganic salts by proteins followed by the formation of a mineral phase comprising crystallites of uniform size, crystallographic orientation, and morphology [1,5]. In most cases the minerals are formed over a biomolecular scaffold resulting in composite materials [6]. These highly complex, hierarchically ordered and multifunctional composites are formed under mild conditions with size ranging from nano- to centimeter scale, exhibiting unusual mechanical properties that outperform synthetic materials. Such superstructures originate from organized assembly of biomacromolecules such as proteins and the inorganic salts [7]. For example, the mollusk shell is mainly composed of two layers, a prismatic layer and nacreous layer. Both layers are in the form of calcium carbonate crystals; however the prismatic layer forms calcite and the nacreous layer forms aragonite. Such crystal polymorphism in the two closely situated layers is a highly elaborate phenomenon in the mollusks. In such regulated processes it is known that soluble organic matrices such as aspartic acid-rich calcium binding proteins play critical roles [8].

A number of organisms produce inorganic materials either intracellularly or extracellularly [9]. Some well-known examples of bio-organisms synthesizing inorganic materials include magnetotactic bacteria which synthesize magnetite [10], diatoms which synthesize siliceous materials [11], S layer bacteria that have gypsum and $CaCO_3$ as surface layers [12], precipitation of calcium carbonates and phosphates in sea urchins

[13], mammalian skeletons [14] and teeth [15]. Studies of these biogenic mineral deposits have highlighted the role of proteins in mediating the formation of biogenic materials. The proteins regulate the balance between crystal saturation and precipitation in solution, nucleation of mineral crystals, termination of crystal growth, and the overall structure of the crystal [1,16]. It is commonly accepted that acidic proteins are intimately associated with the minerals and regulate crystal formation. For example, an acidic protein (statherin) found in saliva, adsorbs to the surface of teeth and more precisely to hydroxyapatite to inhibit crystal growth [17].

Previous studies in this laboratory illustrate beautifully the reaction of metal ions with microorganisms such as fungi and actinomycetes [18] - the by-products from the process of metal ion detoxification are often an interesting metal, metal sulfide and metal oxide nanomaterial formed by enzymatic pathway. We have recognized an important advance in developing this strategy to encompass synthesis of minerals using microorganisms.

Laboratory processes for the synthesis of metal carbonate minerals have mostly relied on an external source of CO_2 for reaction with desired metal cations in the presence of synthetic molecules or very specific proteins from mineral producing organisms to achieve polymorph and morphology control [6-8]. In this chapter, we address the following questions. Can the morphology and crystallography of metal carbonate minerals in solution be modulated by proteins/biomolecules not normally associated with such microorganisms? Many fungi and actinomycetes are known to produce reasonable amounts of CO_2 during growth [19]. We take advantage of this feature and show in this study that CO_2 and characteristic proteins released from the fungi and actinomycetes may be reacted with appropriate aqueous metal cations to produce truly biogenic minerals such as $CaCO_3$, $BaCO_3$ and $SrCO_3$ crystals.

7.2 Biological synthesis of minerals using microorganisms

Fungi such as *Trichothecium* sp., *Verticillium* sp., *Fusarium* sp., *Fusarium oxysporum* and actinomycetes such as *Rhodococcus* sp., *Thermomonospora* sp. were maintained on potato-dextrose-agar (PDA) slants. Stock cultures were maintained by sub culturing at monthly intervals. After growing at pH 7 and 27 ^{o}C for four days the slants

were preserved at 15 ^{o}C. From an actively growing stock culture, subcultures of both the fungi and actinomycetes were made on fresh slants and after four days of incubation at pH 7 and 27 ^{o}C were used as the starting materials for fermentation experiments. For the isolation of minerals, the fungi and actinomycetes were grown in 500 ml Erlenmeyer flasks containing 100 ml MGYP medium which is composed of malt extract (0.3 %), glucose (1 %), yeast extract (0.3 %) and peptone (0.5 %). After adjusting the pH of the medium to 7, the cultures were grown under continuous shaking on a rotary shaker (200 rpm) at 27 ^{o}C for 96 hours. After 96 hours of fermentation, mycelia of the respective fungi and actinomycetes were separated from the culture broth by centrifugation (5000 rpm) for 20 minutes at 20 ^{o}C and then the mycelia were washed thrice with distilled water under sterile conditions. The harvested mycelial mass (20 g wet wt. of mycelia) of fungi and actinomycetes were then resuspended in 100 ml of electrolyte solution in 500 ml Erlenmeyer flasks. The biotransformation of initial precursor ions into the desired carbonate minerals was monitored by separating the fungal mycelia from the aqueous component by filtration at different times, this reaction being clearly visible in terms of the reaction medium becoming turbid and milky white. The filtrates were subjected to centrifugation at 10000 rpm and the pellets obtained were washed repeatedly with copious amounts of double distilled water. The purified pellets were solution-cast in the form of films onto different solid supports for further analysis. Prior to analysis, considerable care was taken to remove uncoordinated proteins in the reaction medium from the biogenic minerals by washing the minerals synthesized using fungi and actinomycetes.

7.3 Biological synthesis of $CaCO_3$ crystals using fungi

In typical experiments, 20 g each of *Trichothecium* sp., *Verticillium* sp., *Fusarium* sp. and *Fusarium oxysporum* biomass were suspended in 10^{-3} M aqueous $CaCl_2$ solution in conical flasks after thorough washing and centrifugation under sterile conditions as described in section 7.2. These flasks were then cotton plugged and incubated at 27 ^{o}C. Aliquots of the aqueous component were separated from the mycelia periodically and subjected to SEM, EDAX, FTIR and XRD analysis.

7.3.1 Scanning electron microscopy studies

7.3.1.1 Synthesis of $CaCO_3$ crystals using the fungus, *Trichothecium* sp.

Fig.7.1A shows a representative SEM image recorded from $CaCO_3$ crystals synthesized by the reaction of aqueous Ca^{2+} ions with the fungus, *Trichothecium* sp. for 3 days. A large number of plate-shaped crystals of $CaCO_3$ are observed. To understand the plate formation process better, the kinetics of crystallization was monitored as a function of time of reaction of $CaCl_2$ with the fungus, *Trichothecium* sp. Fig.7.1B-E show representative SEM images of $CaCO_3$ crystals formed after 12 h, 1 day, 2 days and 3 days of reaction of calcium ions with this fungus respectively.

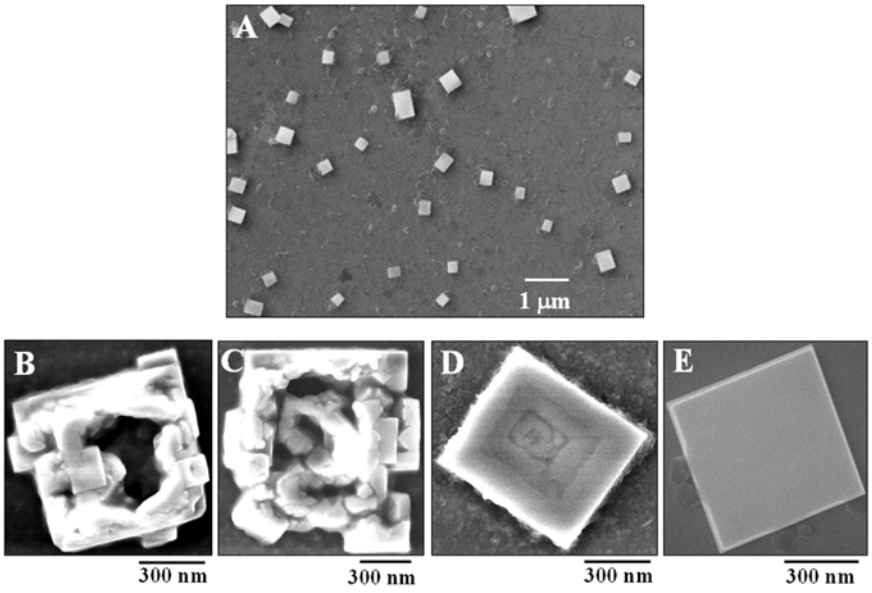

Fig.7.1: *A) Low magnification SEM micrograph of $CaCO_3$ crystals after 3 days of reaction of aqueous Ca^{2+} ions with Trichothecium sp. SEM micrographs of $CaCO_3$ crystals formed after 12 hours, 1 day, 2 days and 3 days of reaction of aqueous Ca^{2+} ions with Trichothecium sp. are shown in B-E respectively.*

After 12 h of reaction (Fig.7.1B), immature crystals of $CaCO_3$ are observed with a flat, open-structured morphology. It is interesting to observe the evolution of the crystal morphology as the growth proceeds from structures with a high degree of defects (Fig.7.1B-D) to a smooth, plate-like structure after 3 days of reaction (Fig.7E). The defects are in the form of hopper crystals. Hopper crystals are crystals that have hollow areas formed by preferred crystal growth on edges. The edges of the crystal grow at a faster rate than the interior of the crystal giving a staircase-like step pattern toward the

middle of the crystal face and have been previously observed in calcite crystals grown in the presence of propanol [20]. It is believed that the formation of hopper crystals is a kinetically controlled (limited diffusion of constituent ions to the growing crystal face) growth phenomenon and not a thermodynamically controlled process. In the study by Dickinson and McGrath, hopper crystal growth was shown not to be controlled explicitly by alcohol functionality but the solution viscosity was thought to play as an important factor in the formation of hopper crystals [20].

[*Hopper crystals are crystals that have formed hollow areas, form due to hopper instability. Hopper instability occurs as surface effects dominate crystal growth when the crystals are small. As the crystal grows larger, the corner and edges stick out the most and therefore grow the fastest. The edges also rob water molecule from center, which then grow even slower than they already are. This makes the hollow area even more prominent*]

7.3.1.2 Synthesis of $CaCO_3$ crystals using the fungus, *Verticillium* sp.

Fig.7.2A & B show representative SEM images of the $CaCO_3$ crystals obtained by the reaction of aqueous Ca^{2+} ions with the fungus, *Verticillium* sp. After 3 days of reaction, the formation of very uniform $CaCO_3$ nanocrystallites was observed (Fig.7.2A). The size of the crystallites determined from the SEM image was in the range 70-100 nm.

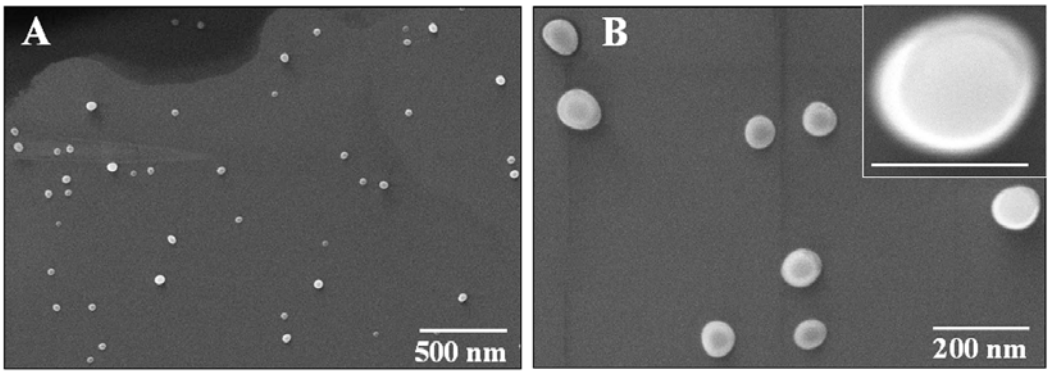

Fig.7.2: *(A & B) Representative SEM micrographs of $CaCO_3$ crystals grown after 3 days of reaction of aqueous Ca^{2+} ions with Verticillium sp. The inset in B shows a magnified view of one of the flat, circular $CaCO_3$ crystals (scale bar = 100 nm).*

The higher magnification SEM image clearly shows that the $CaCO_3$ crystallites are circular in shape with some evidence of their being flat (Fig.7.2B). One of the circular $CaCO_3$ crystals is shown in the inset of Fig.7.2B. Such spherical/circular morphology of $CaCO_3$ crystals is indicative of formation of the highly unstable vaterite polymorph [8a].

7.3.1.3 Synthesis of $CaCO_3$ crystals using the fungus, *Fusarium* sp.

Fig.7.3 shows SEM images recorded from $CaCO_3$ crystals formed after exposure of aqueous $CaCl_2$ solution to the fungus, *Fusarium* sp. for 1 day (A) and 3 days (B). After one day of reaction, a large number of cruciform-shaped crystallites are observed. The inset of Fig.7.3A shows a magnified view of one of the crystallites that appears rather porous. After 3 days of reaction, mature crystals exhibit the same cruciform structure (Fig.7.3B) wherein the porous nature of the crystals is more clearly seen. Secondary nucleation of rhombohedral crystals has taken place on the underlying cruciform-shaped crystal.

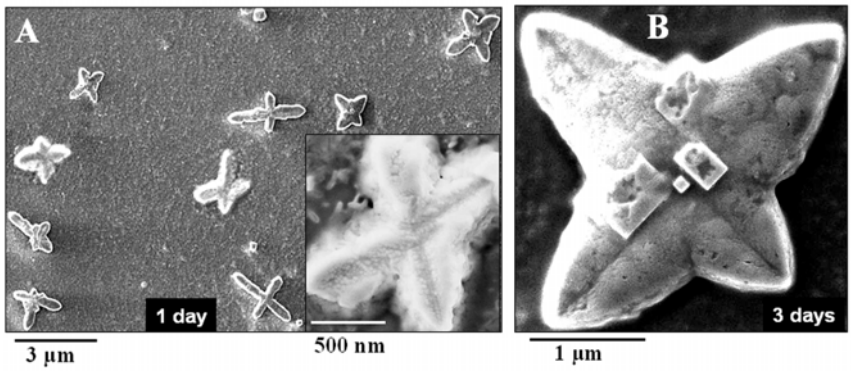

Fig.7.3: *A) SEM picture of $CaCO_3$ crystals after 1 day of reaction of Ca^{2+} ions with Fusarium sp. The inset shows a magnified image of one of the crystals. B) SEM picture of a single mature $CaCO_3$ crystal after 3 days of reaction of Ca^{2+} ions with Fusarium sp.*

7.3.1.4 Synthesis of $CaCO_3$ crystals using the fungus, *Fusarium oxysporum*

Fig.7.4 shows SEM images recorded from $CaCO_3$ crystals formed after exposure of aqueous $CaCl_2$ solution to the fungus, *Fusarium oxysporum* for 1 day (A), 2 days (B) and 3 days (C and D). After 1 day of reaction, the formation of very small $CaCO_3$ crystallites is observed (Fig.7.4A). An interesting feature of the SEM image is the assembly of the $CaCO_3$ crystallites into a circular superstructure with a smaller percentage of randomly distributed crystallites. The central regions of the circular aggregates also appear to contain much smaller $CaCO_3$ crystallites, although at a smaller density. After 2 days of reaction of $CaCl_2$ with *Fusarium oxysporum* (Fig.7.4B), the contrast between the perimeter of the circular aggregates and the central core is much more pronounced. The $CaCO_3$ crystallites at the perimeter of the circular assemblies are

larger than those observed after 1 day of reaction (Fig.7.4A). The SEM images of the $CaCO_3$ crystals after 3 days of reaction (Fig.7.4C & D) are essentially identical in overall morphology to those obtained after 2 days of reaction. The higher magnification SEM image of the circular $CaCO_3$ crystallite assemblies (Fig.7.4D & inset) indicates that the individual elongated $CaCO_3$ crystallites are arranged in a quasi-bilayer structure in the circular annular region.

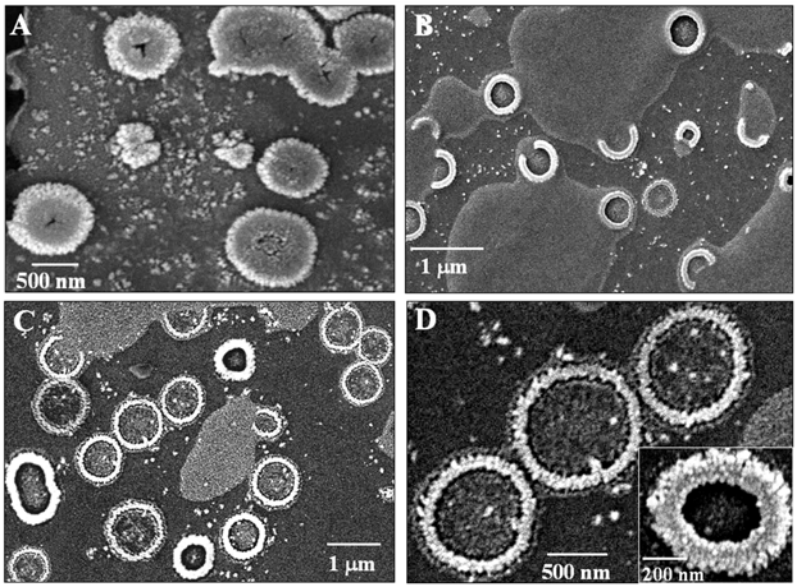

Fig.7.4: *SEM micrographs of $CaCO_3$ crystals after, A) 1day; B) 2 days and C & D) 3 days of reaction of aqueous Ca^{2+} ions with Fusarium oxysporum. The inset in D shows a magnified image of one of the circular $CaCO_3$ crystal superstructures.*

7.3.1.5 Calcination of biogenic calcite plates grown using the fungus, *Trichothecium* sp.

The formation of plate-like calcite crystals by the reaction of aqueous Ca^{2+} with *Trichothecium* sp. (Fig.7.1A) indicates that specific protein(s) secreted by this plant organism are responsible for the shape control of $CaCO_3$ crystals. The location of the protein(s) in the crystals (surface adsorption vs uniformly intercalated in the crystals) may be indirectly determined by removal of the proteins by calcination. Fig.7.5A shows an SEM image of biogenic calcite plates grown using *Trichothecium* sp. after heating at 300 ^{o}C for 3 h. Upon calcination, the originally compact crystals (Fig.7.1A) become highly porous and indicate removal of proteins uniformly intercalated into the crystalline

framework. It is interesting to note that the overall plate-like morphology of the calcite crystals is not much altered after calcination. The higher magnification SEM image shown in the inset of Fig.7.5A clearly reveals the porous nature of the calcite plates upon removal of intercalated/occluded proteins after calcination. In order to understand better the removal of occluded proteins from the originally compact, plate-like calcite crystals during calcination, the kinetics of the process was studied by heating the crystals for different duration at 300 ^{o}C and monitoring the changes in the crystals by SEM.

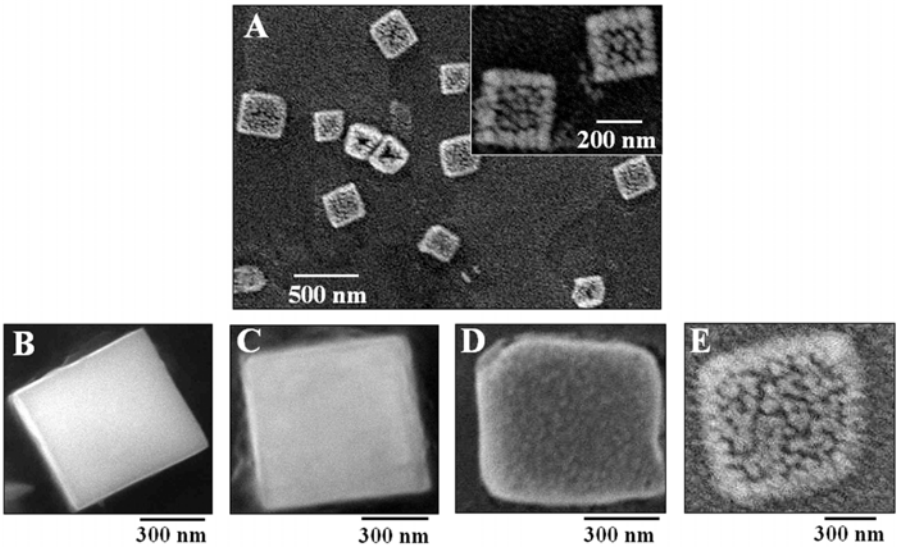

Fig.7.5: *A) SEM micrograph of $CaCO_3$ crystals (shown in Fig.7.1A) after calcination at 300 ^{o}C for 3 h. The inset shows a magnified view of a pair of calcined $CaCO_3$ crystals grown using Trichothecium sp. B-E) SEM micrographs of $CaCO_3$ crystals after 3 days of reaction of aqueous Ca^{2+} ions with Trichothecium sp. as a function of time of calcination at 300 ^{o}C : 0 h (B), 1 h (C), 2 h (D) and 3 h (E).*

Fig.7.5B-E show representative SEM images obtained from films of $CaCO_3$ crystals synthesized using *Trichothecium* sp. as a function of time of heating at 300 ^{o}C. Fig.7.5B shows the SEM image of as-prepared plate-like calcite crystals obtained by the reaction of Ca^{2+} with *Trichothecium* sp. for 3 days. The same sample after 1 h of calcination at 300 ^{o}C shows no discernable change in the originally compact plate-like morphology of the calcite crystals (Fig.7.5C). After 2 h of calcination (Fig.7.5D), defects start appearing in the calcite platelets and the morphology becomes fairly porous. Upon further calcination (3 h, Fig.7.5E), the porosity in the calcite platelets is much more pronounced

indicating removal of proteins that were originally uniformly intercalated into the calcite crystals.

7.3.1.6 Calcination of biogenic vaterite crystals grown using *Verticillium* sp.

Fig.7.6 shows an SEM image of biogenic vaterite crystals grown using *Verticillium* sp. after heating at 300 ^{o}C for 3 h. Upon calcination, the original spherical/circular crystals (Fig.7.2A) are transformed into more faceted crystals (Fig.7.6A). Fig.7.6B shows a magnified view of the faceted crystals, which show an increase in the surface roughness suggesting removal of proteins occluded into the crystalline framework on heating. The morphology change from circular to polyhedral suggests a concomitant variation in the crystal structure upon heat treatment.

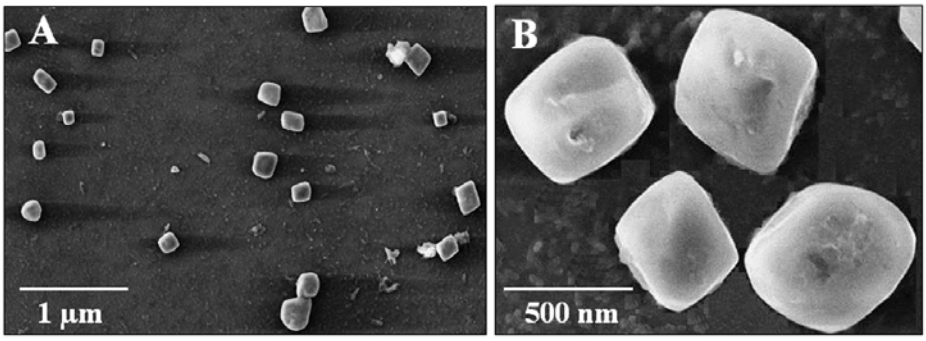

Fig.7.6: *Low and high magnification SEM images of $CaCO_3$ crystals grown using Verticillium sp. (shown in Fig.7.2) after calcination at 300 ^{o}C for 3 h.*

7.3.1.7 Synthesis of $CaCO_3$ crystals using fungal extracts

Control experiments were performed wherein *Trichothecium* sp., *Verticillium* sp., *Fusarium* sp. and *Fusarium oxysporum* biomass were immersed in water for 3 days and the aqueous components separated by filtration. The aqueous fractions were taken separately with 10^{-3} M $CaCl_2$ and CO_2 was bubbled very slowly through these solutions. The $CaCO_3$ crystals formed in this manner were analyzed by SEM. SEM analysis revealed the formation of flat plate-like calcite crystals (Fig.7.7A) similar to those shown in Fig.7.1. Fig.7.7B shows a SEM image of $CaCO_3$ crystals grown using the fungal extract of *Verticillium* sp. The formation of spherical crystallites, very similar to those synthesized in the presence of fungus (Fig.7.2) was observed. The inset of Fig.7.7B

shows a higher magnification SEM image of spherical $CaCO_3$ crystals obtained, indicating that the crystallites in the control experiment are bigger (size ~ 500 nm) than those synthesized in the presence of the fungus (70-100 nm, Fig.7.2).

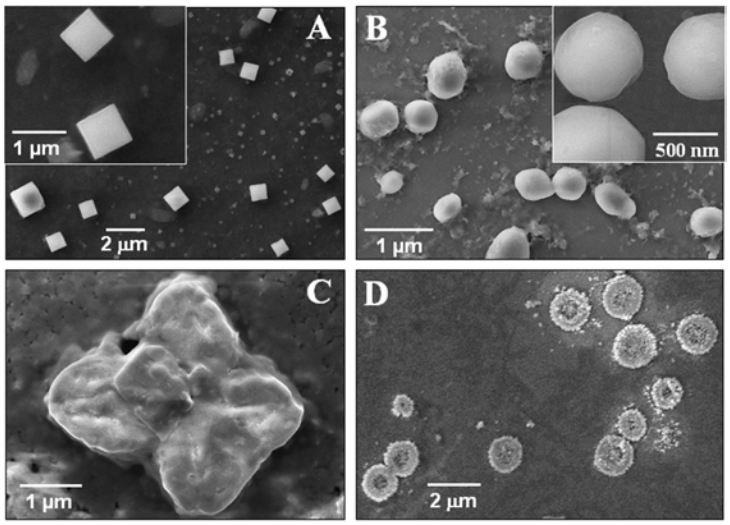

Fig.7.7: *Representative SEM micrographs of $CaCO_3$ crystals grown using extracts of Trichothecium sp. (A), Verticillium sp. (B), Fusarium sp. (C) and Fusarium oxysporum (D).*

Fig.7.7C and D show representative SEM images of $CaCO_3$ crystals grown using the fungal extract of *Fusarium* sp. and *Fusarium oxysporum* respectively. The formation of cruciform (Fig.7.7C) and ring like (Fig.7.7D) $CaCO_3$ crystals are very similar to those synthesized in the presence of respective fungus (Fig.7.3 & 7.4). From above it is clear that that the proteins secreted by these fungus into solution are responsible for the morphology control and polymorph selectivity and more importantly, that the growth of these crystals does not take place within specific reaction sites in the fungal biomass.

7.3.2 Energy dispersive analysis of X-rays (EDAX) measurements

The EDAX spectrum recorded from the plate like calcite crystals synthesized using the fungus, *Trichothecium* sp. is shown in Fig.7.8A, curve 1. In addition to the expected Ca, C and O signals, strong N and S signals are also observed indicating the presence of proteins within the plate-like crystallites. Spot-profile EDAX spectra recorded from the calcined calcite platelets synthesized using *Trichothecium* sp. are shown as curves 2, 3 and 4 in Fig.7.8A and correspond to samples calcined for 1 h, 2 h and 3h respectively.

From the EDAX spectra, it is observed that as the calcination time increases, the intensity of the N and S signals decreases rapidly while a smaller loss in intensity is observed for the C signal (the O signal is essentially unaffected by heating). The fact that the C signal does not decrease to the extent that the N and S signals do is due to the fact that the C signal comes from both the $CaCO_3$ crystals as well as the occluded proteins. A quantitative analysis of the Ca and C signals from curve 2 (1 h of calcination at 300 ^oC) yielded a Ca : C ratio of 1 : 1.53. The corresponding Ca : C ratios after 2 h (curve 3) and 3 h (curve 4) of calcination yielded the values 1 : 1.33 and 1 : 1.08 respectively clearly showing the reduction of the carbon component upon calcination. After calcination for 3 h, almost complete disappearance of N and S signals is observed from the calcite crystals indicating complete removal of the occluded proteins. The strong Ca, C and O signals observed after completion of the heating cycles indicate that the calcite phase is intact after calcination. That the proteins are uniformly occluded into the calcite plate-like structures is shown by the regularly distributed pores in the calcined particle (SEM image accompanying curve 4 in Fig.7.8A).

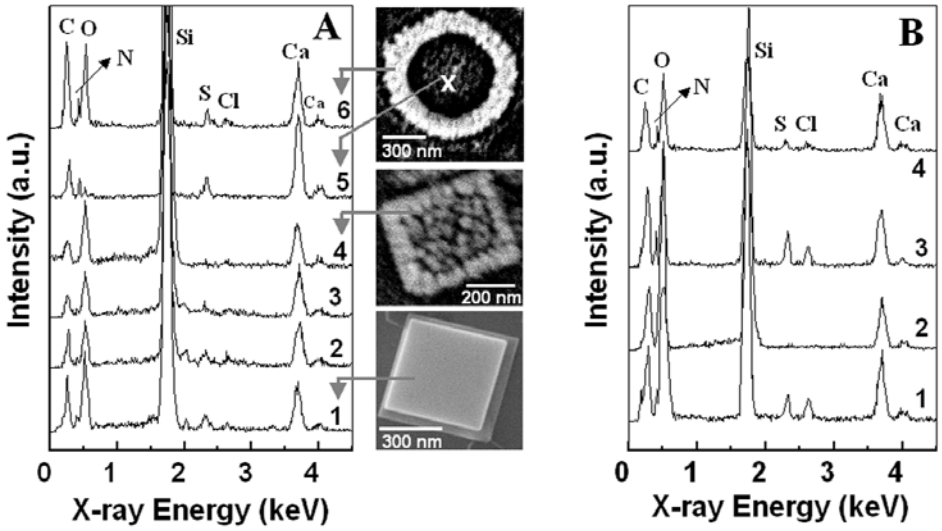

Fig.7.8: *(A) Spot-profile EDAX spectra recorded from films of $CaCO_3$ crystals synthesized using Trichothecium sp. (curve 1) and Fusarium oxysporum (curves 5 and 6). The respective SEM images are shown indicating the precise regions from which the EDAX spectra were recorded. The EDAX spectra recorded from calcite crystals synthesized using Trichothecium sp. after calcination at 300 ^oC for 1 h, 2 h and 3 h are shown as curves 2-4 respectively. (B) Spot-profile EDAX spectra recorded from films of $CaCO_3$ crystals synthesized using Verticillium sp. before (curve 1) and after calcination at 300 ^oC for 3 h (curve 2). Curve 3 corresponds to the EDAX spectrum recorded from $CaCO_3$ crystals grown using extracts of Verticillium sp. Curve 4 corresponds to the EDAX spectrum recorded from $CaCO_3$ crystals synthesized using Fusarium sp.*

The spot-profile EDAX analysis of circular calcite crystallite assemblies obtained using the fungus *Fusarium oxysporum* are shown as curves 5 & 6 in Fig.7.8A. Curves 5 and 6 in this figure correspond to the regions within and on the perimeter of the circular patterns as clearly illustrated in the accompanying SEM micrograph (Fig.7.8A). Towards the center of the circular region, strong Ca, C, S and N signals are observed. The presence of N and S signals is clearly indicative of the presence of proteins in the circular assemblies. The strong Ca signal in this region together with a weak O signal suggests that these ions complex with the proteins secreted by *Fusarium oxysporum* leading to the formation of circular aggregates of the proteins mediated by Ca^{2+} counterions and also that there is a negligibly small percentage of calcite crystals in this region. Strong N and S signatures are also observed in the prominent calcite crystallites lining the perimeter of the circular assembly (Fig.7.8A, curve 6) along with increased C and O signals relative to that recorded from the central region (curve 5). These two observations indicate that the calcite crystals in the circular assembly are present with proteins that are possibly occluded into the annular structure.

To understand the chemical composition of the vaterite crystallites synthesized using the fungus *Verticillium* sp. (shown in Fig.7.2), spot-profile EDAX measurement of one of the circular vaterite crystals is shown as curve 1, Fig.7.8B. In addition to the expected Ca, C and O signals, we observe the presence of N and S signals in the vaterite crystals. This indicates the presence of proteins within the circular vaterite crystallites. The spot-profile EDAX spectrum recorded from the biogenic vaterite crystals after calcination at 300 ^{o}C for 3 h is shown as curve 2 in Fig.7.8B. As expected, strong Ca, C and O signals are observed but this is accompanied by complete disappearance of N and S signals from the $CaCO_3$ crystals indicating removal of the occluded proteins. The presence of proteins involved in stabilizing the vaterite polymorph in the control experiment (where the protein extract from the fungus *Verticillium* sp. was reacted with $CaCl_2$ and thereafter with CO_2) was detected by EDAX measurement, which shows the presence of strong N and S signals together with Ca, C and O signals (curve 3, Fig.7.8B). The presence of proteins within the cruciform calcite crystalline framework (Fig.7.3) is indicated by strong N and S signals along with signals of Ca, C and O with expected stoichiometry in the EDAX spectrum (curve 4 in Fig.7.8B).

7.3.3 Fourier transform infrared (FTIR) spectroscopy studies

The FTIR spectrum recorded from the plate-shaped calcite crystals synthesized using *Trichothecium* sp. is shown as curve 1 in Fig.7.9A. Strong absorption bands centered at 875 and 712 cm^{-1} are seen in the FTIR spectrum that is characteristic of the calcite phase of $CaCO_3$ [8a]. The presence of proteins in the *Trichothecium* sp.-biogenic calcite crystals is also indicated in the FTIR spectrum from this sample (curve 1, inset of Fig.7.9A) where prominent amide I and II bands from the proteins are seen. The FTIR spectrum recorded from the circular $CaCO_3$ crystallite assemblies obtained using the fungus *Fusarium oxysporum* is shown as curve 2 in Fig.7.9A. The absorption bands centered at 712 and 876 cm^{-1} are characteristics of the calcite polymorph while the weak absorption band at 744 cm^{-1} is due to vaterite crystallites [8a]. The signal due to proteins secreted by the fungus is supported by the presence of the amide I and II bands at 1650 and 1550 cm^{-1} respectively, in the $CaCO_3$ crystals formed using *Fusarium oxysporum*.

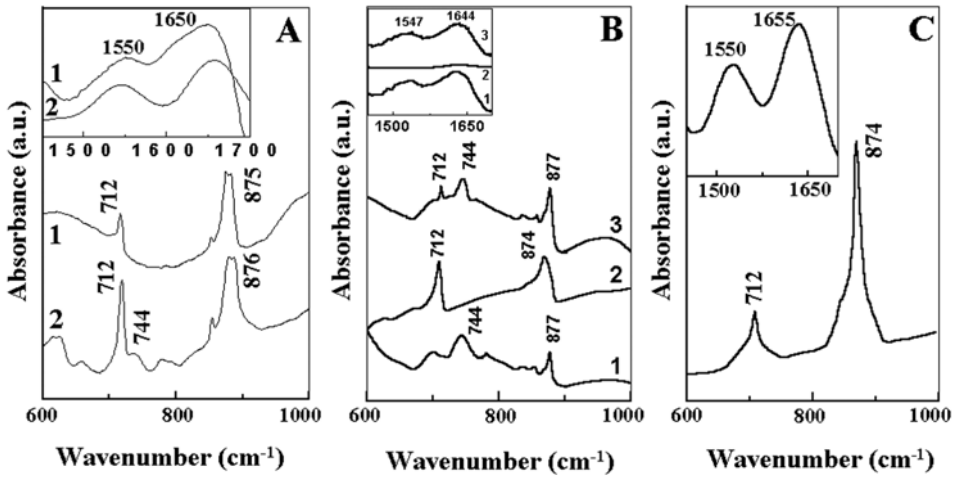

Fig.7.9: A) *FTIR spectra recorded from $CaCO_3$ crystals obtained by the reaction of aqueous Ca^{2+} ions for 3 days with the fungus Trichothecium sp. (curve 1) and Fusarium oxysporum (curve 2) in different spectral windows. B) FTIR spectra in different spectral windows recorded from $CaCO_3$ crystals obtained by the reaction of aqueous Ca^{2+} ions for 3 days with the fungus Verticillium sp. before (curve 1) and after calcination at 300 ^oC for 3 h (curve 2) and $CaCO_3$ crystals grown using extract from Verticillium sp. (curve 3). C) FTIR spectra of $CaCO_3$ crystals by the reaction of Ca^{2+} ions with Fusarium sp. in different spectral windows.*

The FTIR spectrum recorded from the spherical $CaCO_3$ crystals synthesized using *Verticillium* sp. is shown as curve 1 in Fig.7.9B. The absorption bands at 744 and 877 cm^{-1} are characteristic of vaterite polymorph of $CaCO_3$ [8a]. Along with the signatures for

vaterite polymorph, the presence of amide I and II bands at 1644 and 1547 cm^{-1} respectively are also observed in the FTIR spectrum. This observation indicates that the vaterite crystals in the spherical/circular morphology are present with proteins that are possibly occluded into the crystals or are bound to the surface of the crystals. The FTIR spectrum of the calcined biogenic $CaCO_3$ crystals synthesized using *Verticillium* sp. exhibited absorption bands at 712 and 874 cm^{-1} (curve 2, Fig.7.9B) accompanied by complete disappearance of N and S signals (curve 2 in the inset of Fig.7.9B) from the $CaCO_3$ crystals indicating removal of the occluded proteins. The calcination-induced morphology variation seen in the SEM images is due to transformation of vaterite into calcite [21]. The FTIR spectrum recorded from the $CaCO_3$ crystals in the control experiment (where the protein extract from the fungus *Verticillium* sp. was reacted with $CaCl_2$ and thereafter with CO_2) exhibited absorption bands at 744 and 877 cm^{-1}, which indicate the formation of the vaterite polymorph (curve 3 in Fig.7.9B). This occurs together with a weak absorption band at 712 cm^{-1} that is characteristic of calcite [8a]. The presence of proteins in stabilizing the vaterite polymorph was also observed in the EDAX spectrum (curve 3, inset of Fig.7.9B) showing the presence of strong N and S signals. Fig.7.9C shows the FTIR spectrum recorded from the cruciform $CaCO_3$ crystals synthesized using the fungus *Fusarium* sp. Absorption bands centered at 874 and 712 cm^{-1}, characteristic of the calcite phase of $CaCO_3$ are seen [8a]. The presence of proteins within the calcite crystalline framework is indicated by strong amide I and II signatures in the FTIR spectrum (inset of Fig.7.9C).

7.3.4 X-ray diffraction (XRD) measurements

The XRD pattern recorded from the plate-shaped calcite crystals synthesized using the fungus *Trichothecium* sp. is shown as curve 1 in Fig.7.10A. It is clear that the Bragg reflections from this film correspond to the calcite polymorph. The high intensity of the (104) and (113) Bragg reflections relative to the other reflections indicates that the calcite crystals synthesized using *Trichothecium* sp. are preferentially oriented along these crystallographic directions. This is not surprising given the extremely flat morphology of the calcite particles (Fig.7.1A) that would favor organization of the crystals with (104) and (113) crystallographic planes parallel to the substrate. The XRD pattern recorded from the calcite plate-shaped structures after calcination for 2 h shows

no marked change relative to the pattern recorded from the as-prepared calcite crystals (curve 2, Fig.7.10A). However, large differences in the XRD pattern obtained from the plate-shaped calcite crystals calcined for 3 h are observed (curve 3, Fig.7.10A). The most striking aspect is a broadening of the Bragg reflections relative to the as-prepared calcite crystals (curve 1, Fig.7.10A). This broadening of the Bragg reflections of the calcite crystals is an indicator that the crystallites are becoming smaller consequent to calcination. This result is in agreement with the SEM data (compare images in Fig.7.5B and E) that clearly shows the compact, calcite platelets decomposing into porous calcite crystallites of nanoscale dimensions after calcination. Two main inferences may be made from this result. One is that the proteins present in the calcite platelets promote crystallization of $CaCO_3$ and once they are removed by heating, the mosaic structure collapses leading to formation of smaller calcite crystallites. The second inference is that the proteins present in the calcite crystals are not present on the surface of the crystals but are occluded within the crystals. It is very unlikely that proteins present merely on the surface of the crystals could promote calcite crystallization as observed in this study and also that once removed, they would yield porous assemblies of smaller calcite crystallites.

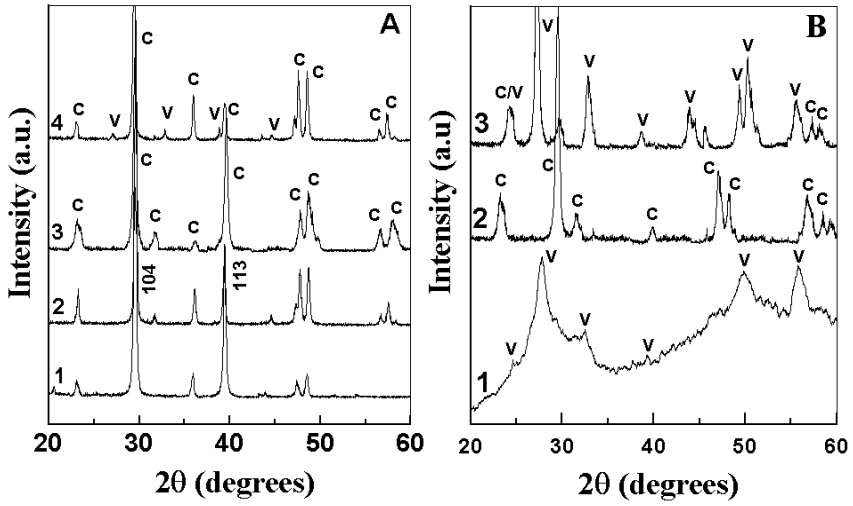

Fig.7.10: *A) XRD patterns recorded from solution-cast films of $CaCO_3$ crystals synthesized using Trichothecium sp on glass substrate (curve 1) and the same sample after calcination at 300 ^oC for 2 h (curve 2) and 3 h (curve 3). Curve 4 corresponds to XRD pattern recorded from solution-cast film of $CaCO_3$ crystals synthesized using Fusarium oxysporum. B) XRD patterns recorded from solution-cast films of $CaCO_3$ crystals synthesized using Verticillium sp. on glass substrate before (curve 1) and after calcination at 300 ^oC for 3 h (curve 2). Curve 3 corresponds to the XRD pattern recorded from a solution-cast film of $CaCO_3$ crystals grown using extract from Verticillium sp. (curve 3). In the XRD spectra, 'V' stands for vaterite and 'C' for calcite.*

XRD analysis of the $CaCO_3$ crystallite assemblies formed by the reaction of aqueous Ca^{2+} ions with *Fusarium oxysporum* for 3 days was performed and the pattern obtained is shown as curve 4 in Fig.7.10A. The XRD analysis confirms the formation of the calcite polymorph of $CaCO_3$ [22] with some evidence of a much smaller percentage of vaterite [23]. It is clear that the $CaCO_3$ crystallites assembled into ring-like superstructures (Fig.7.4) are dominated by the calcite polymorph.

XRD analysis of the $CaCO_3$ crystallites formed by the reaction of aqueous Ca^{2+} ions with *Verticillium* sp. for 3 days was performed and the pattern obtained is shown as curve 1 in Fig.7.10B. The Bragg reflections identified by 'V' agree excellently with those reported for vaterite [23]. The broad Bragg reflections in the XRD spectrum are clearly indicative of small crystallites in agreement with the SEM results (Figs.7.2A & B). The XRD pattern recorded from the calcined biogenic-vaterite crystals shows the presence of Bragg reflections characteristic of calcite (peaks marked 'C' in curve 2, Fig.7.10B) thus supporting the phase transformation inferred from the FTIR results. XRD analysis of the $CaCO_3$ crystals in the control experiment where the $CaCO_3$ crystals were synthesized using the protein extract from *Verticillium* sp. confirms the formation of vaterite (curve 3, Fig.7.10B; peaks labeled by 'V') with evidence of a much smaller percentage of calcite (peaks labeled by 'C') [22,23]. It is clear that the circular $CaCO_3$ crystallites are dominated by the vaterite polymorph.

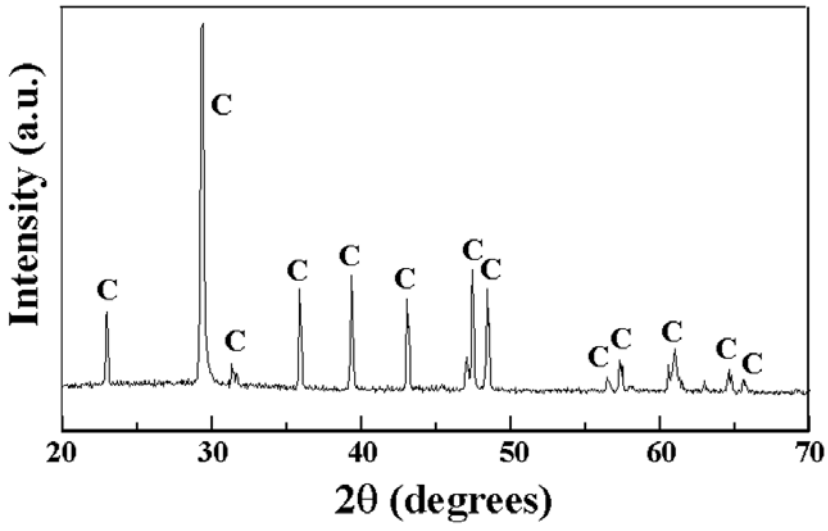

Fig.7.11: *XRD pattern recorded from solution-cast films of $CaCO_3$ crystals synthesized using Fusarium sp. In the XRD spectrum 'C' stands for calcite.*

XRD analysis of the cruciform biogenic $CaCO_3$ crystallites formed by the reaction of aqueous Ca^{2+} ions with the fungus, *Fusarium* sp. for 3 days was performed and the pattern obtained is shown as Fig.7.11. The 2 θ values of the Bragg reflections correspond excellently with those reported for calcite (peaks labeled by 'C') [22,23].

7.3.5 Summary

The biological synthesis of $CaCO_3$ crystals of variable morphology with polymorph selectivity by challenging non-calcareous microorganisms such as fungi with aqueous Ca^{2+} ions has been demonstrated. The CO_2 and characteristic proteins released from the fungi was used for their reaction with aqueous Ca^{2+} ions to produce truly biogenic $CaCO_3$ crystals. While calcite crystals of variable morphology were observed with *Trichothecium* sp., *Fusarium oxysporum* and with *Fusarium* sp., highly unstable vaterite polymorph of $CaCO_3$ in a spherical morphology was observed with the *Verticillium* sp. Significant differences in the morphology and polymorph selectivity of $CaCO_3$ crystals is observed indicating that the proteins secreted by the respective fungus play a crucial role in directing the morphology and crystallography of $CaCO_3$ crystals.

7.4 Biological synthesis of $CaCO_3$ crystals using actinomycetes

Actinomycetes are microorganisms that share important characteristics of fungi and prokaryotes such as bacteria [24]. Even though they are classified as prokaryotes due to their close affinity with mycobacteria and the coryneforms (and thus amenable to genetic manipulation by modern recombinant DNA techniques), they were originally designated as "Ray Fungi" (Strahlenpilze). Focus on actinomycetes has primarily centered on their phenomenal ability to produce secondary metabolites such as antibiotics [25].

In typical experiments, 20 g each of actinomycete, *Rhodococcus* sp. and *Thermomonospora* sp. biomass were separately suspended in 10^{-3} M aqueous $CaCl_2$ solution in conical flasks after thorough washing and centrifugation under sterile conditions as described in section 7.2. These flasks were then cotton plugged and incubated at 27 ^{o}C. Aliquots of the aqueous component were separated from the mycelia periodically and subjected to SEM, EDAX, FTIR and XRD analysis.

7.4.1 Scanning electron microscopy studies

7.4.1.1 Synthesis of $CaCO_3$ crystals using the actinomycete, *Rhodococus* sp.

Fig.7.12 shows SEM images recorded from solution-cast films of the aqueous $CaCl_2$ solution after exposure to *Rhodococcus* sp. for 1 day (A) and 3 days (B). The $CaCO_3$ crystals formed are circular in cross-section having porous surface (Fig.7.12A). The porous nature of which is reduced significantly in the mature crystals (Fig.7.12B). The $CaCO_3$ morphology formed in this case is observed to be very similar to that of biosynthesized using the fungus *Verticillium* sp. Such circular morphology of $CaCO_3$ is indicative of the formation of the highly unstable vaterite polymorph [8a].

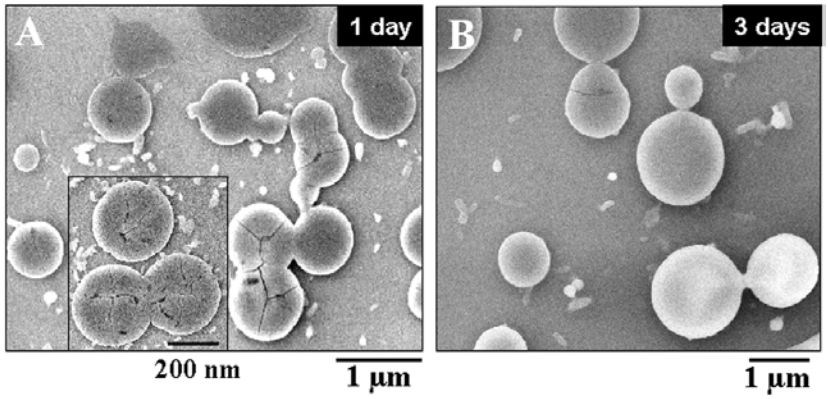

Fig.7.12: *A) SEM micrograph of $CaCO_3$ crystals after 1 day of reaction of Ca^{2+} ions with the actinomycete Rhodococcus sp. The inset shows a magnified image of an assembly of the crystallites. B) SEM micrograph of $CaCO_3$ crystals after 3 days of reaction of Ca^{2+} ions with Rhodococcus sp.*

Studies on the synthesis of vaterite crystals are relatively scarce with the synthesis having been achieved in the presence of divalent cations [26a], using AOT microemulsions [26b], and poly(vinyl) alcohol [26c]/double hydrophilic block copolymers as additives [26d,e]. Vaterite is thermodynamically the most unstable polymorph among the three crystal structures of $CaCO_3$ and is used for specific applications requiring high specific surface area, high solubility, high dispersion, and smaller specific gravity [26f]. The pH of the Ca^{2+} - *Rhodococcus* sp. reaction medium after 3 days of reaction was measured to be 5.5. It is known that synthesis of vaterite is facilitated by low pH conditions [27] – clearly, the synthesis of vaterite by *Rhodococcus* sp. is not due to pH effects and is due to specific proteins secreted by the microorganism.

7.4.1.2 Synthesis of $CaCO_3$ crystals using the actinomycete, *Thermomonospora* sp.

7.4.1.2.1 Extracellular synthesis

Thermomonospora sp. upon reaction with aqueous Ca^{2+} ions resulted in the formation of $CaCO_3$ crystals both extracellularly and intracellularly (on the mycelia of the biomass). Figs.7.13A–C show representative SEM images of extracellularly grown $CaCO_3$ crystals after reaction of aqueous Ca^{2+} ions with *Thermomonospora* sp. for 3 days. The $CaCO_3$ crystals in this case exhibit a morphology completely different from those biosynthesized using the actinomycete, *Rhodoccous* sp.

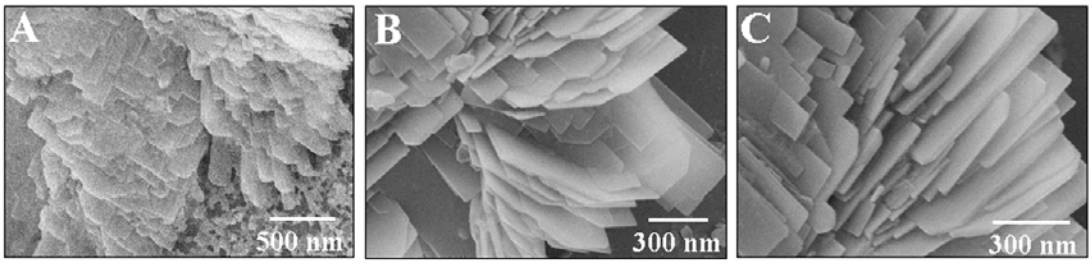

Fig.7.13: *(A–C) Representative SEM micrographs of extracellular $CaCO_3$ crystals after 3 days of reaction of aqueous Ca^{2+} ions with Thermomonospora sp.*

A large number of plate-shaped crystals of $CaCO_3$ are observed which are organized in a composite superstructure (Figs.7.13A & B). Viewed at higher magnification (Fig.7.13C), the $CaCO_3$ plates appear to be quite uniform in thickness with smooth surfaces that are stacked on top of each other (Fig.7.13C). The thickness of the $CaCO_3$ plates is calculated from the SEM images to be in the range 20-30 nm. Composite inorganic materials created by biological organisms from calcium salts and proteins are known to be architecturally complex and functionally diverse. These composites are known to provide superior mechanical stability in biological systems [28]. Such a brick and mortar structure for composite crystals is known to occur in biominerals such as aragonite in gastropod nacre [8,16c]. The bricks are flat crystals of $CaCO_3$ whereas the mortar is composed of biomacromolecules such as hydrophobic proteins and chitin [8,16c,29]. These hybrid structures are known to have high mechanical strength and unusual optical properties.

7.4.1.2.2 Intracellular synthesis

Figs.7.14A-C show representative SEM images of $CaCO_3$ crystals that were growing on the surface of the actinomycete biomass (residue) after 3 days of reaction of aqueous Ca^{2+} ions with *Thermomonospora* sp. It is observed that the $CaCO_3$ crystals grow radially outward from the biomass surface in the form of highly elongated flat plates. The nature of the $CaCO_3$ crystals growing on the biomass is rather similar to those synthesized extracellularly (Figs.7.13A-C)– the crystals are essentially in the form of flat plates that are then assembled into close-packed superstructures. One significant difference is observed and that concerns the in-plane dimensions of the $CaCO_3$ plates. While the in-plane dimensions of the crystals is quite large in the case of extracellular growth, the $CaCO_3$ crystals growing on the biomass are in the form of slender plates (Figs.7.14A-C) that are much larger in length (5-15 μm) than in width (200 – 700 nm). The thickness of the $CaCO_3$ plates was measured to be 80 – 100 nm. It is clear that such a constraint would not occur for growth in solution and this is mirrored by the larger crystals grown extracellularly (Figs.7.13A-C).

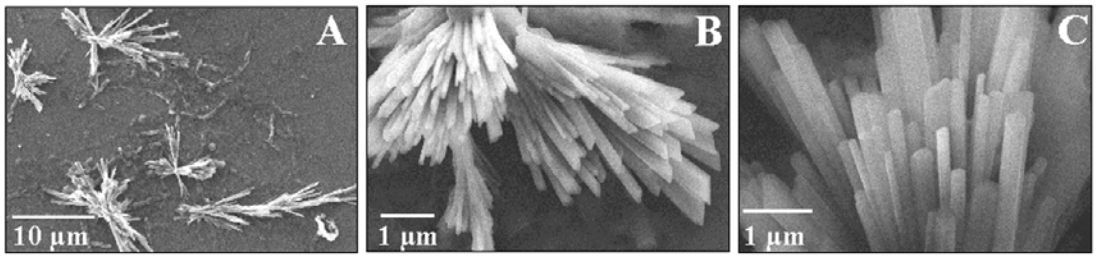

Fig.7.14: *A–C) SEM micrographs of intracellular $CaCO_3$ crystals after 3 days of reaction of aqueous Ca^{2+} ions with Thermomonospora sp.*

7.4.1.3 Calcination of biogenic $CaCO_3$ crystals grown using actinomycetes

Fig.7.15A shows an SEM image of biogenic vaterite crystals grown using *Rhodococcus* sp. after heating at 300 ^oC for 3 h. Upon calcination the originally compact crystals are transformed into highly porous and more faceted crystals. Increase in porosity indicates removal of proteins uniformly intercalated into the crystalline framework while the morphology change suggests possible variation in crystal structure. The calcination-induced morphology variation seen in the SEM images is due to transformation of vaterite into calcite. To remove occluded proteins from the $CaCO_3$

composites grown using *Thermomonospora* sp., the protein-$CaCO_3$ composite crystals were calcined at 300 ^oC for 3 h.

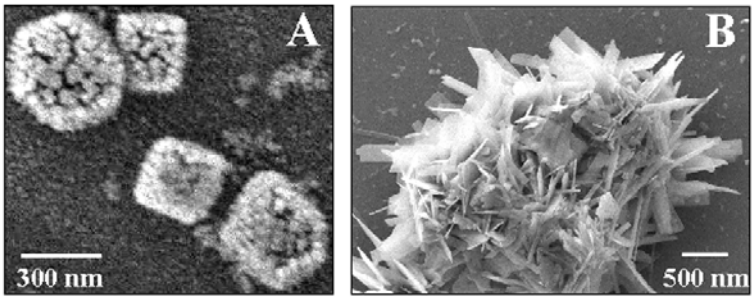

Fig.7.15: *A) SEM micrograph of $CaCO_3$ crystals grown using Rhodococcus sp. after calcination at 300 ^oC for 3 h. B) SEM micrograph of extracellular $CaCO_3$ crystals grown using Thermomonospora sp. after calcination at 300 ^oC for 3 h.*

Fig.7.15B shows SEM image of the extracellularly synthesized $CaCO_3$ crystals after calcination. It is observed that upon protein removal by calcination the originally compact $CaCO_3$ plates collapse with no semblance of the original organized structure (Fig.7.13A). However, on a gross level the $CaCO_3$ crystallites have maintained their overall flat plate-like morphology after calcination.

7.4.1.4 Synthesis of $CaCO_3$ crystals using protein extracts from actinomycetes

Control experiments were performed wherein *Rhodococcus* sp. and *Thermomonospora* sp. biomass were immersed in water for 3 days and the aqueous components separated by filtration. The aqueous fractions were taken separately with 10^{-3} M $CaCl_2$ and CO_2 was bubbled very slowly through these solutions. The $CaCO_3$ crystals formed in this manner were analyzed by SEM.

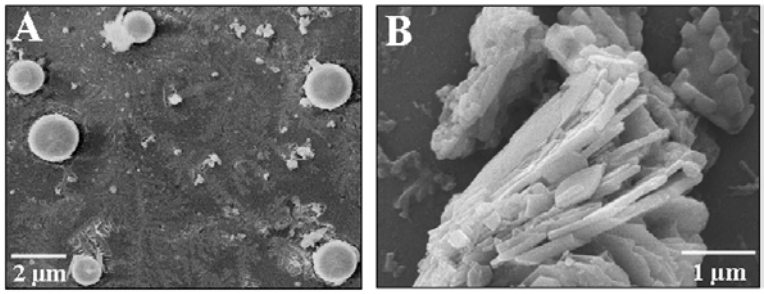

Fig.7.16: *Representative SEM micrographs of $CaCO_3$ crystals grown using extracts of Rhodococcus sp. (A) and Thermomonospora sp. (B).*

The SEM images show the formation of circular vaterite (Fig.7.16A) indicating that the proteins secreted by this microorganism are responsible for the morphology control and polymorph selectivity. The SEM image of $CaCO_3$ crystals grown using the protein extracts of *Thermomonospora* sp. is shown in Fig.7.16B. This picture clearly shows the formation of flat $CaCO_3$ plates assembled into a superstructure rather similar to that observed for the crystals grown extracellularly during direct exposure to *Thermomonospora* sp. (Fig.7.13C).

7.4.1.5 Detachment of proteins from biogenic $CaCO_3$ crystals

In order to locate the large amount of proteins which are either deposited on the surface of the crystals or intercalated within the crystals, the solution containing biogenic $CaCO_3$ crystals were treated with 4 % sodium hypochlorite (NaOCl) solution to remove any surface adsorbed proteins while preserving the proteins within the crystals. NaOCl treatment is known to be an efficient method to denature surface bound proteins due to its oxidizing capability. Fig.7.17A and B show SEM images recorded from solution-cast films of the biogenic $CaCO_3$ crystals synthesized using *Thermomonospora* sp. before (A) and after NaOCl treatment (B). NaOCl treatment of $CaCO_3$ crystals synthesized using *Thermomonospora* sp. leads to the collapse of originally organized $CaCO_3$ plate-composites (Fig.7.17A) into smaller individual plates (Fig.7.17B).

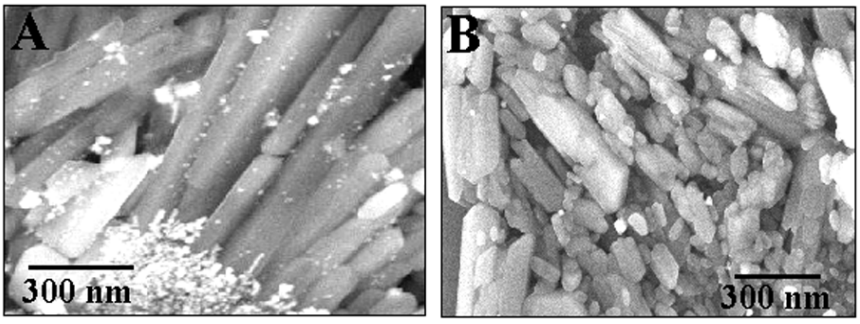

Fig.7.17: *(A and B) Representative SEM micrographs of $CaCO_3$ crystals grown after 3 days of reaction of aqueous Ca^{2+} ions with Thermomonospora sp. before (A) and after (B) treatment with NaOCl solution.*

This suggests that most of the proteins, which were present on the surface of the crystalline framework have been removed upon addition of NaOCl and contribute to the change in the crystal structure and morphology described above.

7.4.2 Energy dispersive analysis of X-rays measurements

To understand the chemical composition of the vaterite crystallites synthesized using the *Rhodococcus* sp. (Fig.7.12), spot-profile EDAX measurement of one of the circular vaterite crystals was carried out and is shown as curve 1, Fig.7.18A. In addition to the expected Ca, C and O signals, we observe the presence of N and S signals in the vaterite crystals. This indicates the presence of proteins within the circular vaterite crystallites. The spot-profile EDAX spectrum recorded from the biogenic vaterite crystals after calcination at 300 ^{o}C for 3 h is shown as curve 2 in Fig.7.18A. As expected, strong Ca, C and O signals are observed but this is accompanied by complete disappearance of N and S signals from the $CaCO_3$ crystals indicating removal of the occluded proteins.

The EDAX spectra recorded from *Thermomonospora* sp.-biogenic $CaCO_3$ composite crystals synthesized extracellularly (curve 1) and intracellularly (curve 2) are shown in 7.18B. In addition to Ca, C and O signals, strong N and S signals are observed in both the cases indicating the presence of proteins within these composite crystals. The spot-profile EDAX spectrum recorded from the calcined $CaCO_3$ crystals is shown as curve 3 in Fig.7.18B. The complete disappearance of N and S signals from the EDAX spectrum indicates removal of proteins from the $CaCO_3$ composites.

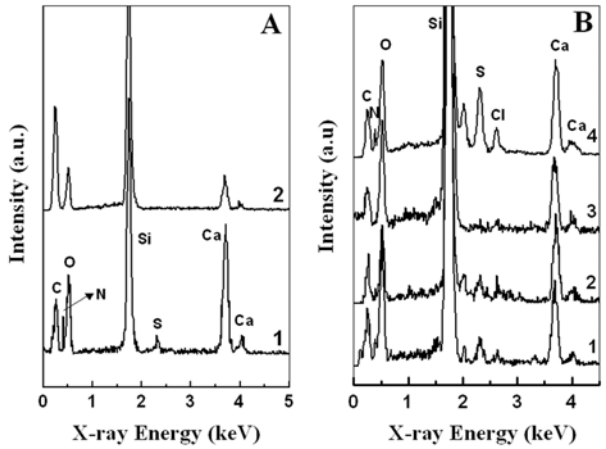

Fig.7.18: *A) Spot-profile EDAX spectra recorded from films of $CaCO_3$ crystals synthesized using Rhodococcus sp. before (curve 1) and after calcination at 300 ^{o}C for 3 h (curve 2). B) Spot-profile EDAX spectra recorded from the films of $CaCO_3$ crystals synthesized extracellularly (curve 1) and intracellularly (curve 2) using Thermomonospora sp. Curve 3 corresponds to the EDAX spectrum for extracellularly synthesized $CaCO_3$ sample after calcination at 300 ^{o}C for 3 h (curve 3). Curve 4 corresponds to the EDAX spectrum recorded from $CaCO_3$ crystals grown using extracts from Thermomonospora sp.*

The EDAX analysis of $CaCO_3$ crystals grown by using protein extracts from *Thermomonospora* sp. resulted Ca, C and O with expected stoichiometry along with strong N and S signals indicating the presence of proteins as well (curve 4, Fig.7.18B).

7.4.3 Fourier transform infrared spectroscopy studies

The FTIR spectrum recorded from the circular $CaCO_3$ crystals synthesized using *Rhodococcus* sp. is shown as curve 1 in Fig.7.19A. Strong absorption bands centered at 744 and 877 cm^{-1} are seen in the FTIR spectrum that is characteristic of the vaterite [8a]. The presence of proteins in the *Rhodococcus* sp.-biogenic vaterite crystals is also indicated in the FTIR spectrum (curve 1, inset of Fig.7.19A) where prominent amide I and II bands from the proteins are seen. The FTIR spectrum of the calcined *Rhodococcus* sp.-biogenic $CaCO_3$ crystals exhibited absorption bands at 712 and 874 cm^{-1} (curve 2, Fig.7.19A) accompanied by complete disappearance of N and S signals (curve 2 in the inset of Fig.7.19A) from the $CaCO_3$ crystals indicating removal of the occluded proteins.

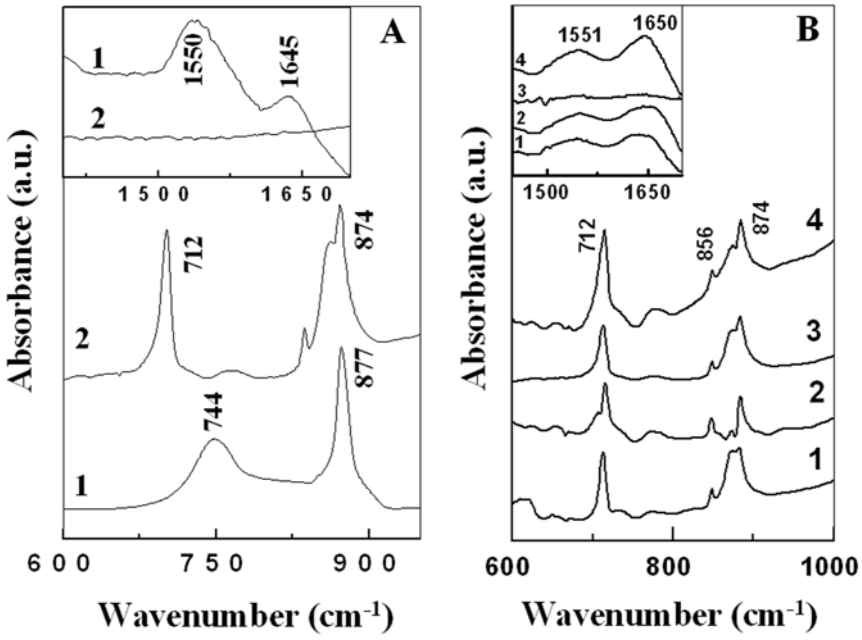

Fig.7.19: *(A and inset) FTIR spectra recorded in different spectral windows from $CaCO_3$ crystals synthesized by the reaction of aqueous Ca^{2+} ions for 3 days with Rhodococcus sp. before (curve 1) and after calcination at 300 ^oC for 3 h (curve 2). (B and inset) FTIR spectra recorded in different spectral windows from $CaCO_3$ crystals synthesized extracellularly (curve 1) and on the biomass (curve 2) by the reaction of aqueous Ca^{2+} ions for 3 days with Thermomonospora sp.; the extracellularly synthesized sample after calcination at 300 ^oC for 3 h (curve 3) and FTIR spectrum recorded from $CaCO_3$ crystals grown using extract of Thermomonospora sp. (curve 4).*

The FTIR spectrum recorded from the *Thermomonospora* sp.-biogenic $CaCO_3$ composite crystals (Figs.7.13A–C) is shown in Fig.7.19B, curve 1. Three absorption bands are observed at 712, 856 and 874 cm^{-1} that provide evidence of the formation of a mixed phase of calcite (712 and 874 cm^{-1}) and aragonite (856 cm^{-1}) [8a]. The presence of proteins in the *Thermomonospora* sp.-biogenic $CaCO_3$ crystals is also indicated in the FTIR spectrum from this sample (curve 1, inset of Fig.7.19A) where prominent amide I and II bands from the proteins are seen. The FTIR spectrum recorded from the $CaCO_3$ crystals on the actinomycete biomass (Figs.7.14A-C) is shown in Fig.7.19B, curve 2. Absorption bands are observed at 712, 856 and 874 cm^{-1} in this case as well indicating the formation of a mixed phase of calcite and aragonite. The aragonite absorption bands (856 cm^{-1}, curve 2 in Fig.7.19B) are enhanced relative to those observed with extracellularly synthesized $CaCO_3$ crystals (curve 1 in Fig.7.19B). The presence of proteins in the elongated $CaCO_3$ plates synthesized using *Thermomonospora* sp. was determined by FTIR measurements with the appearance of amide I and II signals (curve 1 and 2 in the inset of Fig.7.19B). FTIR measurements of the calcined $CaCO_3$ samples still show the presence of a mixed calcite and aragonite phase with an increase in the percentage of calcite in the calcined crystals (curve 3 in Fig.7.19B) with disappearance of amide bands (curve 3 in the inset of Fig.7.19B). The FTIR spectrum of $CaCO_3$ crystals synthesized using the extracts of *Thermomonospora* sp. is shown as curve 4 in Fig.7.19B. FTIR measurement revealed the formation of a mixed phase of aragonite and calcite. The presence of proteins in the $CaCO_3$ crystals in the control experiment was ascertained by the presence of amide I and II bands in FTIR spectrum (curve 4 in the inset of Fig.7.19B).

7.4.4 X-ray diffraction measurements

The XRD pattern of $CaCO_3$ crystals synthesized using *Rhodococcus* sp. is shown in Fig.7.20. The Bragg reflections identified by ‘V’ agree excellently with those reported for vaterite [23]. A small percentage of calcite is also observed in the XRD pattern (peaks labeled with ‘C’). The XRD pattern agrees very well with the morphology observed in the SEM images (Fig.7.12).

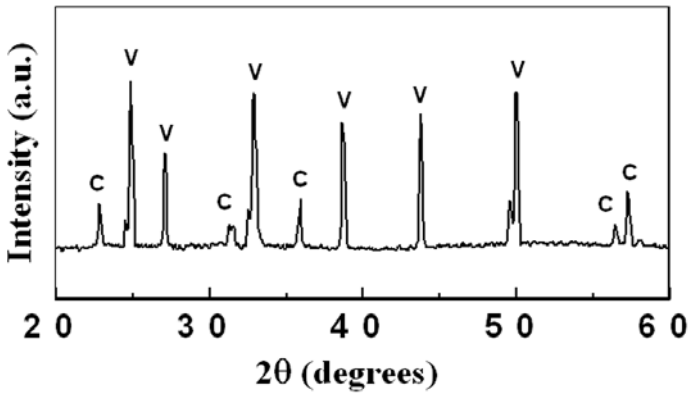

Fig.7.20: *XRD pattern recorded from solution-cast films of $CaCO_3$ crystals synthesized using Rhodococcus sp. In the XRD spectrum 'V' stands for vaterite and 'C' stands for calcite.*

The XRD pattern recorded from the $CaCO_3$ composites synthesized using *Thermomonospora* sp. is shown as curve 1 in Fig.7.21. It is observed that the $CaCO_3$ composite crystals consist of a mixed phase of the aragonite and calcite [22,30] (reflections identified by 'A' for aragonite and 'C' for calcite) which is in agreement with the FTIR results. The XRD pattern provides clear support to the FTIR result showing that the percentage contribution of aragonite to the mixed phase with calcite is enhanced in the case of $CaCO_3$ grown on the *Thermomonospora* sp. biomass (curve 2 in Fig.7.21).

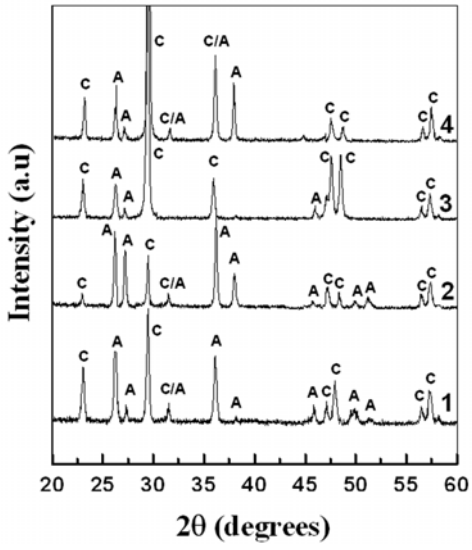

Fig.7.21: *XRD patterns recorded from solution-cast films of $CaCO_3$ crystals synthesized extracellularly (curve 1) and on the biomass (curve 2) using Thermomonospora sp. on glass substrates and the extracellularly synthesized crystals after calcination at 300 ^oC for 3 h (curve 3). Curve 4 corresponds to the XRD pattern recorded from a solution-cast film of $CaCO_3$ crystals grown using extract from Thermomonospora sp. In the XRD spectra, 'A' stands for aragonite and 'C' for calcite.*

The $CaCO_3$ composites synthesized using *Thermomonospora* sp. after calcination at 300 ^oC is shown as curve 3 in Fig.7.21. The calcined $CaCO_3$ samples still show the presence of a mixed calcite and aragonite phase with an increase in the percentage of calcite in the calcined crystals. Curve 4 in Fig.7.21 shows the XRD pattern recorded from $CaCO_3$ crystals grown using extract of *Thermomonospora* sp. indicating the formation of mixed phase of calcite and aragonite crystals.

7.4.5 Summary

We investigate that, the CO_2 and characteristic proteins released from actinomycetes such as *Rhodococcus* sp. and *Thermomonospora* sp. may be reacted with aqueous Ca^{2+} and Ba^{2+} ions to produce truly biogenic $CaCO_3$ crystals. While extracellular synthesis of the highly unstable vaterite polymorph of $CaCO_3$ in circular/spherical morphology was observed with *Rhodococcus* sp., both extra- and intra-cellular formation of $CaCO_3$ in the form of composites of flat plates and branched elongated flat plates were observed with *Thermomonospora* sp. indicating that specific proteins secreted by the respective actinomycetes play a crucial role in directing the $CaCO_3$ morphology and polymorph selection.

7.5 Biological synthesis of $BaCO_3$ crystals using a fungus and an actinomycete

To demonstrate the generality of using microorganisms for biosynthesis of minerals, we have also examined the synthesis of another important metal carbonate, $BaCO_3$ with a fungus, *Verticillium* sp. and an actinomycete, *Thermomonospora* sp. In a typical experiment, 20 g each of *Verticillium* sp. and *Thermomonospora* sp. biomass were suspended in 10^{-3} M aqueous $BaCl_2$ solution in conical flasks after thorough washing and centrifugation under sterile conditions as described in section 7.2. These flasks were then cotton plugged and incubated at 27 ^oC. Aliquots of the aqueous component were separated from the mycelia and subjected to SEM, EDAX and XRD analysis.

7.5.1 SEM and EDAX measurements

7.5.1.1 Synthesis of $BaCO_3$ crystals using the fungus, *Verticillium* sp.

Fig.7.22A & B correspond to representative SEM images recorded from solution-cast films of the aqueous $BaCl_2$ solution after exposure to *Verticillium* sp. for 2 days. The formation of spheroidal $BaCO_3$ particles along with needle like structures is observed in this experiment (Fig.7.22A). The formation of $BaCO_3$ in a needle-like morphology is known to commonly occur in solution whereas the formation of spheroidal $BaCO_3$ is possibly mediated by proteins secreted from the fungus. The higher magnification SEM image (Fig.7.22B) clearly shows the $BaCO_3$ spheroids in greater detail. The size of the $BaCO_3$ spheroids are calculated to be in the range of 200–500 nm. The surface of the spheres is highly irregular and they appear to be composed of smaller crystallites. The spot-profile EDAX measurement of one of the spherical $BaCO_3$ crystals yielded Ba, C and O signals close to the expected stoichiometric values along with the presence of N and S signals that is indicative of the presence of proteins within the spherical $BaCO_3$ superstructures. It is observed that the $BaCO_3$ spheroids consist of nanosized subunits in the form of needles. It is quite possible that the nanosized precursors (needles) are formed initially which act as nucleating agents for the subsequent growth/aggregation into spheroids and stabilized by protein.

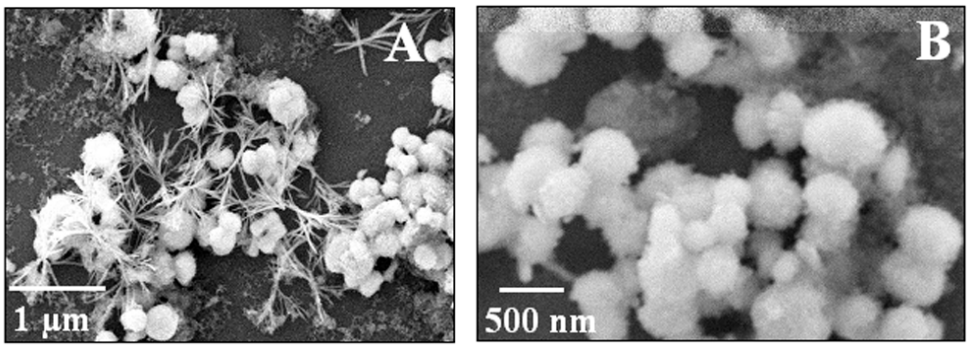

Fig.7.22: *(A and B) Representative SEM micrographs of $BaCO_3$ crystals after 2 days of reaction of aqueous Ba^{2+} ions with Verticillium sp.*

$BaCO_3$ in a spheroidal morphology has previously been observed in the presence of double hydrophilic block copolymers as a template [27]. Matijevic *et al.*, have observed

similar spheroidal morphology for $BaCO_3$ crystals synthesized by the enzyme-catalyzed decomposition of urea by urease at low temperatures [31].

7.5.1.2 Synthesis of $BaCO_3$ crystals using the actinomycete, *Thermomonospora* sp.

Fig.7.23A & B correspond to representative SEM images recorded from solution-cast films of the aqueous $BaCl_2$ solution after exposure to *Thermomonospora* sp. for 2 days.

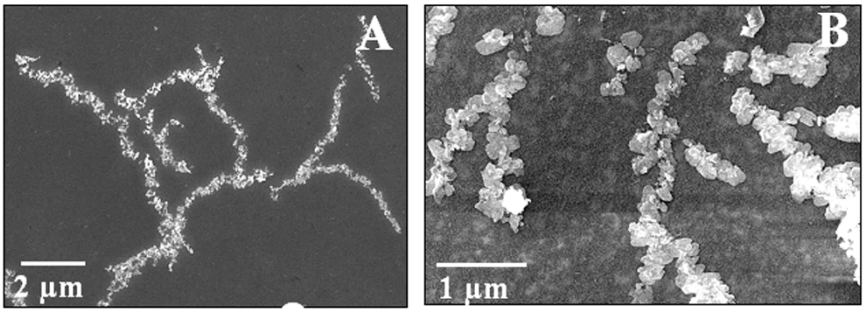

Fig.7.23: *(A and B) SEM micrographs of $BaCO_3$ crystals after 2 days of reaction of aqueous Ba^{2+} ions with Thermomonospora sp.*

The lower magnification SEM image (Fig.7.23A) shows the formation of small $BaCO_3$ crystallites assembled into a branched structure. At higher magnification (Fig.7.23B), the quasi-linear structures are seen to be composed of individual plate-like $BaCO_3$ crystallites. The size of these individual $BaCO_3$ plates is calculated to be in the range of 100–500 nm. EDAX measurements from the $BaCO_3$ assemblies indicated the presence of occluded proteins.

7.5.2 X-ray diffraction measurements

The XRD pattern recorded from the $BaCO_3$ spheroids synthesized using *Verticillium* sp. is shown as curve 1 in Fig.7.24. A number of Bragg reflections are identified and have been indexed with reference to the unit cell of the witherite structure of $BaCO_3$ (orthorhombic structure with cell constants a = 5.315 Å, b = 8.904 Å, c = 6.433 Å and space group *Pnma*) [32].

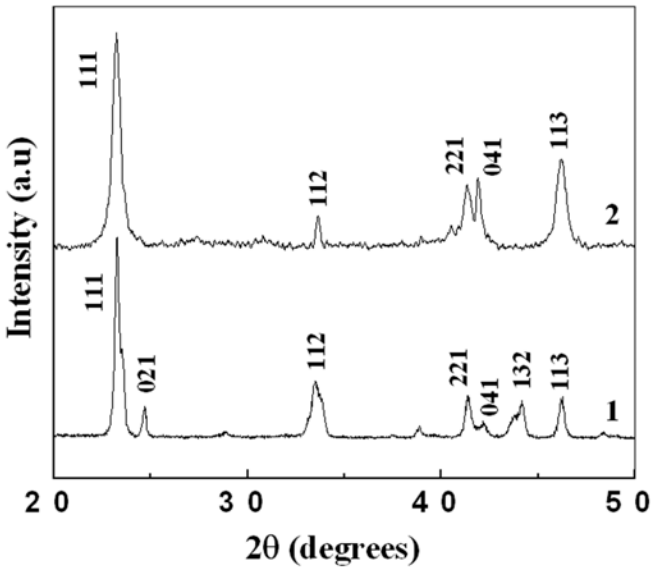

Fig.7.24: *XRD patterns recorded from solution-cast films of $BaCO_3$ crystals synthesized using Verticillium sp. (curve 1) and Thermomonospora sp. (curve 2). The Bragg reflections are identified in both the spectrum.*

The XRD pattern recorded from these $BaCO_3$ assemblies synthesized using *Thermomonospora* sp. is shown as curve 2 in Fig.7.24. The Bragg reflections in the XRD spectrum are identified and have been indexed with reference to the unit cell of the Witherite structure of $BaCO_3$ [32].

7.5.3 Summary

Reaction of Ba^{2+} ions with a fungus, *Verticillium* sp. and an actinomycete, *Thermomonospora* sp. in the extracellular synthesis of $BaCO_3$ crystals of spherical and flat, plate-like morphologies respectively has been described. As in the case of $CaCO_3$ synthesis using the fungus and the actinomycete where significant differences in the crystal morphology (and indeed, crystal structure) were observed, we observe large differences in the $BaCO_3$ crystal morphology as well underlining the extremely important role played by the proteins secreted by these two microorganisms in morphology control.

7.6 Biosynthesis of $SrCO_3$ crystals using a fungus, *Fusarium oxysporum*

In a typical experiment, 20 g of the fungus, *Fusarium oxysporum* biomass was suspended in 10^{-3} M aqueous $SrCl_2$ solution in a conical flask after thorough washing and then centrifuged under sterile conditions as described in section 7.2. The flask was then

cotton plugged and incubated at 27 ^{o}C. Aliquot of the aqueous component was separated from the mycelia and subjected to SEM, EDAX, FTIR, XRD, TGA, UV-Vis and Gel electrophoresis analysis.

7.6.1 Scanning electron microscopy studies

7.6.1.1 Synthesis of $SrCO_3$ crystals using *Fusarium oxysporum*

Fig.7.25 shows SEM images recorded from solution cast films of the aqueous $SrCl_2$ solution after exposure to *Fusarium oxysporum* for 3 days. Highly dense branching of $SrCO_3$ needles populating the substrate surface is observed in Fig.7.25A. The $SrCO_3$ needles appear to grow outward and radially from central primary crystals and are often greater than 12 μm in length.

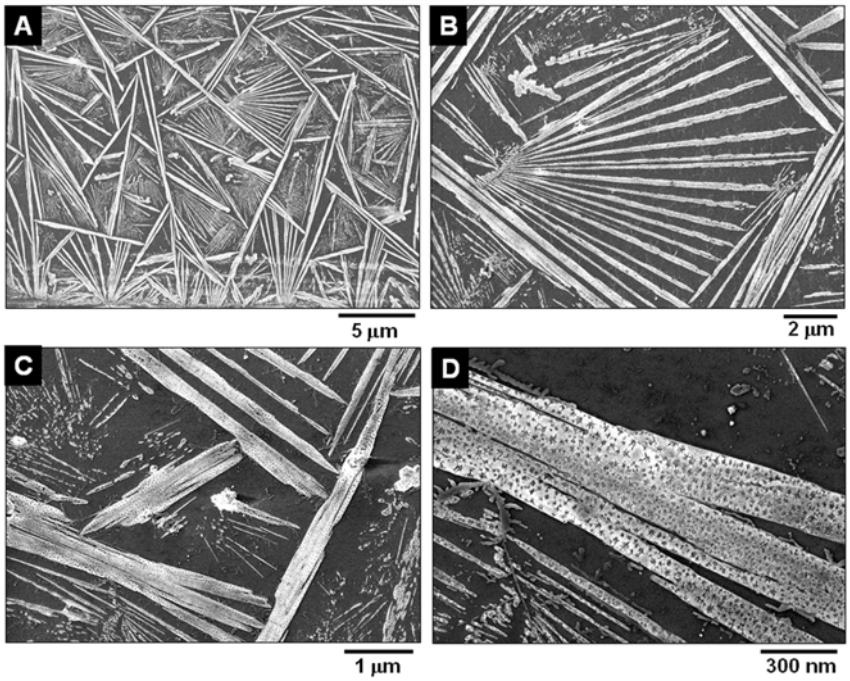

Fig.7.25: *(A-D) SEM micrographs at different magnifications showing $SrCO_3$ crystals formed after 3 days of reaction of aqueous Sr^{2+} ions with Fusarium oxysporum.*

Fig7.25B shows a higher magnification SEM image of $SrCO_3$ needles branching out from a central point. Fig.7.25C & D clearly show the structures of the individual $SrCO_3$ needles in greater detail. It can clearly be seen that the individual $SrCO_3$ needles are porous with the pores dotting the whole crystal surface quite uniformly. The pores were

estimated to range in size from 10 to 50 nm. The morphology of $SrCO_3$ needle-like crystals and their assembly into higher order superstructures observed in this study are very much different from the strontianite growth observed in previous studies [22,31,33].

7.6.1.2 Synthesis of $SrCO_3$ crystals using protein extracts of *Fusarium oxysporum*

The important role played by the proteins secreted by *Fusarium oxysporum* in directing the strontianite needle-like morphology may be highlighted by means of a simple control experiment. In this experiment, *Fusarium oxysporum* biomass was incubated in water for 3 days and the aqueous component was separated by filtration. The aqueous fraction containing proteins released by the fungus was taken with 10^{-3} M $SrCl_2$, and CO_2 was bubbled very slowly through this solution. The $SrCO_3$ crystals formed in this manner were analyzed by SEM (Fig.7.26).

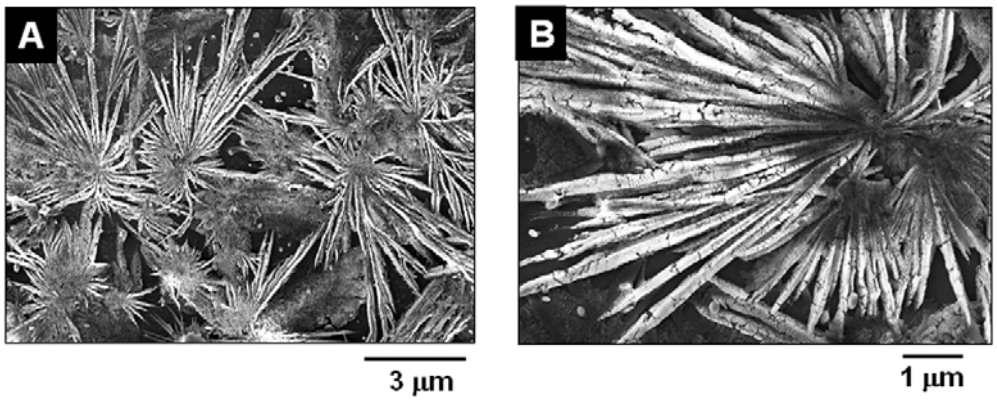

Fig.7.26: *(A & B) SEM micrographs at different magnifications showing $SrCO_3$ crystals grown using extracts from Fusarium oxysporum.*

The SEM images of these strontianite crystals indicate that they are remarkably similar in overall morphology (porous and quasi-linear) to those obtained by the direct reaction of Sr^{2+} ions with *Fusarium oxysporum* (Fig7.26A & B), indicating that the proteins secreted by *Fusarium oxysporum* into solution are responsible for the strontianite morphology control and, more importantly, that the growth of the crystals is not likely to occur within specific reaction sites in the fungal biomass. Clearly, the growth of strontianite occurs extracellularly.

7.6.1.3 Detachment of proteins from biogenic $SrCO_3$ crystals

To understand the nature of proteins that were either deposited on the surface of the crystals or intercalated within the crystals, the solution containing biogenic $SrCO_3$ crystals was treated with 4% sodium hypochlorite (NaOCl) solution to remove any surface-bound proteins while preserving the proteins intercalated within the crystals. NaOCl treatment is known to be an efficient method to denature any surface-bound proteins due to its oxidizing capability. Fig.7.27A shows a SEM image recorded from solution-cast films of the biogenic $SrCO_3$ crystals after NaOCl treatment. It is observed that the individual $SrCO_3$ needles become highly porous (Fig.7.27A) upon NaOCl treatment in comparison with the original $SrCO_3$ crystals (Fig.7.25).

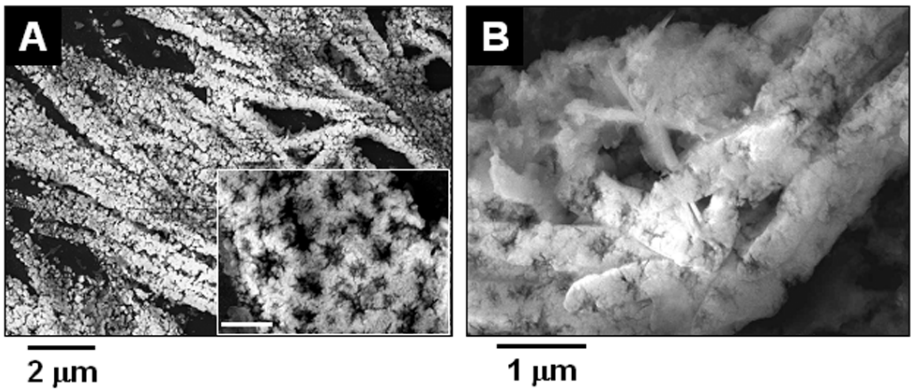

Fig.7.27: *(A & B) SEM micrographs of biogenic $SrCO_3$ crystals after treatment with NaOCl solution and the same sample after calcination at 300 °C, respectively. The inset in image A shows a magnified view of a particular region of $SrCO_3$ needles shown in the main figure. The scale bar in the inset of image A corresponds to 300 nm.*

The inset in the Fig.7.27A shows a higher magnification SEM image of the NaOCl-treated biogenic $SrCO_3$ crystals. It is observed that there is an increase in the average pore size uniformly over the crystal surface after NaOCl treatment, indicating removal of proteins from the original strontianite crystals. The pores in this case were estimated to be in excess of 100 nm as compared with the 10-50 nm pore size observed in the case of untreated biogenic $SrCO_3$ crystals (Fig.7.25D). This suggests that most of the proteins, which were present on the surface of the crystalline framework, have been removed upon addition of NaOCl and thus the porosity increases on the crystal surface. The NaOCl-treated biogenic $SrCO_3$ crystals were then calcined at 300 °C. Upon calcination, the originally porous strontianite crystals collapsed (Fig.7.27B). It is clear

that small amount of proteins intercalated within the $SrCO_3$ crystalline framework remains even after NaOCl treatment of the biogenic $SrCO_3$ crystals This indicates that the intercalated proteins stabilize the crystal structure to a significant extent and only upon their removal is complete removal in the crystal morphology is observed.

7.6.2 EDAX and FTIR measurements

To understand the chemical composition of the needlelike $SrCO_3$ assemblies obtained from *Fusarium oxysporum*, spot-profile EDAX spectrum recorded from one of the $SrCO_3$ needles and is shown as curve 1 in Fig.7.28A. In addition to the expected Sr, C, and O signals, strong N and S signals are also observed. The presence of N and S signals is clearly indicative of the presence of proteins in the $SrCO_3$ needles. These signals are believed to arise from proteins either on the surface of the $SrCO_3$ crystals or occluded into the crystals.

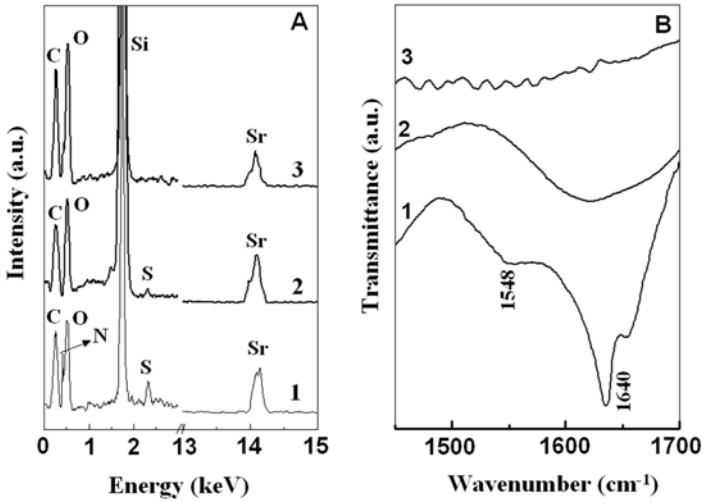

Fig.7.28: *(A) Spot-profile EDAX spectra recorded from films of $SrCO_3$ crystals synthesized using Fusarium oxysporum (curve 1), the biogenic $SrCO_3$ crystals after NaOCl treatment (curve 2) and the NaOCl-treated biogenic $SrCO_3$ crystals after calcination at 300 °C (curve 3). (B) FTIR spectra recorded from biogenic $SrCO_3$ crystals obtained by the reaction of aqueous Sr^{2+} ions with Fusarium oxysporum (curve 1), the biogenic $SrCO_3$ crystals after NaOCl treatment (curve 2) and the NaOCl-treated biogenic $SrCO_3$ crystals after calcination at 300 °C (curve 3). The amide I and II bands are identified in the figure.*

The EDAX spectrum recorded from the NaOCl-treated biogenic $SrCO_3$ crystals is shown as curve 2 in Fig.7.28A. In addition to the expected Sr, C and O signals, the reduction of S and almost complete disappearance of N signals observed in the spectrum indicates removal of a large amount of proteins from the biogenic $SrCO_3$ crystals. The spot-profile

EDAX spectrum recorded from the NaOCl-treated biogenic $SrCO_3$ crystals after calcinations at 300 °C is shown as curve 3 in Fig.7.28A. As expected, strong Sr, C, and O signals are observed but this is accompanied by complete disappearance of N and S signals from the strontianite needles indicating complete removal of the occluded proteins.

The FTIR measurement of biogenic $SrCO_3$ needles clearly show the presence of amide I and II bands at 1640 and 1548 cm^{-1}, respectively indicating the presence of proteins (curve 1 in Fig.7.28B). After NaOCl treatment, the FTIR spectrum shows a broad band around 1620 cm^{-1} with no distinct amide signatures (curve 2 in Fig.7.28B). The complete disappearance of amide bands after calcination is also observed in the FTIR spectrum (curve 3 in Fig.7.28B), clearly shows the complete removal of proteins.

7.6.3 Thermogravimetric analysis (TGA) measurements

To understand better the nature of protein occlusion into the $SrCO_3$ crystals, TGA measurements of the purified biogenic $SrCO_3$ powder were done. Curve 1 in Fig.7.29 shows the TGA curve obtained from purified powder of biogenic $SrCO_3$ crystals. It is observed that there are two prominent weight losses of ca. 40 and 30% at 100 and 230 °C, respectively. The first weight loss is clearly due to release of water entrapped in protein-$SrCO_3$ biocomposite crystals, whereas the higher temperature weight loss is attributed to decomposition/desorption of proteins bound to the strontianite crystals.

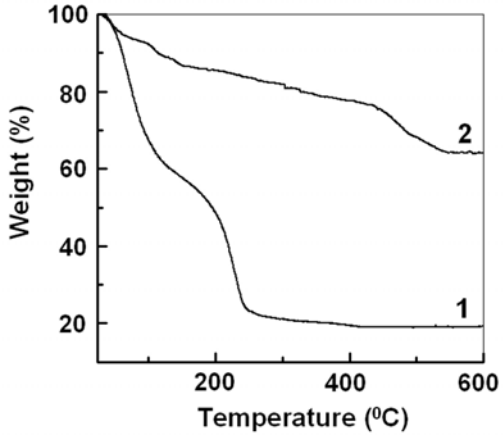

Fig.7.29: *TGA data obtained from purified biogenic $SrCO_3$ crystal powder (curve 1) and the biogenic $SrCO_3$ crystals after treatment with NaOCl.*

The TGA curve shows an overall loss in weight of 35% (curve 2 in Fig.7.29) after NaOCl treatment of biogenic $SrCO_3$ crystals, which is much smaller than the total weight loss (74%) recorded for the untreated biogenic $SrCO_3$ crystals (curve 1 in Fig.7.29). This confirms that after treatment with NaOCl, a large percentage of surface-bound proteins were removed from the biogenic $SrCO_3$ crystals.

7.6.4 X-ray diffraction Studies

XRD analysis of the biogenic $SrCO_3$ crystals formed by the reaction of aqueous Sr^{2+} ions with *Fusarium oxysporum* for 3 days was performed, and the diffraction pattern obtained is shown as curve 1 in Fig.7.30. A number of Bragg reflections are identified and have been indexed with reference to the unit cell of the strontianite structure (a = 5.107 Å, b = 8.414 Å, c = 6.029 Å; space group *Pmcn*) [34]. XRD analysis thus confirms the formation of the crystalline strontianite by the reaction of Sr^{2+} ions with *Fusarium oxysporum*.

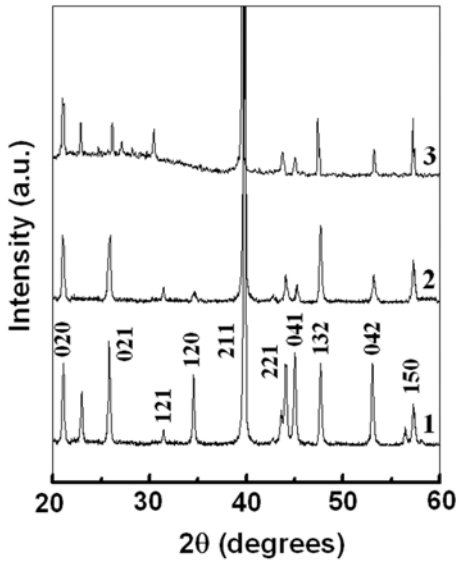

Fig.7.30: *XRD patterns recorded from solution-cast films on glass substrates of $SrCO_3$ crystals synthesized using Fusarium oxysporum before (curve 1) and after calcination at 300 °C (curve 2) and the XRD pattern recorded from the biogenic $SrCO_3$ crystals after NaOCl treatment (curve 3).*

The XRD spectrum recorded from the biogenic strontianite crystals after calcination at 300 °C (curve 2) is shown in Fig.7.30. Loss of occluded proteins (curve 2) from the biogenic crystals does not lead to loss in the strontianite structure of the crystals. The

SEM image (Fig.7.27) along with the XRD result (curve 3 in Fig.7.30) of the $SrCO_3$ crystals after protein removal clearly indicate the reduction in crystalline properties of the strontianite needles. Even though there is a significant amount of trapped water in the strontianite needles (to the extent of 40 wt %), removal of water does not destabilize the linear superstructure (Figure 4A), thus underlining the very important role played by the proteins in stabilizing the superstructure. It is clear that removal of proteins from the strontianite crystals affects the crystallinity, morphology, and growth pattern of the crystals.

The XRD pattern recorded from the NaOCl-treated biogenic $SrCO_3$ crystals is shown as curve 3 in Fig.7.30. The XRD spectrum shows no discernible change (curve 3) in comparison with the XRD spectrum recorded from the biogenic strontianite crystals after calcination at 300 °C (curve 2). It is thus clear that consequent to protein removal, there is no loss in the strontianite structure (either by calcination or by NaOCl treatment) except for a collapse in the internal structure as observed in SEM. It is also observed that upon protein removal, many of the intense peaks are reduced with some unaffected Bragg peaks. The presence of some unaffected Bragg peaks even after protein removal may be because of the growth of a few $SrCO_3$ crystallites possibly in solution without mediation of any proteins, or it is also possible that preferred orientation is likely the most common cause of intensity variations in XRD powder experiments.

7.6.5 UV-Visible spectroscopy measurements

The removal of surface-bound proteins was also confirmed by UV-vis spectroscopy (Fig.7.31) where a comparative study of the as-prepared $SrCO_3$ crystals and those after treatment with NaOCl at different time intervals was performed. Curve 1 in Fig.7.31 shows the UV-vis spectrum of the as-prepared $SrCO_3$ crystals synthesized using *Fusarium oxysporum*. An absorption peak is observed at ca. 260 nm, indicating the presence of proteins bound to the $SrCO_3$ crystals. After NaOCl treatment for 1 h, it is observed that the absorption peak shifted to 288 nm, indicating the detachment of surface-bound proteins from the $SrCO_3$ crystals and their dissolution (curve 2). After 3 h of reaction, the intensity of the peak at 288 nm has reduced considerably (curve 3), and after 24 h, the protein absorption band has almost completely disappeared (curve 4).

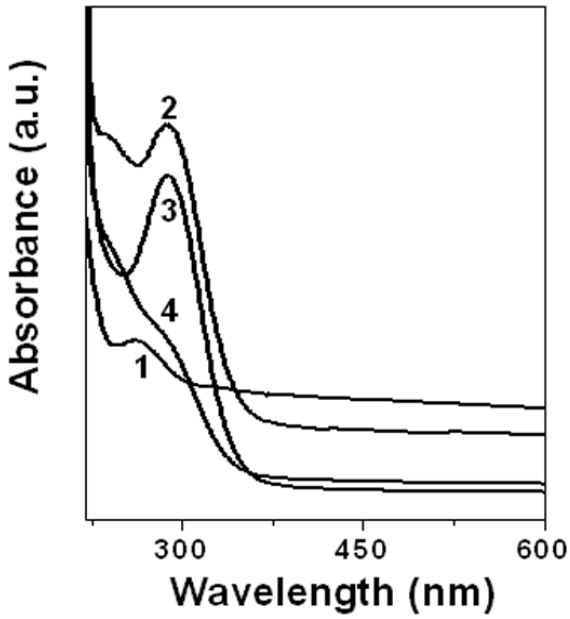

Fig.7.31: *Time-dependent UV-vis spectra of the $SrCO_3$ solution after treatment with NaOCl. Curve 1: $SrCO_3$ synthesized using Fusarium oxysporum without NaOCl treatment. Curves 2, 3, and 4: NaOCl-treated $SrCO_3$ crystals after 1, 3, and 24 h of reaction, respectively.*

The UV-vis spectroscopy results thus indicate that the denaturation and oxidation of the strontianite-bound proteins occur over a period of 1 day during NaOCl treatment.

7.6.6 Protein identification

To identify the proteins bound to the $SrCO_3$ crystals that are possibly responsible for the strontianite shape control, the biogenic $SrCO_3$ crystals were washed thoroughly and were treated with dilute acetic acid solution. This mild acid treatment resulted in the dissolution of $SrCO_3$ crystals, and the crystal-bound proteins detached from the $SrCO_3$ crystals in solution were separated by centrifugation and analyzed by 10% SDS-PAGE (sodium dodecyl sulfate polyacrylamide gel electrophoresis) carried out at pH 8.2 according to standard procedures [35]. Gel electrophoresis measurements of the proteins detached by acid treatment (Fig.7.32) indicate two prominent protein bands having molecular weights of ~33 and 50 kDa. We believe that either of these two proteins most likely contributed in modulating the crystal morphology of $SrCO_3$, while contribution of other minor proteins in the crystal growth cannot be ruled out.

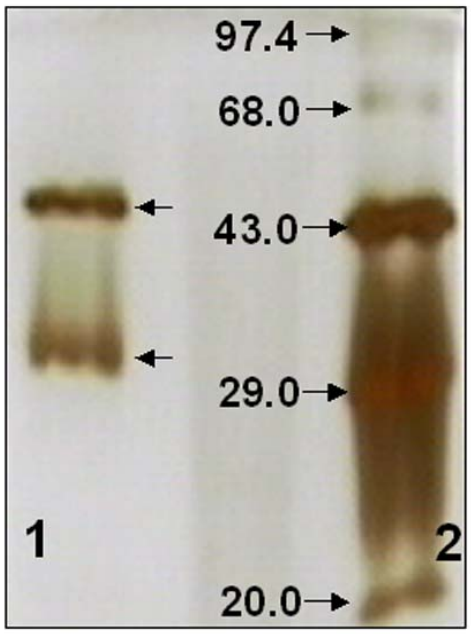

Fig.7.32: *SDS-PAGE data showing the proteins that were originally bound to the surface of the $SrCO_3$ crystals after dissolution of the crystals by mild acidic treatment. The arrows highlighting the bands in lane 1 indicate the proteins bound to $SrCO_3$ crystals and their approximate molecular weights. Lane 2 shows standard protein molecular weight markers with the corresponding molecular weights in kilo Daltons indicated by arrows.*

7.6.7 Summary

The biological synthesis of $SrCO_3$ crystals of needlelike morphology by challenging the fungus *Fusarium oxysporum* with aqueous Sr^{2+} ions has been described. The source of carbonate ions that react with aqueous Sr^{2+} ions is the fungus itself. The secretion of specific proteins during growth of the fungus, *Fusarium oxysporum* is responsible for modulating the morphology of strontianite crystals and directing their hierarchical assembly into higher order superstructures. The action of specific proteins secreted by this microorganism in directing the strontianite morphology has been discussed.

7.7 Discussion

The difference in morphology of the $CaCO_3$, $BaCO_3$ and $SrCO_3$ crystals synthesized using fungi and actinomycetes may be attributed to the different proteins secreted by these microorganisms. For example, it is possible that specific proteins secreted by the fungus, *Trichothecium* sp. kinetically control the growth phenomenon of plate like $CaCO_3$ crystals. The proteins present in the growing $CaCO_3$ crystallites affect

the diffusion of both Ca^{2+} and CO_3^{2-} ions to the crystallite surface and thus kinetically control their growth thus leading to the formation of hopper crystals. A possible explanation for the formation of porous biogenic strontianite needles could be the following. Further to addition of Sr^{2+} ions to the fungal biomass, the reaction of the Sr^{2+} ions with carbonate ions in the presence of secreted proteins produced by *Fusarium oxysporum* leads to the growth of strontianite crystals yielding a porous, templated strontianite needle. The pores on the crystal surface are most likely due to the loss of trapped water (associated with the presence of proteins) in the strontianite needles (as evidenced from TGA results) during drying/exposure to a vacuum during SEM analysis. The ca. 40% weight loss due to water entrapped in the strontianite framework would explain the large density of pores in the crystals. The formation of radial strontianite structures could be due to isotropic growth in solution modulated by proteins secreted by the fungus; free-growing crystals have been observed to commonly form sheaves or radially assembled structures. A more or less uniform supply of ions to the growing surface leads to preferred growth of crystals.

The above experiments clearly indicate that the proteins secreted by respective fungus and actinomycete is significantly different and capable of not only crystal morphology control but also polymorph selectivity. We believe the growth of these crystals proceeds in the following manner. In the first step, the $Ca^{2+}/Ba^{2+}/Sr^{2+}$ ions (in the form of counterions) complex with the proteins secreted by the microorganisms leading to the formation of stable aggregates in solution. The entrapped $Ca^{2+}/Ba^{2+}/Sr^{2+}$ ions then react with CO_2 in-situ thereby forming $CaCO_3/BaCO_3/SrCO_3$ crystals in the mosaic structures. This would explain the large concentration of proteins occluded in the crystals and provide a basis for understanding the morphology and polymorph control. On a more fundamental level, a clearer understanding of the mode of binding of specific proteins secreted by the microorganisms with different exposed faces of the crystals would be important. The control experiments involving proteins secreted by the fungus and actinomycete, clearly establish the important role played by the proteins in dictating morphology and polymorph control in the mineral synthesis. The fact that these microorganisms also act as a source of CO_2 makes this a truly biogenic method for the synthesis of minerals and is thus not merely biomimetic.

7.8 Conclusions

The exciting possibility of total biological synthesis of metal carbonate crystals of variable morphology and in polymorph selectivity during the mineralization process as a result of proteins secreted by organisms such as fungi and actinomycetes which are not normally (if ever) exposed to such metal ions is an exciting outcome of this work and underlines the untapped potential of biological methods in expanding the scope of crystal engineering. We term this process 'total biosynthesis' since the source of carbonate ions is the microorganisms themselves and is thus at variance with other biomimetic methods wherein an external source of CO_2 was used to grow the minerals. Microorganisms such as a fungi and actinomycetes should be capable of crystal growth and engineering at a high level of sophistication opens up the exciting possibility that other microorganisms when challenged with metal ions may lead to similar if not more exciting results. From the point of view of scale-up of production of minerals, the use of a renewable source of CO_2 and crystal-modifying proteins from microorganisms is obvious.

7.9 References

[1] Lowenstam, H. A. *Science* **1981**, *211*, 1126.

[2] Sarikaya, M. *Proc. Natl. Acad. Sci. U.S.A.* **1999**, *96*, 14183.

[3] Aizenberg, J.; Tkachenko, A.; Weiner, S.; Addadi, L.; Hendler, G. *Nature* **2001**, *412*, 819.

[4] Boskey, A. L. *Calcif Tissue Int.* **2003**, *72*, 533.

[5] Soten, I.; Ozin, G. A. *Curr. Opin. Colloid. Interface Sci.* **1999**, *4*, 325.

[6] (a) Berman, A.; Addadi, L.; Weiner, S. *Nature* **1988**, *331*, 546. (b) Heuer, A. H.; Fink, D. J.; Laraia, V. J.; Arias, J. L.; Calvert, P. D.; Kendall, K.; Messing, G. L.; Blackwell, J.; Rieke, P. C.; Thompson, D. H.; Wheeler, A. P.; Veis, A.; Caplan, A. I. *Science* **1992**, *255*, 1098.

[7] Albeck, S.; Aizenberg, J.; Addadi, L.; Weiner, S. *J. Am. Chem. Soc.* **1993**, *115*, 11691.

[8] (a) Falini, G.; Albeck, S.; Weiner, S.; Addadi, L. *Science* **1996**, *271*, 67. (b) Wheeler, A. P.; George, J. W.; Evans, C. A. *Science* **1981**, *212*, 1397. (c) Weiner, S.; Hood, L. *Science* **1975**, *190*, 987. (d) Miyamoto, H.; Miyashita, T.; Okushima, M.; Nakano,

S.; Morita, T.; Matshushiro, A. *Proc. Natl. Acad. Sci. USA* **1996**, *93*, 9657. (e) Gao, H.; Ji, B.; Jager, I. L.; Arzt, E.; fratzl, P. *Proc. Natl. Acad. Sci. USA* **2003**, *100*, 5597.

[9] (a) Simkiss, K.; Wilbur, K. M. *Biomineralization* (Academic Press, New York) **1989**. (b) Sarikaya, M. *Proc. Natl. Acad. Sci. USA* **1999**, *96*, 14183.

[10] (a) Loveley, D. R.; Stolz, J. F.; Nord, G. L.; Phillips, E. J. P. *Nature* **1987**, *330*, 252. (b) Spring, H.; Schleifer, K. H. *Syst. Appl. Microbiol.* **1995**, *18*, 147. (c) Dickson, D. P. E. *J. Magn. Mater.* **1999**, *203*, 46.

[11] (a) Mann, S. *Nature* **1993**, *365*, 499. (b) Oliver, S.; Kupermann, A.; Coombs, N.; Lough, A.; Ozin, G. A. *Nature* **1995**, *378*, 47. (c) Kroger, N.; Deutzmann, R.; Sumper, M. *Science* **1999**, *286*, 1129. (d) Wetherbee, R. *Science* **2002**, *298*, 547.

[12] (a) Pum, D.; Sleytr, U. B. *Trends Biotechnol.* **1999**, *17*, 8. (b) Sleytr, U. B.; Messner, P.; Pum, D.; Sara, M. *Angew. Chem., Int. Ed. Engl.* **1999**, *38*, 1034.

[13] (a) Meldrum, F. C. Seshadri, R. *Chem. Commun.* **2000**, 29. (b) Peled-Kamar, M.; Hamilton, P.; Wilt, F. H. *Exp. Cell Res.* **2002**, *272*, 56. (c) Donnay, G.; Pawson, D. L.; *Science* **1969**, *166*, 1147.

[14] Tancred, D. C.; McCormack, B. A. O.; Carr, A. J. *Biomaterials* **1998**, *19*, 2303.

[15] (a) Hubbard, M. J.; Bradley, M. P.; Kardos, T. B.; Forrester, *Calcif. Tissue. Int.* **1981**, *33*, 545. (b) Hubbard, M. J. *Connect. Tissue res.* **1998**, *38*, 17.

[16] (a) Lowenstam, H. A.; Weiner, S. *On Biomineralization* (Oxford University Press), New York, **1989**. (b) Berman, A.; Hanson, J.; Leiserowitz, L.; Koetzle, T.F.; Weiner, S.; Addadi, L. *Science* **1993**, *259*, 776. (c) Zaremba, C.M.; Morse, D.E.; Mann, S.; Hansma, P.K.; Stucky, G.D. *Chem.Mater.* **1998**, *10*, 3813.

[17] Long, J. R.; Dindot, J. L.; Zebroski, H.; Kihne, S.; Clark, R. H.; Campell, A. A.; Stayton, P. S.; Drobny, G. P. *Proc. Natl. Acad. Sci. USA* **1998**, *95*, 12083.

[18] (a) Mukherjee, P.; Ahmad, A.; Mandal, D.; Senapati, S.; Sainkar, S. R.; Khan, M. I.; Ramani, R.; Pasricha, R.; Ajaykumar, P. V.; Alam, M.; Sastry, M.; Kumar, R. *Angew. Chem. Int. Ed.* **2001**, *40*, 3585. (b) Ahmad, A.; Mukherjee, P.; Mandal, D.; Senapati, S.; Khan, M. I.; Kumar, R.; Sastry, M. *J. Am. Chem. Soc.* **2002**, *124*, 12108. (c) Mukherjee, P.; Senapati, S.; Mandal, D.; Ahmad, A.; Khan, M. I.; Kumar, R.; Sastry, M. *Chem Bio Chem* **2002**, *3*, 461. (d) Ahmad, A.; Senapati, S.; Khan, M. I.; Kumar, R.; Sastry, M. *Langmuir* **2003**, *19*, 3550. (e) Ahmad, A.; Senapati, S.;

Khan, M. I.; Kumar, R.; Ramani, R.; Srinivas, V.; Sastry, M. *Nanotechnology* **2003**, *14*, 824. (f) Mukherjee, P.; Ahmad, A.; Mandal, D.; Senapati, S.; Sainkar, S. R.; Khan, M. I.; Parischa, R.; Ajaykumar, P. V.; Alam, M.; Kumar, R.; Sastry, M. *Nano. Lett.* **2001**, *1*, 515. (g) Sastry, M.; Ahmad, A.; Khan, M. I.; Kumar, R. in *Nanobiotechnology* (Eds.: Niemeyer, C. M. and Mirkin, C. A.), Wiley-VCH, **2004** p.126.

[19] C. Couriol, A. Amrane, Y. Progent, *J. Bioscience Bioeng.* **2001**, *91*, 570.

[20] (a) McGrath, K. M.; *Adv. Mater.* **2001**, *13*, 989. (b) Dickinson, S. R.; McGrath, K. M. *J. Mat. Chem.* **2003**, *13*, 928.

[21] Sondi, I.; Matijevic, E. *J. Colloid Interface Sci.* **2001**, *238*, 208.

[22] Kuther, J.; Nelles, G.; Seshadri, R.; Schaub, M.; Butt, H.-J.; Tremel, W. *Chem. Eur. J.* **1998**, *4*, 1834.

[23] Nassrallah-Aboukais, N.; Boughriet, A.; Laureyns, J.; Aboukais, A.; Fischer, J. C.; Langelin, H. R.; Wartel, M. *Chem. Mater.* **1998**, *10*, 238.

[24] Okami, Y.; Beppu, T.; Ogawara, H. *Biology of Actinomycetes*, Japan Scientific Societies Press: Tokyo, **1988**; p 508.

[25] Sasaki, T.; Yoshida, J.; Itoh, M.; Gomi, S.; Shomura, T.; Sezaki, M. *J. Antibiot.* **1988**, *41*, 835.

[26] (a) Brecevic, L.; Nothing-Laslo, V.; Kralji, D.; Popovic, S. *J. Chem. Soc., Faraday Trans.* **1996**, *92*, 1017. (b) Lopezmacipe, A.; Gomezmorales, J.; Rodriguezclemente, R. *J. Cryst. Growth* **1996**, *166*, 1015. (c) Didymus, J. M.; Oliver, P.; Mann, S.; Devries, A. L.; Hauschka, P. V.; Westbroek, P. *J. Chem. Soc., Faraday Trans*. **1993**, *89*, 2891. (d) Colfen, H.; Antonietti, M. *Langmuir* **1998**, *14*, 582. (e) Colfen, H.; Qi, L. *Chem. Eur. J.* **2001**, *7*, 106. (f) Naka, K.; Tanaka, Y.; Chujo, Y. *Langmuir* **2002**, *18*, 3655.

[27] Yu, S. H. ; Colfen, H. ; Antonietti, M. *J. Phys. Chem. B* **2003**, *107*, 7396.

[28] Addadi. L.; Weiner, S. *Nature* **1997**, *389*, 912.

[29] Kato, T.; Sugawara, A.; Hosoda, N. *Adv. Mater.* **2002**, *14*, 869.

[30] The XRD patterns were indexed with reference to the unit cell of the aragonite structure from *ASTM* chart card no. 5-0453.

[31] Sondi, I. ; Matijevic, E. *Chem. Mater.* **2003**, *15*, 1322.

[32] The XRD patterns were indexed with reference to the unit cell of the witherite structure of $BaCO_3$ from *ASTM* chart (a = 5.315 Å, b = 8.904 Å, c = 6.433 Å; space group *Pnma*, ASTM chart card no. 5-0378).

[33] (a) Kuther, J.; Bartz, M.; Seshadri, R.; Vaughan, G. B. M.; Tremel, W. *J. Mater. Chem.* **2001**, *11*, 503. (b) Kuther, J.; Seshadri, R.; Tremel, W. *Angew. Chem., Int. Ed.* **1998**, *37*, 3044.

[34] The XRD patterns were indexed with reference to the unit cell of the strontianite structure from the ASTM chart (*a* = 5.107 Å, *b* = 8.414 Å, c = 6.029 Å; space group *Pmcn*, ASTM chart card no. 5-0418).

[35] Laemmli, U. K. *Nature* **1970**, *227*, 680.

CHAPTER VIII

Conclusions

This chapter details the salient feature the work presented in the thesis and emphasized on possible future scope in this field.

8.1 Summary of the work

A potential promising avenue of research in materials science is to reveal some of the strategies used by natural organisms to produce designed composite materials out of highly anisotropic building blocks [1]. Organisms appear to have had to solve this and many other problems relating to their structural and functional materials during million years of on-the-job testing [2]. Some of the strategies used and solutions derived from nature may well have practical applications in the world of synthetic composite materials. So, the strive towards a common theme of designing strategies of many biological materials, and in particular those that are required to fulfill more general functions [3] is a need of current research.

Material scientists working at the interface of organic and inorganic chemistry have developed several techniques in recent years that enable the synthesis of inorganic materials with controlled morphologies [4]. In this thesis, we have described the use of new chemical and biological protocols for the controlled synthesis of (bio)minerals. Recognizing the importance of organic matrix mediated mineralization process in nature; we have attempted to synthesize various minerals within an anisotropic constrained environment by using thin films of thermally evaporated lipid bilayers stacks as templates. The growth of minerals within the lipid hosts were successfully achieved by process of sequential electrostatic entrapments of appropriate ions resulted in the morphology and polymorph control. The formation of the minerals is believed to occur via hydrophobic association of the respective crystallites that are covered by a monolayer of the surfactant used. Furthermore, a dynamic charged liquid-liquid interface for mineral growth was established with a motivation of assembling crystallites into higher ordered superstructures. This was successfully accomplished by using a Hele-Shaw set up. A comparison of mineral growth at dynamic and static charged liquid-liquid interface clearly revealed the importance of nature of interface on mineral growth. By aiming a large-scale synthesis method for inorganic materials, we have used an underexploited dynamic biomimetic template i.e. liquid lamellae in aqueous foam. The large interfacial area in aqueous foam populated with stabilizing surfactant was shown to be a versatile template for mineral growth in the foam lamellae. In order to achieve a potential biocompatible surface for inducing growth of bioceramics for possible biomedical application such as bone implants, we have used gold nanoparticles in a polymeric

background for the growth of inorganic crystals. Prior to mineralization, the gold nanoparticle membrane was derivatized with suitable functional groups capable of inducing mineral growth. The nature of mineral crystals formed was found to be a strong function of the nanogold surface modifier. Finally, we have shown a complete biological process for the synthesis of minerals by challenging microorganisms such as fungi and actinomycetes. The source of carbonate ions is the microorganisms themselves. We took advantage of this and showed that CO_2 and characteristic proteins released from the microorganism during their growth can be reacted with appropriate metal ions and makes it a truly biogenic method for the synthesis of biominerals and is thus not merely biomimetic.

8.2 Scope for future work

The prospective applications of bio-inspired crystal design are limited only by the imagination of the researcher. But it is hard to predict at his stage what applications these intriguing and complex structures might find, since we are still only just beginning to explore the range of morphology that can be made. Their most intermediate value is in showing just how far we can go in controlling the structure of materials over a range of length scales. As the need for such control becomes even more vital in the development of new advanced materials, we can hope that clever science might replace complicated, expensive, and labor-intensive technologist. Moreover, the question remains how the biominerals are grown into almost even sized? How does the biominerals obtain identical crystallographic orientation, identical shape within a living creature? How organic species interact with the growing crystal to alter its polymorphic expression and symmetry? Continued study in this area is important and essential. This mineralization processes may have very important applications in the future industrial processes, especially, this can be an environmentally friendly process.

8.3 References

[1] Weiner, S.; Addadi, L.; Wagner, H. D. *Mat. Sci. & Eng. C* **2000**, *11*, 1.

[2] Lowenstam, H. A. *Science*, **1981**, *211*, 1126.

[3] (a) Addadi, L.; Weiner, S. *Angew. Chem. Int. Ed.* **1992**, *31*, 153. (b) Sarikaya, M. *Proc. Natl. Acad. Sci. USA* **1999**, *96*, 14183.

[4] Kato, T.; Sugawara, A.; Hosoda, N. *Adv. Mater.* **2002**, *14*, 869.

List of Publications

1. **Rautaray, D.**; Kumar, A.; Reddy, S.; Sainkar, S.R.; Pavaskar, N.R.; Sastry, M. *CrystEngComm* **2001**, *45*, 1-4.

2. **Rautaray, D.**; Kumar, A.; Reddy, S.; Sainkar, S.R.; Sastry, M. *Crystal Growth & Design* **2002**, *2,* 197-203.

3. **Rautaray, D.**; Sainkar, S. R.; Pavaskar, N. R.; Sastry, M. *CrystEngComm* **2002**, *4*, 626.

4. **Rautaray, D.**; Sainkar, S. R.; Sastry, M. *Langmuir* **2003**, *19*, 888-892.

5. Reddy, S.; **Rautaray, D.**; Sainkar, S.R.; Sastry, M. *Bull. Mater. Sci.* **2003**, *26,* 283-288.

6. Shankar, S.; **Rautaray, D.**; Pasricha, R.; Pavaskar, N.R.; Mandale, A.B.; Sastry, M. *J. Mater. Chem.* **2003**, *13*, 1108-1111.

7. **Rautaray, D.**; Banpurkar, A.; Sainkar, S.R.; Limaye, A.V.; Ogale, S.B.; Sastry, M. *Crystal Growth & Design* **2003**, *3*, 449-452.

8. **Rautaray, D.;** Banpurkar, A.; Sainkar, S.R.; Limaye, A.V.; Pavaskar, N.R. Ogale, S.B.; Sastry, M. *Advanced Materials* **2003**, *15*, 1273-1278.

9. **Rautaray, D.**; Sainkar, S.R.; Sastry, M. *Chem. Mater.* **2003**, *15*, 2809-2814.

10. **Rautaray, D.**; Sainkar, S.R.; Sastry, M. *CrystEngComm* **2003**, *5*, 400-404.

11. **Rautaray, D.;** Sainkar, S.R.; Sastry, M. *Langmuir* **2003,** *19*, 10095-10099.

12. **Rautaray, D.**; Ahmad, A.; Sastry, M. *J. Am. Chem. Soc.* **2003**, *125*, 14656-14657.

13. Mandal, S.; **Rautaray, D.**; Sastry, M. *J. Mater. Chem.* **2003**, *13*, 3002-3005.

14. **Rautaray, D.**; Kumar, S. P.; Wadgaonkar, P.; Sastry, M.; *Chem. Mater.* **2004**, *16*, 988-993.

15. **Rautaray, D.;** Sinha, K.; Shiv Shankar, S.; Adyanthaya, S. D.; Sastry, M. *Chem. Mater.* **2004,** *16*, 1356-1361**.**

16. Mandal, S.; **Rautaray, D.**; Sanyal, A.; Sastry, M. *J. Phys. Chem. B*. **2004**, *108*, 7126-7131.

17. **Rautaray, D.**; Ahmad, A.; Sastry, M.; *J. Mater. Chem.* **2004**, *14*, 2333-2340.

18. **Rautaray, D.**; Sanyal, A.; Adyanthaya, S. D.; Ahmad, A.; *Sastry*, M.; *Langmuir* **2004**, *20*, 6827-6833.

19. Bansal, V.; **Rautaray, D.**; Ahmad, A.; Sastry, M. *J. Mater. Chem.* **2004**, *14*, 3303-3305.

20. Ahmad, A.; **Rautaray, D.**; Sastry, M.; *Advanced Functional Materials* **2004**, *14*, 1075-1080.

21. **Rautaray, D.**; Sanyal, A.; Ahmad, A.; Sastry, M. *Crystal Growth & Design* **2004**, (*ASAP Article*: DOI:10.1021cg0341858).

22. **Rautaray, D.**; Sinha, K.; Sainkar, S.R.; Pasricha, R.; Pavaskar, N.R.; Sastry, M.; *J. Am. Ceram. Soc.* **2004**, (In Press).

23. **Rautaray, D.**; Kavathekar, R.; Sastry, M.; *Faraday Discussion* **2004**, (*In Press*).

24. Bansal, V.; Sanyal, A.; **Rautaray, D.**; Ahmad, A.; Sastry, M.; *Adv. Mater.* **2004**, (Accepted).

25. **Rautaray, D.**; Mandal, S.; Sastry, M. *Langmuir* **2004**, (Accepted).

26. **Rautaray, D.**; Sastry, M. *J. Mater. Chem.* **2004**, (Accepted).

27. Sanyal, A.; **Rautaray, D.**; Bansal, V.; Ahmad, A.; Sastry, M. *Langmuir* **2004**, (Communicated).

28. Bansal, V.; **Rautaray, D.**; Bharde, A.; Ahire, K.; Sanyal, A.; Ahmad, A.; Sastry, M. *Advanced Functional Materials* **2004**, (Communicated).

29. Bharde, A.; **Rautaray, D.;** Bansal, V.; Ahmad, A.; Sarkar, I.; Yusuf, S. M.; Sanyal, M.; Sastry, M. *Nano. Lett.* 2004 (Communicated).

30. **Rautaray, D.**; Sastry, M. *CrystEngcomm* **2004** (Communicated).

31. Ankambar, B.; **Rautaray, D.**; Sastry, M. *J. Am. Chem. Soc.* **2004** (Communicated).

List of Patents Filed

1. Murali Sastry, **Debabrata Rautaray**, Kaustav Sinha "*A new process for the preparation of micron/nano size inorganic particles*" US & Indian Patent filed, CSIR308fn2003.

2. Murali Sastry, **Debabrata Rautaray** "*A new process for the preparation of micron/nano size inorganic particles*" US & Indian Patent filed, ncl-28-2003

3. Absar Ahmad, **Debabrata Rautaray**, Murali Sastry "*A biological process for the preparation of highly shaped and polymorph controlled mineral crystals*" US & Indian Patent filed, ncl-42-2003.

4. Murali Sastry, Absar Ahmad and **Debabrata Rautaray** "*A biological process for the removal of toxic metal ions in the form of carbonates*" US & Indian Patent filed, ncl-45-2004.

5. Absar Ahmad, **Debabrata Rautaray**, Ambrish Sanyal, Murali Sastry "*A biological process for the preparation of mineral crystals using seeds*" US & Indian Patent filed, ncl-55-2003.

6. Absar Ahmad, Murali Sastry, **Debabrata Rautaray** "*A biological process for the synthesis of oxide nanoparticles*" US & Indian Patent filed, ncl-65-2003

7. Murali Sastry, Absar Ahmad and **Debabrata Rautaray** "*A bioleaching process for the synthesis of silica nanoparticles using fungus*" US & Indian Patent filed, ncl-64-2004.

8. Murali Sastry, **Debabrata Rautaray** "*A new process for the preparation of minerals*" US & Indian Patent filed, ncl-71-2003.